

DISSERTATION

Flow induced vibrations of a U-shaped belt

ausgeführt zum Zwecke der Erlangung des akademischen Grades eines Doktors der
technischen Wissenschaften unter der Leitung von

Herr Ao.Univ.Prof. Dr. Herbert Steinrück
E322
Institut für Strömungsmechanik und Wärmeübertragung

eingereicht an der Technischen Universität Wien
Fakultät für Maschinenwesen und Betriebswissenschaften

von

Dipl. Ing. Johannes Strecha
Matrikelnummer 0626212
Heinrich-Waßmuth Straße 4/1/11, 2380 Perchtoldsdorf

Wien, im Juni 2015

Kurzfassung

Winderregte Schwingungen prismatischer Strukturen sind für Ingenieure und Architekten von großer Bedeutung. Umströmte, aerodynamisch stumpfe Körper wie Brücken, Maste oder Türme können durch mehrere Mechanismen zu Schwingungen angeregt werden. Die vorliegende Arbeit untersucht winderregte zwei-Freiheitsgrad Schwingungen (Flattern) eines Prismas mit U-Querschnitt mit bestimmten Aspektverhältnis.

Grundsätzlich wird das Verhalten des U-Profiles mittels Computational Fluid Dynamics (CFD) Simulation in einem zwei-dimensionalen Rechengebiet mit *ANSYS Fluent* untersucht. Ein Turbulenzmodell wurde aufgrund zahlreicher Validierungssimulationen ausgewählt. Um die Bewegung des U-Profiles zu ermöglichen wurde ein Teil des Rechengitters bewegt und deformiert. Die Lösung der Bewegungsgleichung erfolgt mit einer User defined function.

Untersuchung der Umströmung des festgehaltenen U-Profiles zeigt, dass, abhängig vom Anstellwinkel, unterschiedliche Strömungsformen vorliegen. Beide Strömungsformen sind zeitlich periodisch. Der prinzipielle Unterschied betrifft die Entwicklung der freien Scherschicht aus der sich Wirbel entweder in der Tasche des U-Profiles oder dahinter bilden. Der Vergleich mit Windkanalexperimenten zeigt, dass beide Strömungsformen der Simulation bis zu einem gewissen Grad der Realität entsprechen.

Die Neigung des U-Profiles zu sogenannten selbsterregten Schwingungen wird mit der Methode der aerodynamischen Ableitungen untersucht. Dabei wird die Abhängigkeit der Luftkräfte von der Bewegung des U-Profiles näherungsweise durch Untersuchung der Strömung um das zwangsbewegte Profil bestimmt.

Gekoppelte Simulationen zeigen dass das U-Profil Schwingungen in zwei Parameterbereichen ausführen kann. Zum einen kann die Wirbelbildung bei der jeweiligen Strömungsform Schwingungen anregen. Diese sind auf ein schmales Intervall von Strömungsgeschwindigkeiten begrenzt und hängen in ihrem Charakter stark von der Strömungsform ab. Bei höheren Strömungsgeschwindigkeiten können, wie von der Methode der aerodynamischen Ableitungen angedeutet, Flatter-Schwingungen ausgeführt werden. Ein Wirbel, der durch die Drehbewegung des Profils erzeugt wird konnte als Anregemechanismus identifiziert werden. Diese Schwingungen wurden ab einer bestimmten, kritischen Geschwindigkeit auch in Windkanalversuchen beobachtet und weisen größere Amplituden auf als die zuvor erwähnten wirbelerregten Schwingungen.

Die relevanten Strömungsphänomene wurden qualitativ auch bei begrenzten Rechenkapazitäten erfasst. Jedoch zeigen die Windkanalexperimente auch die Grenzen der derzeitigen Simulationsmethodik auf. Die eingesetzten Simulationsmethoden erlauben quantitative Vorhersagen nur sehr eingeschränkt.

Abstract

Wind-induced vibrations of prismatic structures in cross-flow are of greatest importance for engineers and architects. Aerodynamically bluff bodies such as bridge decks of suspension bridges, towers or masts can be excited to vibrations by several mechanisms. This thesis studies wind-induced flutter vibrations of a prism with U-shaped cross section.

The investigation relies on Computational Fluid Dynamics (CFD) simulations carried out in a two-dimensional computational domain in *ANSYS Fluent*. The choice of the turbulence model is based on several validation simulations. Motion of the U-profile was handled by deforming and moving parts of the calculation mesh. The structural equations of motion were solved with a User-defined function.

Numerically, it was found that there are two distinct, time-periodic patterns of the flow around the U-profile. Depending on the angle of inclination vortices either form in the cavity of the U or behind it. Comparison with wind tunnel experiments shows that both flow patterns have certain resemblance with the real flow.

The possibility of so-called self-excited vibrations was analysed with the method of aerodynamic derivatives. The dependence of the aerodynamic forces on the profile motion is approximated by studying the flow around a U-profile which is forced to move.

Coupled simulations of free vibrations show that the U-profile can be excited to vibrations in two different parameter regimes. Firstly, the vortex shedding under either flow pattern can excite vibrations. These vibrations are confined to a narrow interval of flow velocities. Their appearance depends on the flow pattern. Secondly, as was indicated by the aerodynamic derivatives, self-excited flutter vibrations are possible at large flow velocities. A vortex induced by a small pitching motion of the profile was identified as excitation mechanism. These vibrations were also observed in wind tunnel experiments for flow velocities greater than a certain critical flow velocity. Their amplitude is larger than the amplitude of the previously mentioned vortex induced vibrations.

The qualitative nature of the vibration regimes could be captured by 2D simulations. However, the wind tunnel experiments also highlight the limitations of the simulation approach. The predictive power of the applied simulation methods turned out to be very limited.

Acknowledgements

I owe my deepest gratitude towards Professor Herbert Steinrück, supervisor of my thesis. His guidance of my research not only made this thesis possible but also greatly enhanced my understanding of fluid mechanics and science itself. His patience with a doctoral student having a wife and kids will ever be remembered.

I would also like to thank Prof. Stanislav Pospíšil from the Institute of Theoretical and Applied Mechanics, Prague. The collaboration started with him and his group has greatly enhanced the scope of this thesis through many discussions and by enabling many jointly carried out experiments at the Centre of Excellence Telč (CET).

I also thank my colleagues at the CET: Prof. Sergey Kuznetsov for many hours spent carrying out wind tunnel tests and discussing; Radomil Král for discussion and the test-stand; the staff at the CET for always being helpful and creative and never looking down on academics doing practical work.

Furthermore I am indebted to Prof. Alois Steindl who has provided substantial help with mechanic models and also through discussions.

This thesis would not exist without the support of many more people: I thank my colleagues at the Institute of Fluid Mechanics: Harald Neth and Iris Mansky for help and guidance at our laboratory; Thomas Hofstätter for help with coordinating bachelor students. Thomas and Markus Müllner, Georg Meyer, Christoph Buchner and many others for fruitful discussions.

The bachelor students Matthias Schreiner, Lorenzo Spitzzy, Johanna Dragan, Phillip Gartlehner, Fabian Klappbacher, Elke Lesch, Felix Enichlmayer, Kerstin Schwaiger, David Himmelbauer and Sebastian Trummer worked at our institute and contributed to this research with findings from their theses.

Last but not least I thank my wife Corina and my family. Their unfailing support was and is invaluable to me.

Contents

1. Introduction	1
1.1. Simulation of fluid flow	2
1.2. The flow around bluff bodies	3
1.3. Vibrations in cross-flow	5
1.3.1. Vortex-induced vibrations	5
1.3.2. Self-excited vibrations and aerodynamic derivatives	6
1.3.3. Aerodynamic interferences, conjoint galloping and vortex shedding	8
2. Numerical methods and wind tunnel tests	9
2.1. Simulations	9
2.1.1. Selecting the turbulence model: separation at a curved boundary	10
2.1.2. Selecting the turbulence model: shear layer re-attachment	15
Calculation mesh and model settings	17
Results	18
2.1.3. Choice of the turbulence model	23
2.1.4. Rigid body motion	23
2.1.5. U-profile: Mesh 1	26
2.1.6. U-profile: Mesh 2	29
2.2. Wind tunnel experiments	33
2.2.1. Mechanical model of the belt	33
2.2.2. Particle Image Velocimetry	35
2.2.3. Two-degree-of-freedom test stand	37
2.2.4. Tensioned belt experiments	38
3. The flow around a stationary U-profile	41
3.1. 2D Simulation at several angles of inclination	41
3.1.1. The R-flow pattern	43
3.1.2. The U-flow pattern	47
3.1.3. On the initial conditions and the change of flow patterns	52
3.1.4. Influence of the angle of inclination	56
3.2. Comparison with PIV wind tunnel tests	59
3.2.1. Time-averaged flow fields	59
3.2.2. Flow-field snapshots (R-flow pattern)	60
3.2.3. Flow-field snapshots (U-flow pattern)	62
3.2.4. Influence of the angle of inclination	64
3.2.5. Implications	66

4. Aeroelastic stability by forced motion simulations	68
4.1. Aerodynamic derivatives of a U-profile	68
4.2. Determining stability using the aerodynamic derivatives	71
4.2.1. The k-method	72
4.2.2. The p-k method	73
4.2.3. Results	73
5. 2D Simulation of flow induced vibrations	77
5.1. Simulations	77
5.1.1. SDoF heave vibrations	78
5.1.2. SDoF pitch vibrations	84
5.1.3. 2DoF flutter vibrations	91
5.2. Rigid section model experiments	95
5.2.1. Verifying the critical velocity for self-excited vibrations	95
5.2.2. Verifying vibrations at low reduced velocities	95
5.3. Tensioned belt experiments	97
6. Conclusions	101
6.1. The flow around a stationary profile	101
6.2. Aeroelastic stability by forced motion simulations	102
6.3. 2D Simulation of flow induced vibrations	102
6.3.1. Unique aspects of this thesis	103
A. Simulation data	104
B. Rigid body solver	120

Glossary

- 2D-CFD** CFD simulations in a two-dimensional computational domain. [41](#), [59](#), [61](#), [63](#), [64](#), [66](#), [69](#), [70](#), [101](#), [102](#)
- 2DoF** Double Degree of Freedom. [xiv](#), [26](#), [37](#), [38](#), [91–93](#), [95](#), [102](#)
- BARC** Benchmark on the Aerodynamics of a rectangular 5:1 Cylinder. [2](#), [3](#), [102](#)
- CC** Curvature Correction. [18](#), [20](#), [21](#)
- CET** Centre of Excellence Telč. [33](#), [39](#)
- CFD** Computational Fluid Dynamics. [2–4](#), [7](#), [23](#), [77](#), [103](#)
- CTA** Constant Temperature Anemometry. [37](#), [64](#)
- DDES** Delayed Detached Eddy Simulation. [3](#)
- DES** Detached Eddy Simulation. [2](#), [3](#)
- EWT** Enhanced Wall treatment. [17](#), [20](#), [21](#)
- IIE** Instability Induced Excitation. [5](#), [86](#)
- ILEV** Impinging Leading Edge Vortices. [4](#), [101](#)
- k ω -SST* *k ω* Shear Stress Transport (turbulence model). [xii](#), [7](#), [9–12](#), [14–22](#), [41](#)
- LES** Large Eddy Simulation. [2](#), [3](#), [5](#), [9](#), [102](#)
- LEVS** Leading Edge Vortex Shedding. [4](#), [101](#)
- LR** Low Reynolds number corrections. [18](#), [20](#), [21](#)
- MIE** Motion Induced Excitation. [5](#), [6](#), [86](#)
- PIV** Particle Image Velocimetry. [xii](#), [xiii](#), [35](#), [36](#), [59](#), [60](#), [63–65](#), [101](#)
- RANS** Reynolds-averaged Navier-Stokes. [2](#), [3](#), [5](#), [7](#), [10](#), [101](#), [102](#)
- RMS** Root mean square. [12](#), [13](#)

SDoF Single Degree of Freedom. [xiv](#), [78](#), [79](#), [82](#), [84](#), [85](#), [87](#), [88](#), [90](#), [91](#), [93](#), [102](#), [103](#)

SG Structured Grids. [18](#), [20](#), [21](#)

SO Second Order discretizations. [17](#), [20](#), [21](#)

TKE turbulent kinetic energy. [59](#), [60](#)

UDF User-defined function. [10](#), [24](#), [26](#)

URANS unsteady RANS. [2](#), [3](#), [9](#), [10](#), [23](#), [61](#), [62](#), [102](#)

VIV Vortex Induced Vibrations. [4–6](#), [8](#), [77](#), [78](#), [80](#), [86](#), [87](#), [91](#), [95](#)

WF (Log-law) Wall functions. [18](#), [20](#), [21](#)

List of Symbols

Lowercase letters

		Unit	on Pages (digest)
c	damping constant	kg/s	73
c_D	drag coefficient	–	10, 42
c_{Fy}	vertical force coefficient	–	16
c_L	lift coefficient	–	42
c_M	torsional moment coefficient	–	42
c_φ	rotational damping constant	kg m ² /rad s	10
c_y	linear damping constant	kg/s	10
d	cylinder diameter	m	11
f	frequency	Hz	68
f_0	eigenfrequency	Hz	77
\hat{f}_{\max}^*	frequency pertaining to the the fourier coefficient with maximum amplitude of a quantity	Hz	xiv, 82, 90
f_{vs}	vortex shedding frequency	Hz	37
g	fictive damping	–	72
i	imaginary unit	–	72
k	turbulent kinetic energy	m ² /s ²	41
k_φ	torsional spring constant	Nm/rad	10
k_y	linear spring constant	N/m	10
m	mass	kg	71
p	static pressure (only in equation (2.1))	Pa	9
s	tension acting on a fiber of the belt base	N/m ²	34
$s_{ u }$	standard deviation of the flow velocity magnitude	m/s	60
t	time	s	44
t_0	reference time	s	44
t_b	thickness of the base of the U-profile	m	33
t_s	sampling time	s	59
\tilde{t}	dimensionless time	–	43
\bar{u}	average flow velocity, Reynolds-averaged quantity in equation(2.1)	m/s	60
u_i	sampled values of the flow velocity (magnitude)	m/s	59

u_∞	far-field flow velocity	m/s	11, 16, 42, 77
u_i, u_j	flow velocity components, $i, j = 1, 2, 3$	m/s	9
w	displacement of the base of the belt in vertical direction	m	34
x_1	horizontal coordinate	m	23
$x_1^{(o)}$	horizontal original location of a mesh node	m	23
x_2	vertical coordinate	m	23
$x_2^{(o)}$	vertical original location of a mesh node	m	23
x_i, x_j	coordinate (see x_1, x_2)	m	34
y	vertical degree of freedom	m	34, 77
y^+	dimensionless wall distance	–	11
z	vector describing a harmonic motion (two degrees of freedom)		71, 72
\bar{z}	complex coefficients describing a harmonic motion (two degrees of freedom)		72

Capital letters

		Unit	on Pages (digest)
A_i^*	aerodynamic derivative, pitch motion ($i=1 \dots 4$)	–	69
$A_{12},$ A_{34}	matrices of aerodynamic derivatives		71
B	width of a solid structure	m	33, 42
C_f	Skin friction coefficient		14
D	aerodynamic drag force	N	10, 16, 42
F_y	aerodynamic force in vertical direction	N	16
H	frontal height of a solid structure	m	16, 35, 42
H_i^*	aerodynamic derivative, heave motion ($i=1 \dots 4$)	–	69
I	turbulence intensity	–	41, 73
I_T	mass moment of inertia	kg m ²	71
K	reduced frequency	–	68
K_0	reduced eigenfrequency	–	72
L	aerodynamic lift force	N	16, 42, 68
\hat{L}_φ	average peak of the harmonic response of the lift force due to pitching motion	N	70
\hat{L}_y	average peak of the harmonic response of the lift force due to heaving motion	N	69, 70
D	aerodynamic torsional moment force	N	42, 68
M	mass matrix		71

\hat{M}_φ	average peak of the harmonic response of the aerodynamic torsional moment due to pitching motion	Nm	70
\hat{M}_y	average peak of the harmonic response of the aerodynamic torsional moment due to heaving motion	Nm	70
\Re	(operator) real part of a complex number		73
R_1	Radius of the rigid mesh region	m	23
R_1	Radius of the deforming mesh region	m	23
S	tensioning force acting on the belt	N	33, 39
U^*	reduced velocity	–	72, 78
U_{fm}^*	reduced velocity, made dimensionless with a different frequency	–	68

Greek letters

		Unit	on Pages (digest)
δ	logarithmic decrement, a subscript specifies the respective degree of freedom	–	38
μ	dynamic viscosity of air	Pa s	41
μ_t	turbulent eddy viscosity	Pa s	41
N	Total number of samples	–	60
ν	kinematic viscosity of air	m ² /s	10, 15, 41
ω	angular frequency	rad/s	68
ω_0	angular eigenfrequency	rad/s	71
φ	rotational degree of freedom	rad	34, 77
$\psi_{L,\varphi}$	phase shift of the harmonic response of the lift force due to a pitching motion	–	70
$\psi_{L,y}$	phase shift of the harmonic response of the lift force due to a heaving motion	–	69, 70
$\psi_{M,\varphi}$	phase shift of the harmonic response of the aerodynamic torsional moment due to a pitching motion	–	70
$\psi_{M,y}$	phase shift of the harmonic response of the aerodynamic torsional moment due to a heaving motion	–	70
ρ	density of air	kg/m ³	42, 69
τ_w	wall shear stress	N/m ²	14

Subscripts and Superscripts

Unit on Pages
(digest)

$\bar{}$	(overbar) average of a quantity	xiii, 45
Δ	(prefix Delta) difference of a quantity at two time instances	26
$\dot{}$	(overdot) derivative with respect to time	68
$\hat{}$	(hat) average peak value	68, 78
i	(subscript straight i) index number	25, 60
i, j	(subscript italic i or j) indicates the component of a vector ($i, j = 1, 2, 3$)	9
\max	(subscript max) maximum of a quantity	59
(P)	(superscript P) experimentally determined quantity	59
(R)	(superscript R) quantity under R-flow conditions	43
\sim	(overset tilde) dimensionless quantity	43
(U)	(superscript U) quantity under U-flow conditions	47

Dimensionless numbers

		Unit	on Pages (digest)
Re	Reynolds number	—	10, 15, 41
Sc	Scruton number	—	38
St	Strouhal number	—	37

List of Figures

2.1. Circular cylinder (sketch)	11
2.2. Sketch of the computational domain (to scale).	11
2.3. Section of the calculation mesh close to the cylinder.	12
2.4. Time-average of the wall- y^+ at $\text{Re} = 8 \cdot 10^4$, $I = 1\%$, $\mu_t/\mu = 1$	13
2.5. Time-averaged flow-field of the flow around a circular cylinder	14
2.6. Time-average of the signed skin friction coefficient C_f	15
2.7. Separation angle and mean drag coefficient for several simulation setups.	16
2.8. Square prism (sketch)	16
2.9. Sketch of the computational domain (to scale).	17
2.10. Section of the calculation mesh close to the square prism.	18
2.11. Snapshot of the wall- y^+ values over the dimensionless length s/H for all sides of the square at $\text{Re} = 22400$, $\varphi = 12.6^\circ$, $I = 1\%$, $\mu_t/\mu = 1$	19
2.12. Vertical force coefficient under the $k\varepsilon$ -model	20
2.13. Vertical force coefficient under the $k\omega$ Shear Stress Transport (turbulence model) ($k\omega$ -SST) model	21
2.14. Square prism: flow-field snapshots at the time instant of maximum lift force.	22
2.15. Mesh deformation strategy: The inner region is moved as a rigid body. The outer region is deformed.	24
2.16. Iterative coupling (flow chart)	25
2.17. Example: Difference between a solution with and without implicit update for several time-step sizes.	27
2.18. Convergence of the lift coefficient c_L during a time-step.	28
2.19. Computational domain (sketch)	28
2.20. Mesh resolution at the U-profile.	29
2.21. Computation mesh (U-profile variant 1)	30
2.22. Computational domain (sketch)	31
2.23. Computation mesh (U-profile variant 2).	32
2.24. Schematic drawings of the wind tunnel at the CET [49].	33
2.25. Sketch of the belt.	34
2.26. Displaced cross-ection of the belt.	34
2.27. Photo of the plexi-glass model mounted on the auxiliary plate.	36
2.28. Sample image acquired during the Particle Image Velocimetry (PIV) experiments.	36
2.29. The two-degree of freedom test-stand.	37
2.30. Photos of the balsa wood model.	38

2.31. Test stand photo (tensioned U-belt)	39
3.1. U-profile (sketch)	42
3.2. Flow patterns visualised by particle pathlines	42
3.3. Snapshots of the flow-field under the R-flow pattern	44
3.4. Aerodynamic forces under the R-flow pattern	45
3.5. Spectrum of the mean-free lift coefficient $c_L - \bar{c}_L$ under the R-flow pattern. \hat{c}_L^* is the Fourier coefficient, N is the number of timesteps considered in the discrete Fourier transform.	45
3.6. Flow field at the leeward flange of the U (R-flow pattern)	46
3.7. Snapshots of the flow field under the U-flow pattern	48
3.8. Aerodynamic forces under the U-flow pattern	49
3.9. Spectrum of the mean-free lift coefficient $c_L - \bar{c}_L$ under the U-flow pattern. \hat{c}_L^* is the Fourier coefficient, N is the sample size.	49
3.10. Pressure contours at the time instance of maximum lift and large torsional moment (snapshot figure 3.7,d).	50
3.11. Time-series of the lift coefficient under the U-flow pattern.	50
3.12. Flow field at the leeward flange under the U-flow pattern	51
3.13. Scheme of the simulation strategy to test which flow pattern can be re- alised at a given inclination angle: The angle of inclination during three typical simulation runs.	52
3.14. Snapshots of the flow field during the flow pattern change	54
3.15. Lift coefficient during the transition from U-flow to R-flow pattern. Labels correspond to subfigures in figure 3.14, $\tilde{t}_0 = 7.5$	55
3.16. Average aerodynamic forces for several angles of inclination	57
3.17. Fluctuation of the aerodynamic forces for several angles of inclination	58
3.18. U-profile: Time-averaged flow field (PIV).	60
3.19. U-profile: Time-averaged flow-field (2D-CFD simulation)	61
3.20. Snapshot of the simulated flow-field (R-flow pattern) with two u-velocity profiles and a turbulence intensity isoline, $I = 15\%$	62
3.21. Snapshot of the simulated flow-field (U-flow pattern) with a u-velocity profile and a turbulence intensity isoline, $I = 15\%$	62
3.22. Snapshot of the flow-field (PIV), visualised by arrows and a horizontal- velocity profile. The shear layer is curved weakly.	63
3.23. Three successive snapshots of the flow-field (PIV), visualised by arrows and a u-velocity profile.	65
3.24. Frequency spectrum of the flow velocity magnitude in the wake of the U-profile at inclination $\varphi = 5^\circ$	66
3.25. Frequency spectrum of the flow velocity magnitude in the wake of the U-profile at inclination $\varphi = -5^\circ$	67
4.1. Lift coefficient under heave motion (Simulation)	69
4.2. Spectrum of the aerodynamic forces under forced motion	70
4.3. Aerodynamic derivatives	71

4.4. Stability as predicted by aerodynamic derivatives (damping)	74
4.5. Stability as predicted by the aerodynamic derivatives (reduced frequencies)	75
4.6. Stability as predicted by aerodynamic derivatives (damping)	75
4.7. Stability as predicted by the aerodynamic derivatives (reduced frequencies)	76
5.1. Displaced U-profile (sketch)	77
5.2. SDoF heave simulations: vibration amplitudes	79
5.3. Snapshots of the flow-field at $U^* = 7.4$ showing the “hybrid” U-R-flow pattern. $\tilde{t} = t \cdot \text{St}^{(R)} u_\infty / H$	81
5.4. Frequency corresponding to the maximal heave Fourier coefficient under Single Degree of Freedom (SDoF) heave vibrations.	82
5.5. Time-averaged flow velocity in horizontal direction at in the wake behind the U-profile.	83
5.6. SDoF pitch simulations: vibration amplitudes	85
5.7. Amplification of the torsional moment fluctuation at several reduced ve- locities.	86
5.8. Time-series of the mean-free moment coefficient $c_M - \bar{c}_M$ under the R-flow pattern, compared for the stationary case and $U^* = 14$ (R-flow pattern, SDoF pitch).	87
5.9. Time-series of the mean-free moment coefficient $c_M - \bar{c}_M$ and pitch angle φ at $U^* = 14$ (R-flow pattern, SDoF pitch).	88
5.10. Snapshots of the vorticity contour at $U^* = 14$ (R-flow pattern, SDoF pitch)	88
5.11. Snapshots of the surface pressures acting on the horizontal sides of the U-beam.	89
5.12. Frequency corresponding to the maximal pitch Fourier coefficient under SDoF pitch vibrations.	90
5.13. Double Degree of Freedom (2DoF) simulation: vibration amplitudes . . .	92
5.14. Frequency corresponding to the maximal heave or pitch Fourier coefficient in case of 2DoF vibrations.	93
5.15. Snapshot of the vorticity magnitude under the R-flow pattern at $U^* = 14$ at the time-instance of minimal torsional moment.	94
5.16. Free vibration wind tunnel tests (rigid section model, low eigenfrequency)	96
5.17. Free vibration wind tunnel tests (rigid section model, high eigenfrequency)	97
5.18. Free vibration wind tunnel tests (tensioned belt, zero inclination)	99
5.19. Free vibration wind tunnel tests (tensioned belt, non-zero inclination) . .	100

List of Tables

2.1. Model properties (rigid section model experiments)	38
2.2. Damping and eigenfrequency of the rigid section model test setup	39
2.3. Model properties (tensioned U-belt)	40
2.4. Damping and eigenfrequencies (tensioned U-belt)	40

1. Introduction

Vibrations due to fluid flow are manifold in character and impact. Standard references cover the topics of fluid-conveying pipes, vibrations of aircraft wings, vibrations of prismatic bodies in cross-flow, vibrations of buildings like masts, bridges or towers, and scenarios where multiple structures are involved, such as pipe bundles, or arrays of buildings [11, 73, 79, 80, 81].

For civil engineers, vibrations due to wind action are of great interest because of their paramount importance for the safety and reliability of bridges, towers, masts and so on. Events like the collapse of the Tacoma Narrows Bridge [39] or the collapse of three cooling towers of the Ferrybridge Power Station in Ferrybridge, England [92] due to wind caused enormous interest of engineers and scientists alike. Since these events several approaches to determining the response of a structure to wind were followed. Seldomly, the response of a structure can be given as a closed form solution. More often, approximate relations, that rely on input from experiments can be employed, such as the method of aerodynamic derivatives (see below). More recently efforts are made to reduce the need for experiments by employing computer simulations. However, the correct choice of numeric methods and models, especially models for turbulent flow conditions, has to be determined.

In this thesis, flow-induced vibrations of a prismatic structure in cross flow, specifically a tensioned belt with U-shaped cross section and a given aspect ratio are discussed. The motivation of this investigation originates in the aerodynamic stability analysis of a freely suspended conveyor belt. The tension of the belt has the greatest influence on its eigenfrequencies. In contrast, the eigenfrequencies of bridge decks, towers etc. are given by their stiffness. Therefore, the eigenfrequencies of their first bending (heaving) and torsion (pitching) mode are not equal in general. On the other hand, the eigenfrequencies of the tensioned belt are almost equal (see section 2.2.1). Furthermore, we will assume that the cross section of the belt does not deform under vibration. Thus, the belt can be abstracted as a profile with U-shaped cross section for the purpose of computer simulations.

In a historic context, the U-profile can be seen as a simplification of the Tacoma Narrows bridge deck. In a scholarly context, the U-profile is an extension to the often discussed rectangular prisms and H-shaped prisms. However, the aerodynamic and aeroelastic properties of a U-profile were the focus of only a few scientific investigations. Of the many references to follow, the U-profile was studied in [5]. Most other studies focus on generic bridge deck sections (trapezoids), rectangular prisms, H-shaped prisms or scale models of real bridges with a more complex geometry. As explained in more detail below, we expect that the cavity of the U-profile will yield interesting flow field configurations and vortex formation patterns. Such observations have been made for the

flow around H-shaped prisms and the flow over open cavities (see below, section 1.2).

The focus of the investigations are excitation mechanisms of flow induced vibrations relevant for a tensioned belt with U-shaped profile. The flow field and flow induced vibrations of this U-profile are studied with the help of [Computational Fluid Dynamics \(CFD\)](#) simulations. Computationally inexpensive methods are employed to render parametric studies feasible. Wind tunnel tests are carried out to verify the validity of the chosen approach. Thus, this work aims to extend the knowledge in the following fields:

- The aerodynamic and aero-elastic properties of structures with U-shaped cross-section.
- The fidelity of computationally inexpensive methods to simulate bluff body flows.
- The feasibility and usefulness of coupled flow and motion simulations.

1.1. Simulation of fluid flow

Over the past years a growing set of numeric methods was developed. A vast amount of papers describe the use of [Reynolds-averaged Navier-Stokes \(RANS\)](#) turbulence models in a two-dimensional computational domain. Our own experience with this setup is described in chapter 2. Simulations in a three-dimensional domain demand much more computational power. Naturally, the necessary resolution in spanwise direction increases the computational degrees of freedom drastically. Simulations are further complicated by the unknown necessary spanwise depth of the domain and the necessary resolution. Additionally, results published by Fröhlich and Terzi [32] discourage the use of [unsteady RANS \(URANS\)](#) methods for complex three-dimensional flows. Pure [Large Eddy Simulation \(LES\)](#) of wall-bounded flows at high Reynolds numbers are still too expensive to conduct. Spalart et al. [96] not only estimated the cost for the [LES](#) of an aircraft wing, but also proposed [Detached Eddy Simulation \(DES\)](#) to reduce the computational cost. The subgrid model should act as a [RANS](#) model in near-wall regions. Following this idea many other *hybrid RANS/LES* formulations were proposed e.g. [94, 66, 28, 36, 104]. Note, that not every approach (in particular un-modified [DES](#)) is suitable for the application to bluff body flow since the modified subgrid-model may have an adverse effect on the correct prediction of the flow at shear layer re-attachment points [76].

Studies of the application of [LES](#)-related techniques to bluff-body flow are sparse in number compared to the available [RANS](#)-based studies. Sun et al. [99] reports the use of pure [LES](#) to simulate flow-induced vibrations of a circular cylinder and a rectangular cylinder at Reynolds-numbers 200 and 500. Despite considerable effort he found the [LES](#) results to be inaccurate and relates this to an inadequate resolution in near-wall regions. Later, Bai and Qin [4] employ [DES](#) simulations on calculation meshes having $2 \cdot 10^6 \dots 3 \cdot 10^6$ cells. Simulation results of the flow around an airfoil, a U-shaped prism and generic bridge deck sections are compared with wind tunnel results. The results obtained by 3D simulations were reported to be more accurate than 2D simulations. Another set of publications revolves around the [Benchmark on the Aerodynamics of a rectangular 5:1](#)

Cylinder (BARC) benchmark [6], targeting the flow around a 5:1 rectangular prism. Two studies employ alternative URANS methods, namely linearisations of explicit algebraic Reynolds stress models [60, 59]. In the latter reference a direct comparison between simulations employing URANS and DES methods is given. It is described that the RANS simulations predict time-periodic aerodynamic forces where DES simulations predict seemingly chaotic time-series. Furthermore the three-dimensionality of the flow-field is much more pronounced in DES simulations than it is in URANS simulations. Further studies focus on the application of DES [58] and point out the influence of the spanwise discretisation [12]. An overview of the progress within the scope of the BARC [13] shows that many details regarding numerical methods and grid discretisations are still unclear, and that there is no “best-practice” guideline to this day. Therefore, we limit our efforts to simulations in a two-dimensional computational domain and desist from making precise quantitative predictions. In a way, Fröhlich and Terzi [32] summarizes many conclusions drawn in the above mentioned works by stating that (2D) URANS can be more successful than RANS simulations, but that such an approach is “delicate” and that experiments are required for validation.

Simulation studies that couple fluid flow and structural motion are described in [53] and [5]. In the first reference, the flow around a freely vibrating circular cylinder was studied by means of Delayed Detached Eddy Simulation (DDES) simulations. In the second reference the flow around a circular cylinder and a rectangular prism was studied by means of LES simulations. Both studies successfully used an iterative coupling approach, instead of solving the fluid and structure governing equations together. Yet, the employed simulation techniques (LES and DES) are relatively expensive. Shimada and Ishihara [93] successfully employed an URANS turbulence model to determine flutter onset velocities of rectangular prisms with various aspect ratios by CFD simulations in a two-dimensional computational domain.

Chapter 3 covers simulations of the flow around a stationary U-profile. Simulations with forced motion are covered in chapter 4 and coupled simulations, where the flow-field is solved together with the equations of motion are discussed in section 5.1.

1.2. The flow around bluff bodies

A prism with U-shaped cross-section belongs to the class of aerodynamically “bluff” bodies which share the property that the ratio of their characteristic cross-streamwise to streamwise lengths is of the order of unity [81]. In comparison to the flow around streamlined bodies such as airfoils, the flow around bluff bodies has additional interesting features.

The first to mention is the well known von Kármán vortex street, which develops due an instability in the wake of a bluff body [11]. The shedding of vortices causes fluctuations in the aerodynamic forces which are the subject of numerous research projects. The overview by [77] reviews several interesting effects: The vortex shedding can synchronise to the motion of the cylinder. The vortex shedding frequency and spanwise correlation depend on the Reynolds number. Predicting the point of separation in the flow around

a circular cylinder is a popular benchmark case for novel CFD codes, such as [107].

In the flow around a square prism, a bluff body more akin to the U-prism than the circular cylinder, the points of separation are given: The flow always separates from two corners of the prism, at least at small inclination angles. However, the flow may re-attach at some point on the side of the square, leading to more complex dynamics [56]. The re-attachment point is influenced by the free-stream turbulence intensity such that for higher turbulence intensities only one stable limit cycle exists [50]. Furthermore the local pressure distribution along the side of prismatic bodies depends greatly on the turbulence characteristics of the oncoming flow [54, 44, 65, 101]. The first three references report measured surface pressures on bluff bodies at different free-stream turbulence intensities. Special attention to re-attachment points and separation bubbles is paid. The last reference includes the effect of corner shapes which is important for industrial applications where perfectly straight edges are uncommon.

The flow around elongated bluff bodies, such as rectangular prisms with an aspect ratio greater than unity, is again more complex than the flow around bodies with aspect ratios close to unity. In the latter case, vortices form behind the body by roll-up of the free shear layer. This is called **Leading Edge Vortex Shedding (LEVS)**. When the aspect ratio of the body is greater than three, vortices form along the side of the prism. They impinge on the body surface and are therefore called **Impinging Leading Edge Vortices (ILEV)** [25]. Other elongated bluff bodies such as H-prisms also lead to ILEV conditions. Moreover, it was reported that the number of vortices travelling along the surface of the prism could be influenced by vibrating the prism [46, 47]. The travelling vortices also give rise to **Vortex Induced Vibrations (VIV)** [72]. The failure of the Tacoma Narrows bridge was could have been related to such surface vortices [8, 52, 63, 35]. Studies of the flow over open cavities similar to the cavity of the U-profile also indicate non-trivial flow conditions in the cavity [3, 42].

Different vortex formation patterns were also observed in the flow around short rectangular prisms with an aspect ratio much smaller than unity [70, 100]. The flow around such prisms is reported to be non-periodic. There appear to be two distinct flow-patterns characterised by the strength of the shear-layer roll-up. The flow changes intermittently between the two patterns which is reflected in the time-dependent aerodynamic lift and drag forces.

As it turns out the behaviour of free shear-layers will be of greatest importance in chapter 3, where the flow around a stationary U-profile is discussed. The notion of impinging vortices is especially important in the flow around such a body. Comparison with wind tunnel experiments will show that the simulations are qualitatively correct, but the real flow field is much more complex. The employed models do not allow an extensive study of the influence of the free-stream turbulence intensity, but it is shortly discussed by experiments. The different flow and vortex formation patterns will be of great importance to vibrations of the U-profile in cross-flow.

1.3. Vibrations in cross-flow

One suitable classification of flow induced vibrations is given in [74]. Relevant to this thesis are the **Instability Induced Excitation (IIE)** and the **Motion Induced Excitation (MIE)**. In the context of bluff body flow, the former (IIE) is related to the formation of vortices due to an instability of the wake [83] which cause fluctuating aerodynamic forces. The latter (MIE) is also known as *self-excited vibrations*. Vibrations are due to the response of the flow-field to a small motion of the body.

1.3.1. Vortex-induced vibrations

The scope of this thesis includes **VIV**, where an eigenmode of the structure is excited through periodic vortex formation. Vibrations of a circular cylinder are related to the well-known von Kármán vortex street and are extensively studied. Fundamental effects like synchronisation of the vortex shedding to the body motion (the so-called *frequency lock-in*) can be studied in this simple case [9, 34]. Thus, vortex shedding is more complex than a forcing of an oscillator with constant frequency. Yet, prismatic bodies with non-circular cross section may further increase the complexity of the flow. Vortices may travel along the surface of elongated prismatic bodies [70, 25]. It will be shown that such vortices are of great importance in the flow around a body with U-shaped cross section. Furthermore, the existence of intermittent flow pattern change, as described in [70, 100], which were observed in the flow around a short rectangular prism is also highly relevant, as will be seen in chapter 3.

Apart from experimental studies and simulations, so-called *wake-oscillator* models [37] are employed to study **VIV**. The fluctuating aerodynamic force due to the vortex shedding is considered as additional degree of freedom. Typically, it is represented by a Rayleigh-type or van der Pol equation. The trivial solution of these equations is unstable. In the homogeneous case the additional variable undergoes limit cycle oscillations. The wake oscillator equation is coupled with the equation of motion for the body. Even very simple models are capable of describing the frequency lock-in and hysteresis behaviour [51]. More complex phenomena like travelling waves on long cables [30] can be described. Recently, wake oscillators were also utilised to treat vibrations of bluff bodies like square cylinders [61], bridge decks [62] and systems with two-degree of freedoms [4]. The analytic nature of this approach lends itself to the inclusion of non-linear terms [78] to cover more and more complex phenomena like frequency dependent coupling terms. However, such wake oscillators can only be considered as a model for **VIV** do not describe the physics of the flow. This leaves crucial aspects, such as the choice of free parameters or even the nature of the coupling between structure and wake oscillator open [29]. Critics of wake oscillator models point out that there is no limit to the inclusion of additional terms, and thus the predictability and generality is very limited. Sarpkaya [89] even gives the advice to “make great strides to enhance the powers of computers [and] numerical methods” and to make use of “robust codes based on various versions of **RANS** and **LES**, which was taken to heart in chapter 5, especially so since every new wake-oscillator formulation has to rely on inputs from experiments

or simulations.

1.3.2. Self-excited vibrations and aerodynamic derivatives

A subclass of bluff bodies are susceptible to the second excitation mechanism noted above, **MIE**. Bodies of revolution like the circular cylinder are immune to **MIE** since a motion of the cylinder in cross-flow only changes the direction of the aerodynamic force acting on it, but not its magnitude [81]. Obviously, this does not apply to the profile with U-shaped cross-section investigated in this thesis. Compared to **VIV**, **MIE** can occur in larger parameter intervals and lead to vibrations with larger amplitude.

One of the first observations of **MIE** were the so-called *galloping* (i.e. transverse oscillations normal to the direction of the oncoming flow) vibrations of iced electric transmission lines [38]. The single-degree of freedom case can be conveniently studied: invoking the so-called *quasi-steady* assumption, it suffices to study the dependence of the aerodynamic forces on the inclination angle of the body. To justify this assumption it is required that any change of the flow-field due to a motion of the body is swept down sufficiently fast, which is often formulated in terms of a dimensionless flow velocity and the Strouhal number St (e.g. Blevin's criterion [11]). A prominent example is the study of galloping vibrations of a square cylinder [82]. In addition to the critical flow velocity, the amplitude of limit cycles can be predicted. These astounding results motivated many works aiming to generalize this concept for torsional or multi-degree of freedom vibrations. However, it was shown by Nakamura and Matsukawa [71] that the quasi-steady assumption cannot be upheld even for single degree of freedom torsional vibrations. Other approaches are required.

Theodorsen was successful in determining the stability of aircraft wings by an analytic method [102]. He considered aerodynamic forces that depend on the momentary position, velocity and acceleration of the profile. The factors before these quantities became known as *aerodynamic derivatives*. In the case of thin airfoils they could be computed analytically. In the 1970s, many works focused on applying his method to bluff structures and especially bridge decks, although they were formulated for aircraft wings and do not include flow separation. The framework of the aerodynamic derivatives was adapted for application to bridge decks by Scanlan and co-workers, e.g. [90, 91]. The aerodynamic derivatives describe the influence of a small motion of the body on aerodynamic forces. In contrast to the aforementioned quasi-steady theory, it is assumed that the small motion and the response are harmonic. This method can be applied to more general cases than transverse vibrations (galloping), but since it is a linear method only critical flow velocities can be predicted.

Typically, aerodynamic derivatives are obtained by wind tunnel experiments. The original works of Scanlan and co-workers calculated them from the structural response after an initial excitation.

Recently, system identification techniques were employed [86, 7]. The sensitivity of the aerodynamic derivatives and therefore of the critical flow velocities to the extraction method is studied extensively in [87, 17]. In computer simulations, it is easily possible to extract the aerodynamic derivatives by simulating the flow around the body performing

forced motion. Several publications exist, e.g. [33, 41, 88, 15, 69, 75]. Here, RANS turbulence models and a two-dimensional computational domain were used. The studies target Reynolds-numbers (based on the length of the model profile) of $Re \sim 10^5$. Ge and Xiang [33] employ a finite element method and a random vortex method in addition to a finite volume method with an unspecified RANS turbulence model. Ge and Xiang further report that the numerically obtained eighteen aerodynamic derivatives (heave, pitch, sway) of a H-prism differ substantially from experimental results ($\sim 25\%$). Huang et al. [41] reports the use of *ANSYS Fluent* in conjunction with the RNG- $k\varepsilon$ turbulence model. They used a grid topology where the cells in the vicinity of the profile are only moved, but not distorted. The eight aerodynamic derivatives (heave, pitch) for several generic bridge decks are calculated from simulation of the flow around the bridge deck undergoing forced motion. “Good agreement” with experimental results is reported. Šarkić et al. [88] reports the use of the open source CFD toolbox *OpenFOAM* and the $k\omega$ -SST turbulence model. “Good agreement” of the eight aerodynamic derivatives (heave, pitch) of a generic bridge deck section with experimental results was achieved. The turbulence model did not have an adverse effect on the accuracy of the aerodynamic derivatives, although some weaknesses in the prediction of the flow near flow separation points are mentioned. Brusiani et al. [15] relies on *ANSYS Fluent* and advocates the use of the $k\omega$ -SST turbulence model in conjunction with experiments for validation as well as the grid topology used in [41]. It is mentioned that the position of the re-attachment point is predicted incorrectly. Miranda et al. [69] calculate the aerodynamic derivatives of several rectangular prisms with different aspect ratios ranging from five to twenty. The commercial solver *ANSYS Fluent* and the $k\omega$ and $k\omega$ -SST turbulence models are used. Miranda et al. note that “good agreement” could not be achieved and reason that the behaviour of the shear layers is not predicted correctly in the simulations. Nieto et al. [75] reports the use of *OpenFOAM* and the $k\omega$ -SST turbulence model. Notably, use of relations between the aerodynamic derivatives introduced by Tubino [103] was made. The necessary computational effort to obtain eight aerodynamic derivatives could be reduced by half. However, the validity of these relationships could be disputed since Tubino [103] reported that a complete validation by experiments could not be achieved.

The aerodynamic derivatives are used to obtain critical velocities for vibration modes. While this is almost trivial for single-degree of freedom cases the analysis is more involved for coupled mode flutter because the derivatives depend on a dimensionless frequency. A good introduction is given in [40]. Iterative approaches, that are also applied in section 4, are described therein. Others express the frequency dependent aerodynamic derivatives by rational functions to avoid iterations [22]. Under certain circumstances even closed-form expressions for modal characteristics can be found [21, 20]. Some try to avoid the frequency dependence of the aerodynamic derivatives. In analogy to airfoils, a time-domain equivalent of the aerodynamic derivatives (the so-called *indicial functions*, [10]) can be found [16, 68].

In this thesis the aerodynamic derivatives are obtained by simulating the flow around the U-profile undergoing forced motion, described in chapter 4. Critical flow velocities are estimated and found to depend on the forcing amplitude greatly. It is also shown that this method yields unreliable results at low reduced velocities due to the non-linear

interaction of profile motion and vortex formation.

The main criticism of the aerodynamic derivatives targets their linear nature. The influence of the motion amplitudes applied when determining the derivatives is investigated in [31] and [23], as well as in chapter 4 of this thesis. Diana et al. [26] discusses possible non-linear extensions and presents results how limit cycle oscillations may occur below the conventionally predicted critical velocity. Matsumoto et al. [64] finds that the onset velocity of torsional flutter may be overestimated when relying on forced motion experiments, especially if the onset velocity is at low reduced velocities. This is related to specific vortex formation patterns not triggered by the forced motion that was applied to determine the derivatives.

1.3.3. Aerodynamic interferences, conjoint galloping and vortex shedding

Naturally, each mode of vibration has a critical flow velocity. When the respective critical velocities are close to each other, the structural damping influences which vibration mode is selected [63]. A recent experimental study focusing on the interaction between vortex shedding and galloping of a rectangular prism is described in [57].

The final set of simulation and wind tunnel results discussed in chapter 5 touches upon the interference of **VIV** and self-excited vibrations. It is shown that the flow patterns discussed earlier influence the amplitude and mode of **VIV** greatly. The comparison between single-degree of freedom and two-degree of freedom scenarios is used to illustrate the dependence of the vortex formation on the profile motion. Self-excited vibrations predicted by the aerodynamic derivatives are confirmed in experiments and simulations to some extent. The predictive power of coupled simulations and the method of aerodynamic derivatives is compared with experimental results.

2. Numerical methods and wind tunnel tests

In this chapter, numerical methods employed in the computer simulations (section 2.1) and the wind tunnel tests (section 2.2) are introduced. The design of the computer simulations and wind tunnel tests is based on a mechanical model for the belt. The most important aspects of this model, which is introduced in section 2.2.1, are:

- The ratio of the belt's heave and pitch eigenfrequencies is equal to one.
- The cross section of the belt does not deform under vibration.

2.1. Simulations

It was chosen to employ an **URANS** approach in a two-dimensional computational domain. Thus, the fluid flow is governed by the well known Reynolds-averaged continuity equation and the Navier-Stokes equations for incompressible flow [97]:

$$\frac{\partial \bar{u}_i}{\partial x_i} = 0 \quad (2.1a)$$

$$\frac{\partial \bar{u}_i}{\partial t} + \bar{u}_j \frac{\partial \bar{u}_i}{\partial x_j} = -\frac{1}{\rho} \frac{\partial \bar{p}}{\partial x_i} + \frac{\partial}{\partial x_j} \left(\nu \left(\frac{\partial \bar{u}_i}{\partial x_j} + \frac{\partial \bar{u}_j}{\partial x_i} \right) - \overline{u'_i u'_j} \right), \quad (2.1b)$$

$i = 1, 2(, 3)$. Since the simulations are performed in a two-dimensional computational domain, the averaged velocity in direction 3 is zero ($\bar{u}_3 \equiv 0$), but its fluctuation, accounted for by the turbulence model, is not zero ($u'_3 \neq 0$). The Einstein summation convention applies, an overbar denotes a Reynolds-averaged quantity and a prime denotes the turbulent fluctuation of a quantity. The turbulence model provides an approximation for the unknown Reynolds stress tensor (equation(2.1), red term). As turbulence models, the *realizable* $k\varepsilon$ model and the $k\omega$ -SST model were considered, both in the formulation of [1]. Our aim for qualitative results and the need for tested and computationally efficient methods allows the use of a two-dimensional computational domain. Thus, time-periodic results obtained by simulations correspond to the phase-average of a turbulent flow with infinite spanwise correlation length [15].

Large Eddy Simulations itself were deemed too expensive in terms of computational cost. Bruno (see [14]) carried out **LES** simulations of the flow around a rectangular cylinder at a Reynolds number of magnitude 10^4 on a computation mesh containing $1.75 \cdot 10^6$ cells. He reported that a single simulation required 15 days CPU-time. It

was estimated that about 10^7 cells were needed to simulate the flow around a U-profile at a Reynolds number of magnitude $\text{Re} \sim 10^5$, rendering parametric studies infeasible. Cell counts ranging from $3 \cdot 10^4$ to $\sim 2 \cdot 10^5$ were used for two-dimensional simulations employing URANS models.

According to the introductory discussion of the belt, we assume that the structure placed in the flow is rigid. Its center of mass and initial position is at the position $(0, 0)^T$. The structure has two degrees of freedom: vertical translation (y) and rotation about its long axis (φ). It is supported by springs with a linear characteristic. The equations of motion describing such a structure are

$$\frac{d}{dt} \begin{pmatrix} y \\ \varphi \\ \dot{y} \\ \dot{\varphi} \end{pmatrix} = \begin{pmatrix} 0 & 0 & 1 & 0 \\ 0 & 0 & 0 & 1 \\ -k_y/m & 0 & -c_y/m & 0 \\ D/I_T & -k_\varphi/I_T & 0 & -c_\varphi/I_T \end{pmatrix} \begin{pmatrix} y \\ \varphi \\ \dot{y} \\ \dot{\varphi} \end{pmatrix} + \begin{pmatrix} 0 \\ 0 \\ L/m \\ M/I_T \end{pmatrix}, \quad (2.2)$$

where the moment M is taken around the point $(0, 0)^T$.

The RANS equations(2.1) are solved using the CFD solver *ANSYS Fluent* in versions 13.0 (chapter 2.1) and later 14.5 (chapters 3 to 5). The equations of motion (2.2) are solved using a User-defined function (UDF) written as part of this research (see appendix B). The computation meshes were created in *IcemCFD* using a two-dimensional blocking containing unstructured blocks. All meshes contained only quadrilateral cells.

In the following two subsections, several variants of the $k\varepsilon$ and the $k\omega$ -SST turbulence models together with several computational meshes will be assessed in order to choose a suitable model for the simulations in chapters 3 to 5. The tests comprise the separation of a boundary at a curved wall and the re-attachment of a free shear layer. The flow separation at a curved boundary will be studied by simulating the flow around a circular cylinder. Shear layer re-attachment will be studied by simulating the flow around a square prism. In both cases the flow is not stationary and vortices form – as in the flow around the U-profile. Measured data is available for both test cases.

2.1.1. Selecting the turbulence model: separation at a curved boundary

The flow around a circular cylinder is used as the first test case. The cylinder with diameter d is placed in cross-flow with the flow velocity u_∞ . The time-dependent aerodynamic forces lift L and drag D per unit length act on the cylinder (figure 2.1). In this section the flow at a Reynolds-number of

$$\text{Re} = u_\infty d / \nu = 8 \cdot 10^4 \quad (2.3)$$

is considered. Two simulation studies in the same Reynolds-number regime are [55] and [85]. The time-dependent drag coefficients

$$c_D = D / \frac{1}{2} \rho u_\infty^2 d \quad (2.4)$$

obtained by the *realizable* $k\varepsilon$ turbulence model and the $k\omega$ -SST turbulence model are used for comparison.

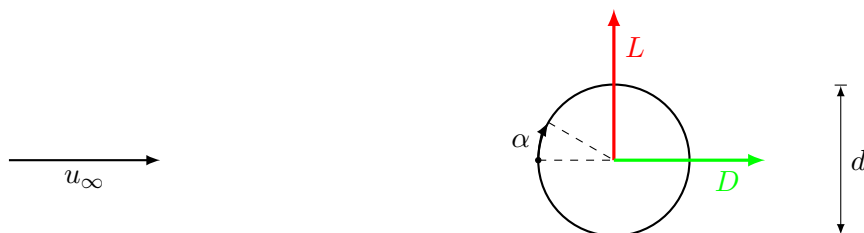


Figure 2.1.: Sketch of the circular cylinder in uniform flow and the aerodynamic forces lift L , drag D .

The cylinder is placed in a two-dimensional computation domain (figure 2.2). Uniform flow velocity is prescribed at the inlet boundary which was at a distance of $8.33d$ to the cylinder. Above and below the cylinder (at $\pm 12.5d$) the domain is bounded by symmetry conditions. The outflow boundary is placed at a distance of $25d$ behind the cylinder.

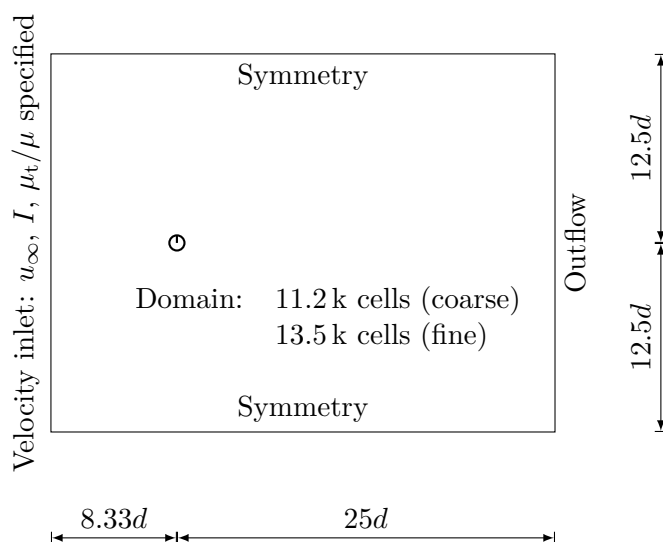
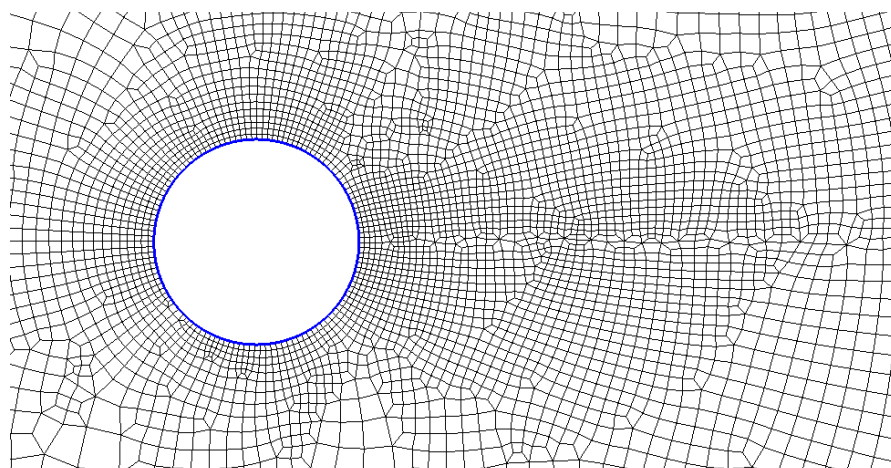
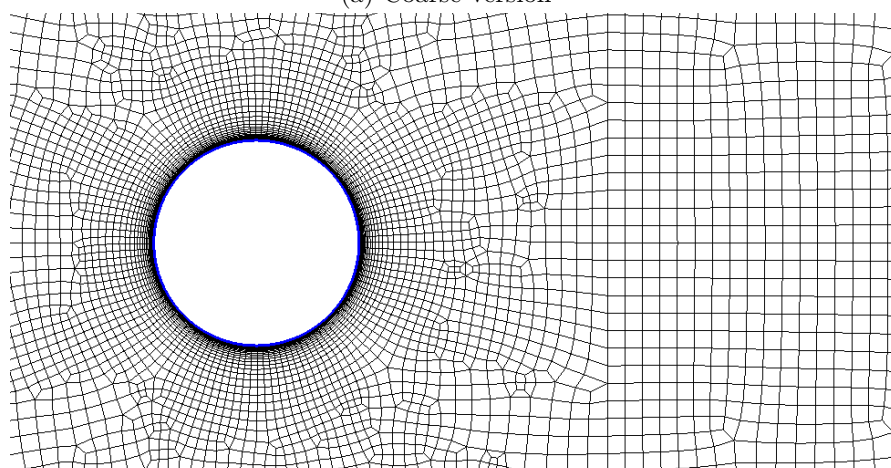


Figure 2.2.: Sketch of the computational domain (to scale).

Both calculation meshes were unstructured and had quadrilateral cells. The cylinder wall was resolved by 124 elements. The coarse mesh (figure 2.3a) consisted of approximately 11200 cells. The wall-normal resolution was chosen for standard wall functions implying that the first cell center is at a distance where the logarithmic law of the wall is valid ($y^+ > 30$). The fine mesh (figure 2.3b) consisted of 13500 cells and the wall-normal resolution was chosen for enhanced wall treatment, i.e. the first cell center should lie within the viscous sublayer ($y^+ \sim 1$). The enhanced wall treatment available in *ANSYS Fluent* blends viscous sublayer and log-law formulations according to the actual value of y^+ , promising y^+ independent results [1].



(a) Coarse version



(b) Fine version

Figure 2.3.: Section of the calculation mesh close to the cylinder.

The flow-field was time-averaged over four vortex shedding periods. The time-averaged y^+ values are shown in figure 2.4. It can be seen that the calculation meshes lead to wall- y^+ values as intended.

The time-averaged flow fields are compared in figure 2.5. Contours of the time-averaged velocity magnitude and **Root mean square (RMS)** velocity magnitude are shown. The $k\varepsilon$ at $I = 1\%$ and $\mu_t/\mu = 1$ leads to almost stationary flow conditions around the cylinder (figures 2.5a and 2.5b). As indicated by the **RMS** contours, vortices form behind the cylinder. A large almost stationary wake region is behind the cylinder. There is not much visual difference between the coarse (non-equilibrium wall functions) and the fine (enhanced wall treatment) computation mesh.

The $k\omega$ -**SST** turbulence model at $I = 1\%$ and $\mu_t/\mu = 1$ on the fine grid predicts that non-stationary flow conditions set in much earlier (figure 2.5c). As seen by the **RMS**

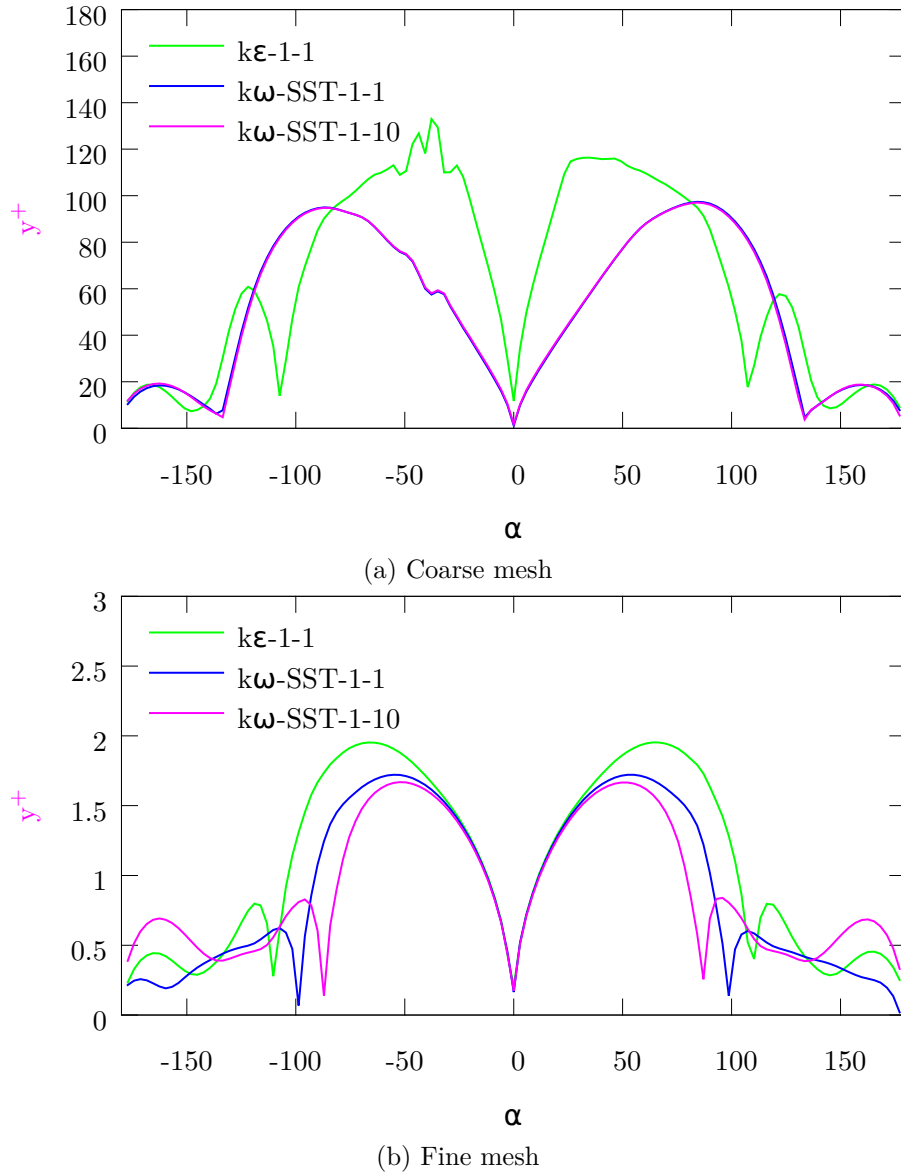


Figure 2.4.: Time-average of the wall- y^+ at $\text{Re} = 8 \cdot 10^4$, $I = 1\%$, $\mu_t/\mu = 1$.

velocity magnitude contours, the flow is weakly unsteady already before the cylinder. Large temporal variations of the velocity magnitude are predicted near the separation points. The flow behind the cylinder is strongly time-dependent. The same turbulence model in conjunction with the coarse computation mesh predicts a drastically different flow-field. On the coarse mesh the results are visually similar to the $k\varepsilon$ model simulations (figure 2.5d). The flow around the cylinder is almost stationary. The RMS contours indicate that only the flow behind the cylinder is time-dependent.

Change of the free-stream eddy viscosity ratio to $\mu_t/\mu = 10$ (the upper limit for

quiet ambient conditions given in [2]) does not change the result much. Again the $k\omega$ -SST turbulence model on the fine grid reports strongly time-dependent flow conditions immediately behind the cylinder (figure 2.5e). On the coarse mesh an almost stationary near-wake is predicted (figure 2.5f).

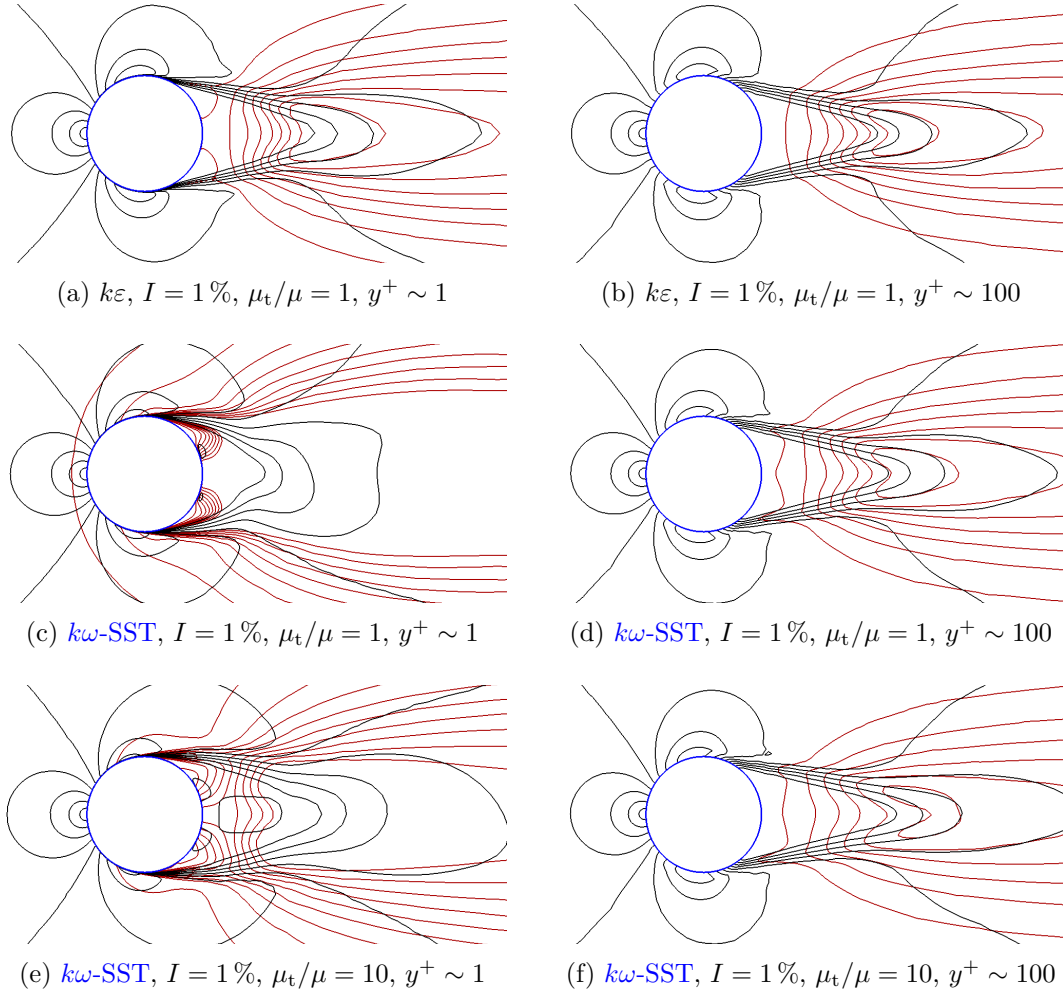


Figure 2.5.: Time-averaged flow-field of the flow around a circular cylinder: Contours of the normalised velocity magnitude (black, values: 0, 0.2, ..., 1.8) and the normalised root mean square of the velocity magnitude (red, values: 0, 0.05, ..., 0.45).

The skin friction coefficients C_f ,

$$C_f = \text{sign}(\vec{\tau}_w \cdot \vec{u}_\infty) \frac{\tau_w}{\frac{1}{2}\rho u_\infty^2} \quad (2.5)$$

for every simulated case are shown in figure 2.6. In the stagnation point at $\alpha = 0$ the skin friction coefficient is zero. It increases with α and then decreases again when α

approaches the separation angle. The symmetry of the curves shows that the sampling time chosen for averaging was long enough. In the skin friction coefficient curves obtained on the coarse calculation mesh influences of the mesh can be seen at $\alpha \approx 50^\circ$. The $k\varepsilon$ model appears to be more sensitive to this than the $k\omega$ -SST model. Nonetheless this is a strong indication that body-fitted boundary layers have to be part of future calculation meshes.

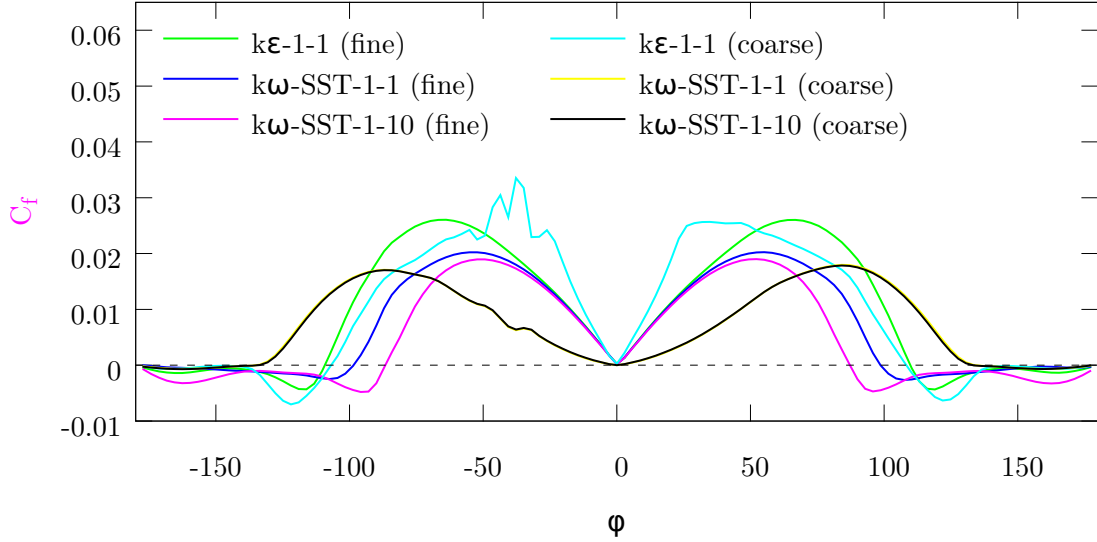


Figure 2.6.: Time-average of the signed skin friction coefficient C_f , equation (2.5)

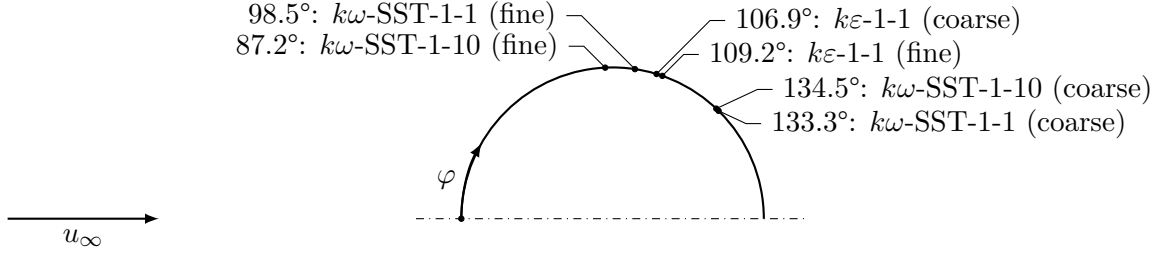
The time-averaged separation angles obtained by the $k\varepsilon$ model on the coarse and the fine grid are closely spaced (figure 2.7). The drag coefficient predicted by on the coarse mesh is slightly larger than the prediction obtained on the fine mesh, $c_D = 1.12$ and $c_D = 0.93$, respectively. However, the separation angle is larger on the coarse mesh than on the fine mesh. The $k\omega$ -SST model is much more sensitive to the grid resolution. For either eddy viscosity ratio the separation angle is greater than 130° on the coarse mesh and smaller than 100° on the fine mesh. Accordingly, the drag coefficient obtained on the coarse mesh is smaller than on the fine mesh.

These results show the importance of a fine resolution under the $k\omega$ -SST turbulence model. Varying the free-stream eddy viscosity ratio doesn't have a tremendous influence on the results.

2.1.2. Selecting the turbulence model: shear layer re-attachment

Simulations of the flow around a square prism were used to further refine the turbulence model settings. Data from [82] was used. Parkinson measured the aerodynamic forces on a square prism for several inclination angles (see figure 2.8). at a Reynolds-number of

$$Re = \frac{u_\infty H}{\nu} = 22300. \quad (2.6)$$



Configuration	Drag coefficient	Separation angle
$k\varepsilon, I = 1\%, \mu_t/\mu = 1, y^+ \sim 1$	1.12	109.2
$k\varepsilon, I = 1\%, \mu_t/\mu = 1, y^+ \sim 100$	0.93	106.9
$k\omega\text{-SST}, I = 1\%, \mu_t/\mu = 1, y^+ \sim 1$	1.20	98.5
$k\omega\text{-SST}, I = 1\%, \mu_t/\mu = 1, y^+ \sim 100$	0.92	134.5
$k\omega\text{-SST}, I = 1\%, \mu_t/\mu = 10, y^+ \sim 1$	1.09	87.2
$k\omega\text{-SST}, I = 1\%, \mu_t/\mu = 10, y^+ \sim 100$	0.91	133.3

Figure 2.7.: Separation angle and mean drag coefficient for several simulation setups.

The oncoming flow was smooth.

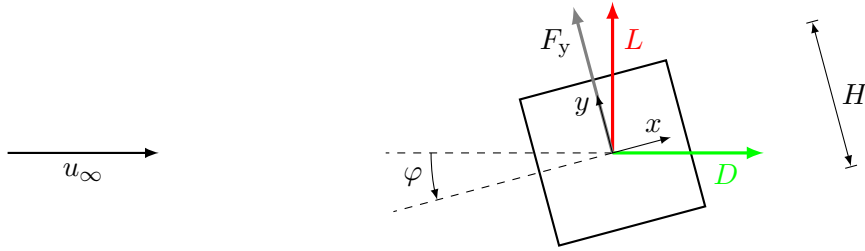


Figure 2.8.: Sketch of the inclined square prism in uniform flow and the aerodynamic forces lift L , drag D and vertical force F_y .

Parkinson reports that the vertical force per unit length

$$F_y = -L \cos \varphi + D \sin \varphi = c_{Fy} \cdot \frac{1}{2} \rho u_\infty^2 H \quad (2.7)$$

acting on the square prism has a positive slope with respect to variations of the angle of attack around zero degrees [82]. A point of inflection in the inclination dependent vertical force coefficient can be observed at about 8° inclination. A vertical force coefficient $c_{Fy} \approx 0.6$ is reached at about 13° inclination. For even higher inclination angles the vertical force decreases again. The point of inflection is thought to be only visible in low-turbulence flows [50]. Both, the point of inflection and the peak vertical force are related to the time-dependent re-attachment of the shear layer [56]. Because of the known

difficulties when free shear-layers in turbulent flows are involved, special attention will be paid to the maximal vertical force coefficient and the inflection point.

Calculation mesh and model settings

The square prism is embedded in a rectangular domain (figure 2.9). Symmetry conditions are defined at the top and bottom of the domain. They are placed at a vertical distance of $12.5H$ to the prism. The velocity inlet is placed at $8.5H$ upstream and the outflow is $25H$ downstream. A single side of the prism was discretised by 14 elements (coarse version) or 148 elements (fine version).

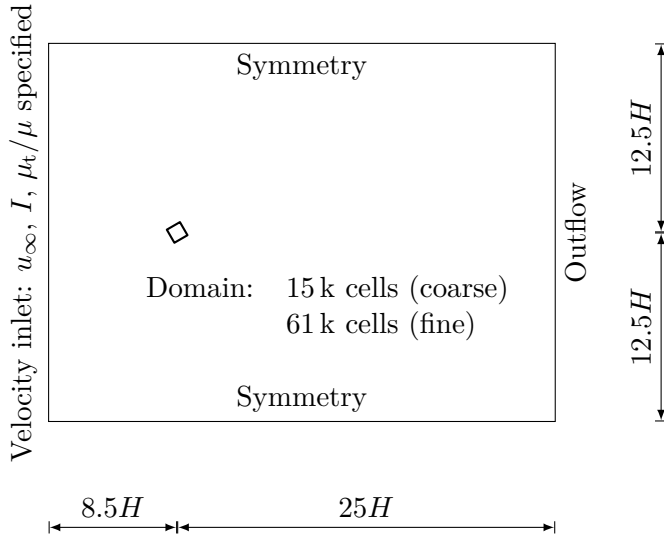


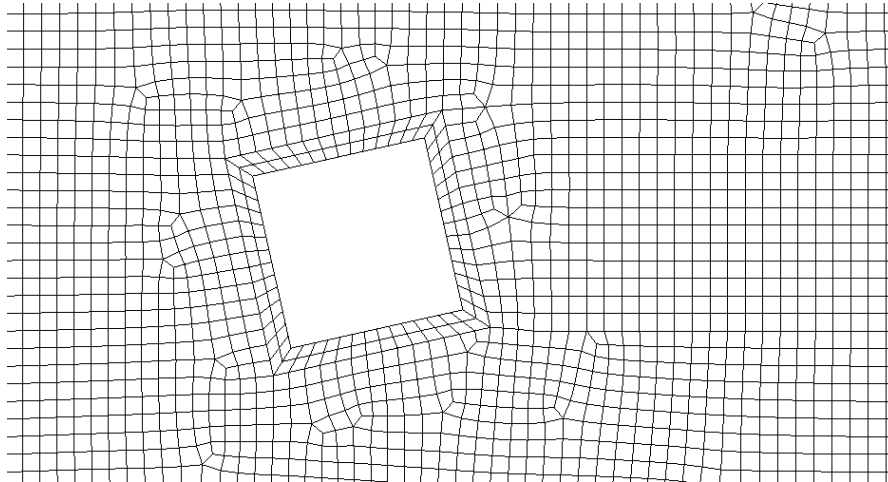
Figure 2.9.: Sketch of the computational domain (to scale).

Two different calculation meshes were used. A coarse version designed for $y^+ > 30$ (figure 2.10a) and a fine version designed for $y^+ \approx 1$ (figure 2.10b). The actual y^+ -values of a flow-field snapshot at $\varphi = 12.7^\circ$ are shown in figure 2.11.

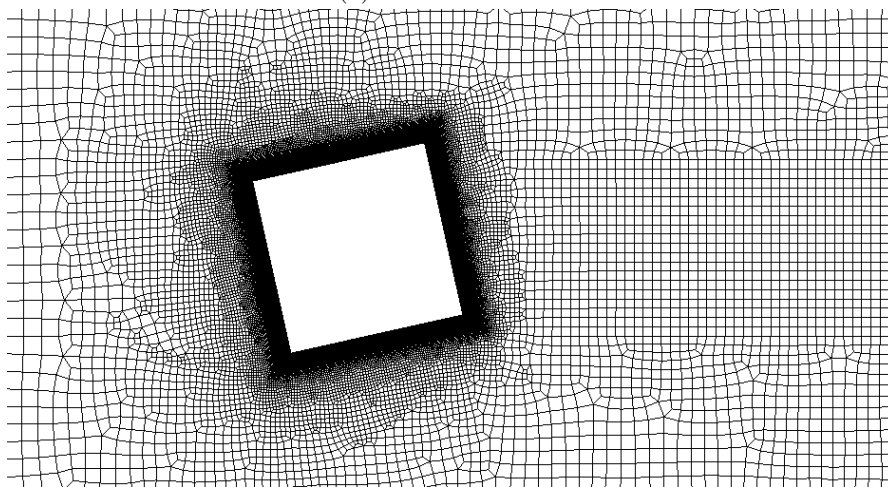
In all simulations the inlet turbulent boundary conditions were set to $I = 1\%$ turbulence intensity and a viscosity ratio (eddy viscosity over molecular viscosity) of $\mu_t/\mu = 1$. This choice was based on the results of the previously described simulations of the flow around a circular cylinder. These settings are appropriate for low-turbulence wind conditions [2].

Two simulation series employing the *realizable kε* turbulence model and the *kω-SST* turbulence model were carried out. The influence of the following settings and methods was investigated:

- [Second Order discretizations \(SO\)](#).
- [Enhanced Wall treatment \(EWT\)](#) (two-layer approach with blending for y^+ insensitive solutions) [43]. Note that this setting is implied in ω -based turbulence models.



(a) Coarse version



(b) Fine version

Figure 2.10.: Section of the calculation mesh close to the square prism.

- (Log-law) Wall functions (WF) (first cell midpoint at $30 < y^+ < 300$).
- Curvature Correction (CC) of the k production terms in the $k\omega$ -SST model [95].
- Low Reynolds number corrections (LR) for $k\omega$ based models (unrelated to the wall-treatment) ([106], Wilcox2006-LRN in [105]).
- Structured Grids (SG) vs. unstructured Grids.

Results

In the first simulation series $k\varepsilon$ based turbulence models were tested. Only the *realizable* $k\varepsilon$ model was considered. The point of inflection was not reproduced by the simulations

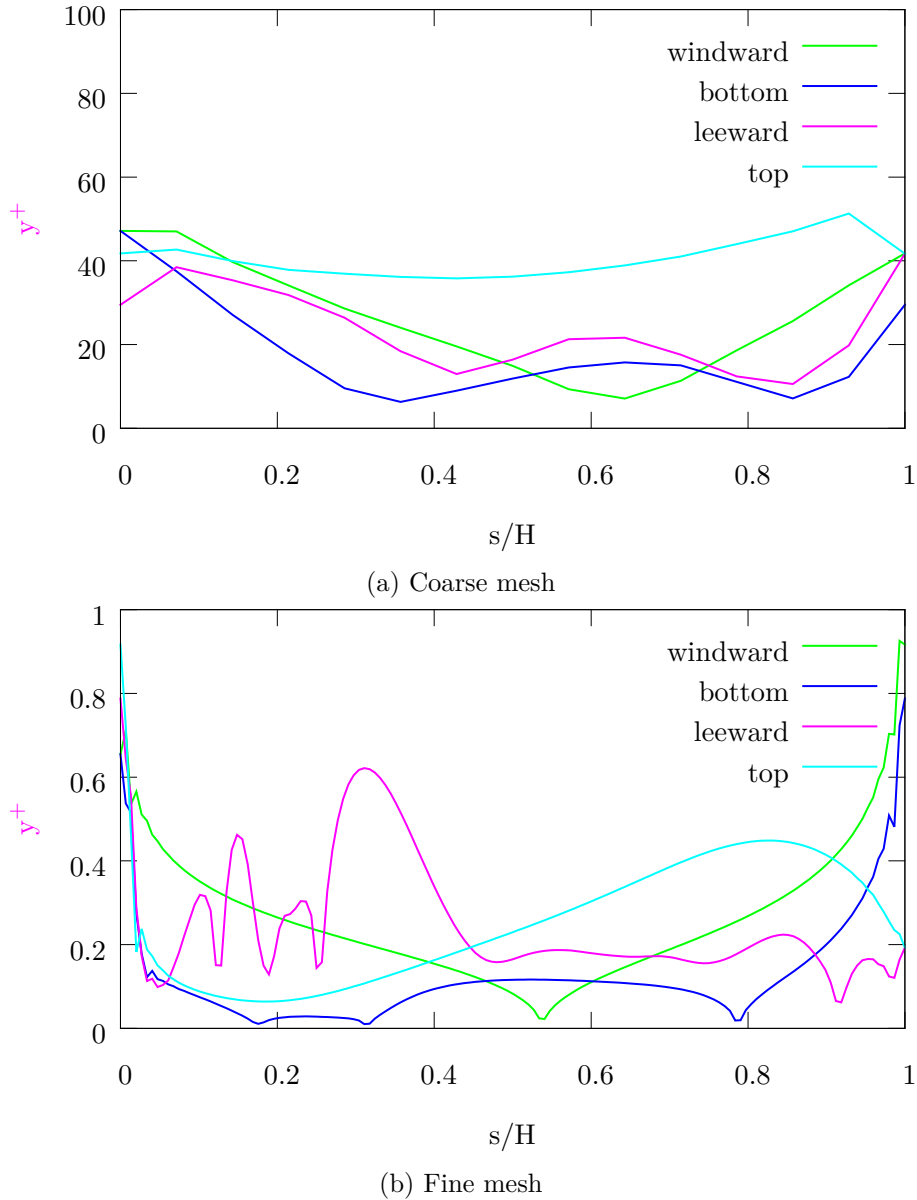
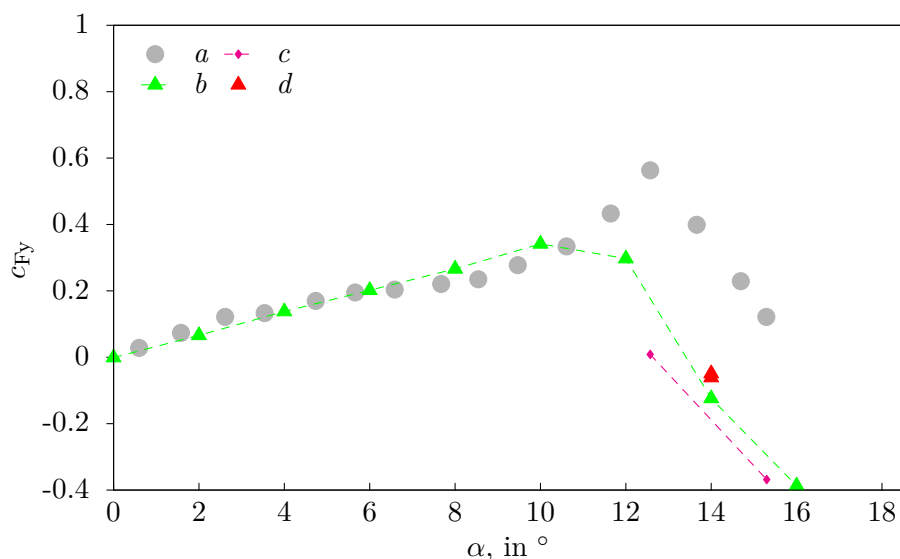


Figure 2.11.: Snapshot of the wall- y^+ values over the dimensionless length s/H for all sides of the square at $Re = 22400$, $\varphi = 12.6^\circ$, $I = 1\%$, $\mu_t/\mu = 1$.

(figure 2.12). The maximum peak vertical force coefficient (see figure 2.12, series b) was underestimated and occurred at a smaller inclination angle than in the experiments. When log-law wall-functions were employed, the use of structured grids did not improve the simulation results (figure 2.12 series b,d). The use of enhanced wall-treatment lead to no substantial change of the force coefficients (series c).

The second simulation series was based on the *k ω -SST* turbulence model. The point


 (a) Vertical force coefficient c_{Fy} plotted over the angle of attack α .

	SO	EWT	WF	CC	LR	SG
<i>a</i>						Measurements, [82]
<i>b</i>	✓		•			✓
<i>c</i>	✓	•	•			
<i>d</i>	✓		•			

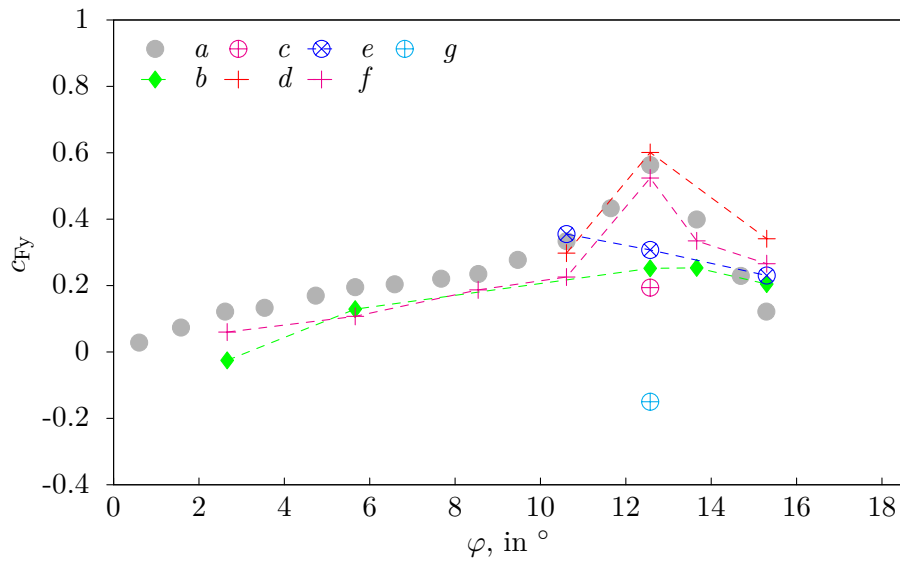
(b) Settings of the turbulence model.

 Figure 2.12.: Simulation of the flow around a square prism using the *realizable* $k\varepsilon$ turbulence model. If not indicated otherwise, the default values for all settings and coefficients in *ANSYS Fluent* 13.0 were used.

of inflection was not reproduced. The peak c_{Fy} could be reproduced better (see figure 2.13). We observed that it is very important to use second order discretisation for all field quantities (compare configurations *b,d*). The use of log-law wall-functions with the $k\omega$ -SST turbulence model had a severe (negative) impact on the simulation results (compare configurations *d,g*). When the Low-Reynolds number corrections and curvature corrections were de-activated the peak vertical force could not be predicted correctly (configuration *e*).

The peak vertical force (influenced mainly by the peak lift force) depends on the re-attachment behaviour of the free shear layer above the prism. In figure 2.14 results obtained under three different model settings are compared. The flow field, coloured by the velocity magnitude, is shown at the time instance of maximal lift force. The shear layer separating from the upper windward corner re-attaches slightly at the upper leeward corner. The “strength” of the re-attachment influences the lift force. Since the curvature correction is in effect when the streamlines are curved this setting is crucial

in such regions. The shear layer separating from the lower windward corner does not re-attach. The low instantaneous lift of configuration g is not due to the large values of y^+ , but rather due to the insufficient resolution of the flow field (figure 2.14c).



(a) Vertical force coefficient c_{Fy} plotted over the angle of attack α .

	SO	EWT	WF	CC	LR	SG
a						
		Measurements, [82]				
b		•				✓
c		•				
d	✓	•				✓
e	✓	•				
f	✓	•		✓		
g	✓		•			✓

(b) Settings of the turbulence model.

Figure 2.13.: Simulation of the flow around a square prism using the $k\omega$ -SST turbulence model. If not indicated otherwise, the default values for all setting and coefficients in *ANSYS Fluent* 13.0 were used (simulation g : version 14.5).

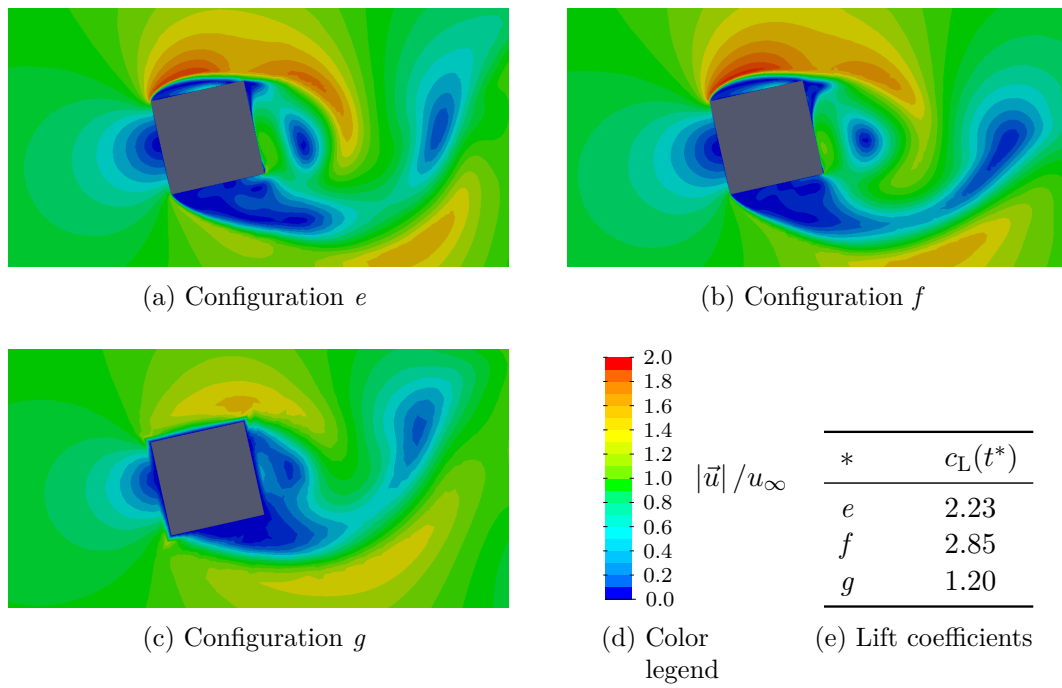


Figure 2.14.: Snapshots of the flow-field obtained under different settings of the $k\omega$ -SST turbulence model at the time instance t^* of maximum lift force, $\varphi = 12.6^\circ$.

2.1.3. Choice of the turbulence model

Good results were achieved with $y^+ \sim 1$, second order discretisations and Low-Reynolds number corrections. The Low-Reynolds number corrections can be interpreted as a crude model for laminar – turbulent transition [1], which is not desirable in our case. Using curvature correction for URANS turbulence models improves the accuracy of the simulations. In all subsequent simulations (chapters 3 to 5) the following simulation setup was employed (configuration f in figure 2.13):

- second order discretisations
- Unstructured grids with a fine resolution of the wall regions
- The $k\omega - SST$ turbulence model with curvature correction terms [1, 67, 95].

2.1.4. Rigid body motion

To allow motion of the rigid body the mesh has to be adapted in some way. An approach inspired by [5] was chosen: The domain is split into three parts. An outer, stationary region, an annulus shaped deforming region and a circular inner region containing the body. The mesh in the inner region around the body is displaced with the body. The cells are not deformed, preserving eventual body fitted cells. The annulus shaped region, containing this inner region is deformed. The deforming region connects the moving inner region to the stationary outer region and the mesh boundaries. Thus, no re-meshing during a simulation run and no sliding interfaces are required. In the initial state the deforming region is a perfect annulus containing a structured mesh, figure 2.15a. A node with the initial position $(x_1^{(o)}, x_2^{(o)})^T$ in the inner region is displaced according to

$$\begin{pmatrix} x_1 \\ x_2 \end{pmatrix} = \begin{pmatrix} \cos \varphi & -\sin \varphi \\ \sin \varphi & \cos \varphi \end{pmatrix} \begin{pmatrix} x_1^{(o)} \\ x_2^{(o)} \end{pmatrix} + \begin{pmatrix} 0 \\ y \end{pmatrix}, \quad (2.8)$$

where $(x_1, x_2)^T$ is the new position of the node and y and φ are given by the equations of motion (2.2). The deforming region has to connect the moving inner region to the stationary outer region. The nodes are moved by the same relation as above, but the displacement is weighted by the position of the node according to

$$\begin{pmatrix} x_1 \\ x_2 \end{pmatrix} = \frac{\sqrt{x_o^2 + y_o^2} - R_1}{R_2 - R_1} \begin{pmatrix} \cos \varphi & -\sin \varphi \\ \sin \varphi & \cos \varphi \end{pmatrix} \begin{pmatrix} x_1^{(o)} \\ x_2^{(o)} \end{pmatrix} + \begin{pmatrix} 0 \\ y \end{pmatrix}, \quad (2.9)$$

where R_1 and R_2 are the radii of the inner and outer boundaries of the annulus, respectively. The original node coordinates can be stored as “user defined scalar” and can be conveniently accessed during the simulation. After displacement the cells in the deforming region are sheared and squeezed (figure 2.15b).

The mesh is moved according to the equations governing the rigid body motion (equation(2.2)). Choosing the ANSYS Fluent CFD solver implies the use of segregated (or partitioned) solving strategies for the rigid body motion and the fluid flow. Such solving

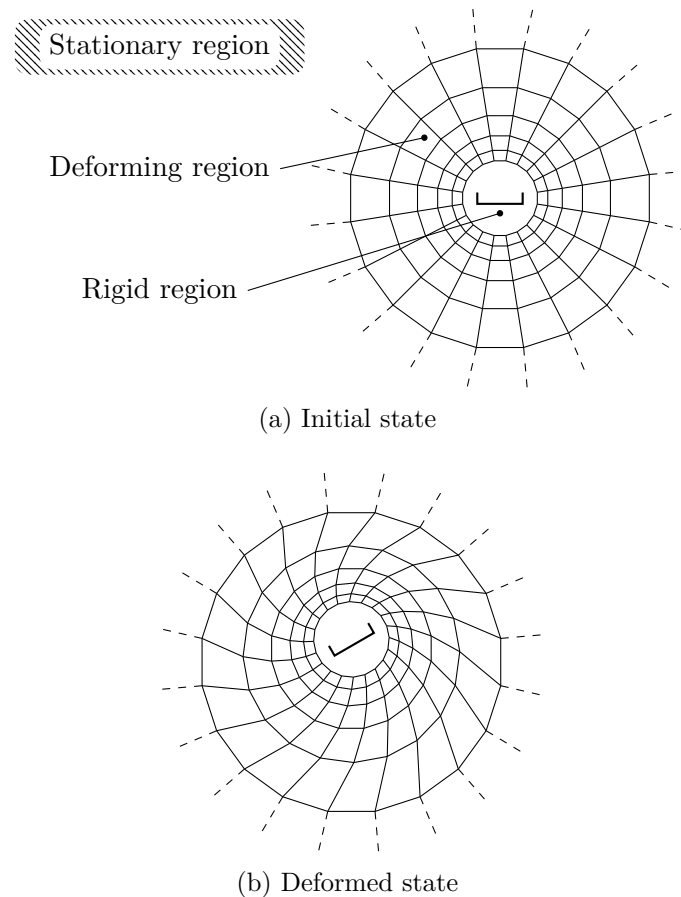


Figure 2.15.: Mesh deformation strategy: The inner region is moved as a rigid body. The outer region is deformed.

strategies can lead to stability and convergence issues in some parameter ranges [18]. However, the problematic parameter ranges involve scenarios where the density of fluid and solid are very similar, e.g. blood flow in a flexible artery. Here, the fluid (air) has a much smaller density than the structure. Thus, we are confident that a segregated approach is suitable.

A UDF-based Runge-Kutta scheme was used to solve the equations governing the movement of the rigid body (see appendix B). This requires knowledge of the time-dependent aerodynamic forces “in the future” (time levels $(j+0.5)$ and $(j+1)$, where (j) denotes the current time-step). The forces at time level $(j+0.5)$ were interpolated linearly from time levels (j) and $(j+1)$. The forces of the latter time level need to be extrapolated (estimated) at the beginning of a time-step (see figure 2.16).

With the *ANSYS Fluent* the solving strategy in figure 2.16 is possible. At the beginning of a time-step $t^{(j)}$ the aerodynamic lift and torsional moment at the end of the current time-step $L^{(j)}$ and $M^{(j)}$ are estimated through linear extrapolation of the past aerodynamic forces $L^{(j-1)}$, $L^{(j-2)}$ etc. The rigid body motion is solved for the first time

using the extrapolated forces. In some cases it may suffice to solve the rigid body motion just once in a time-step. This is achieved by disabling the *implicit update* switch in the case setup and corresponds to never going through the “Update $L^{(j)}$, $M^{(j)}$ ” block in the flow-chart. All fluid solver iterations are performed in a row until flow-field convergence is reached. Though simple and numerically efficient, some test cases showed numeric instabilities that lead to unrealistically large structure displacements. Therefore the *implicit update* switch was activated to obtain an update of the aerodynamic forces that can be used to correct the rigid body motion. Experience has shown that it is good practice to update the aerodynamic forces every N_i -th fluid solver iteration. In the simulation results reported in chapter 5 the setting $N_i = 5$ was used. Convergence is tested in two steps: firstly, the flow-field and, secondly, the mesh motion has to converge. This yields to the same solution that would have been obtained by a monolithic solver [1].

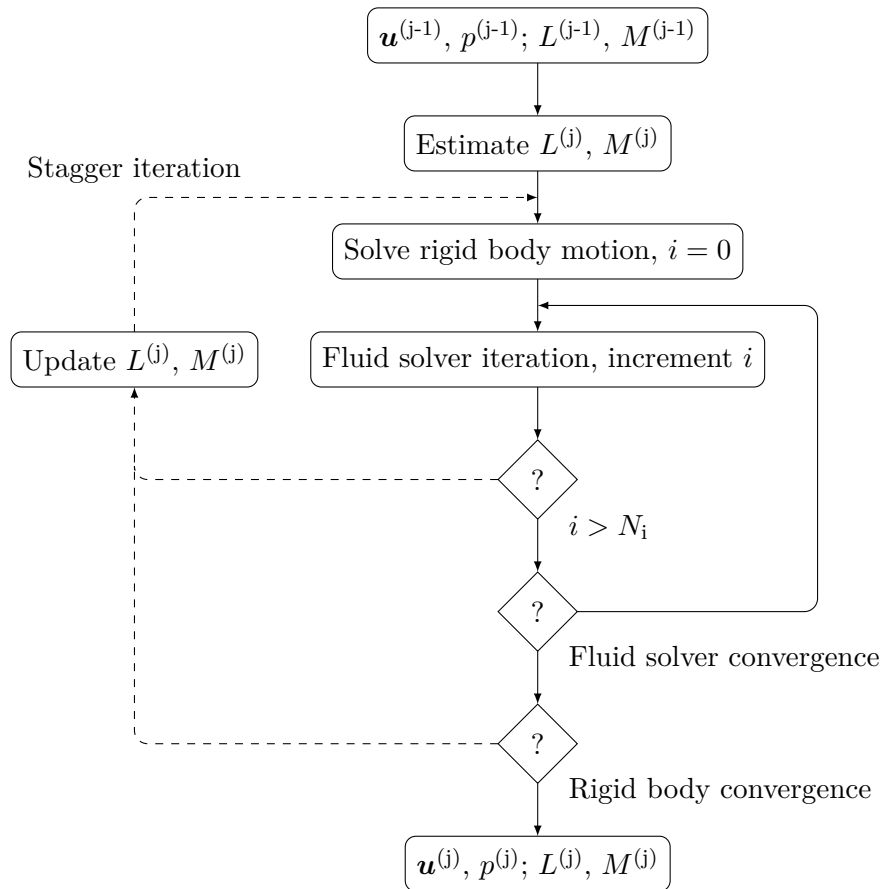


Figure 2.16.: Flow-chart showing the iterative coupling between the equation of motion for the profile and the flow governing equations. Superscripts in parenthesis indicate the time-step.

The influence of the implicit update was studied by using disabling the implicit update function during a simulation run. To avoid the disturbances that were observed at the

restart of a simulation run, the re-calculation of the rigid body position was disabled with a software switch. The rigid body routine was still called by the solver, but it didn't report an updated position. One test run consisted of sixty time-steps. After twenty-eight time-steps the position update was disabled by the software switch. In a second simulation, started with equal initial conditions, the position update was carried out in all time-steps. This test was carried out for a 2DoF scenario at one reduced velocity $U^* = 14$, $f_{0,y} = f_{0,\varphi} = f_0$. The initial conditions are limit cycle oscillation of the profile (section 5.1.3). The test was performed for three different time-step sizes, $\Delta t f_0 = 7.0 \cdot 10^{-4}$, $\Delta t f_0 = 35 \cdot 10^{-4}$, $\Delta t f_0 = 70 \cdot 10^{-4}$. The larger the time-step, the larger the spread of the two predictions (figure 2.17). At the largest time-step displacement prediction differences of up to $\Delta y/H = 4 \cdot 10^{-6}$ and $\Delta\varphi = 0.3^\circ$ were observed. The difference Δy shows a clear trend. The difference $\Delta\varphi$ oscillates. Note, that these differences were observed after twenty-eight time-steps. During a full simulation run at least twenty-thousand (20000) time-steps were simulated. This is clear evidence that an update of the rigid body position during a time-step is required.

Activating implicit update causes the UDF to be called multiple times during a time-step. At subsequent calls updated aerodynamic forces are available. The influence of implicit on the aerodynamic forces can be seen in figure 2.18. This figure shows the convergence of the lift coefficient during a single time-step. The implicit update was deactivated as described above. The data in the figure was taken from the first time-step without implicit update. Therefore the lift coefficient c_L and displacement delta $\Delta y/H$ are equal in iteration zero ($\Delta y = y - y^{(0)}$, $y^{(0)}$ being the displacement obtained with extrapolated aerodynamic forces). The time-step size was $\Delta t/f_0 = 7.0 \cdot 10^{-4}$. The convergence of the lift coefficient is characterised by a sharp peak beginning at iteration one. Then, the lift coefficient slowly converges to its final value. This took sixty iterations in this case. With de-activated implicit update the rigid body position is calculated with extrapolated aerodynamic forces and is constant throughout the time-step. When implicit update is activate and the parameter N_i (figure 2.16 set to $N_i = 5$, the displacement is updated every fifth iteration. It can be seen that the position of the rigid body is updated according to the large peak in the lift coefficient. This first update of the rigid body position is changed every fifth iteration until convergence is reached. The update of the rigid body position also influences the convergence of the lift coefficient. It can be seen that the c_L convergence is slower when the implicit update is active. After the last iteration a small difference of $1.7 \cdot 10^{-8}$ between the updated and non-updated solution remains. The quality of the non-updated solution is due to the good approximation of the lift coefficient obtained by extrapolation.

2.1.5. U-profile: Mesh 1

An unstructured grid with the dimensions $24.6B \times 18.4B$ was created (figure 2.19). The profile is placed at a distance $7.7B$ after the inlet boundary condition. Around the profile a body-fitted, structured boundary region was created (figure 2.21). The smallest cell sizes were set in the region around the profile. The mesh resolution at the profile is described in figure 2.20. The nodes along the walls are equidistant. The wall-normal

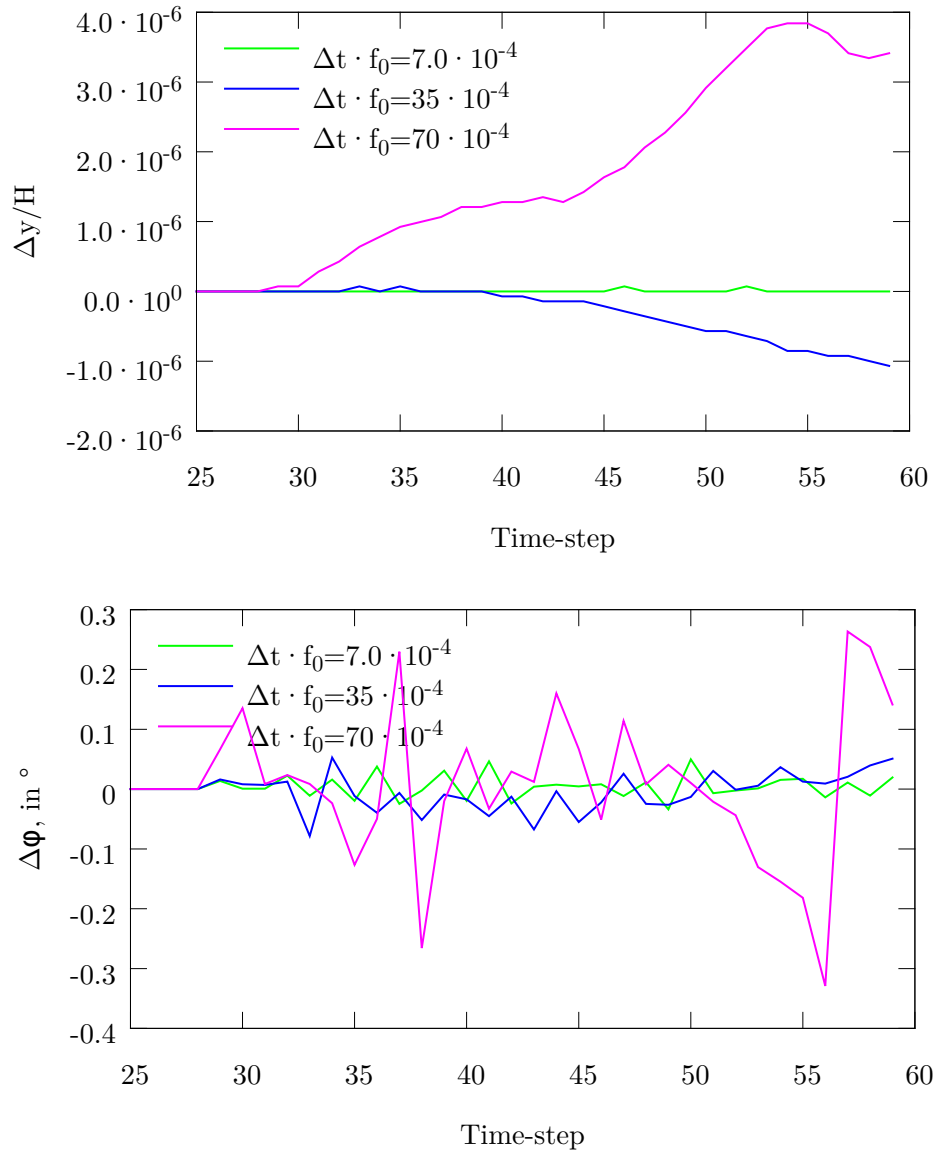


Figure 2.17.: Example: Difference between a solution with and without implicit update for several time-step sizes.

mesh is graded using the *hyperbolic tangent* method implemented in *IcemCFD*. This grid was used for simulation of the flow around a statically inclined U-profile (section 3) or around a U-profile performing forced motion (section 4).

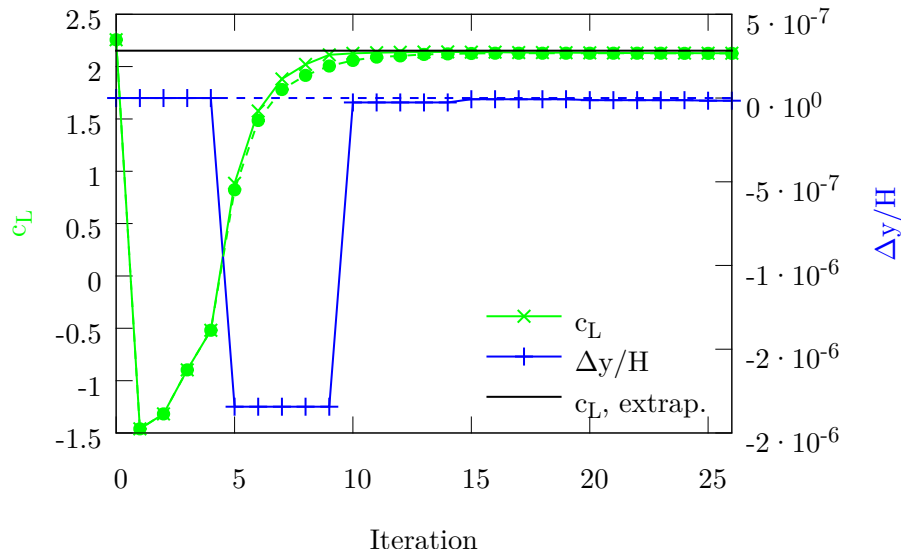


Figure 2.18.: Example: Convergence of the lift coefficient c_L during a time-step; Continuous line: active implicit update, dashed line: without update, Black line: linearly extrapolated lift coefficient.

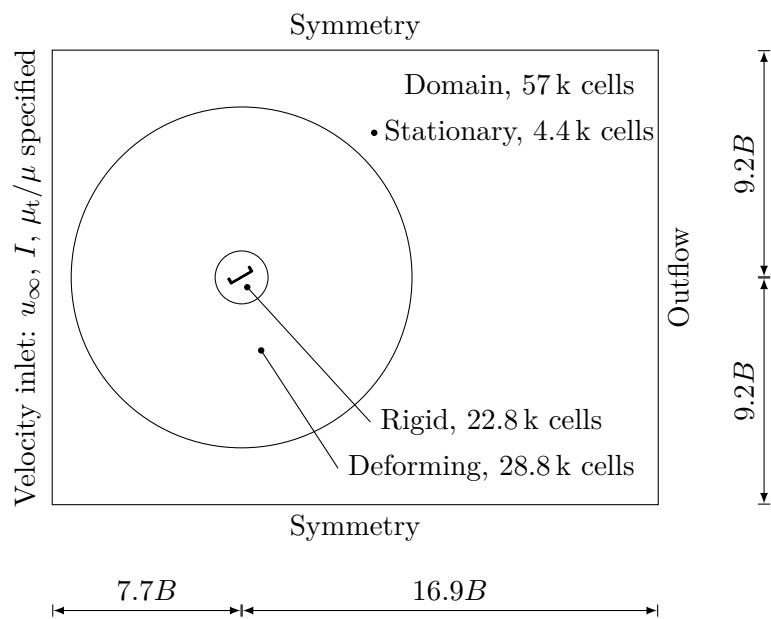


Figure 2.19.: Sketch of the 2D calculation domain with boundary conditions and important dimensions.

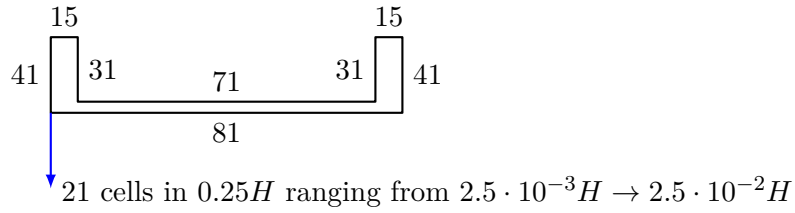


Figure 2.20.: Mesh resolution at the U-profile. Node counts per boundary section indicated by the numbers, Cell sizes in wall-normal direction indicated by the blue arrow.

2.1.6. U-profile: Mesh 2

An unstructured grid with the dimensions $24.6B \times 18.5B$ was created (figure 2.22). The profile is placed at a distance $7.7B$ after the inlet boundary condition. The mesh resolution at the profile is the same as in described in figure 2.20 except that the first cell in wall-normal has the height $5 \cdot 10^{-3}H$. This grid was used for coupled simulation of the flow around a U-profile with two degrees of freedom (section 5).

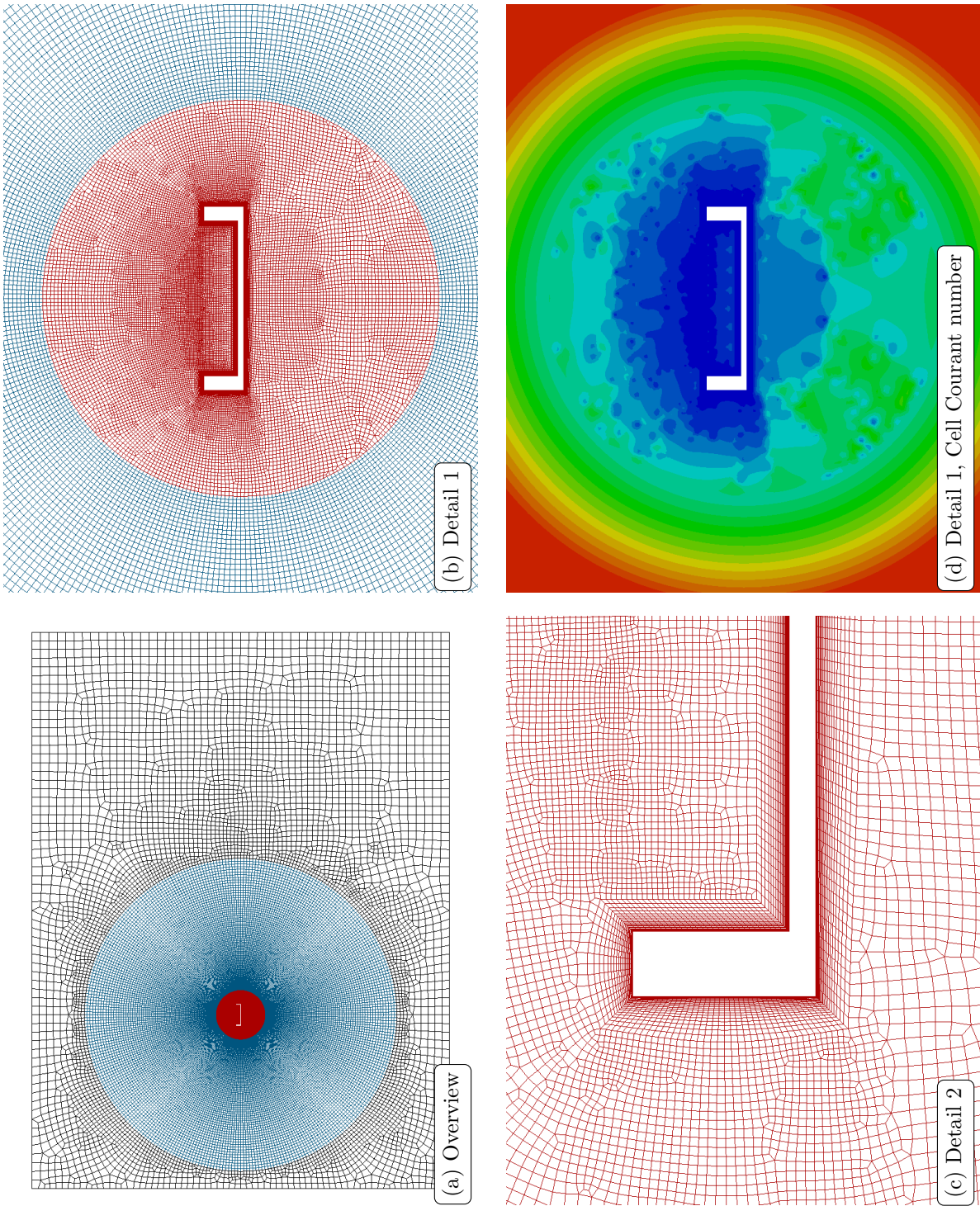


Figure 2.21.: Computation mesh (U-profile variant 1) coloured by region (a to c): Black – stationary, Blue – deforming, Red – moving as rigid body; and the field coloured by the cell area ranging from blue – $A_c/BH = 1.4 \cdot 10^{-5} Ac$ to red – $A_c/BH = 5.5 \cdot 10^{-3}$.

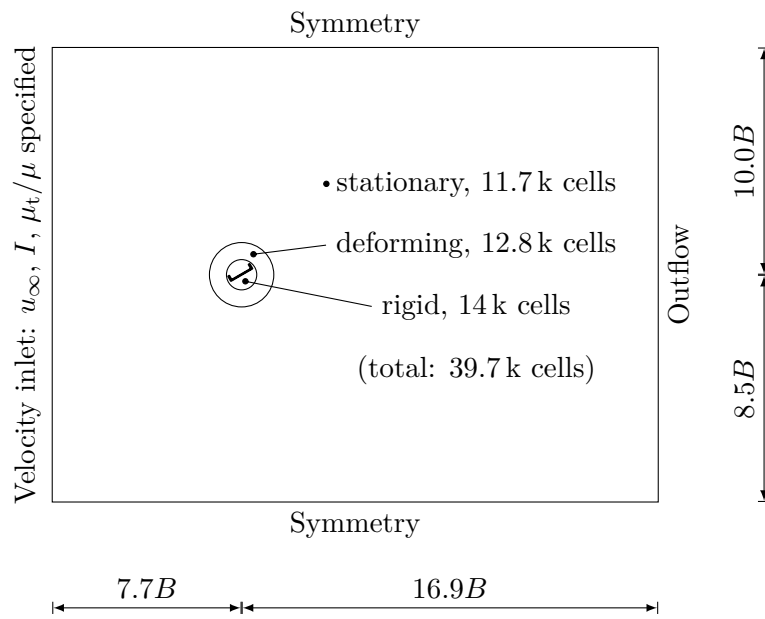


Figure 2.22.: Computational domain in which the flow around the U-profile is simulated. The concentric circles around the U-profile demarcate the deformed and moving regions of the mesh (to scale).

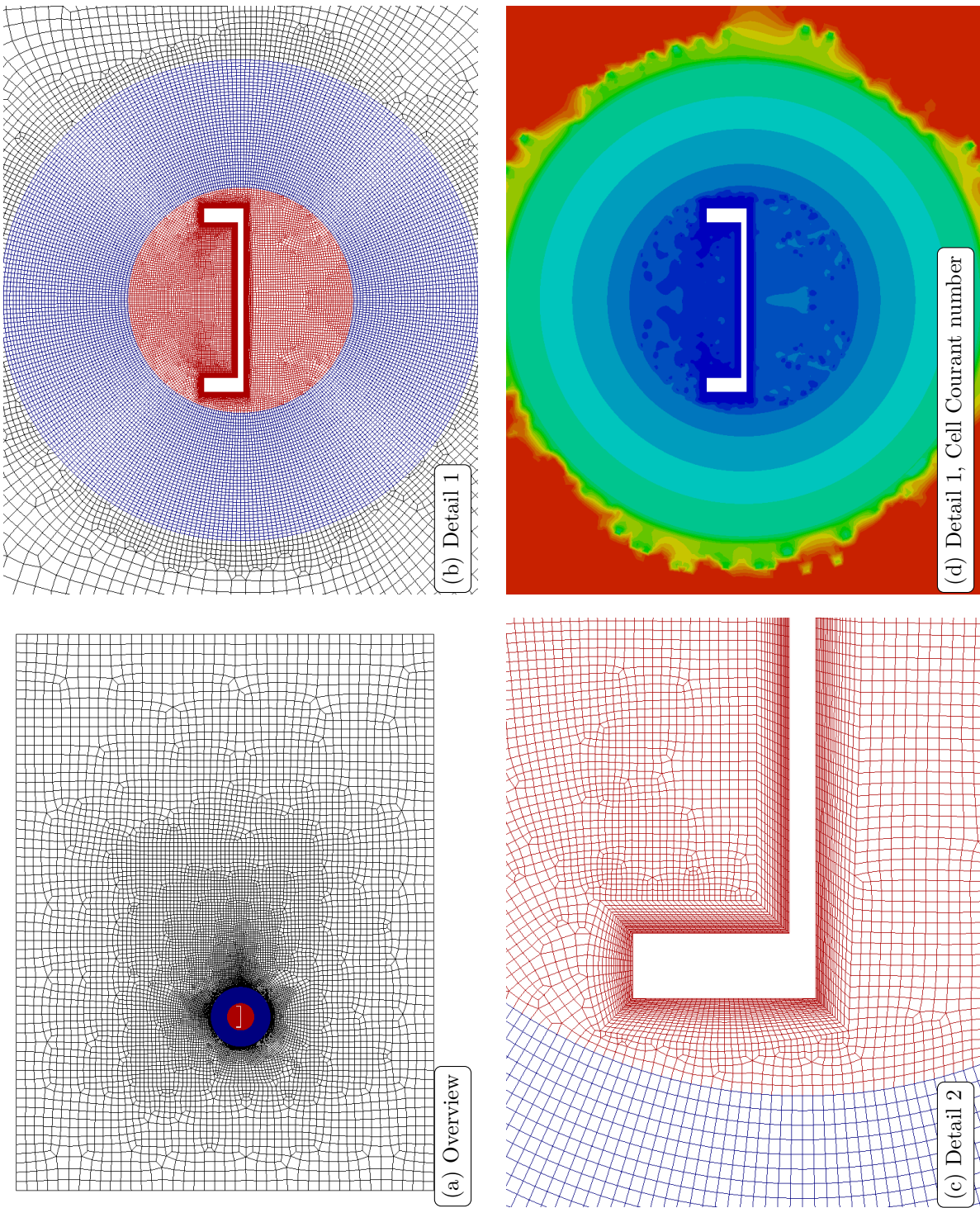


Figure 2.23.: Computation mesh (U-profile variant 2) coloured by region (a to c): Black – stationary, Blue – deforming, Red – moving as rigid body; and the field coloured by the cell area ranging from blue – $A_c/BH = 1.4 \cdot 10^{-5}$ to red – $A_c/BH = 5.5 \cdot 10^{-3}$.

2.2. Wind tunnel experiments

The experiments were carried out at the [Centre of Excellence Telč \(CET\)](#) which is located in the city of Telč, Czech republic. It has a closed-loop wind tunnel with two closed test-sections, the “aerodynamic” section and the “climatic” section. The former has a cross-section of $1.9\text{ m} \times 1.8\text{ m}$ and is equipped with honeycombs to reduce the turbulence intensity to about $I = 1\%$. The latter has a cross-section of $2.5\text{ m} \times 3.9\text{ m}$ but is not equipped with honeycombs [24]. Before introducing the individual wind tunnel tests, the mechanical model of the belt is discussed.

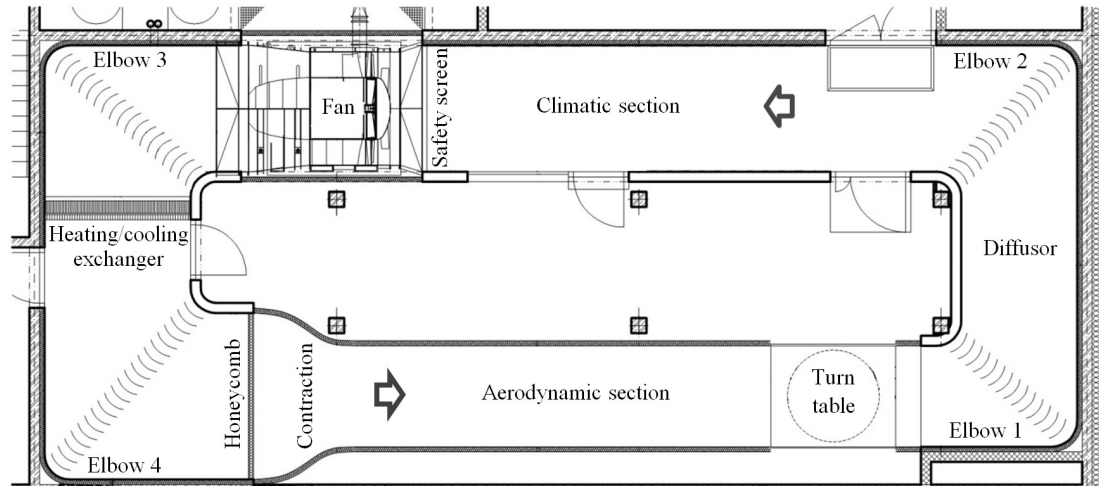


Figure 2.24.: Schematic drawings of the wind tunnel at the CET [49].

2.2.1. Mechanical model of the belt

The following assumptions for the belt under consideration (figure 2.25) apply:

- The length of the belt l is considered to be much larger than the width of its cross-section B : $l \gg B$.
- The width B is much larger than the thickness of the base t_b : $B \gg t_b$.
- The flanges of the profile do not contribute to the stiffness of the belt.
- The cross-section of the belt does not deform under vibration.
- The weight of the base is assumed to be much larger than the weight of the flanges.

Thus, the stiffness of the base with respect to bending about the horizontal axis (x_1 -axis) is negligible. The influence of the flanges is of aerodynamic nature only.

The belt is tensioned by a constant force S . We assume that this force acts evenly in the base of the cross section. Each fiber of the base with the dimensions $t_b \times dx_1$ subject to the tension s :

$$s = \frac{S}{t_b dx_1}. \quad (2.10)$$

Let $\varphi(x_3)$ be the inclination of the belt's cross section and $y(x_3)$ the vertical displacement (figure 2.26). Assuming small inclination φ , the local vertical displacement of the belt's base $w(x_1, x_2)$ is given by

$$w(x_1, x_3) = y(x_3) + x_1 \varphi(x_3). \quad (2.11)$$

Assuming small displacements, the change of length of a fiber is given by

$$\Delta l = \int_0^l \frac{1}{2} \left(\frac{\partial w}{\partial x_3} \right)^2 dx_3, \quad (2.12)$$

The potential energy per fiber due to this change of length is

$$E_s = \int_0^l s t_b \frac{1}{2} \left(\frac{\partial w}{\partial x_3} \right) dx_3. \quad (2.13)$$

Integration over the width of the belt yields:

$$E_S = \int_{-B/2}^{B/2} s x_2^2 dx_2 \int_0^l \frac{\varphi'^2}{2} dx_3 + \int_{-b/2}^{b/2} s dx_2 \int_0^l \frac{y'^2}{2} dx_3. \quad (2.14)$$

Then, the equations for the local vertical displacement and the local inclination of the belt are given by [98]:

$$\ddot{y} = \frac{S}{m} y'' \quad (2.15a)$$

$$\ddot{\varphi} = \frac{SB^2}{12I_T} \varphi'', \quad (2.15b)$$

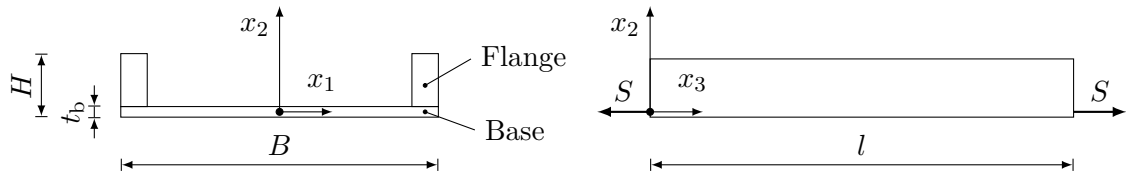


Figure 2.25.: Sketch of the belt.

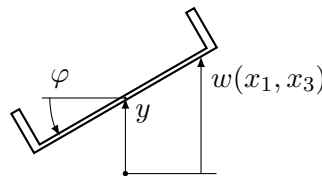


Figure 2.26.: Displaced cross-section of the belt.

where an overdot and a prime denote differentiation with respect to time and the spatial coordinate x_3 , respectively. Moreover, m is the mass per unit length of the belt's base is and I_T is the mass moment of inertia per unit length:

$$I_T = m \frac{B^2}{12}. \quad (2.16)$$

Assuming zero vertical displacement at both ends of the belt,

$$w(x_1, 0) = 0, \quad \text{and} \quad w(x_1, l) = 0, \quad (-B/2 \leq x_1 \leq B/2), \quad (2.17)$$

it can readily be seen that the eigenfrequencies of the first modes of bending and torsion vibrations are equal:

$$f_{0,y} = f_{0,\varphi} = f_0 = \frac{1}{2l} \sqrt{S/m} \quad (2.18)$$

Note, that we neglected the contribution of the belt's stiffness with respect to torsion about the long axis (x_3 axis) in equation (2.15a). This is admissible if the following relation holds:

$$G \frac{Bt_b^3}{3} \ll S \frac{B^2}{12}, \quad (2.19)$$

where G is the shear modulus and $Bt_b^3/3$ is the Saint-Venant's torsion constant for the base of the belt [98].

2.2.2. Particle Image Velocimetry

The PIV experiments were carried out in the aerodynamic test section. Equipment from Dantec and Litron Lasers was used. A Dantec FlowSense EO camera was used to make the snapshots of the flow-field. It had a resolution of 2048×2048 px. A pulsed Nd:YAG laser was used to illuminate the flow. The flow was seeded using a fog generator, which was placed in the climatic test section before the fan and honeycombs, thus creating no disturbance relevant for the flow around the model. The fog generator was activated for a few seconds, then deactivated. Given time, the smoke dispersed, resulting in a homogeneously seeded flow field.

The model dimensions of the model were width $B = 300$ mm and height $H = 65$ mm. The model was 600 mm long. It was mounted in cantilever fashion on an auxiliary plate (figure 2.27). Its front end was open to improve visibility of the flow. The laser illuminated a vertical plane 300 mm before the plate.

The camera's optical axis was pointing towards the center of the horizontal plate of the model. In the sample image in Figure 2.28 the model's cross-section is indicated (red). The regions indicated by the blue rectangles contain shadows cast by the glued edges of the model. Contrast there is low and the results are inaccurate. The blue rectangles are shown in every figure showing a flow-field obtained by PIV.

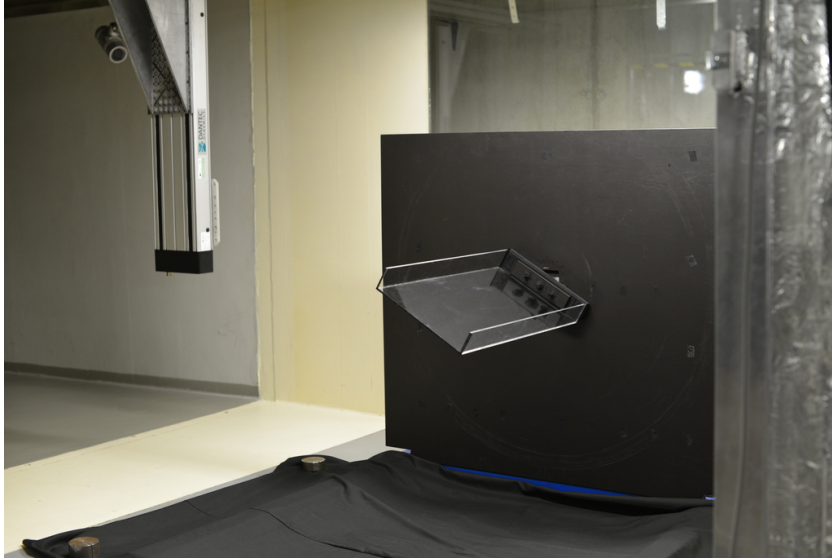


Figure 2.27.: Photo of the plexi-glass model mounted on the auxiliary plate.

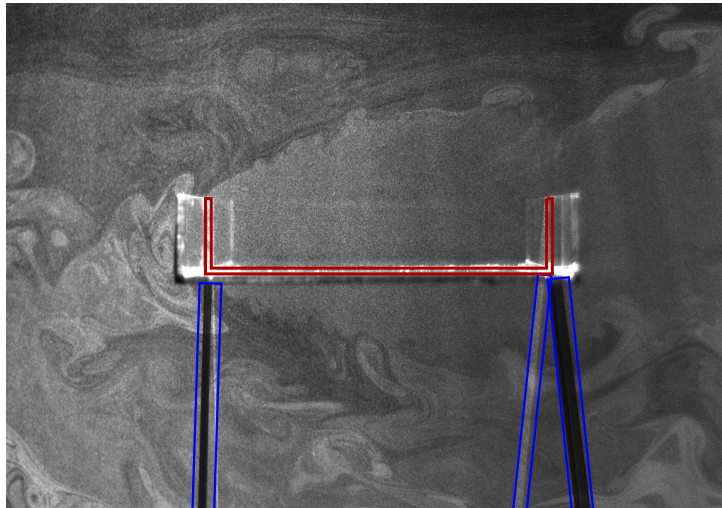


Figure 2.28.: Sample image acquired during the PIV experiments.

A series of 22 double pictures at a rate of 10 Hz was recorded. The time between a pair of images was $400 \mu\text{s}$. A flow velocity of 2.1 m/s was chosen. Given the a posteriori obtained Strouhal number $St = 0.133$ (equation (2.20) below), approximately 4 images per vortex shedding period could be recorded. The Reynolds number is $Re = u_\infty B / \nu_{\text{air}} = 4.3 \cdot 10^4$.

The images were analysed with Dantec DynamicStudio (version 3.31). The adaptive correlation technique was chosen. A final interrogation area size of 64×64 px with three iteration steps was set. The resulting vector field was smoothed using a 3×3 moving

average filter. Smaller interrogation area sizes were tested, but introduced too much errors.

Additionally the wake was studied with the help of a [Constant Temperature Anemometry \(CTA\)](#) probe. The flow velocity magnitude was measured at the distance B behind the model and $0.5H$ units above the top edges. These measurements were used to obtain the vortex shedding frequency f_{vs} which in turn was used to calculate the Strouhal number St

$$St = \frac{H f_{vs}}{u_{\infty}}. \quad (2.20)$$

Flow velocity magnitude spectra were obtained by applying the well known Welch's method (e.g. the MATLAB command `pwelch`) with a window width of eight R-flow periods (*Hamming window*, overlap 0.5) to the recorded flow velocity magnitudes (sample length 129 R-flow periods, sampling frequency approximately 230 times per period).

2.2.3. Two-degree-of-freedom test stand

The experiments on the rigid section model were also carried out in the aerodynamic test section. The model was mounted on a special test-stand. It allowed **2DoF** (heaving and pitching) motion. The heave and pitch eigenfrequencies can be adjusted by tuning a single spring for each mode (figure 2.29, [45]).

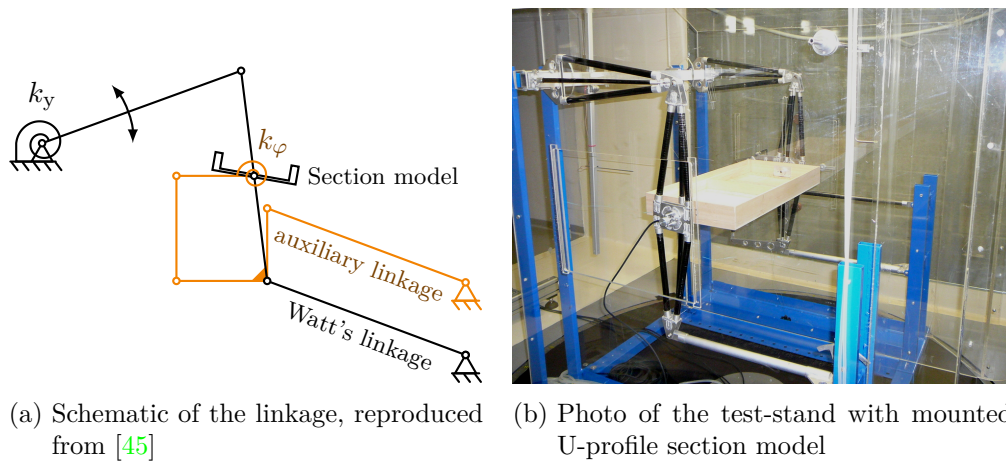


Figure 2.29.: The two-degree of freedom test-stand.

The tests were carried out using a model made of balsa wood (figure 2.30, for the physical properties see table 2.1). Ribs were installed to raise the model stiffness to an acceptable level.

Large eigenfrequencies $f_0 > 5$ Hz lead to strong damping of the profile motion by the test-stand. The achieved Scruton numbers were rather large (see table 2.2). The masses and inertial moments due to the moving parts of the test-stand were taken into account

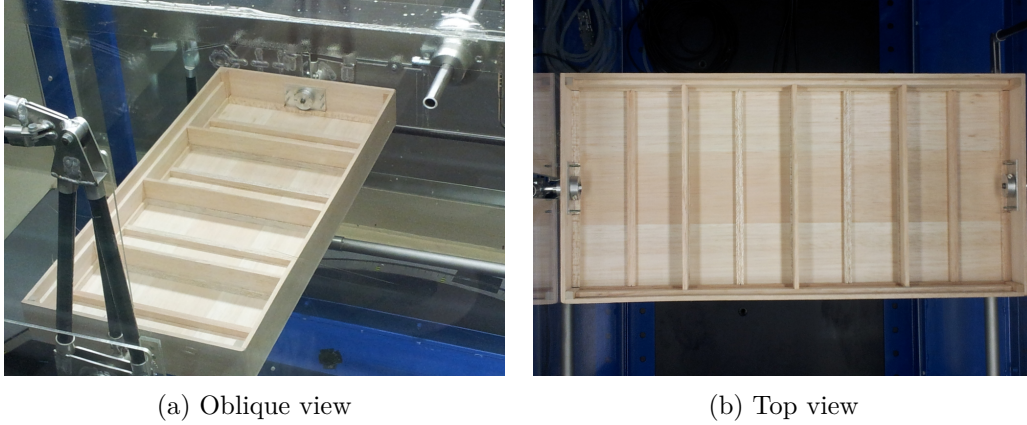


Figure 2.30.: Photos of the balsa wood model.

Property	Value
Model length	618 mm
Width of the U	$B = 300$ mm
Height of the U	$H = 65$ mm
Wall thickness	6 mm
Model mass per unit length	$m = 0.710$ kg/m
Torsional moment of inertia per unit length	$I_T = 0.0542$ kg m ² /m (calculated)
Number of ribs	3

Table 2.1.: Physical properties of the balsa wood model (figure 2.30) used in the rigid section model experiments.

(for numeric values see [45]). The Scruton number Sc is defined (in accordance with [63]) as

$$Sc_y = 2m\delta_y/(\rho H^2) \quad \text{and} \quad (2.21)$$

$$St_\varphi = 2m\delta_\varphi/(\rho H^4), \quad (2.22)$$

where δ_y and δ_φ are the logarithmic decrement of the heaving and pitch motion, respectively.

2.2.4. Tensioned belt experiments

To overcome the limitations imposed by the 2DoF test-stand, mainly the large damping, another experimental approach was employed: A belt with U-shaped cross-section (U-belt), made of rubber with inlaid steel cables and a textile mesh, mounted in a frame, and put under tension (see figure 2.31). The tension was adjusted until a desirable

f_0	δ_y	δ_φ	Sc_y	Sc_φ
2.0 Hz	0.06	0.035	138.65	368.79
4.5 Hz	0.033	0.06	76.26	632.20
9.5 Hz	0.12	0.2	277.31	2107.35

Table 2.2.: Logarithmic decrement and Scruton numbers for the rigid section model and several eigenfrequencies. The mass m and torsional moment of inertia I_T were scaled to a model length of 1m, and added to the respective contribution of the test-stand: $m = 0.710 \text{ kg/m} + 2.91 \text{ kg}$, $I_T = 0.0542 \text{ kg m}^2/\text{m} + 0.0155 \text{ kg m}^2$

eigenfrequency was obtained. The sidewalls were also made of rubber to reduce the influence of their stiffness. See table 2.3 for the physical properties of the belt.

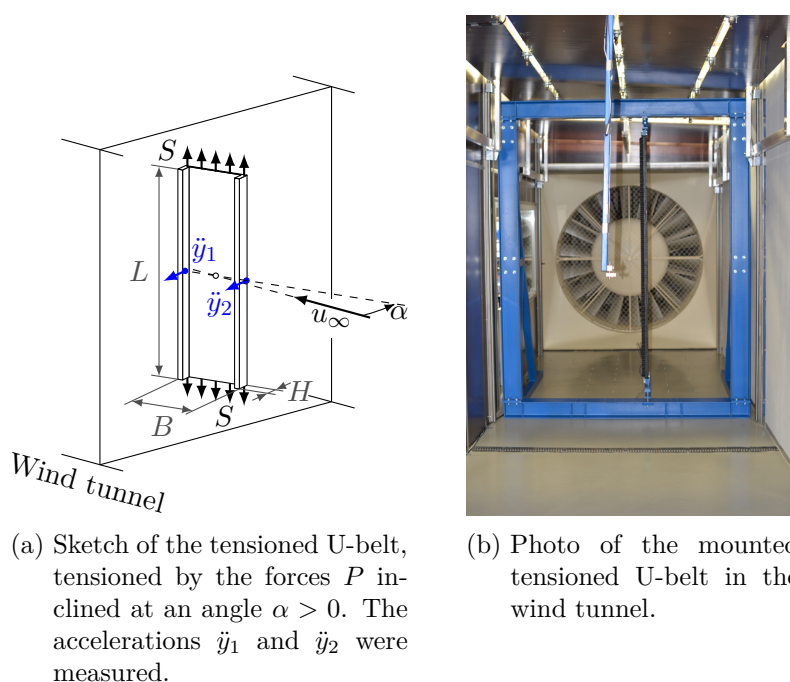


Figure 2.31.: Experimental set-up for testing a tensioned U-belt.

The tests were carried out in the climatic part of the wind tunnel of the CET (dimensions $2.5 \text{ m} \times 3.8 \text{ m}$) due to the size of the supporting frame. The tension was applied with the help of two hydraulic cylinders.

The accelerations of either side of the belt were measured using capacitive, uni-axial accelerometers (see figure 2.31). They were placed at the half length of the belt. Heaving and pitching motion were reconstructed from these two signals. The belt's mode-1 eigenfrequencies as well as the logarithmic decrement were obtained from monitoring the decay of an initial perturbation. The heave to pitch eigenfrequency ratio was suffi-

Property	Value
Free length	2.25 m
Belt width	$B = 300$ mm
Belt height	$B = 65$ mm
Mass per unit length	5.43 kg/m
Torsional moment of inertia per unit length	0.190 kg m ² /m (estimated)

Table 2.3.: Physical properties of the tensioned U-belt

ciently close to 1. The observed logarithmic decrements were very low, as desired (see table 2.4). However, the Scruton number was still large due to the high mass of the belt. Furthermore, the logarithmic decrements in table 2.4 only applied to deflection angles smaller than 2.5°. Larger perturbations were damped stronger.

$f_{0,y}, f_{0,\varphi}$	δ_y	δ_φ	Sc_y	Sc_φ
13.8 Hz, 13.8 Hz	0.012	0.014	25.18	242.74
11.4 Hz, 10.8 Hz	0.021	0.029	60.85	364.11

Table 2.4.: Logarithmic decrement and corresponding Scruton numbers for two different eigenfrequencies. $Sc_y = 2m\delta_y/(\rho_{\text{air}}H^2)$, $Sc_\varphi = 2I_T\delta_\varphi/(\rho_{\text{air}}H^4)$

Heave and pitch displacements were obtained by integrating the acceleration signals twice in Fourier space (i.e. multiplying the spectrum by $-1/\omega^2$ and transforming back into the time domain). To obtain valid displacement signals, the spectra were truncated below 4 Hz. Tests involving a third accelerometer confirmed that although the belt deforms, deformations of the cross-section are damped very strongly and decay much faster than the belt vibrations.

The wind tunnel tests were carried out at flow velocities ranging from 3.9 m/s to the maximum velocity of 12.8 m/s ($8.0 \cdot 10^4 \leq Re \leq 2.6 \cdot 10^5$).

3. The flow around a stationary U-profile

The flow around a bluff body can take on many different forms. The U-profile promises a particular “richness” of flow-patterns. The rectangular prism shares its outline with the U-profile. Depending on the aspect ratio of the prism, there are several different vortex formation patterns [25]. The flow around an H-shaped prism is also known to permit several possible flow patterns [47]. The flow around a short rectangular prism, similar to the flow around the windward flange of the U-profile, shows intermittent change between two flow patterns [70, 100]. It is known from experiments that the galloping stability of rectangular prisms does not only depend on its aspect ratio, but also on the turbulence intensity of the oncoming flow, [19]. The H-prism shares its “open” sidewalls with the U-profile. Influenced by the motion of the profile, vortices are shed from its windward flanges and travel along the length of the profile, [47]. The U-profile has similarities with both H-prism and rectangular prism, and is asymmetric, thus indicating the possibility of interesting flow patterns.

3.1. 2D Simulation at several angles of inclination

The flow around the stationary profile was studied by means of [CFD simulations in a two-dimensional computational domain \(2D-CFD\)](#) employing *ANSYS Fluent* version 14.5. The U-profile (height H , width B) is inclined at a constant angle φ (see figure 3.1). The velocity of the oncoming flow is u_∞ . The simulations described in this section were carried out at a Reynolds number of

$$\text{Re} = u_\infty B / \nu = 2.45 \cdot 10^5. \quad (3.1)$$

At the inlet boundary a turbulence intensity of

$$I = \frac{1}{u_\infty} \sqrt{\frac{2}{3}k} = 1\%, \quad (3.2)$$

where k is the turbulent kinetic energy, and an eddy viscosity ratio of $\mu_t/\mu = 1$ was specified. The [\$k\omega\$ -SST](#) turbulence model with the setting described in section 2.1.2 was employed. The calculation domain described in section 2.1.5 was used. The coefficients of lift, drag and moment are given by

$$c_L = L / \left(\frac{1}{2} \rho u_\infty^2 H \right), \quad (3.3)$$

$$c_D = D / \left(\frac{1}{2} \rho u_\infty^2 H \right), \quad (3.4)$$

$$c_M = M / \left(\frac{1}{2} \rho u_\infty^2 H B \right), \quad (3.5)$$

respectively. L , D and M denote the aerodynamic lift, drag and torsional moment per unit length, respectively.

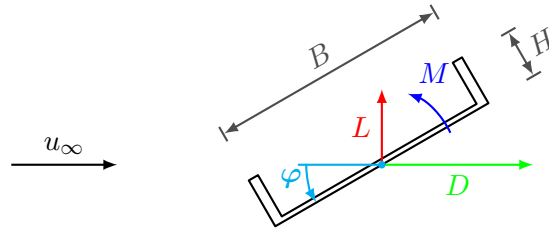
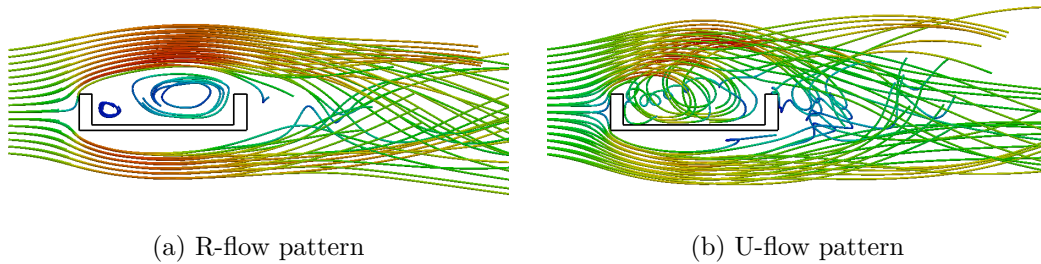


Figure 3.1.: Sketch of the U-profile (width B , height H) in parallel flow (u_∞) inclined at an angle $\varphi > 0$. The aerodynamic lift L , drag D and torsional moment M act on the profile.

At an inclination of $\varphi = 1^\circ$ two distinct flow patterns were observed. Both flow patterns are time-periodic. Selection of either flow pattern is related to the initial conditions of the simulation. The details of the selection mechanism and flow pattern changes are discussed in section 3.1.3. The flow patterns are characterised by different vortex formation patterns. One flow-pattern dubbed ‘‘R-flow’’ resembles the flow around a rectangular prism (see figure 3.2,a). The other flow-pattern, dubbed ‘‘U-flow’’ features a vortex travelling through the cavity of the U-profile (see figure 3.2,b). detail.



(a) R-flow pattern

(b) U-flow pattern

Figure 3.2.: Pathlines of passive particles in the flow around a U-profile, coloured by the velocity magnitude showing two different time-periodic flow-patterns. Simulation at $Re = 2.45 \cdot 10^5$.

3.1.1. The R-flow pattern

The distinctive feature of the flow patterns is the curvature of the shear layer originating from the top windward corner of the U-profile. The shear layer is stretched long and reaches over the cavity of the U-profile. Two almost stationary vortices rest in the cavity of the profile (figure 3.3). The first snapshot shows that the shear layer impinges on the leeward flange. A small portion of the flow is directed into the cavity of the profile. The major part of the flow flows into the wake behind the profile. Thus, the flow field is similar to the flow around a rectangular prism with the same aspect ratio – hence the name “R-flow”. Vortices are formed in the wake of the U-profile by a roll-up of the shear layer. The vortex shedding is similar to the von Kármán vortex street behind a rectangular cylinder. The vortices do not impinge on any part of the profile.

The aerodynamic forces under this flow pattern are almost sinusoidal in character (see figure 3.4). Their fundamental frequency yields a Strouhal number, equation (2.20), in the “usual” range, $St^{(R)} = 0.13$ (figure 3.5). This value of the Strouhal number is used to form the dimensionless time:

$$\tilde{t} = tSt^{(R)}u_\infty/H \quad (3.6)$$

The fundamental frequency is related to the frequency of the formation of vortices in the wake. The vortex formation also influences the aerodynamic forces acting on the profile. The maximum lift force occurs when a vortex is formed by the upper shear layer. At this time instance, the shear layer rolls up behind the leeward flange of the U (figure 3.6a). A small part of the flow is directed into the U-cavity by the leeward flange. A secondary vortex forms in the corner of the U-cavity, where the static pressure is relatively low. This is a major contribution to the total lift force. The time instance of maximum torsional moment coefficient is close to the time instance of maximum lift. This is due to the asymmetric pressure distribution induced by the secondary vortex in the corner of the U-cavity (figure 3.6b).

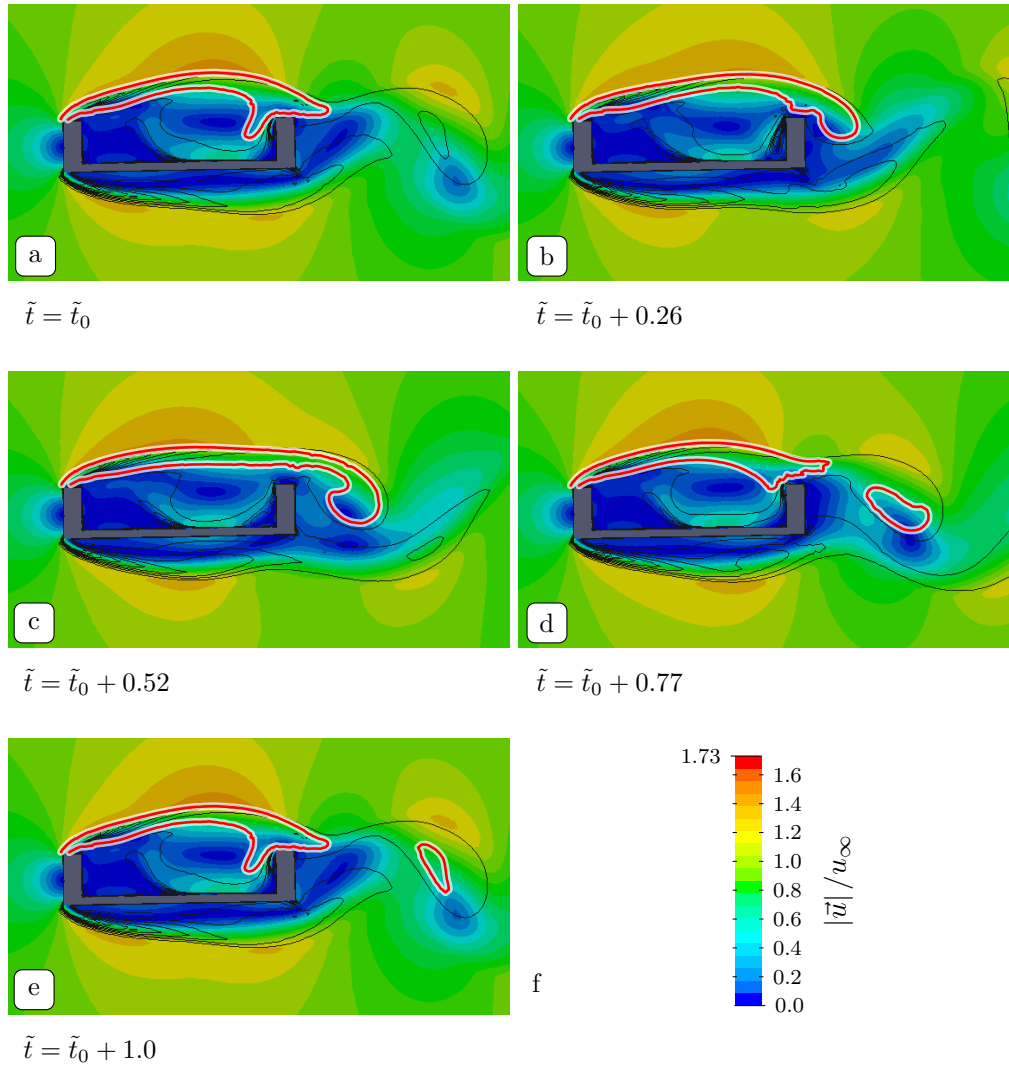


Figure 3.3.: R-flow pattern: snapshots coloured by velocity magnitude and additional vorticity magnitude contours. Some vorticity magnitude contours are highlighted. Simulation at $\varphi = 1^\circ$, $\text{Re} = 2.45 \cdot 10^5$. $\tilde{t}_0 = 153$ dimensionless time units after the simulation was started with trivial initial conditions.

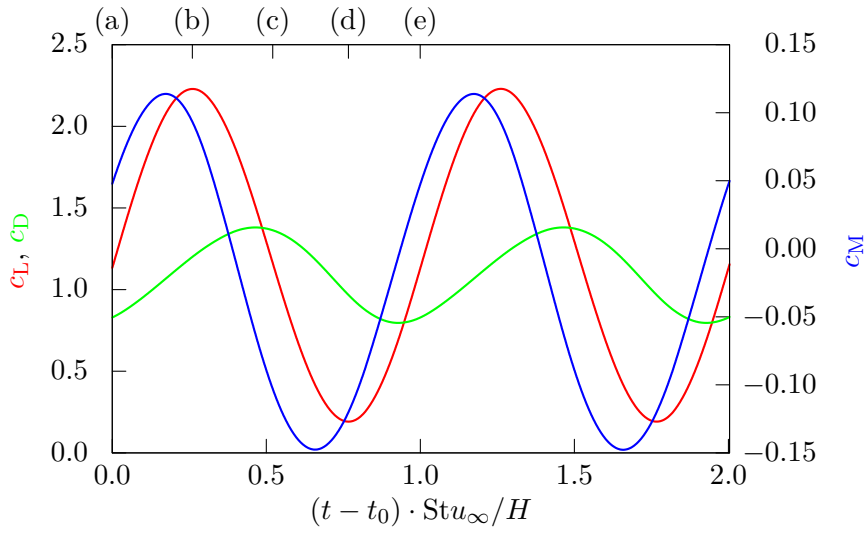


Figure 3.4.: R-flow pattern: Time-dependent aerodynamic forces. Simulation at $\varphi = 1^\circ$, $\text{Re} = 2.45 \cdot 10^5$. $\text{St} = 0.13$, $\tilde{t}_0 = 153$ dimensionless time units after the simulation was started with trivial initial conditions. The top axis marks the positions of the snapshots in figure 3.3.

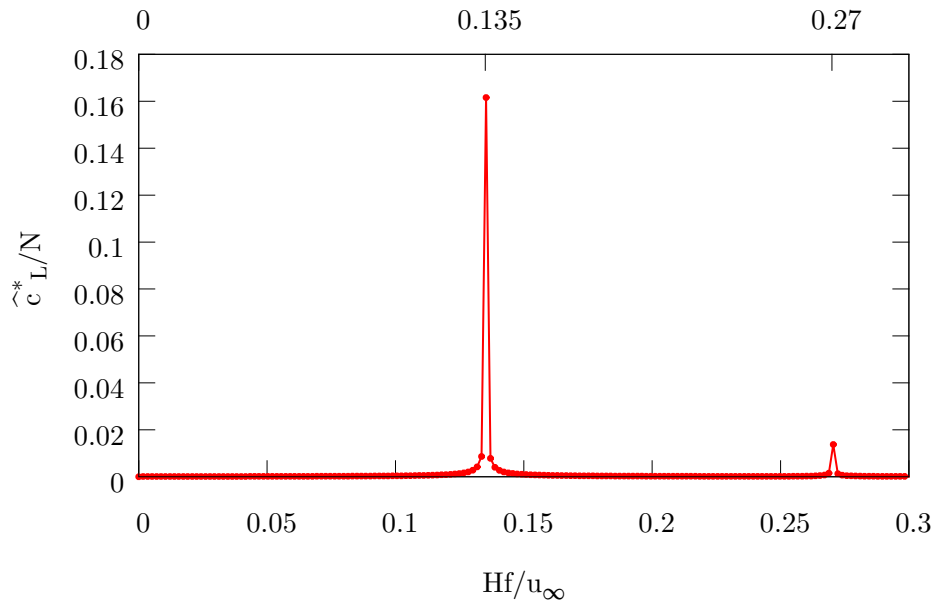
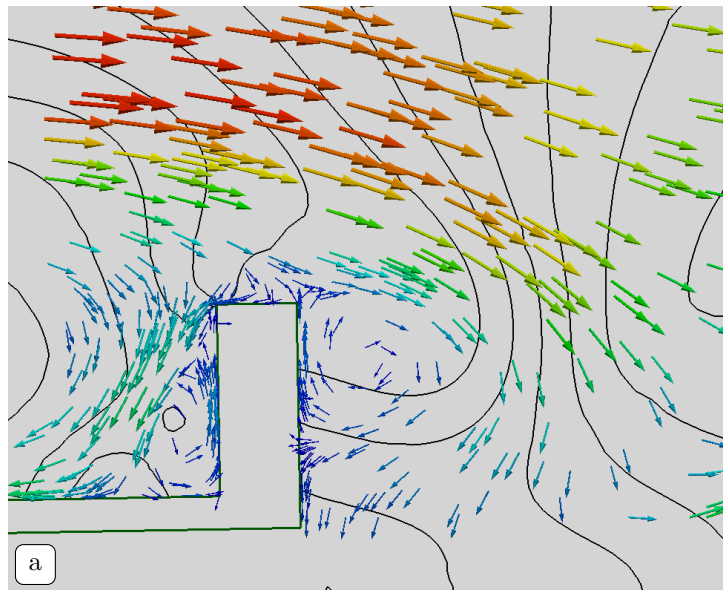
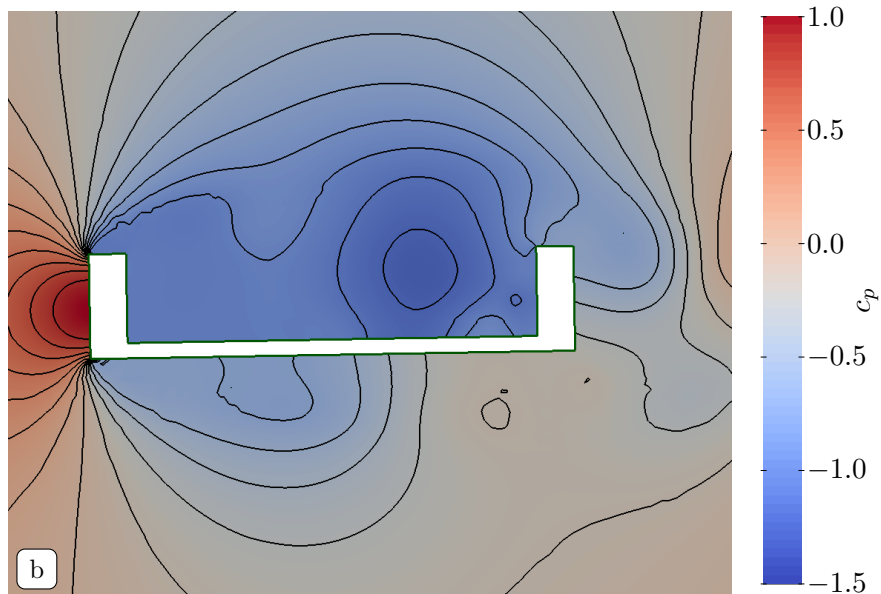


Figure 3.5.: Spectrum of the mean-free lift coefficient $c_L - \bar{c}_L$ under the R-flow pattern. \hat{c}_L^* is the Fourier coefficient, N is the number of timesteps considered in the discrete Fourier transform.



Flow field at the leeward flange visualized by arrows (coloured by the velocity magnitude) and pressure isolines



Contours of the pressure coefficient

Figure 3.6.: Flow-field under the R-flow pattern at the time of maximum lift (see figure 3.3,b). Field coloured by the static pressure. Arrows coloured and scaled by the velocity magnitude. Simulation at $Re = 2.45 \cdot 10^5$ and $\varphi = 1^\circ$.

3.1.2. The U-flow pattern

Under the U-flow pattern the vortex formation is entirely different than under the R-flow pattern. The shear layer rolls up right behind the windward flange of the U-profile (figure 3.7). A vortex forms in the cavity of the U (cavity-vortex). This vortex is not stationary as it detaches from the windward flange. It travels through the cavity of the profile. It is then swept over the leeward flange of the U-profile into the wake. This flow pattern is predominantly observed for negative angles of inclination. The aerodynamic forces under this flow pattern (figure 3.8) differ greatly from the R-flow aerodynamic forces. The fundamental frequency of the aerodynamic forces is related to the vortex formation at the windward flange of the U. When using this frequency to calculate a Strouhal number we obtain the value $St = 0.072$. In dimensionless time units this means that the period length is $\tilde{t}^{(U)} = 1.89$, which is almost two times the R-flow period length. The frequency of the wake vortex-shedding is still present in the spectrum of the aerodynamic forces (figure 3.9). This is due to a secondary vortex forming after the cavity vortex detached from the windward flange, but before it impinges on the leeward flange. This secondary vortex forms behind the leeward flange (figure 3.12a). At this instant of time the lift force has a local maximum (figure 3.8).

The maximum lift occurs when a cavity-vortex is swept over the leeward flange of the U into the wake (see figure 3.12b). When the cavity vortex impinges on the leeward flange, it causes a particularly strong secondary vortex in the corner of the cavity. Very low static pressures in the corner cause a large contribution to the total lift force. In this instance of time the torsional moment coefficient is also very large. This is due to the more pronounced asymmetry in the pressure distribution (figure 3.10). The magnitude of the lift force depends sensitively on the location of the vortices, which varies slightly from flow period to flow period. Therefore the U-flow at inclination $\varphi = 1^\circ$ is not strictly periodic, but slightly modulated (figure 3.11).

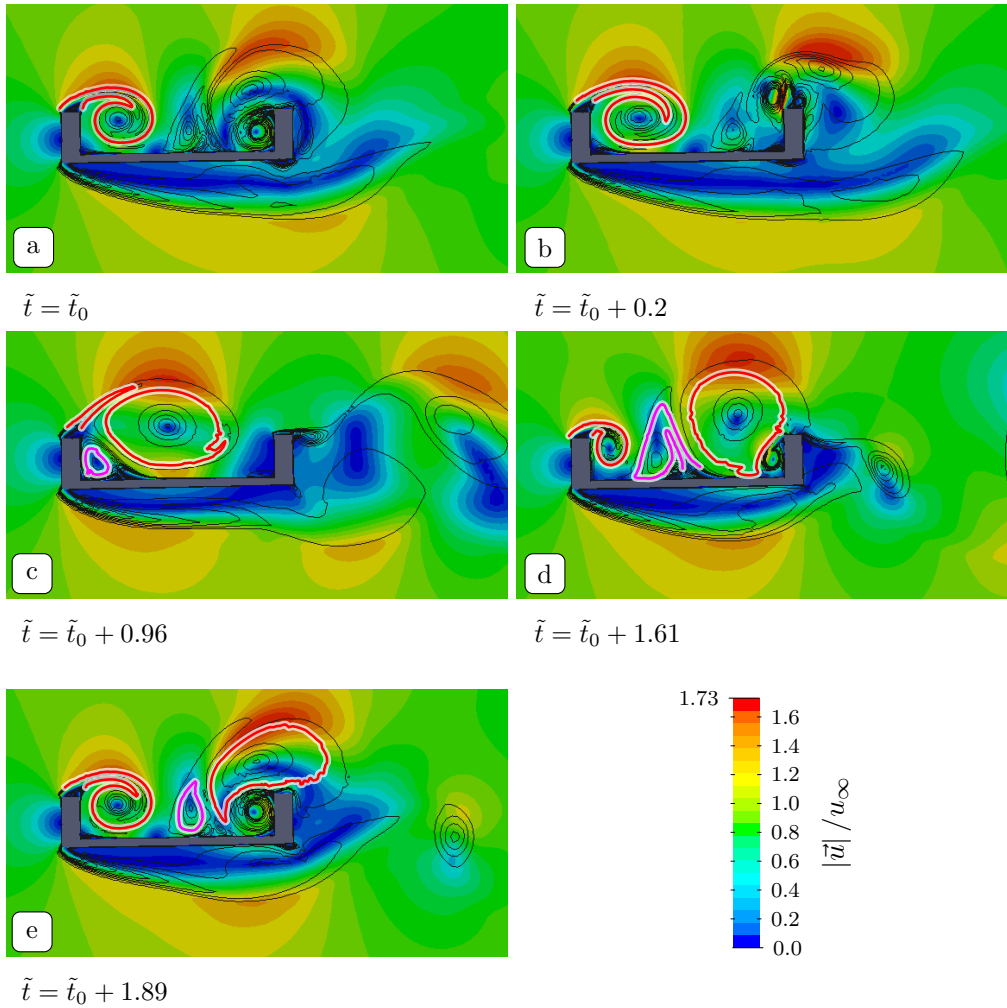


Figure 3.7.: U-flow pattern: snapshots coloured by velocity magnitude and additional vorticity magnitude contours. Some vorticity magnitude contours are highlighted. Simulation at $\varphi = 1^\circ$, $\text{Re} = 2.45 \cdot 10^5$. $\tilde{t}_0 = 147$ dimensionless time units after the simulation was started with developed U-flow.

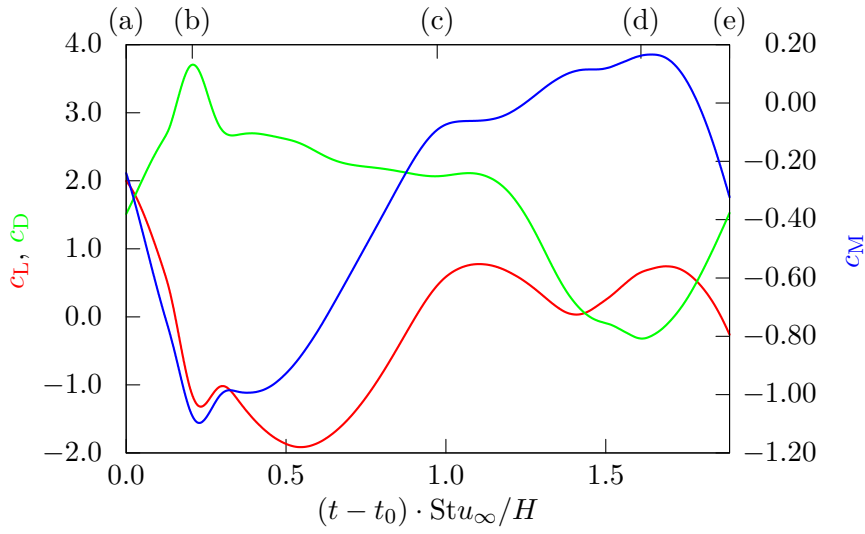


Figure 3.8.: U-flow pattern: Time-dependent aerodynamic forces. Simulation at $\varphi = 1^\circ$, $\text{Re} = 2.45 \cdot 10^5$. $\text{St} = 0.135$, $\tilde{t}_0 = 147$ dimensionless time units after the simulation was started with developed U-flow pattern. The top axis marks the positions of the snapshots in figure 3.7.

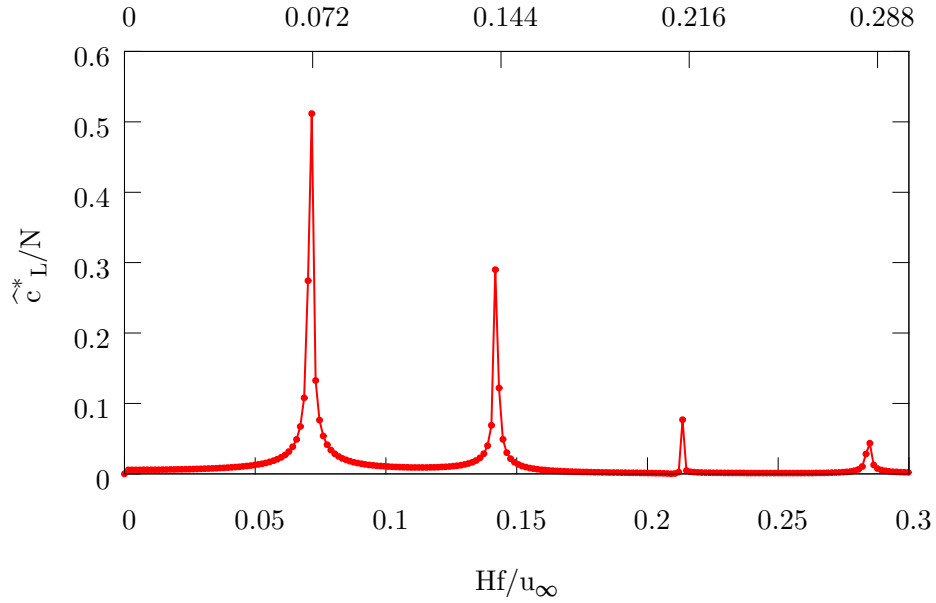


Figure 3.9.: Spectrum of the mean-free lift coefficient $c_L - \bar{c}_L$ under the U-flow pattern. \hat{c}_L^* is the Fourier coefficient, N is the sample size.

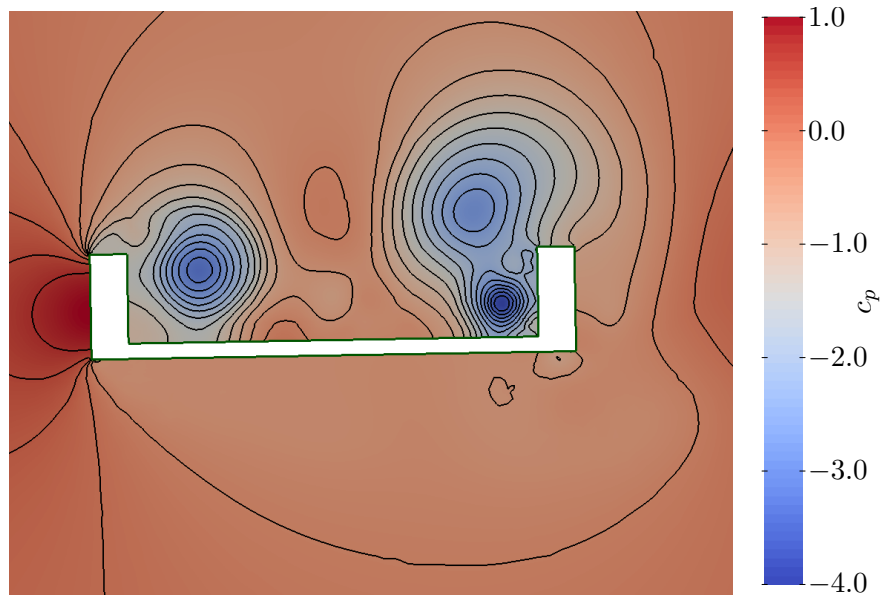


Figure 3.10.: Pressure contours at the time instance of maximum lift and large torsional moment (snapshot figure 3.7,d).

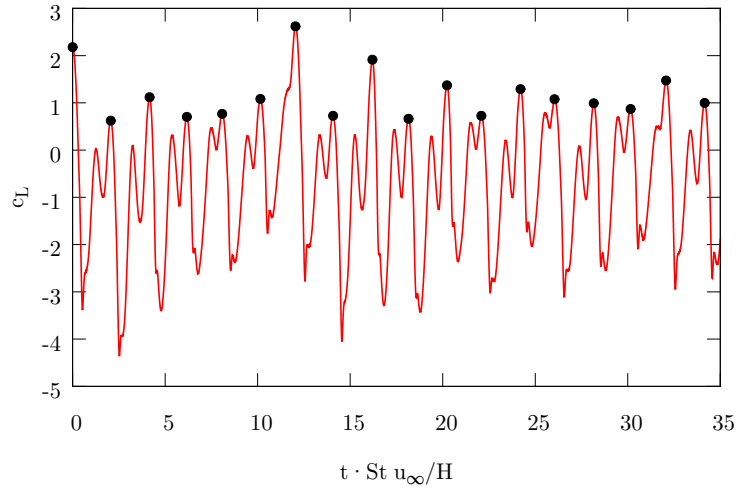
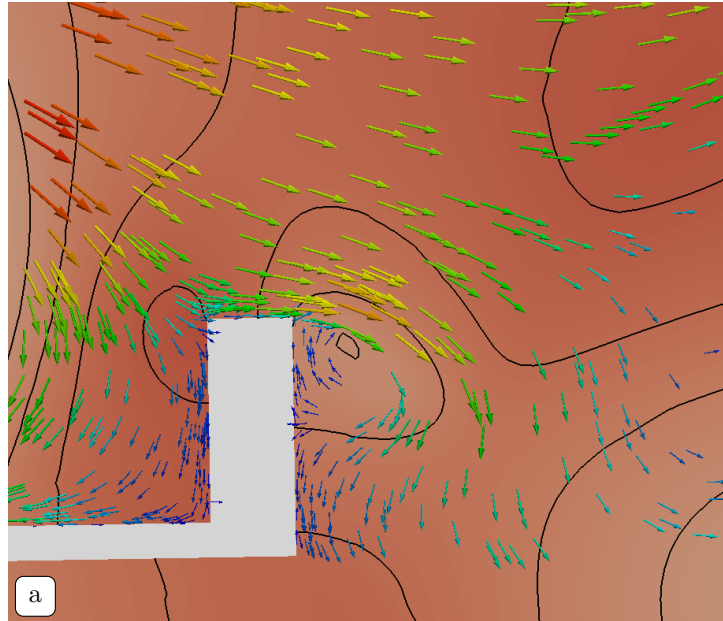
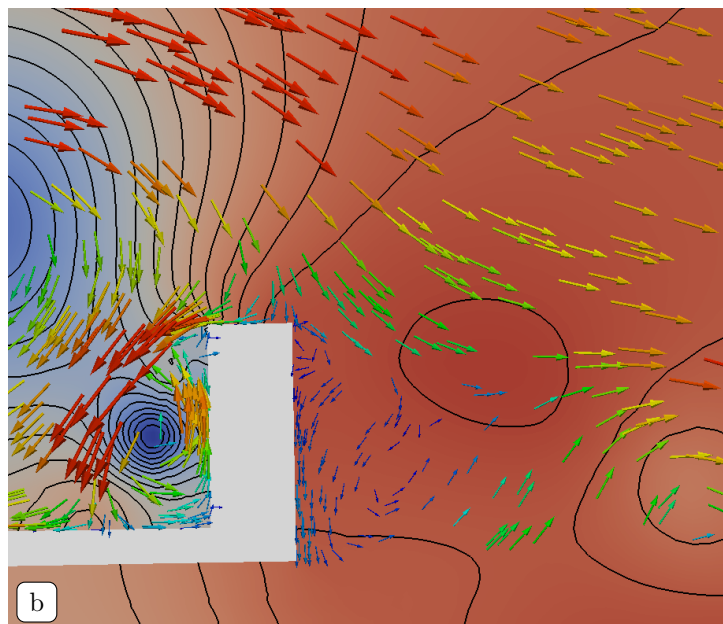


Figure 3.11.: Time-series of the lift coefficient under the U-flow pattern showing the slight modulation. Time instances of peak lift due to cavity vortex impingement are marked with a dot.



$$\tilde{t} = \tilde{t}_0 + 1.06$$



$$\tilde{t} = \tilde{t}_0 + 1.61$$

Figure 3.12.: Flow-field under the U-flow pattern at the leeward flange of the U at the time of maximum lift (a) and at a local maximum of the lift (b). Field coloured by the static pressure. Arrows coloured and scaled by the velocity magnitude. Simulation at $\text{Re} = 2.45 \cdot 10^5$ and $\varphi = 1^\circ$.

3.1.3. On the initial conditions and the change of flow patterns

To prepare the study of the influence of the inclination angle (section 3.1.4) a few details about the simulation setup have to be mentioned. The simulations were started with trivial initial conditions at zero inclination. To set the desired angle of inclination the mesh was rotated during the first one-hundred time-steps (roughly one seventh of a flow period under the R-flow pattern) (see, for example, figure 3.13). The profile was held at rest during the remainder of the simulation (120000 minus one-hundred time-steps). Depending on the target angle of inclination, either the U-flow pattern or the R-flow pattern would develop (example in figure 3.13: the U-flow pattern). Following this strategy we obtained two distinct inclination intervals where either the U-flow pattern would develop ($2^\circ \leq \varphi \leq 10^\circ$) or the R-flow pattern would develop ($-10^\circ \leq \varphi \leq 1^\circ$).

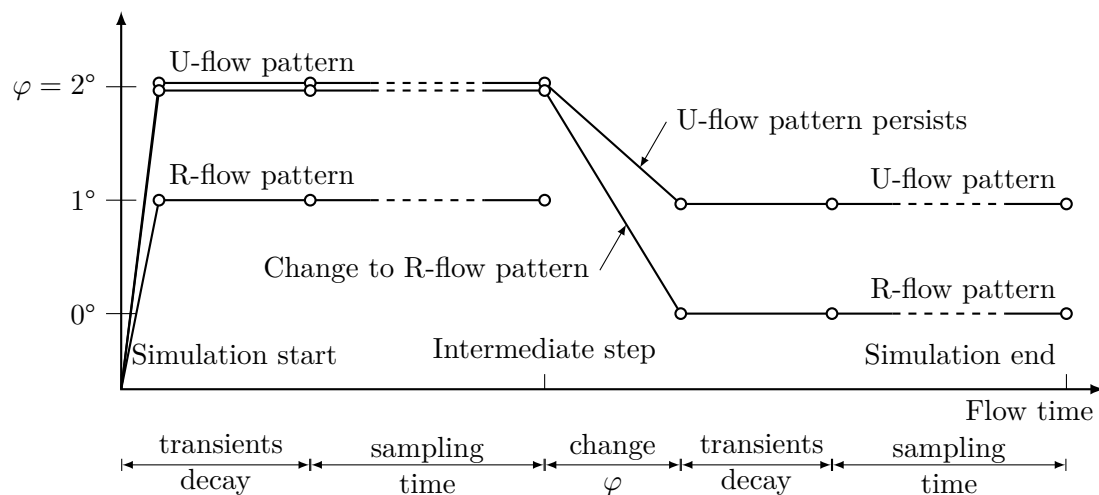


Figure 3.13.: Scheme of the simulation strategy to test which flow pattern can be realised at a given inclination angle: The angle of inclination during three typical simulation runs.

To extend these intervals, another series of simulations was set up. A fully developed flow pattern at a given angle of inclination was used as initial condition (the “intermediate step” in figure 3.13). Then, the profile was rotated during the course of twenty R-flow periods to a new angle of inclination ($\varphi = 1^\circ$ or $\varphi = ang0$ in figure 3.13). Then its position remained fixed throughout the rest of the simulation. Depending on the initial flow pattern and the new inclination of the profile the flow pattern remained the same or changed. Thus, it is possible to achieve both flow patterns at some inclinations on the same calculation mesh under the same flow conditions by preparing the initial conditions.

The change from U-flow to the R-flow pattern is an interesting phenomena and will be important in section 5.1. Recall that under the U-flow pattern, the cavity vortex forms right behind the windward flange of the profile (see figure 3.14a). The secondary vortex is also swept into the wake. Before the change to the R-flow pattern occurs part of the

secondary vortex remains in the corner of the cavity. Then, the formation of the next cavity vortex is impeded by the remainder of the secondary vortex (see figure 3.14b and 3.14c). Finally, the cavity vortex cannot form at all. The free shear layer originating from the top windward corner reaches over the cavity of the U (see figure 3.14d). The R-flow pattern developed from the U-flow pattern. The secondary vortex has become the counterclockwise rotating vortex observed under the R-flow pattern. This change appears to be irreversible in 2D simulations. Transition from the R-flow pattern to the U-flow pattern was only observed at large positive inclinations, $\varphi > 6^\circ$.

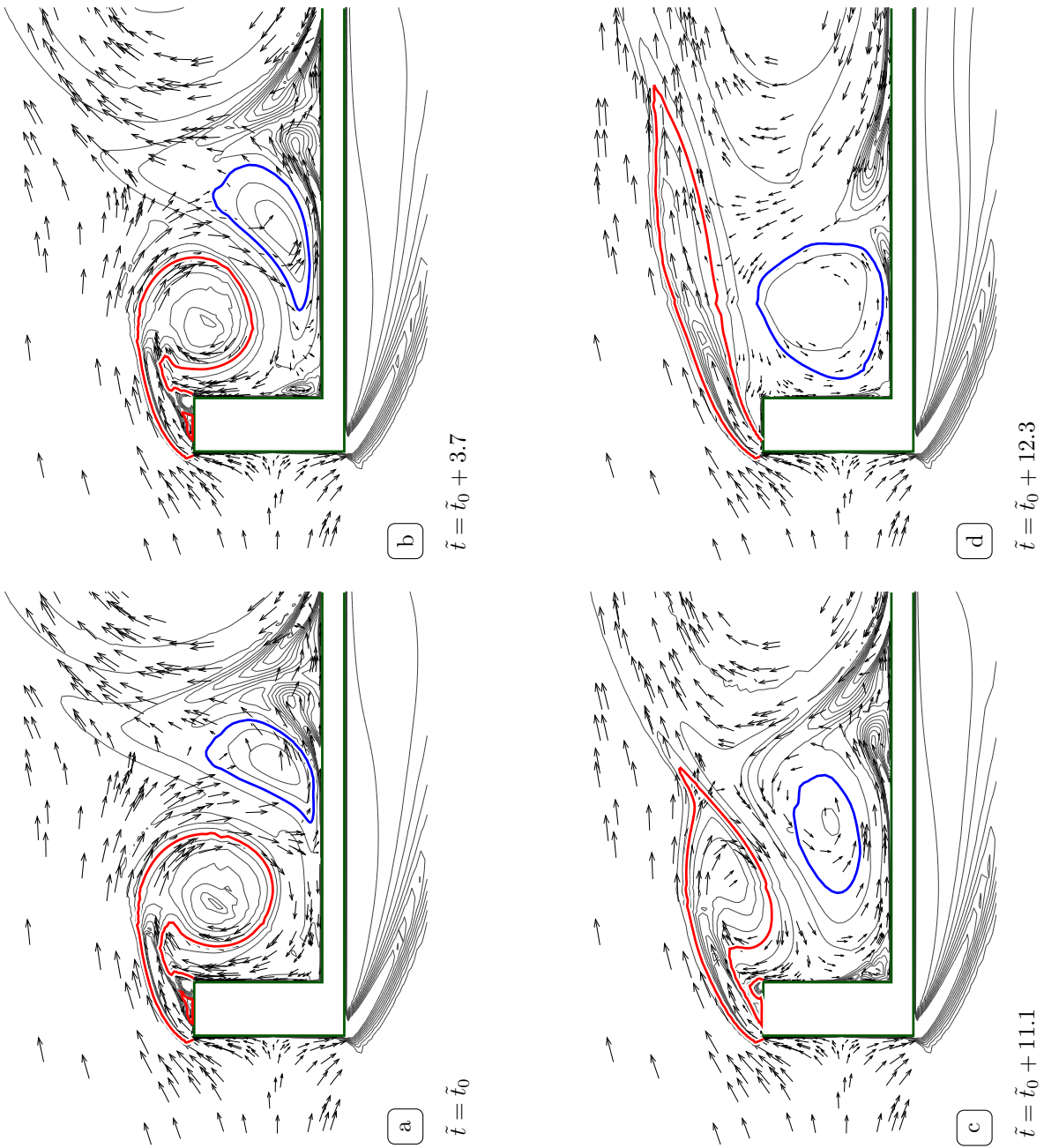


Figure 3.14.: Flow-field snapshots during transition from the U-flow pattern to the R-flow pattern with flow velocity arrows and vorticity iso-lines (red: primary vortex, blue: secondary vortex). The snapshots were taken at time instances of maximum lift (figure 3.15). $\tilde{t}_0 = 7.5$ after the simulation was started with trivial initial conditions.

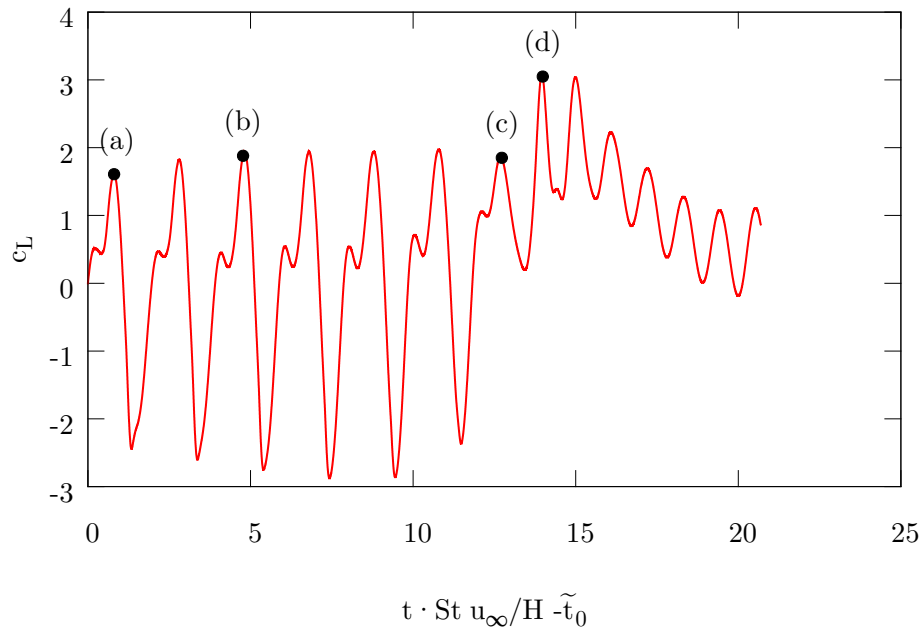


Figure 3.15.: Lift coefficient during the transition from U-flow to R-flow pattern. Labels correspond to subfigures in figure 3.14, $\tilde{t}_0 = 7.5$.

3.1.4. Influence of the angle of inclination

When simulating the flow around an inclined U-profile, the inclination angle influences which flow pattern can be realised. At small inclinations, $\varphi \leq 1^\circ$, only the R-flow pattern can be realised (see figure 3.16). In the interval $2^\circ \leq \varphi < 6^\circ$ both flow patterns could be realised by the above outlined procedure (section 3.1.3 and figure 3.13). For $\varphi \geq 10^\circ$ only the U-flow pattern is possible.

The aerodynamic forces also depend on the inclination angle. The lift coefficient has a negative slope in the range $-5^\circ \leq \varphi \leq 5^\circ$. The drag coefficient has a minimum at $\varphi = 0^\circ$. It increases for $\varphi \leq 0$. The fluctuation of the force coefficients also has a minimum at $\varphi = 0^\circ$ (see figure 3.17).

The aerodynamic forces under the U-flow pattern follows the same trends. The mean lift and moment coefficients are lower than under the R-flow pattern. The mean drag coefficient is higher. The fluctuations about the mean values increase for all coefficients (see figure 3.17).

The U-flow pattern was observed for $\varphi > 1^\circ$ (see figure 3.16). This minimum angle depends on the mesh size near the U-profile. In free vibration simulations (see chapter 5) $\varphi = 0^\circ$ was obtained. Before decreasing the cell sizes further, other models involved in the simulation (specifically the turbulence model and the 2D-assumption) should be reviewed and improved.

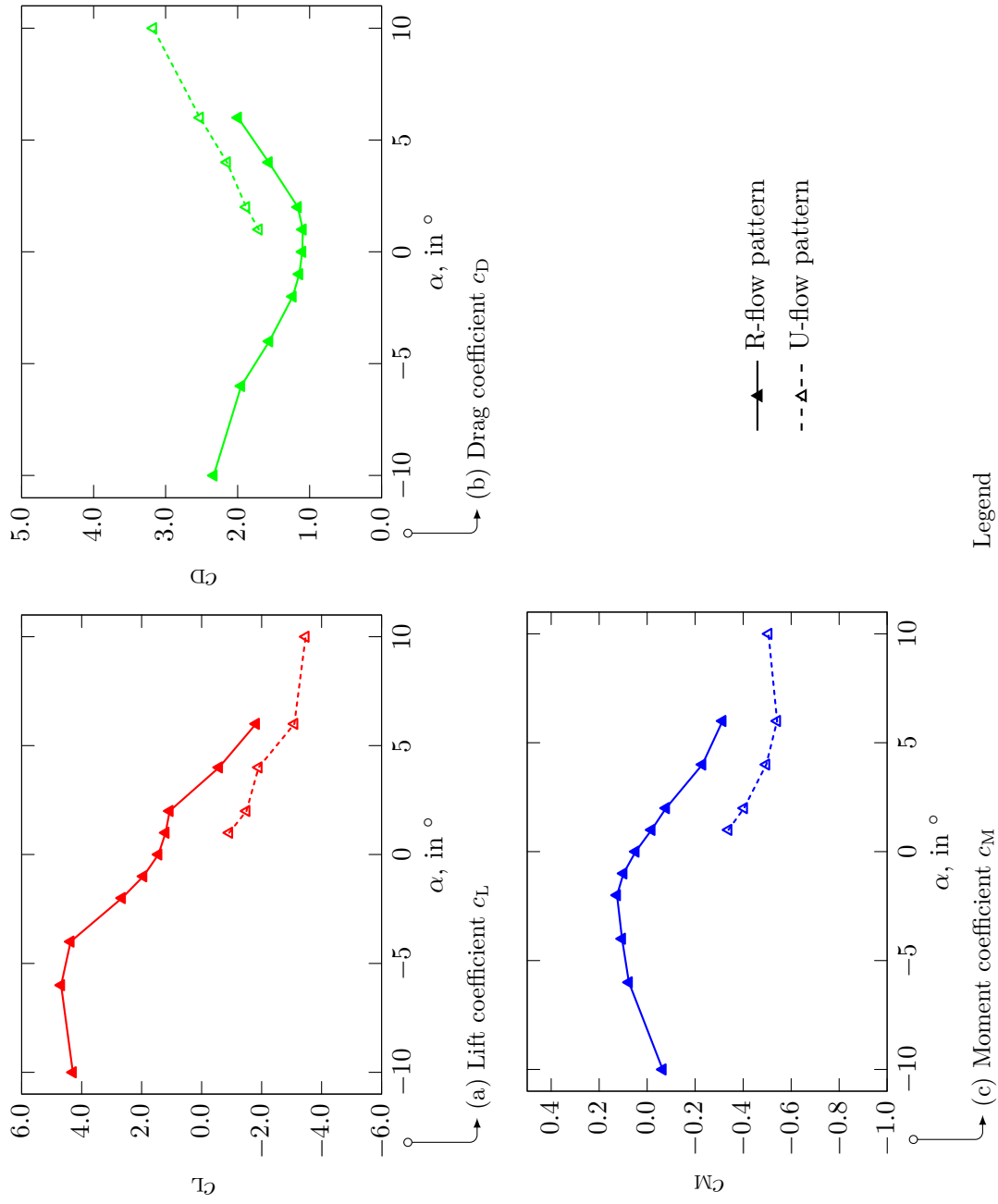


Figure 3.16.: Force coefficients for several angles of inclination. Simulation at $Re = 2.45 \cdot 10^5$.

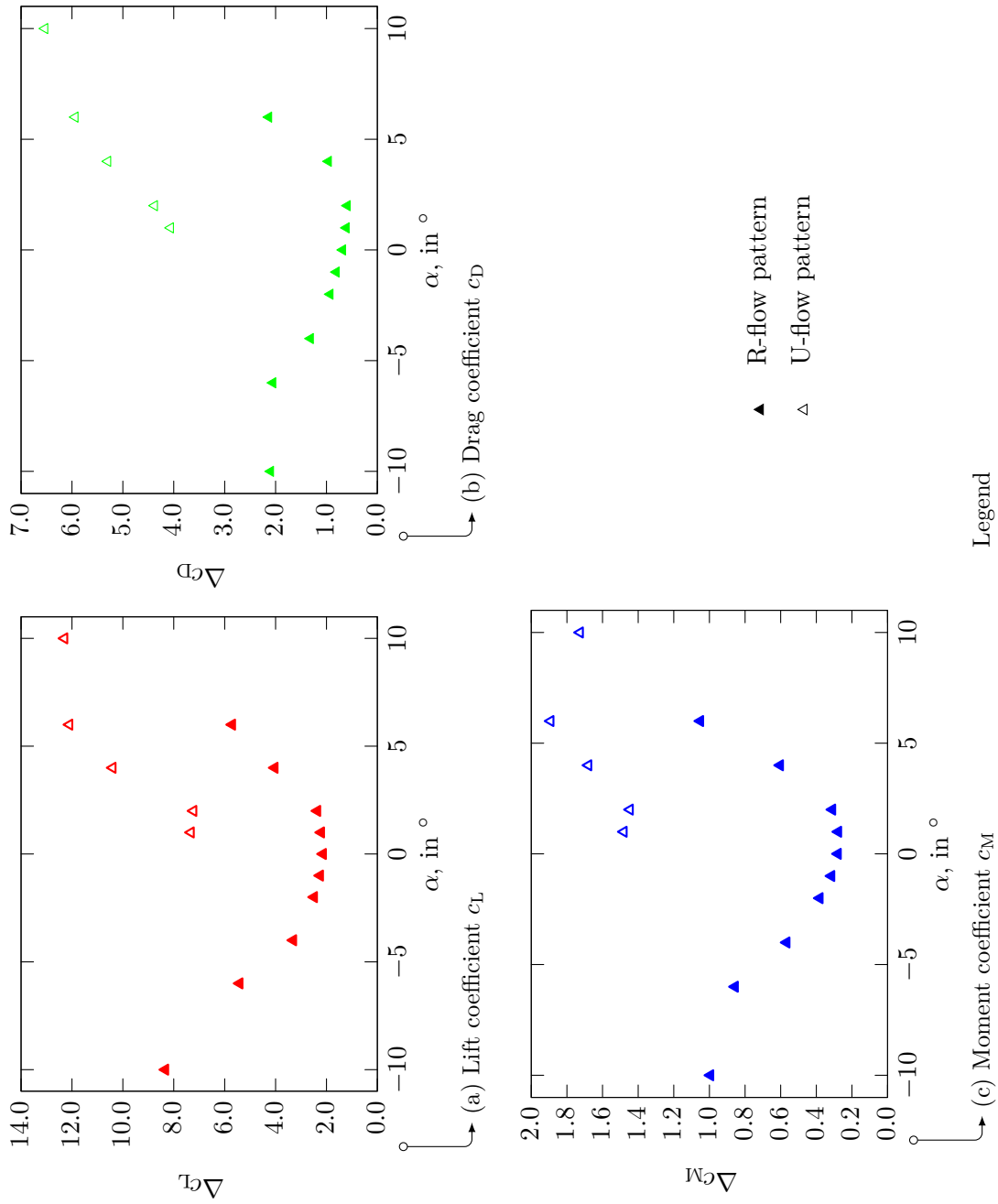


Figure 3.17.: Fluctuation of the force coefficients around their mean value for several angles of inclination. Simulation at $Re = 2.45 \cdot 10^5$.

3.2. Comparison with PIV wind tunnel tests

The available data consists of the time-periodic flow-fields under either flow patterns obtained by **2D-CFD** simulation, and flow-field snapshots obtained by **PIV**. Meaningful comparison of this data requires a careful approach and will be made in two steps. First, the time-averaged flow fields will be compared. Then snapshots of the flow field will be discussed. Finally the influence of the inclination angle is discussed.

3.2.1. Time-averaged flow fields

As a first step the statistics of the flow-field are analysed, i.e. the time-average and standard deviation of the flow velocity. The flow fields obtained by **PIV** experiments and **2D-CFD** simulations are compared. Flow field statistics from **PIV** data were obtained using one complete series of captured flow field snapshots, which includes estimated 9.5 flow periods under the R-flow pattern, i.e. the sampling time was 9.5 times the vortex shedding frequency under the R-flow pattern, $t_s = 9.5/f_{vs}$. Statistics from simulations were calculated using only one flow period, since the simulated flow is time-periodic.

In figure 3.18 the time-averaged flow-field is shown. Additionally, an iso-line of the velocity magnitude standard deviation at the value $0.5 s_{|u|,max}$ is marked (red), where $s_{|u|,max}$ is the maximal standard deviation in the field:

$$s_{|u|,max} = \max_{x_1, x_2} \frac{1}{N+1} \sum_i (|u_i(x_1, x_2)| - |\bar{u}(x_1, x_2)|)^2 \quad (3.7)$$

Areas of large velocity standard deviation indicate regions where the flow is strongly time-dependent. Also note the regions in figure 3.18 where the **PIV** result is unreliable (blue rectangles, see section 2.2.2). In the time-averaged flow-field in figure 3.18 a single vortical structure rotating clockwise can be seen above the leeward half of the cavity. However, this region is also characterised by a large velocity standard deviation, indicating a time-dependent flow field. These regions will be further discussed by studying the snapshots of the flow-field. Furthermore, the evolution of the free shear layer separating from the bottom windward corner of the profile is strongly time-dependent and, naturally, the wake behind the profile. The maximal value of the flow velocity standard deviation, scaled with the far-field flow velocity u_∞ was $s_{|u|,max}^{(P)}/u_\infty = 0.46$.

Time-averaged simulation results of either flow pattern are shown in figure 3.19. The time-averaged flow-field of the U-flow pattern is characterised by a single, large vortical structure in the cavity of the profile (figure 3.19a), rotating clock-wise. This structure is part of a time-dependent region of the flow-field, as indicated by the red standard deviation contour at $0.5 s_{|u|,max}^{(U)}$. In fact, it encompasses the whole cavity, as well as the wake of the profile, owing to the formation of cavity vortices as described above. The maximal, non-dimensional standard deviation was $s_{|u|,max}^{(U)}/u_\infty = 0.94$, including the contribution from the turbulent kinetic energy: The variance of one velocity magnitude is given by the sum of the variance due to coherent structures resolved by the turbulence model, and the variance due to the turbulent fluctuations modelled by the **turbulent kinetic energy (TKE)**,

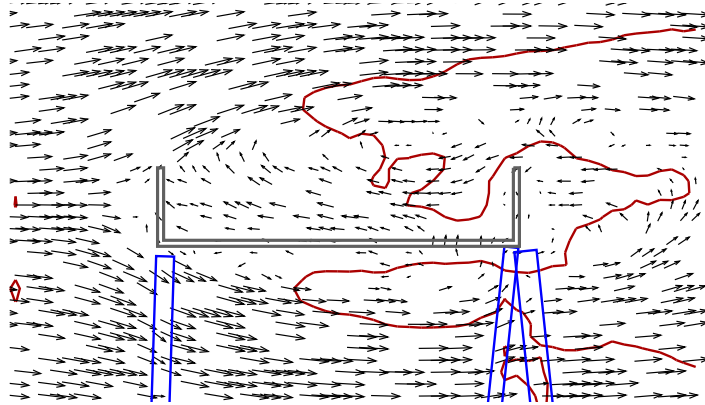


Figure 3.18.: Time-averaged flow field (arrows) with an isoline of the velocity magnitude standard deviation (red), obtained by PIV.

$$s_{|u|}^2 = \frac{1}{N+1} \sum_i (|u|_i - |\bar{u}|)^2 + \frac{2}{3} \overline{\text{TKE}}, \quad (3.8)$$

where the summation was carried out over one flow period and $\overline{\text{TKE}}$ is the time-averaged turbulent kinetic energy.

Unlike the previously discussed flow fields the time-averaged R-flow field (figure 3.19b) is characterised by two vortical structures in the cavity of the profile. One vortex in the leeward half of the cavity is rotating in clockwise direction while the other vortex in the windward half of the cavity is rotating in counter-clockwise direction. Note that the standard-deviation iso-line at $0.5s_{u,\max}^{(R)}$ (where $s_{v,\max}^{(R)}/u_\infty = 0.57$), which already includes the contribution from the turbulent kinetic energy, encompasses only the wake of the profile and a small region in the free shear layer above the cavity and not the two vortical structures.

No conclusive evidence for either flow pattern can be obtained by comparing the time-averaged flow fields. The standard deviations as seen in the PIV data indicate that the flow-field becomes instationary well before the leeward corners of the profile (figure 3.18). Yet, the instationary regions of the U-flow field begins right after the windward flange of the profile. The instationary regions of the R-flow field encompass mainly the wake and it appears that the flow in the cavity and above is almost stationary. The next section discusses snapshots of the flow-field in the light of the already gained insights.

3.2.2. Flow-field snapshots (R-flow pattern)

First, snapshots of the R-flow pattern are discussed. Recall that the snapshots of the R-flow pattern (figure 3.3) revealed that the two vortices in the cavity are almost stationary. Hence the temporal statistics previously discussed show a very small flow velocity standard deviation. A snapshot of the flow-field under the R-flow pattern is shown in figure 3.20. The profiles of the horizontal flow velocity component suggest that the free

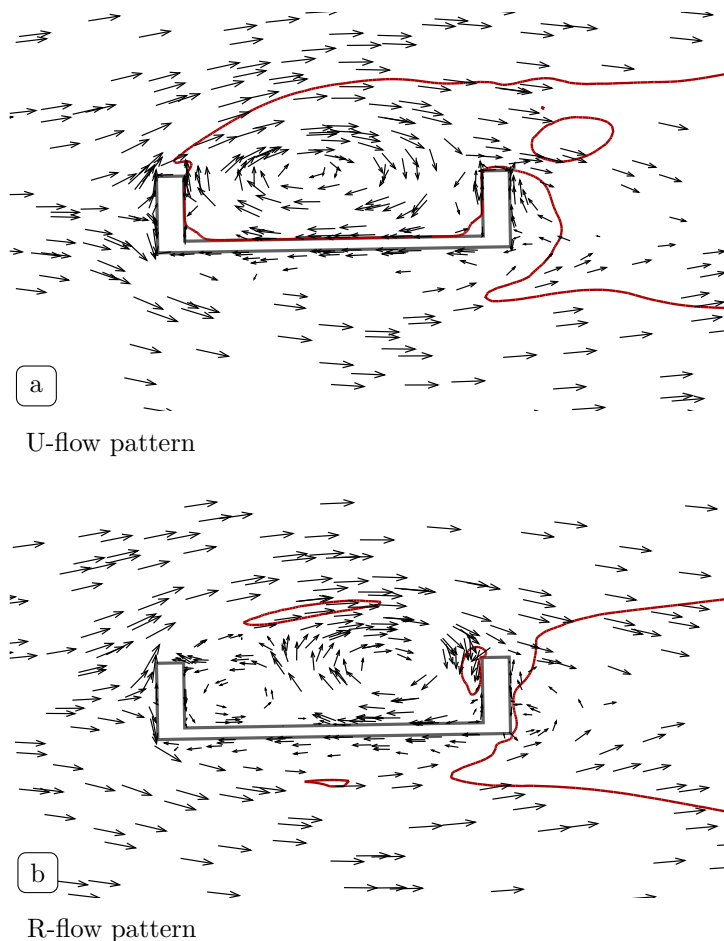


Figure 3.19.: Time-averaged flow field (arrows) with an isoline of the velocity magnitude standard deviation (red), obtained by 2D-CFD Simulation.

shear layer is sensitive to small perturbations. Especially the local velocity profile at $x = -0.32B$ (blue, left profile in figure 3.20) resembles that of the shear layer in a Kelvin-Helmholtz scenario. Indeed, the large values of the turbulence intensity I (estimated from the turbulent kinetic energy, magenta line) indicate that many eddies are formed in the free shear layer. These eddies are not resolved in space and time, but accounted for through the turbulent kinetic energy. Larger vortices, present in the wake of the profile are resolved in space and time. The clear distinction between the resolved and modelled timescales is an implicit assumption of URANS models. Critics of URANS methods argue that the evolution of free shear layers may depend sensitively on small eddies and that the implied separation of timescales is not given in bluff body flows [32].

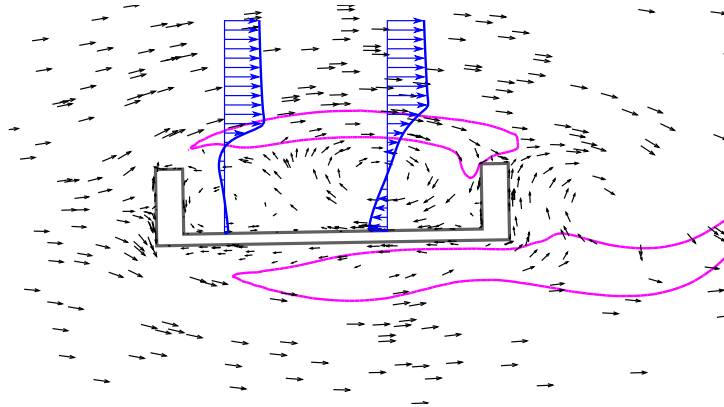


Figure 3.20.: Snapshot of the simulated flow-field (R-flow pattern) with two u-velocity profiles and a turbulence intensity isoline, $I = 15\%$.

3.2.3. Flow-field snapshots (U-flow pattern)

Recall, that the U-flow pattern revealed a strongly time-dependent flow-field in the cavity (figure 3.19a). Indeed, a snapshot of the flow-field shows that unlike under the R-flow pattern, the average flow-field has very little in common with a snapshot (figure 3.21). The velocity profile (blue) shows the roll-up of the shear layer as seen in the snapshots of the U-flow (figure 3.7). The green arrow in figure 3.21 shows the approximate path of the vortex core. Recall that the vortex at the tip of the arrow was formed behind the windward flange (where the green arrow begins) during the previous flow period and has travelled towards the leeward flange. The turbulence intensity is low where the cavity vortex forms but large between the two vortical structures, and also around the shear layer below the profile.

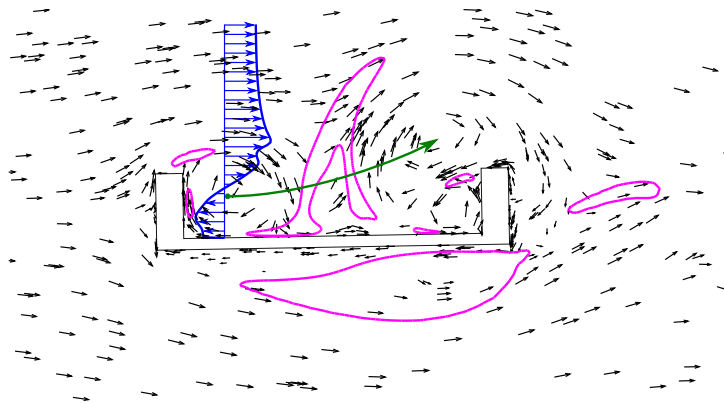


Figure 3.21.: Snapshot of the simulated flow-field (U-flow pattern) with a u-velocity profile and a turbulence intensity isoline, $I = 15\%$.

Another often stated criticism of URANS methods, especially in two-dimensional computational domains, is the slow decay of vortical structures as they travel through the

computational domain. The large turbulence intensities around the second vortex in figure 3.21 suggest that the (three-dimensional) decay of the cavity vortex may be important in reality. Before the influence of the cavity vortices on the aerodynamic forces is discussed, a comparison with snapshots of the flow field obtained by the PIV experiments is given, where evidence for the cavity vortices will be given.

Some snapshots of the flow-field acquired by PIV resemble the aforementioned R-flow patterns in a way (see figure 3.22). The shear-layer is curved weakly and reaches over the cavity of the profile (green arrows). Vortices can be seen in the wake behind the profile. The flow in the cavity itself does not resemble the R-flow pattern. Instead, the orientation of the arrows suggest a three-dimensional flow-field. Despite this, the velocity profile (blue) is similar to the profile shown in figure 3.20, locally resembling a Kelvin-Helmholtz Scenario. In parallel shear-flows such a velocity profile could be unstable by Fjørtoft's criterion [27]. Indeed, a vortex of considerable size can be seen in this snapshot to the right of the velocity profile (green arrows in figure 3.22). These vortices contribute to the turbulent kinetic energy in the simulations of the R-flow pattern as they are not resolved (see figure 3.20). The question is whether these vortices can take on the role of the cavity vortex, which is observed in 2D-CFD simulations under the U-flow pattern.

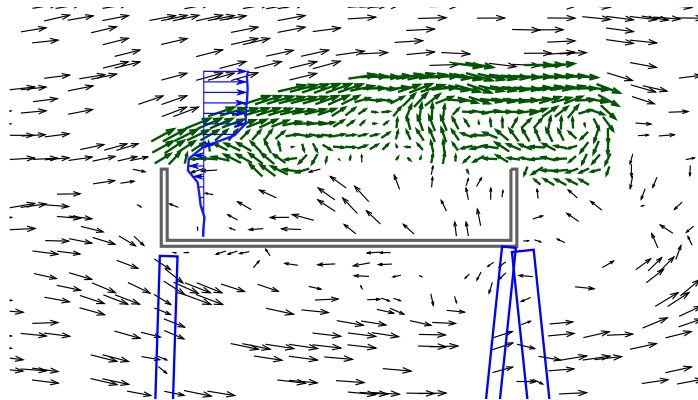


Figure 3.22.: Snapshot of the flow-field (PIV), visualised by arrows and a horizontal-velocity profile. The shear layer is curved weakly.

There is evidence that vortices can form right behind the windward flange of the profile (see figure 3.23, green arrows). By the horizontal-velocity profile (blue) it can be seen that a clockwise-rotating vortex is located at this position. Under the R-flow pattern a counter-clockwise rotating vortex would be present. This vortex is not stationary, but travels through the cavity towards the leeward flange. Also in figure 3.23a a second vortex rotating in clockwise direction can be seen at this position (green arrows). Subsequent snapshots show the left vortex detaching from the windward flange and travelling towards the leeward flange (figures 3.23b, 3.23c). Furthermore it can be observed that many vortical structures are located below the profile. These were also modelled as a contribution to the turbulent kinetic energy in the simulations. The last flow field snapshot shows that the cavity vortex failed to form (figure 3.23c). Instead,

the flow-field appears to be three-dimensional at this location.

Thus, aspects of both flow patterns were observed at the same angle of inclination in the PIV experiments. The figures 3.22 and 3.23 show only four out of 44 recorded flow-field snapshots. These snapshots were analysed how closely they resemble either the U-flow or the R-flow pattern.

- It was chosen to count snapshots where vortices rotated in counter-clockwise direction in the windward half of the cavity as “R-flow frame”.
- Frames where clockwise rotating vortices were located in the cavity of the profile were considered an “U-flow frame”.
- All other frames were counted as “undecidable”.

Of 44 frames spanning 19 flow periods, 13 frames resembled the U-flow pattern by the above described criteria. Only one was considered to represent the R-flow pattern. The remaining 30 frames were deemed “undecidable”. These frames are mainly characterised by small vortices forming in the free shear layer and a possibly three-dimensional flow in the cavity (similar to figure 3.22). The two almost stationary vortices seen in 2D-CFD simulations under the R-flow pattern (figure 3.19b) could be unstable in three dimensions. Thus, the “undecidable” frames may resemble the R-flow pattern. Then, the flow switches between the two flow patterns observed in 2D-CFD simulations. Numerically, no intermittent change between the flow patterns was observed. Change between flow patterns from U-flow to R-flow and back again could only be achieved by substantially varying the inclination angle during a simulation run.

3.2.4. Influence of the angle of inclination

First, let the U-profile be positively inclined, $\varphi_0 = 5^\circ$. Application of the criteria described above lead to the following results: Of 44 available snapshots none resembled the R-flow pattern but 26 showed features of the U-flow pattern. The remaining 18 snapshots were deemed undecidable. When positively inclined, the leeward flange of the profile is closer to the free shear layer and influences the formation of cavity vortices such that they appear more often. Large vortices, such as the cavity vortices are, should be detectable downstream of the profile in its wake. Inspection of the flow velocities in the wake behind the U-profile by means of a CTA probe showed that there is a band of frequencies present, yielding $0.065 \leq St^{(P,U)} \leq 0.083$ (figure 3.24). These frequencies correspond to the formation frequency of cavity vortices. They are lower than the Strouhal number attributed to the “classical” vortex shedding $St^{(P)} = 0.133$, obtained at $\varphi_0 = 0^\circ$, and also lower than the Strouhal numbers others observed in the flow around a rectangular prisms with similar aspect ratio [58].

When the U-profile is negatively inclined, $\varphi_0 = -5^\circ$, none of the 44 available snapshots resemble either U-flow or R-flow pattern. Instead, every frame is “undecidable” by the above described criteria. The snapshots are characterised by a very complex flow in the cavity which appears to be non-periodic and highly three-dimensional. The shear

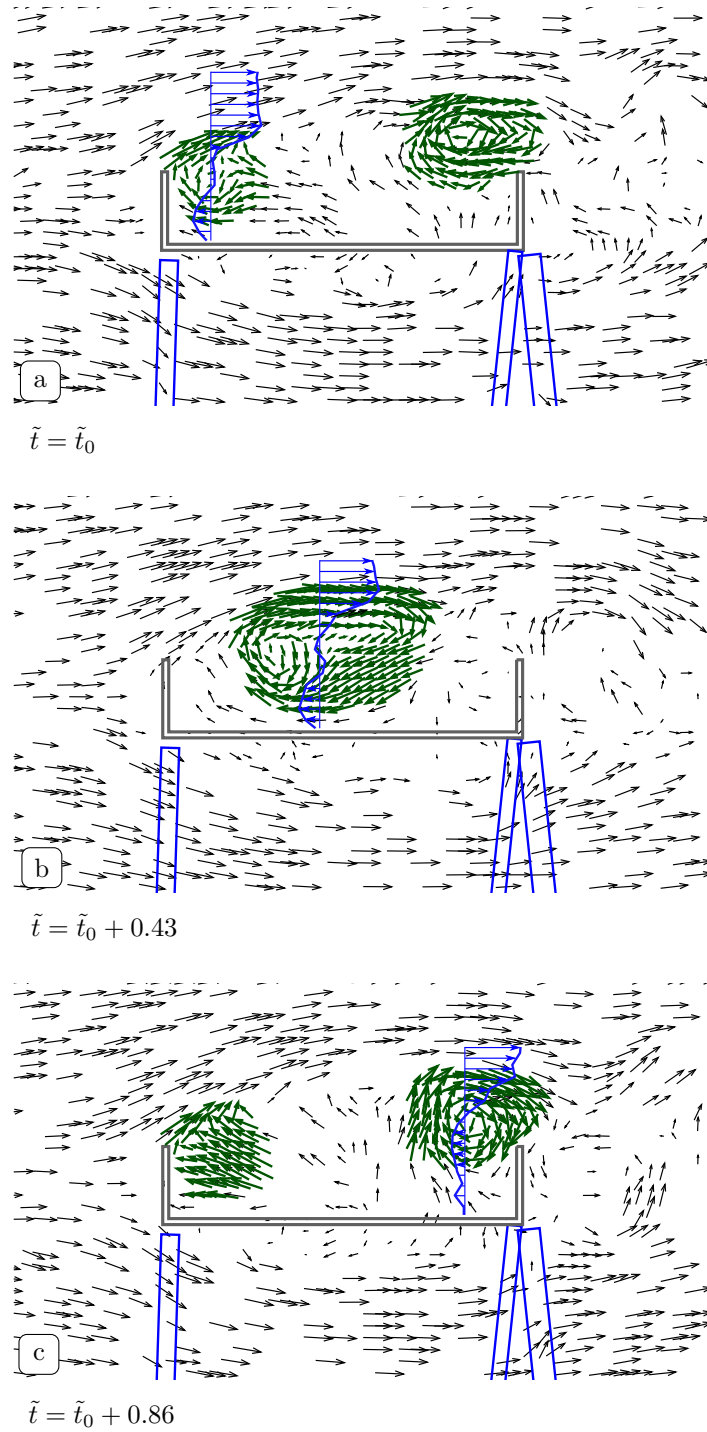


Figure 3.23.: Three successive snapshots of the flow-field (PIV), visualised by arrows and a u-velocity profile.

layer separating from the top windward corner of the profile is still easily perturbed and forms vortices. Yet they move above the leeward flange and do not influence the flow in the cavity much. Inspection of the flow velocities in the wake yield a Strouhal number $St^{(P)} = 0.133$ (figure 3.25) which is numerically equal to the value of St obtained at zero inclination $\varphi_0 = 0^\circ$.

3.2.5. Implications

The existence of two time-periodic flow patterns in the 2D-CFD simulations means that the simulation effort in chapter 5 has doubled. For every parameter set two simulation runs have to be carried out. One run starting with the U-flow pattern, the other with the R-flow pattern. Since the PIV experiments predict intermittent change of the flow patterns, it remains an open question whether profile motion favours one or the other flow pattern. Unfortunately, this question can not be answered with the herein employed numeric methods. Therefore, flow induced vibrations will be studied under either flow pattern. By comparison with wind tunnel tests an attempt to answer the above question will be made.

Principally, the aerodynamic derivatives (chapter 4) would also have to be calculated twice, once for each flow pattern. However, it turns out, that under slow profile motion the U-flow pattern changes to the R-flow pattern. Thus, the aerodynamic derivatives will only be computed for the R-flow pattern.

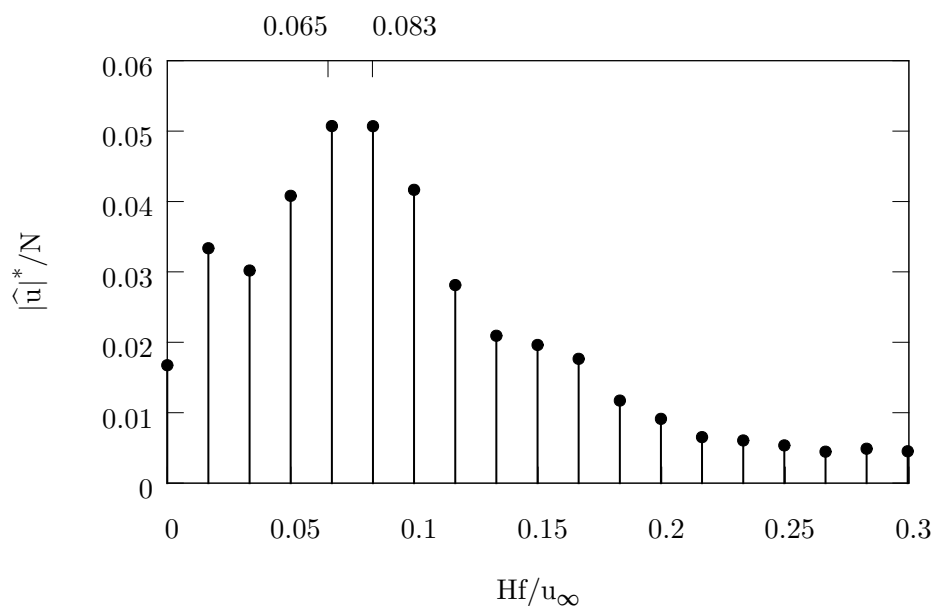


Figure 3.24.: Frequency spectrum of the flow velocity magnitude in the wake of the U-profile at inclination $\varphi = 5^\circ$.

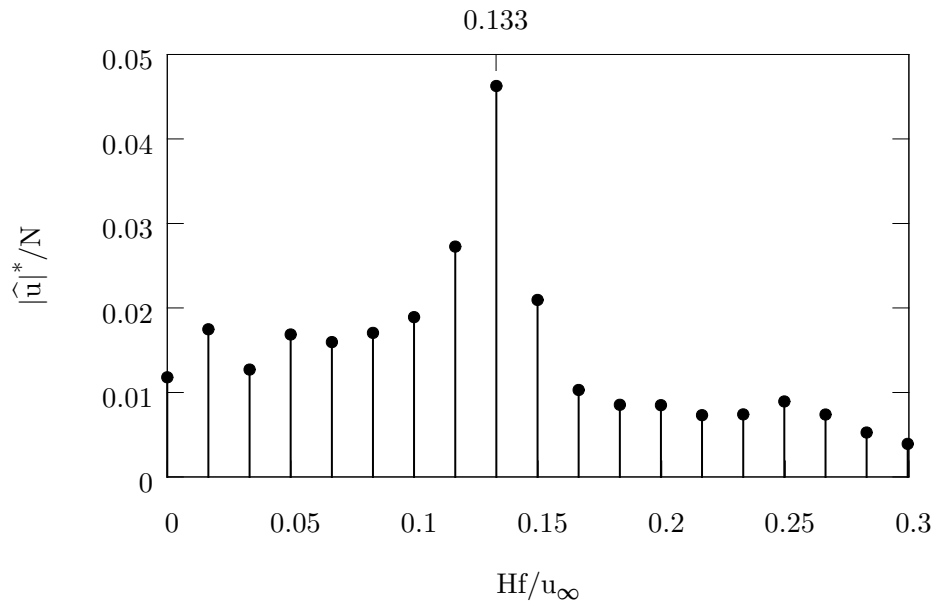


Figure 3.25.: Frequency spectrum of the flow velocity magnitude in the wake of the U-profile at inclination $\varphi = -5^\circ$.

4. Aeroelastic stability by forced motion simulations

The classical analysis for translational galloping (a so-called self-excited vibration) is based on studying the flow around a static, rigid body, [81]. This easy approach is limited to two single-degree of freedom heave (vertical translation) vibrations. To determine the stability of a rigid body with two (or more) degrees of freedom (here: “heave” and “pitch”; i.e. torsional vibrations) a better model for the motion-dependent aerodynamic forces is needed. The so-called aerodynamic derivatives provide such a model.

4.1. Aerodynamic derivatives of a U-profile

The framework of aerodynamic derivatives models motion dependent aerodynamic forces. Scanlan, [90], was among the first to formalize the concept: The aerodynamic lift L and moment M are considered to depend (symbolically) on the displacement and velocity of the profile, e.g.

$$L = L(y, \dot{y}, \varphi, \dot{\varphi}) \quad (4.1)$$

$$M = M(y, \dot{y}, \varphi, \dot{\varphi}) \quad (4.2)$$

for harmonic motion with a certain frequency, such as

$$y = \hat{y} \sin(2\pi ft), \quad \text{or} \quad (4.3)$$

$$\varphi = \hat{\varphi} \sin(2\pi ft). \quad (4.4)$$

Here, small amplitudes, $\hat{y} = 0.01H$ or $\hat{y} = 0.03H$ and $\hat{\varphi} = 1^\circ$ or $\hat{\varphi} = 3^\circ$ have been prescribed. The frequency of the motion f can either be used to form a reduced velocity or, more commonly, a reduced frequency:

$$U_{\text{fm}}^* = u_\infty / (Hf) \quad (4.5)$$

$$K = \omega H / u_\infty = 2\pi f H / u_\infty \quad (4.6)$$

Assuming linear dependence of these forces on a small-amplitude motion, one can write

$$\begin{aligned}
 L &= \frac{1}{2}\rho u_\infty^2(2B) \left(KH_1^*(K)\frac{\dot{y}}{u_\infty} + KH_2^*(K)\frac{B\dot{\varphi}}{u_\infty} + K^2H_3^*(K)\varphi + K^2H_4^*(K)\frac{y}{B} \right) \\
 M &= \frac{1}{2}\rho u_\infty^2(2B^2) \left(KA_1^*(K)\frac{\dot{y}}{u_\infty} + KA_2^*(K)\frac{B\dot{\varphi}}{u_\infty} + K^2A_3^*(K)\varphi + K^2A_4^*(K)\frac{y}{B} \right).
 \end{aligned} \tag{4.7}$$

This choice of coefficients is based on [48]. The aerodynamic derivatives H_i^* and A_i^* depend on the reduced frequency $K = \omega B/u_\infty$ of the motion.

The aerodynamic lift L and moment M respond to the forced motion at the frequency of the forcing, but with a phase shift ψ , e.g.

$$L = \hat{L}_y \sin(2\pi f t + \psi_{L,y}), \tag{4.8}$$

that is the response of the aerodynamic lift to forced harmonic heaving motion with the amplitude \hat{L}_y and the phase shift of the lift force due to a heaving motion $\psi_{L,y}$. Of course vortex shedding also contributes to these forces, albeit at another frequency (exemplary shown in figures 4.1 and 4.2).

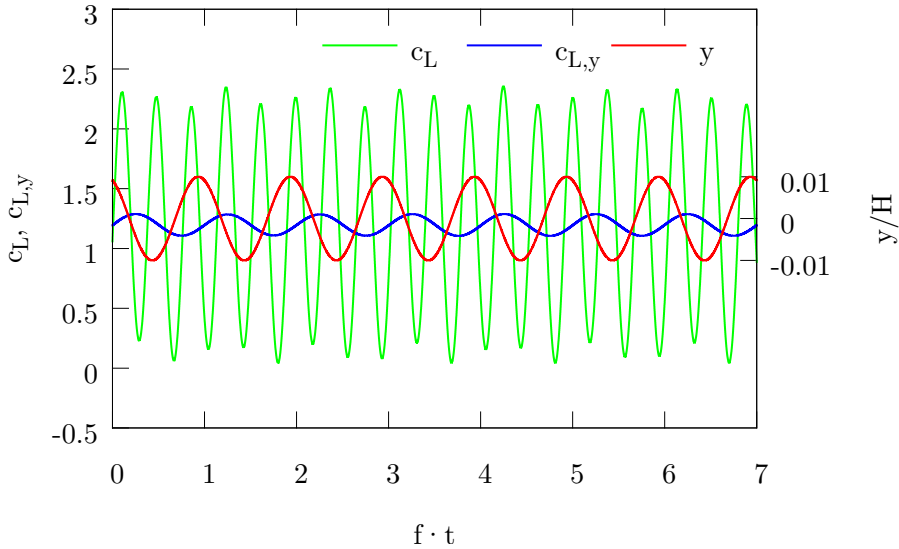


Figure 4.1.: Total, time-dependent lift coefficient c_L and lift coefficient attributed to the profile motion $c_{L,y}$ of the U-profile performing forced heave motion $y = \hat{y} \sin(\cdot)$, $U_{fm}^* = 20$, $\hat{y} = 0.01H$ (2D-CFD simulation).

The part of the spectrum influenced by the forced motion (red dots in the latter figure) was used to calculate the response of the aerodynamic forces (e.g. $c_{L,y}$ in figure 4.1). The vortex shedding is assumed to be independent from the forced motion.

Thus, the response of the aerodynamic forces to the forced motion is extracted. The response amplitudes and phase shifts (e.g. \hat{L} , $\psi_{L,y}$) were identified by non-linear fitting. Plugging the harmonic motion (equations (4.3) and (4.4)) into the ansatz for the aerodynamic forces (equation (4.7)) and solving for the aerodynamic derivatives yields the following equations:

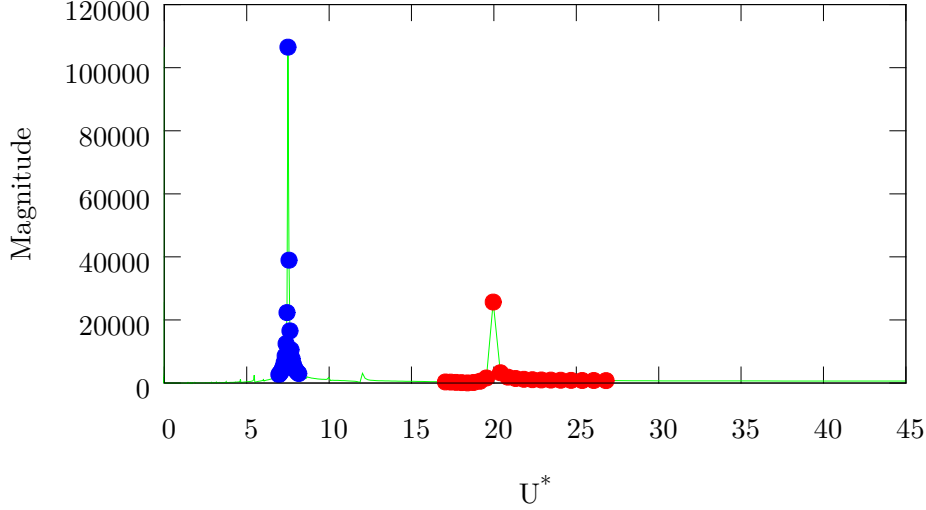


Figure 4.2.: Spectrum of the lift force under forced heaving motion $\hat{y} = 0.03H$ at $U_{\text{fm}}^* = 20$ (2D-CFD simulation). Red dots ●: the influence of the forced motion. Blue dots ●: the influence of the vortex shedding .

$$\begin{aligned}
 H_1^* &= \frac{1}{\frac{1}{2}\rho u_\infty^2 (2B)} \cdot \frac{B}{K^2} \cdot \frac{\hat{L}_y}{\hat{y}} \cdot \sin \psi_{L,y} & A_1^* &= \frac{1}{\frac{1}{2}\rho u_\infty^2 (2B^2)} \cdot \frac{B}{K^2} \cdot \frac{\hat{M}_y}{\hat{y}} \cdot \sin \psi_{M,y} \\
 H_2^* &= \frac{1}{\frac{1}{2}\rho u_\infty^2 (2B)} \cdot \frac{1}{K^2} \cdot \frac{\hat{L}_\varphi}{\hat{\varphi}} \cdot \sin \psi_{L,\varphi} & A_2^* &= \frac{1}{\frac{1}{2}\rho u_\infty^2 (2B^2)} \cdot \frac{1}{K^2} \cdot \frac{\hat{M}_\varphi}{\hat{\varphi}} \cdot \sin \psi_{M,\varphi} \\
 H_3^* &= \frac{1}{\frac{1}{2}\rho u_\infty^2 (2B)} \cdot \frac{1}{K^2} \cdot \frac{\hat{L}_\varphi}{\hat{\varphi}} \cdot \cos \psi_{L,\varphi} & A_3^* &= \frac{1}{\frac{1}{2}\rho u_\infty^2 (2B^2)} \cdot \frac{1}{K^2} \cdot \frac{\hat{M}_\varphi}{\hat{\varphi}} \cdot \cos \psi_{M,\varphi} \\
 H_4^* &= \frac{1}{\frac{1}{2}\rho u_\infty^2 (2B)} \cdot \frac{B}{K^2} \cdot \frac{\hat{L}_y}{\hat{y}} \cdot \cos \psi_{L,y} & A_4^* &= \frac{1}{\frac{1}{2}\rho u_\infty^2 (2B^2)} \cdot \frac{B}{K^2} \cdot \frac{\hat{M}_y}{\hat{y}} \cdot \cos \psi_{M,y}
 \end{aligned} \tag{4.9}$$

In our case, the aerodynamic derivatives shown in figure 4.3 were obtained. It was chosen to evaluate the aerodynamic derivatives for the only for the R-flow pattern.

The lowest reduced velocity at which the aerodynamic derivatives were computed was $U_{\text{fm}}^* = 12$. At this reduced velocity another effect could be seen. In this (and only this) case, a different flow pattern developed for $\hat{\varphi} = 3^\circ$. The flow is similar to the U-flow. The shedding of cavity vortices is possible through the pitching motion. This is reflected in a great difference between the values of A_2^* , A_3^* and H_2^* for either forcing amplitude.

It is our view that the aerodynamic derivatives at such low reduced velocities should not be used to predict stability. It is very likely that non-linear mechanisms like lock-in phenomena and vortex shedding affect the aerodynamic derivatives. Thus non-linear mechanisms are introduced into a linear framework.

The role of the A_4^* and H_4^* derivatives is not entirely clear. According to [81] they can be interpreted as contribution to the mass of the profile since they are scaled with K^2 .

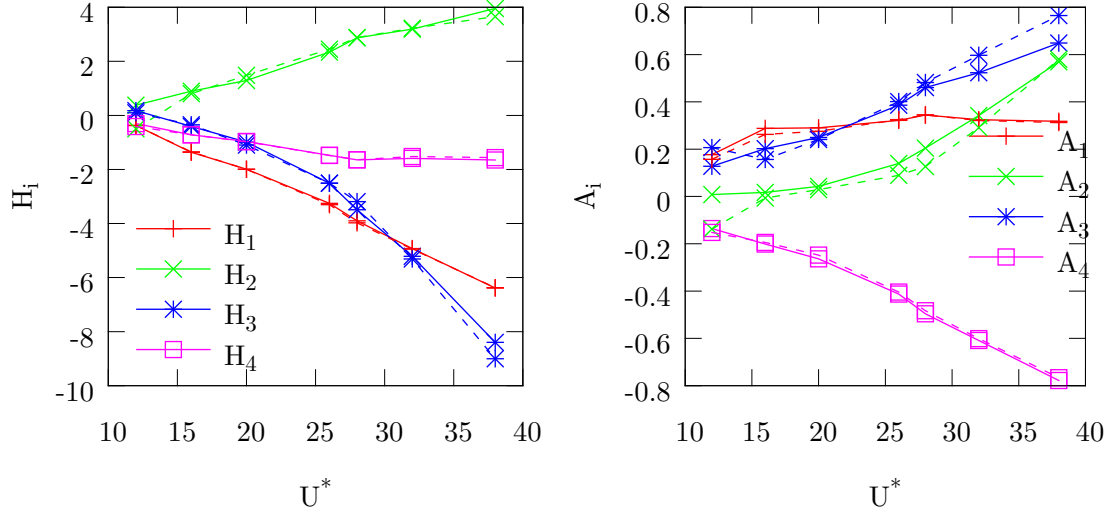


Figure 4.3.: Aerodynamic derivatives of the U-profile of chapter 3, figure 3.1 for several reduced velocities for two forced vibration amplitudes: —: $\hat{y}/H = 0.01$, $\hat{\varphi} = 1^\circ$, - - - -: $\hat{y}/H = 0.03$, $\hat{\varphi} = 3^\circ$.

4.2. Determining stability using the aerodynamic derivatives

To determine aeroelastic stability of the rigid body the modelled aerodynamic forces are plugged into the equations of motion. We introduce a state vector z , the mass matrix M and gather the aerodynamic derivatives in matrices:

$$z = \begin{pmatrix} y \\ \varphi \end{pmatrix}, \quad (4.10)$$

$$M = \begin{pmatrix} m & 0 \\ 0 & I_T \end{pmatrix}, \quad (4.11)$$

$$\begin{pmatrix} L \\ M \end{pmatrix} = \frac{1}{2} \rho u_\infty^2 (2B) \left(\underbrace{\begin{pmatrix} K^2 H_4^*/B & K^2 H_3^* \\ K^2 A_4^* & B K^2 A_3^* \end{pmatrix}}_{A_{34}(K)} z + \frac{B}{u_\infty} \underbrace{\begin{pmatrix} K H_1^*/B & K H_2^* \\ K A_1^* & B K A_2^* \end{pmatrix}}_{A_{12}(K)} \dot{z} \right) \quad (4.12)$$

The state vector consists of the two degrees of freedom (translation y , rotation φ). The mass matrix contains the mass m and inertial moment I_T of the body.

The equations of motion for a rigid body with two degrees of freedom, supported by linear springs take on the following form (we assume equal eigenfrequencies ω_0 for both degrees of freedom):

$$\frac{B^2}{u_\infty^2} (M\ddot{z} + \omega_0^2 Mz) = \rho B^3 \left(A_{34}(K)z + \frac{B}{u_\infty} A_{12}(K)\dot{z} \right). \quad (4.13)$$

The difficulties stem from the dependence of the aerodynamic derivatives on the reduced frequency K . Two established methods to alleviate these difficulties, the so-called p- and p-k-method (see [40]) are employed. The methods are reproduced here, as the description in [40] is written in a more general way.

Both methods assume harmonic motion of the body,

$$z = \bar{z} \exp(u_\infty p / B \cdot t), \quad (4.14)$$

where the dimensionless parameter p incorporates the dimensionless frequency K and the growth rate γ (i is the imaginary unit):

$$p = \gamma K + iK. \quad (4.15)$$

Plugging this ansatz into equation (4.13) yields

$$\left[p^2 \mathbf{M} + K_0^2 \mathbf{M} - \rho B^3 [\mathbf{A}_{34}(K) + iK \mathbf{A}_{12}(K)] \right] \bar{z} = 0. \quad (4.16)$$

To allow for non-trivial values of \bar{z} (the mode shape), the term in the brackets must vanish. The dimensionless parameter K_0 , defined as

$$K_0 = \omega_0 B / u_\infty \quad (4.17)$$

is the eigenfrequency, made dimensionless in the same way as the dimensionless flutter frequency, K (equation (4.6)). It relates to our definition of the reduced velocity U^* (equation (5.2)) as

$$K_0 = 1/U^* \cdot 2\pi B/H. \quad (4.18)$$

4.2.1. The k-method

The k-method is a straightforward approach. Harmonic motion with constant amplitude is prescribed by setting $\gamma = 0$ in equation (4.15). Plugging $p = iK$ into equation (4.16) leads to an eigenvalue problem for K_0^2 :

$$\left[\rho B^3 [\mathbf{A}_{34}(K) + iK \mathbf{A}_{12}(K)] + K^2 \mathbf{M} \right] \bar{z} = K_0^2 \mathbf{M} \bar{z}. \quad (4.19)$$

Generally, these eigenvalues are complex and can be interpreted as $(\Re K_0)(1 + ig)$, where g is a fictitious damping required to sustain harmonic motion with constant amplitude.

- If $g < 0$ the vibration mode is damped.

Inspection shows that the fictitious damping is proportional to the amplitude of the motion, but independent on its frequency. The damping force is

$$D_k = -igm\omega_0^2 \bar{z} \exp(i\omega t). \quad (4.20)$$

Note, that the often used velocity proportional damping force is proportional to the frequency and amplitude of the motion,

$$D = -ic\omega \exp(i\omega t). \quad (4.21)$$

4.2.2. The p-k method

The p-k-method does not prescribe a fictitious damping. The parameter p (equation (4.15)) may be complex. However, the influence of a growing or decaying amplitude on the aerodynamic forces is neglected by only considering the imaginary part of p : $\Im p$ in the matrices A_{12} and A_{34} (equation (4.12)).

Values for p that admit a non-trivial solution to equation (4.16) are obtained as the solution to a (generalized) eigenvalue problem for p^2 derived from this equation:

$$\left[\rho B^3 [A_{34}(\Im p) + i(\Im p)A_{12}(\Im p)] - K_0^2 \mathbf{M} \right] \bar{z} = p^2 \mathbf{M} \bar{z}. \quad (4.22)$$

Because the terms A_{12} and A_{34} depend on $K = \Im p$ an iterative approach is required. For any given K_0 an initial guess for $\Im p$ is required, for example K_0 . Computing p using these values yields the next guess for K , from which the next candidates for p can be obtained. This approach eventually converges towards some value of p , which is complex in general. Thus a combination of a real K_0 and complex K is obtained for which the bracket in equation (4.16) vanishes. The real part of p : $\Re p = \gamma K$, contains the information about growth or decay of the vibration.

- A negative real part of p : $\Re p < 0$ indicates that the vibration mode is damped.

Thus, the p-k method is also an approximation since the aerodynamic influence matrices A_{12} and A_{34} are evaluated at a constant amplitude of the motion. The influence of decaying or increasing amplitude on the aerodynamic forces is not taken into account.

4.2.3. Results

It is known, that the k- and p-k-methods can yield different results, [40]. The difference in these results has to be attributed to the different damping terms implied by both methods. Only for the case of neutral stability, $\gamma = g = 0$ either method yields the same frequency.

Figures 4.4 and 4.5 show the damping g or γ and the related frequency of the vibration, respectively. Both methods predict that a mode becomes unstable at a large reduced velocity. The predicted value of this reduced velocity appears to depend greatly on the values of the aerodynamic derivatives. For the smaller forcing amplitude $U_{c,2}^* = 38$, while $U_{c,2}^* = 28$. At intermediate reduced velocities, a weakly unstable mode is predicted. Its growth rates appear to decrease for increasing forcing amplitude.

The role of the H_4^* and A_4^* derivatives is disputed among the scientific community[81], since the aerodynamic force should not depend on the absolute value of the vertical displacement. However, the second time derivative of the displacement under harmonic

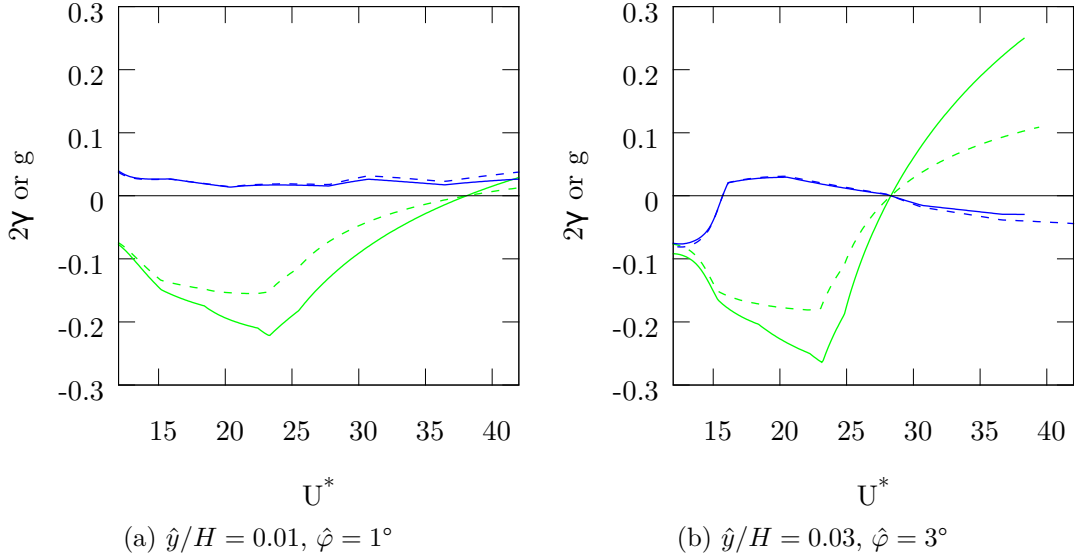


Figure 4.4.: The fictitious damping g (k-method) or damping ratio γ (p-k-method) for several reduced velocities $U^* = u_\infty/(Hf_0)$ and two forced motion amplitudes $\hat{y}/H, \varphi$. - - -: Mode 1, - - -: Mode 2, —: p-k-Method, - - -: k-Method.

motion yields a term proportional to $(2\pi f)^2$. This term also appears in the scaling of the aerodynamic derivatives H_4^* and A_4^* . Thus, these derivatives could be interpreted as a contribution to the aerodynamic forces by the accelerations \ddot{y} and $\ddot{\varphi}$ [81]. Nonetheless, many studies omit these derivatives. Here, this approach leads to different results (figures 4.6 and 4.7). For the aerodynamic derivatives obtained at small forcing amplitudes ($\hat{y}/H = 0.01, \hat{\varphi} = 1^\circ$) one mode is unstable for all reduced velocities. Another mode is stable for all reduced velocities. For larger forcing amplitudes ($\hat{y}/H = 0.03, \hat{\varphi} = 3^\circ$) one mode is always stable. The other mode becomes unstable at $U^* = 14.2$. However, this is due to the flow pattern influence at these low reduced velocities. In both cases the growth rate of the unstable mode shows a more steep increase at reduced velocities $U^* > 25$. The following chapter 5 will show that vibrations indeed occur in this reduced velocity regime.

The fictitious damping in the k-method is seen as severe restriction, [40]. Furthermore, the unstable mode at $U^* = 32$ ($\hat{y}/H = 0.01, \hat{\varphi} = 1^\circ$) was confirmed by numeric integration of the linear equations of motion together with the contribution of the aerodynamic derivatives. A detailed comparison of the stability predictions of the aerodynamic derivatives and the fully coupled simulation results is given in chapter 5.

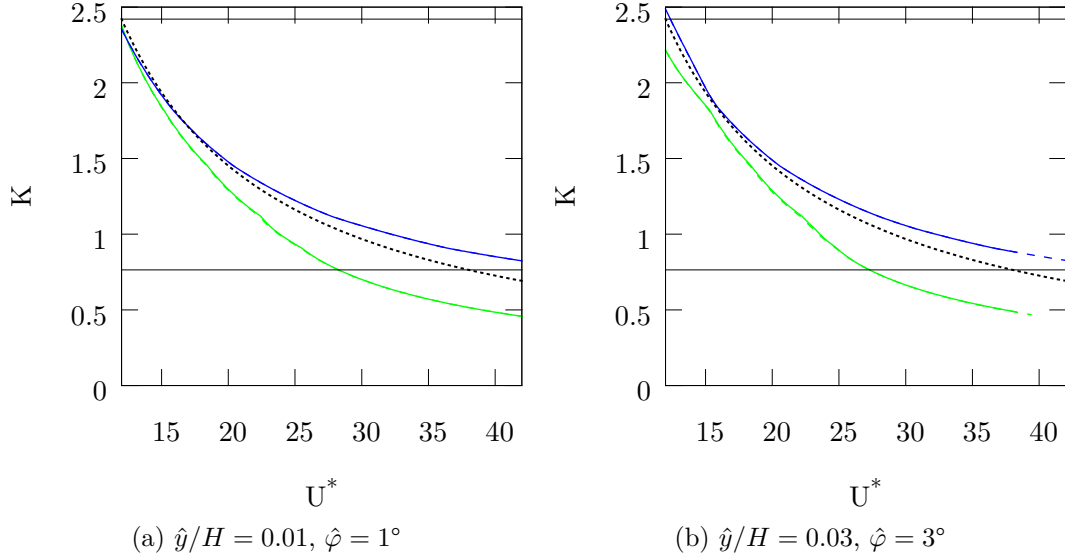


Figure 4.5.: Reduced frequencies K associated with the constant amplitude harmonic motion (k-Method) or damped harmonic motion (p-k-Method) of the profile at several reduced velocities for two forced motion amplitudes $\hat{y}/H, \varphi$. The aerodynamic derivatives were interpolated in the regions between the two straight lines. Outside this range linear extrapolation was used. The dotted line represents the curve for $f_0 = f_{\text{flutter}}$. ---: Mode 1, ---: Mode 2, —: p-k-Method, - - -: k-Method.

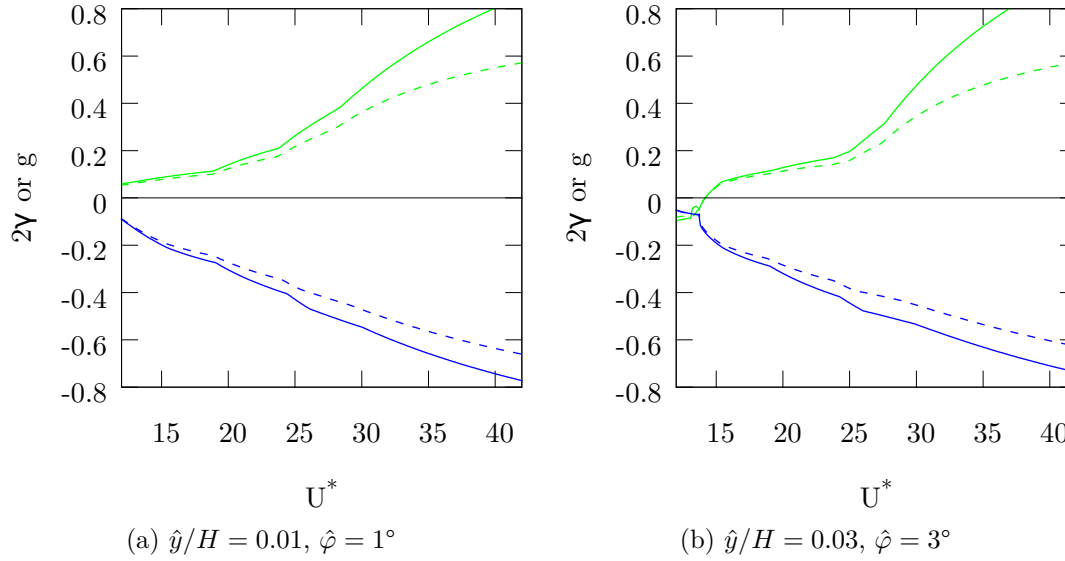


Figure 4.6.: The fictitious damping g (k-method) or damping ratio γ (p-k-method) for several reduced velocities $U^* = u_\infty/(Hf_0)$ and two forced motion amplitudes $\hat{y}/H, \varphi$ when the aerodynamic derivatives A_4^* and H_4^* are omitted. ---: Mode 1, ---: Mode 2, —: p-k-Method, - - -: k-Method.

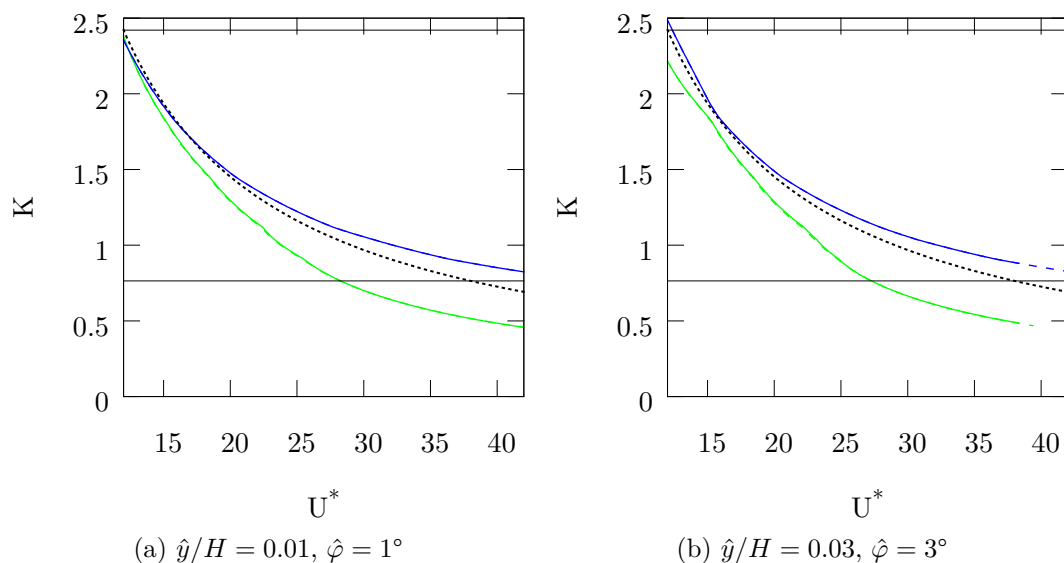


Figure 4.7.: Reduced frequencies K associated with the constant amplitude harmonic motion (k-Method) or damped harmonic motion (p-k-Method) of the profile at several reduced velocities for two forced motion amplitudes $\hat{y}/H, \varphi$ when the aerodynamic derivatives A_4^* and H_4^* are omitted. The aerodynamic derivatives were interpolated in the regions between the two straight lines. Outside this range linear extrapolation was used. The dotted line represents the curve for $f_0 = f_{\text{flutter}}$. - - -: Mode 1, - - -: Mode 2, —: p-k-Method, —: k-Method.

5. 2D Simulation of flow induced vibrations

Several excitation mechanisms for flow-induced vibrations of bluff bodies exist. These excitation mechanisms act at different (dimensionless) reduced flow velocities. Typically, **VIV** be observed at low reduced velocities. Self-excited vibrations are more often observed at large reduced velocities.

The reduced flow velocity ranges for **VIV** be estimated by inspection of the vortex shedding frequencies observed in section 3. The findings in section 4 gave an indication of the critical velocity for self-excited vibrations.

The first part of this chapter is dedicated to the simulation of free vibrations with the **CFD** Software package *ANSYS Fluent*. The second part of this chapter discusses free vibration wind tunnel experiments, designed to verify the simulation results.

5.1. Simulations

The flow around the U-profile was simulated using *ANSYS Fluent* and the same numeric models and program settings as worked out in in chapter 2 and applied in chapter 3.

The U-profile is free to move in vertical direction y and to rotate about its long axis (angle φ). Again the aspect ratio $B/H = 4.62$ and $Re = u_\infty B/\nu = 2.45 \cdot 10^5$ in every simulation result (see figure 5.1). Details regarding the computation mesh and simulation setup are discussed in section 2.1. Using this grid, both U-flow and R-flow patterns could be realised at zero inclination. The respective Strouhal numbers are $St^{(U)} = 0.072$ and $St^{(R)} = 0.135$.

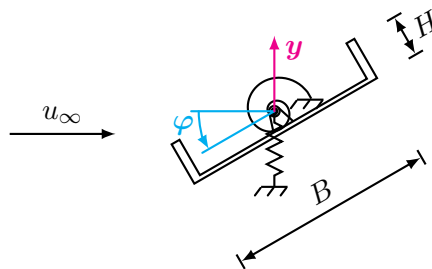


Figure 5.1.: Displaced U-profile

Unless mentioned otherwise the eigenfrequencies of heave and pitch mode are equal,

$$f_{0,y} = f_{0,\varphi} = f_0. \quad (5.1)$$

The far-field flow velocity u_∞ is scaled to yield the reduced velocity

$$U^* = u_\infty / (H f_0), \quad (5.2)$$

where f_0 is the structural eigenfrequency. To reduce the dimension of the parameter space it was chosen to perform the simulations without mechanical damping. The reduced velocity was changed by varying the stiffness in the equations of motion for the rigid body.

5.1.1. SDoF heave vibrations

We first consider single-degree-of-freedom (SDoF) heave vibrations. Results from sections 3.1.4 and 4 indicate that the U-profile should not vibrate at large reduced velocities. Firstly, by Den Hartog's criterion for translational galloping [81]: The slope of the lift coefficient at $\alpha = 0$ in figure 3.16a is negative. Secondly, the direct aerodynamic derivative H_1 is negative for every considered reduced velocity (see figure 4.3), also indicating stability with respect to self-excited vibrations. Such vibrations are observed under neither U-flow nor R-flow pattern (figures 5.2a and 5.2b). Vibration amplitudes at reduced velocities $U^* \geq 28$ are minimal. This leaves the possibility of VIV open. Such vibrations were observed under either flow pattern.

Under the U-flow pattern, VIV observed $U^* = 14$, the U-flow resonance case (see figure 5.2a). The maximal amplitude of $\hat{y}/H = 0.25$ occurred at $U^* = 14$ and vibration amplitudes for $U^* \leq 14$ are smaller. At $U^* = 14$ the structural eigenfrequency $f_{0,y}$ is (almost) equal to the formation frequency of cavity vortices $f_{vs}^{(U)}$ (figure A.15). Both heave and lift frequency spectra have a peak at $f_{0,y}/f_{vs}^{(U)} = 1$ or equivalently $U^* = 14$. However, the Fourier coefficient of the lift coefficient at this frequency is not the global maximum of the spectrum! The maximal Fourier coefficient in the spectrum is at the double cavity vortex formation frequency which is approximately equal to the R-flow vortex frequency, $2f_{vs}^{(U)} \approx f_{vs}^{(R)}$. The flow field still resembles the U-flow pattern, but the lift force is more dominantly influenced by the secondary vortices (see figure 3.12a). The motion of the profile due to the (cavity) vortex shedding reduced the aerodynamic forces induced by these vortices. The fluctuation of the lift force decreases and the vibration amplitude is bounded even without mechanical damping. After some time the profile performs harmonic vibrations with almost constant amplitude (figure A.4).

At reduced velocities $U^* = 12$ and $U^* = 16$ the structural eigenfrequency $f_{0,y}$ and the vortex shedding frequency for a stationary profile $f_{vs}^{(U)}$ are not equal any more. But the U-flow pattern shows some ability to synchronise to the profile motion. At these reduced velocities the largest Fourier coefficient of the vertical displacement \hat{y}^* corresponds neither to the structural eigenfrequency, nor to the vortex shedding frequency at stationary conditions. It lies between these two frequencies, marked by $U^* = 14$ or $U^* = 16$ and $f/f_{vs}^{(U)} = 1$ in figures A.15 and A.16. The synchronisation does not lead to a state of resonance again and the vibration amplitudes observed in these two cases are smaller than for the U-flow resonance case $U^* = 14$. At $U^* = 16$ a slightly modulated harmonic vibration can be observed after initial transients decayed (figure A.5). At $U^* = 12$ there is some interaction of the profile motion with the secondary vortices. The Fourier

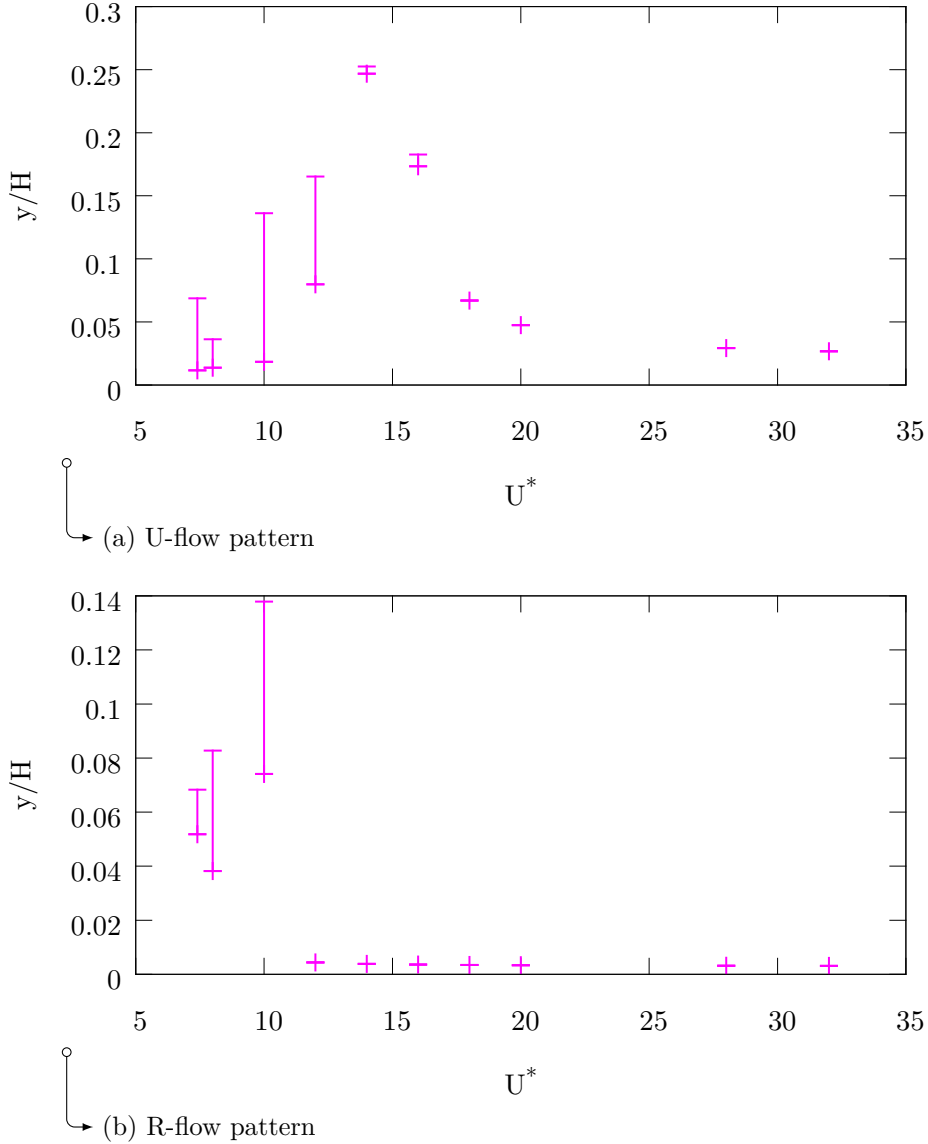


Figure 5.2.: SDoF heave Simulation ($Re = 2.45 \cdot 10^5$): Maximal and minimal average peak amplitudes for several reduced velocities.

coefficients of the aerodynamic lift assume large values at the U-flow vortex shedding frequency $f_{vs}^{(U)}$ and at $2f_{vs}^{(U)}$. The time-series of the heave amplitude is characterised by fast upswings and slow decay (figure A.3).

At the reduced velocity $U^* = 10$ transition to the R-flow pattern occurs. This can be seen by the drastic change in the heave amplitudes in figure A.2 for $\tilde{t} \leq 40$. The R-flow pattern shows a different kind of interaction between the profile motion and the vortex shedding frequency, leading to larger amplitudes at $U^* = 10$ (figure A.2), as will be discussed below.

While the U-flow persists at $U^* = 8$, transition occurs again at the lowest studied reduced velocity, $U^* = 7.4$ (figure A.1), corresponding to the R-flow resonance case. The flow pattern changes to a hybrid of U-flow and R-flow pattern. A stationary counterclockwise rotating vortex rests in the windward half of the cavity, but the shear-layer rolls up to form a cavity vortex on top of it (figure 5.3a). The cavity vortex travels towards the leeward flange and coalesces with the vortex in the leeward half of the cavity (figure 5.3b). Then the large cavity vortex splits in two smaller vortices. One vortex is shed from the profile and is swept into the wake. The other vortex remains in the leeward half of the cavity and will later coalesce with the next cavity vortex (figure 5.3c). This is only possible due to the motion of the profile allowing the formation of the large vortex above the cavity.

The maximal heave amplitude $\hat{y}/H = 0.14$ under the R-flow pattern occurs at $U^* = 10$ and not at the presumed R-flow resonance case $U^* = 1/\text{St}^{(R)} = 7.4$ (figure 5.2a). Instead vibration amplitudes increase from $\hat{y}/H \approx 0.065$ at $U^* = 7.4$ to $\hat{y}/H = 0.082$ at $U^* = 8$ to the value reported above at $U^* = 10$. At $U^* = 12$ and above the heave amplitudes assume minimal values. Inspection of the spectra (figures A.11 to A.13) shows that there is a particular influence of the profile motion on the vortex shedding frequency. At $U^* = 7.4$, the R-flow resonance case the reduced velocity is (almost) equal to the inverse of the Strouhal number computed with the vortex shedding frequency under stationary conditions, $U^* = 1/\text{St}^{(R)}$. Yet, the vortex shedding frequency decreased to a value of $f/f_{\text{vs}}^{(R)} \approx 0.95$! The state of resonance is not maintained due to the profile motion. It is plausible that the vortex shedding frequency should decrease: The Strouhal number does not scale with the width of the body, but with the width of its wake, [81] and [84] therein. The width of the wake is increased due to the profile motion. This can be seen by plotting the averaged horizontal-velocity profile in the wake (figure 5.5). The horizontal flow velocity was sampled 150 times during an R-flow periods for a sampling length of three periods at a distance $11.3B$ behind the profile. The wake width under stationary conditions is smaller than at $U^* = 7.4$, indicating the change in the vortex shedding frequency. The trend continues: larger vibration amplitudes lead to lower vortex shedding frequencies. At reduced velocities $U^* = 8.0$ and $U^* = 10.0$ the structural eigenfrequency is ever closer to the vortex shedding frequency (figures A.12 and A.14), given by the maxima of the lift Fourier coefficients. At $U^* = 10$, the scaled structural eigenfrequency $f_{0,y}/f_{\text{vs}}^{(R)}$ assumes the value $f_{0,y}/f_{\text{vs}}^{(R)} = u_{\infty}/HU^*f_{\text{vs}}^{(R)} = 0.74$, while the ratio of actual vortex shedding frequency to the vortex shedding frequency under stationary conditions is $f/f_{\text{vs}}^{(R)} = 0.71$. For $7.4 < U^* < 10$ the eigenfrequency is larger than the vortex shedding frequency. At reduced velocities $U^* > 10$ the vortex shedding frequency cannot decrease any further. The vortex shedding frequency assumes a value which is closer to the stationary vortex shedding frequency and vibration amplitudes are very low. The eigenfrequency is lower than the vortex shedding frequency. Thus, the R-flow pattern differs from the U-flow pattern in its synchronisation abilities. The U-flow cavity vortices synchronised easily to the profile motion, leading to a broader interval where VIV occur (see also figure 5.4a). The R-flow vortex shedding frequency shifts due to the profile motion, delaying the state of resonance. This can also be seen

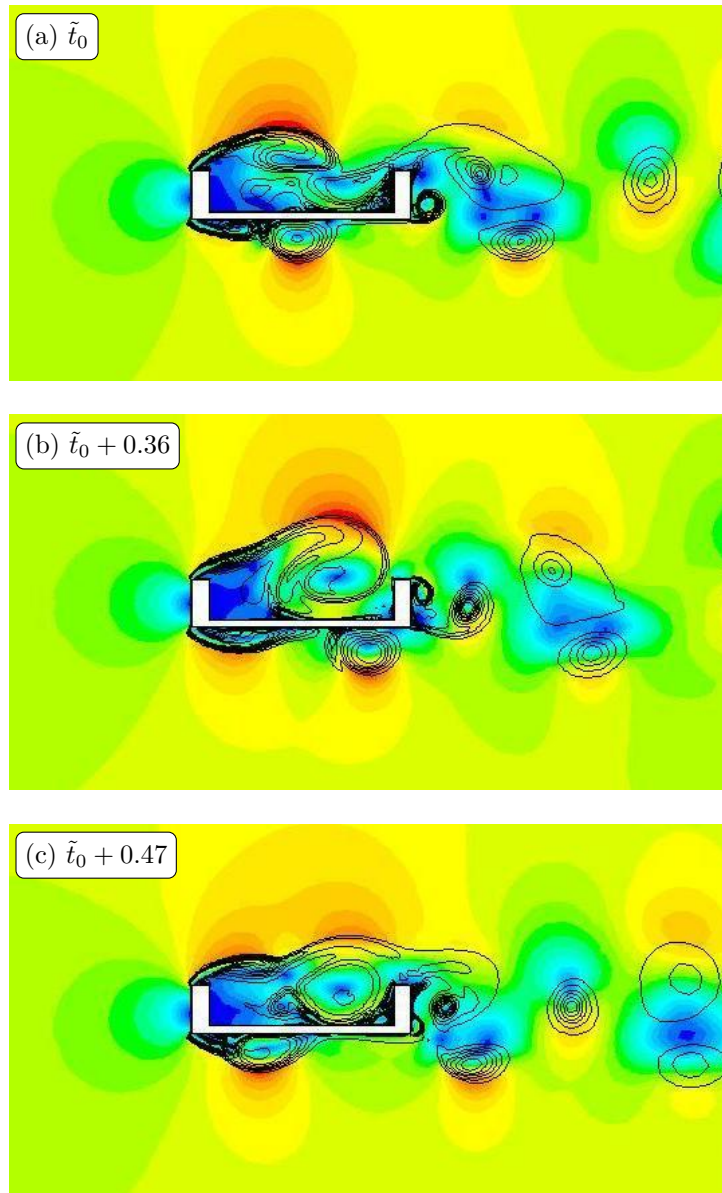


Figure 5.3.: Snapshots of the flow-field at $U^* = 7.4$ showing the “hybrid” U-R-flow pattern. $\tilde{t} = t \cdot \text{St}^{(R)} u_\infty / H$.

in figure 5.4b. A similar effect has been observed for the $B/H = 4$ rectangular prism [64] and the square prism [61]. Finally note, that the peculiar hybrid flow pattern also developed at $U^* = 7.4$ from R-flow initial conditions. With the findings of the previous chapter 3 in mind, namely that the flow patterns change intermittently, it is not yet clear which flow pattern will be selected in reality, if any, at low reduced velocities $U^* \lesssim 14$.

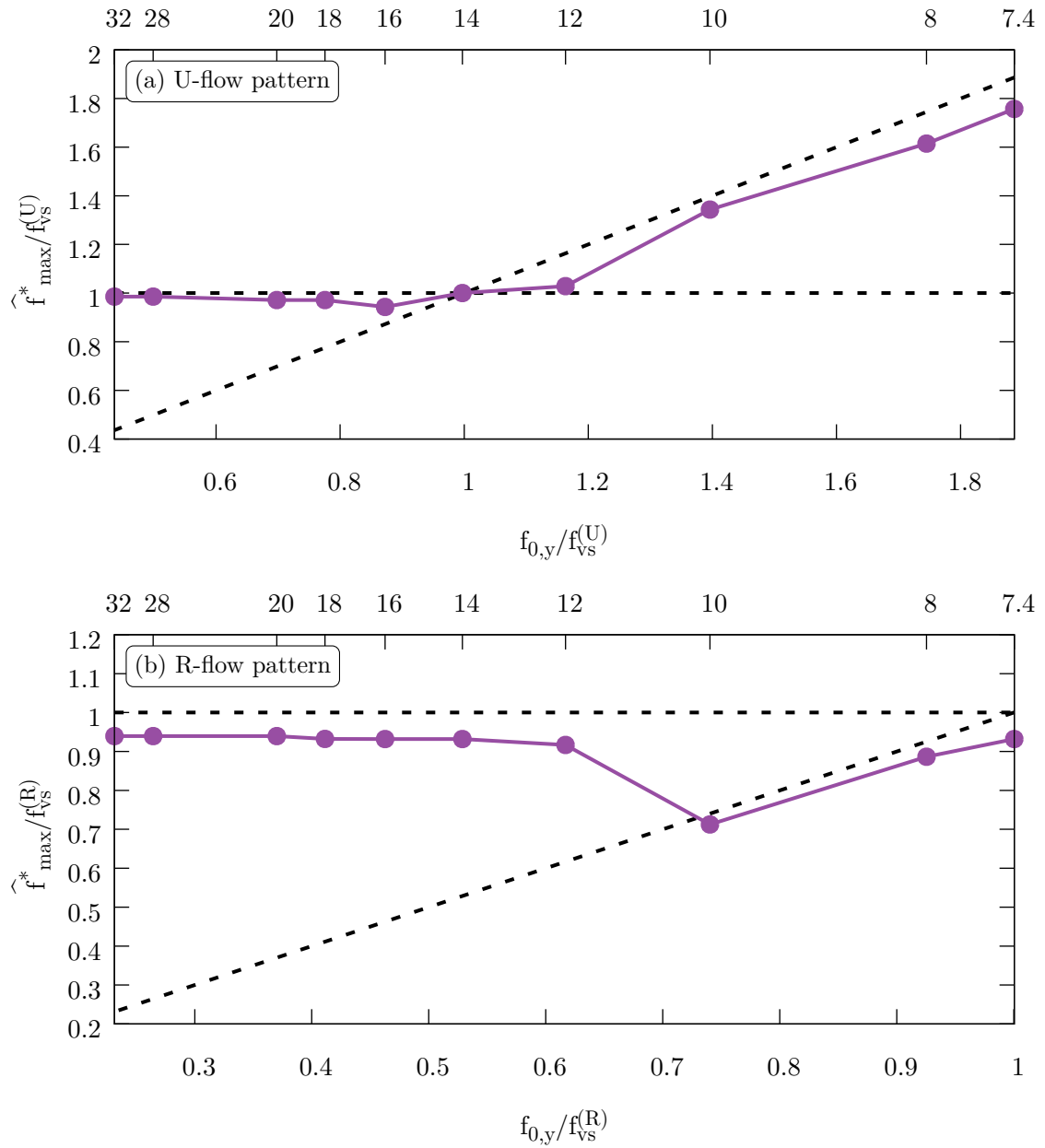


Figure 5.4.: Frequency corresponding to the maximal heave Fourier coefficient under [SDoF](#) heave vibrations.

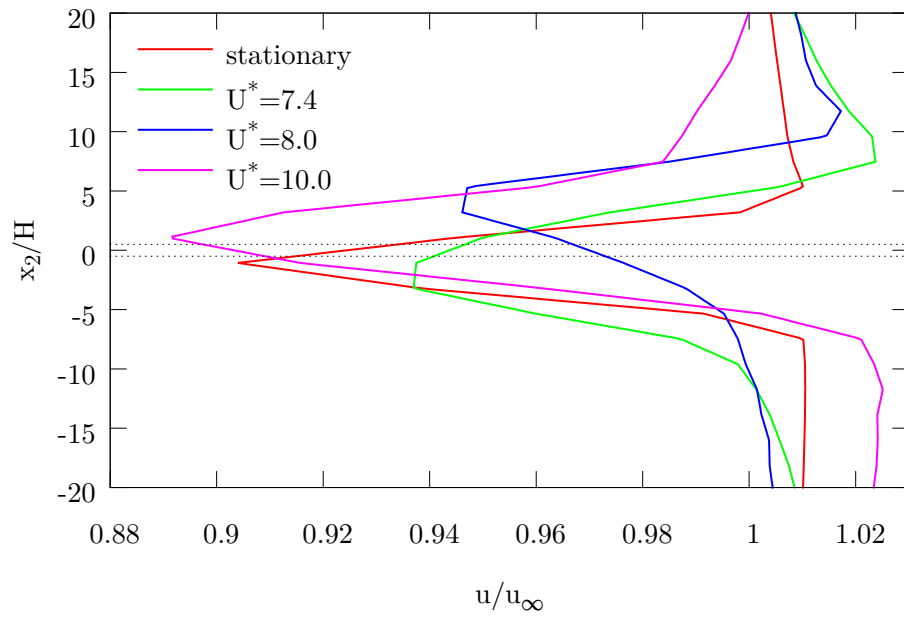


Figure 5.5.: Time-averaged flow velocity in horizontal direction at in the wake behind the U-profile. x_2 is the vertical coordinate. The dotted lines denote the vertical extension of the profile upstream at rest.

5.1.2. SDoF pitch vibrations

We continue with SDoF rotational or pitch vibrations and the behaviour at low reduced velocities. Under the U-flow pattern and at reduced velocities $U^* = 7.4$ and $U^* = 8.0$ excitation by secondary vortices (see figure 3.12a) occurs. The corresponding amplitudes are small $\hat{\varphi} < 3^\circ$ (figure 5.6a). The frequency spectrum of the torsional moment shows that the profile is excited by the secondary vortices and at roughly half the eigenfrequency by the cavity vortices (figure A.18). The shedding of the secondary vortices is only weakly influenced by the profile motion, as can be seen from the almost equal vibration frequencies for $U^* = 7.4$ and $U^* = 8.0$ (figures A.17 and A.18, that do not follow the eigenfrequency of the profile).

At reduced velocities $U^* = 10$ to $U^* = 16$ excitation by the cavity vortices occurs. The excitation in this reduced velocity regime occurs mainly at the vortex shedding frequency. The cavity vortex formation frequency under profile motion does not assume larger values than the stationary formation frequency, for example at $U^* = 12$ (see figure A.20). At $U^* = 12$ significant vibration amplitudes ($\hat{\varphi} \approx 4^\circ$, figure 5.6a) can be observed. At $U^* = 14$ even larger amplitudes occur: $\hat{\varphi} \approx 11^\circ$. Starting from stationary conditions the pitch vibrations reach these large amplitudes quickly, in about ten U-flow periods (figure A.6). Now, the cavity vortex formation frequency is influenced by the profile motion. Due to the large pitch angles the vortex formation slows down (see the frequency spectrum in figure A.20). The fluctuation of the moment coefficient under pitch motion at $U^* = 14$ is much greater than in the stationary case (figure 5.7a). At $U^* = 16$, vibration amplitudes and moment coefficient fluctuations increase once more. The vortex formation frequency is even lower than at $U^* = 14$, resulting in very large amplitudes. Note the difference to the SDoF heave case, where the cavity vortex formation frequency near $U^* = 14$ was always close to the eigenfrequency. The heaving motion allowed the cavity vortices to be swept faster or slower towards the leeward flange of the profile. In case of pitch motion the cavity vortices are only slowed down due to large pitch angles.

At $U^* \geq 18$ the cavity vortices can no longer adapt to the profile motion. The flow pattern changes to the R-flow pattern. This process is not reversible (in our 2D simulations) and thus the results at these reduced velocities are identical to the results of the R-flow simulations described below.

Under the R-flow pattern and the R-flow resonance case $U^* = 7.4$ vibration amplitudes are unexpectedly low $\hat{\varphi} = 0.4^\circ$ (figure 5.6b). Again, the profile motion influences the vortex shedding frequency. Contrasting the influence of a heaving motion, the vortex shedding frequency increases due to pitching motion. At $U^* = 8$ it can be seen that the vortex shedding frequency assumes a larger value than in the stationary case (figure A.19). The profile responds at this frequency, but vibration amplitudes remain low throughout $U^* = 12.0$. At this reduced velocity the vortex shedding frequency assumes the same value as in the stationary case (figure A.21). Again the profile responds to this excitation at the vortex shedding frequency and not at eigenfrequency, which is much lower than the vortex shedding frequency at this reduced velocity. The moment coefficient fluctuation is not larger than in the stationary case for $U^* < 12$ (figure 5.7b).

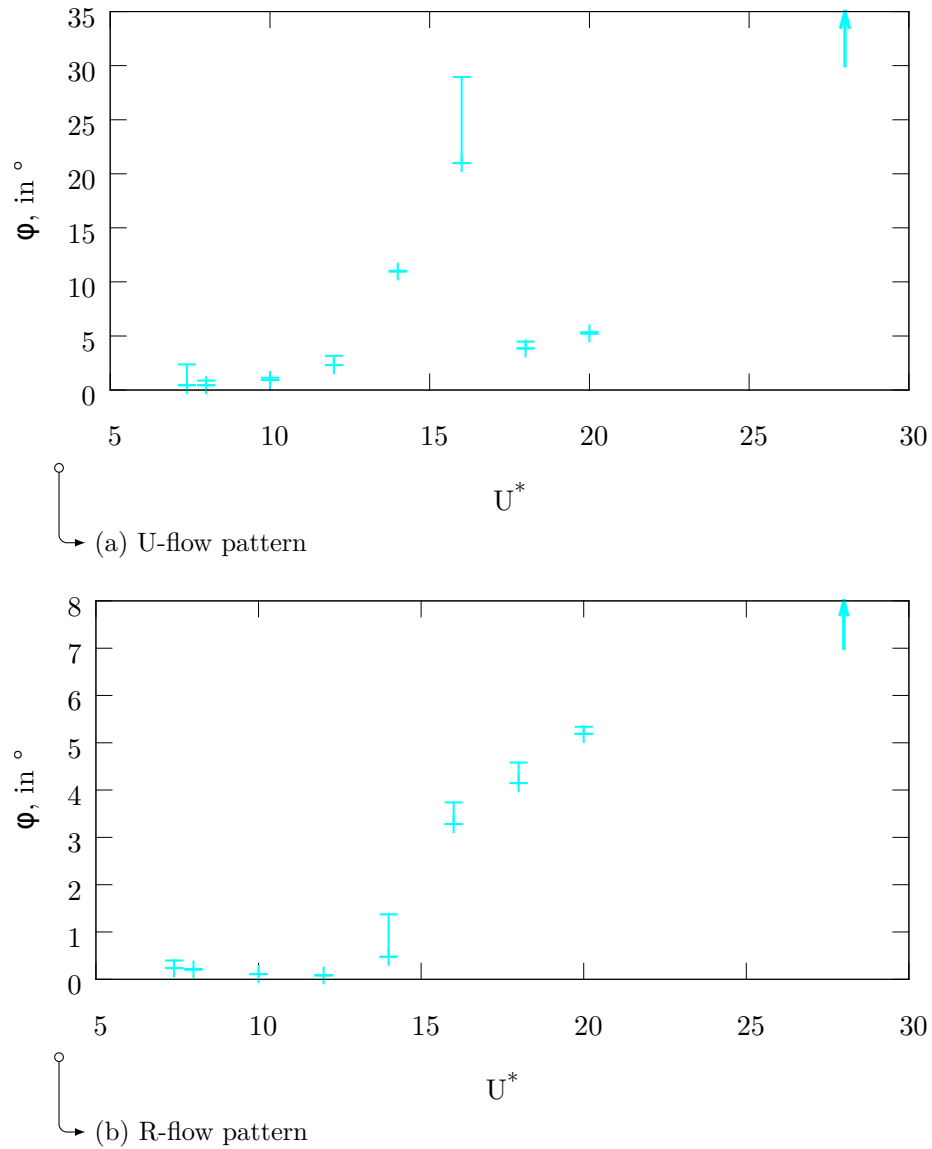


Figure 5.6.: SDoF pitch Simulation ($\text{Re} = 2.45 \cdot 10^5$): Maximal and minimal average peak amplitudes for several reduced velocities.

At $U^* = 14$ a different excitation mechanism comes into play. Although the moment coefficient fluctuations do not increase, the profile responds at eigenfrequency rather than at vortex shedding frequency. A new contribution to the moment coefficient can be seen in the frequency spectrum (figure A.22). It is mere coincidence that this contribution is at the half vortex shedding frequency. This contribution does not exist at lower reduced velocities (figure A.20). At larger reduced velocities it deviates from the half vortex shedding frequency (figure A.23). The excitation mechanism is clearly only possible under profile motion. Therefore it does not belong to the class of instability-induced

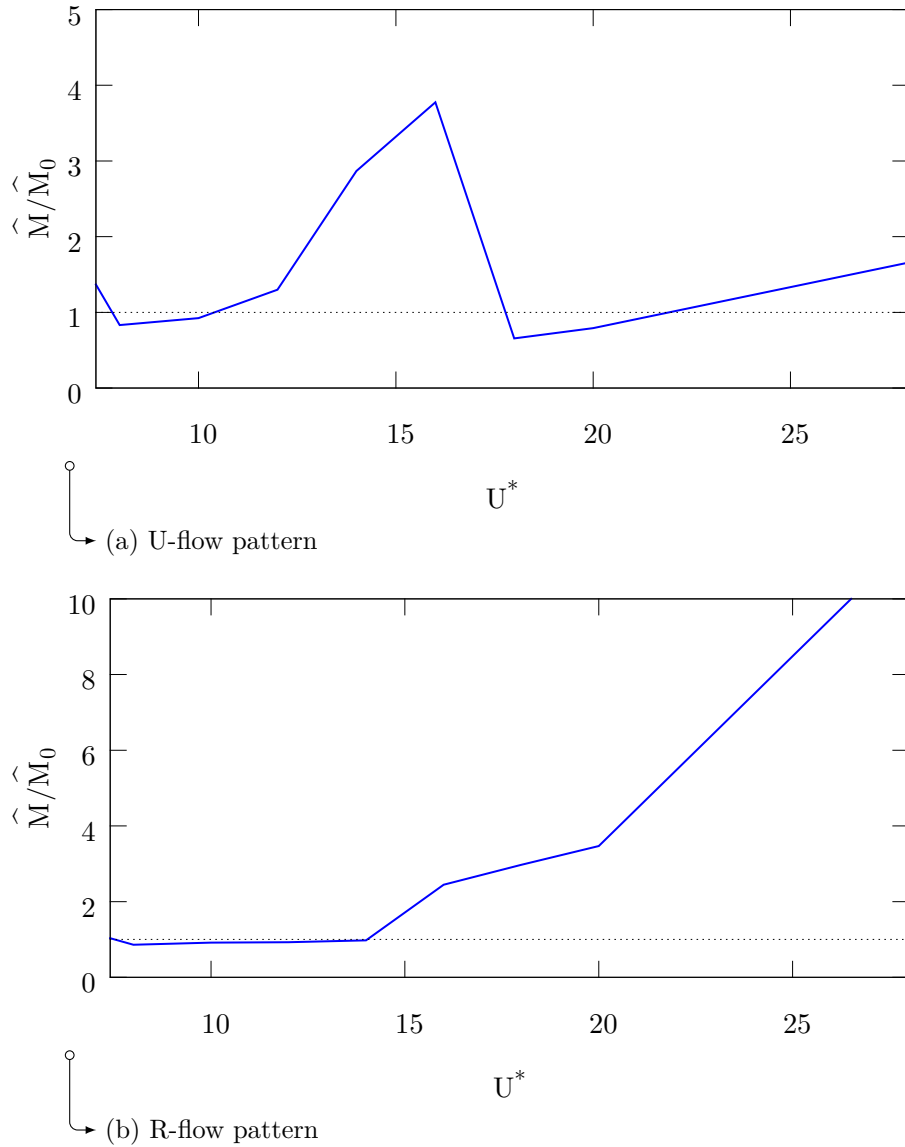


Figure 5.7.: Amplification of the torsional moment fluctuation at several reduced velocities.

excitations (IIE in [74], such as VIV) but to the class of motion induced excitations (MIE in [74]). A first understanding of this excitation mechanism is gained by the time-series of the torsional moment (figure 5.8). Compared to the stationary case, the torsional moment is now modulated with the frequency $1/2f_{vs}^{(R)}$, yet the simulation still shows a time-periodic flow-field. The modulation is such that two successive peaks have an increased amplitude. They are followed by two peaks with lesser amplitude. The profile responds with pitch vibrations with an amplitude of $\hat{\varphi} \approx 1^\circ$ (figure 5.9). The phase between pitching motion and the torsional moment is such that a large negative

peak of the moment precedes a negative peak of the pitch angle. Two snapshots at a large and small negative peak are shown in figure 5.10. In both cases a vortex detaches from the upper leeward corner of the profile. The more interesting region of the flow-field is the smooth side of the profile. At the large negative peak of the torsional moment a small vortex (red line in figure 5.10b) can be seen below the profile. This vortex is not present at the smaller negative peak of the torsional moment (figure 5.10a). This small vortex influences the surface pressures and is responsible for the magnitude of the negative moment peak. Consider the surface pressures in figure 5.11, where the surface pressures for the horizontal parts of the profile, the top part of the sidewalls and the base, and the bottom part of the base, are compared at the time-instances of large and small negative peak of the torsional moment. The surface pressures acting on the top parts is almost the same in both cases. The pressures acting on the bottom part of the profile are influenced by the presence of the small vortex. Thus the small vortex influences the torsional moment. Considering the phase between moment and pitch angle (figure 5.9) it can be seen that the vortex responsible for the large negative moment peak forms when the profile is rotating in clockwise direction. When the profile is rotating in counter-clockwise direction a negative peak with smaller magnitude is present. This vortex is therefore closely related to the motion of the profile and in accordance with [64] will be called *motion induced vortex* in the following.

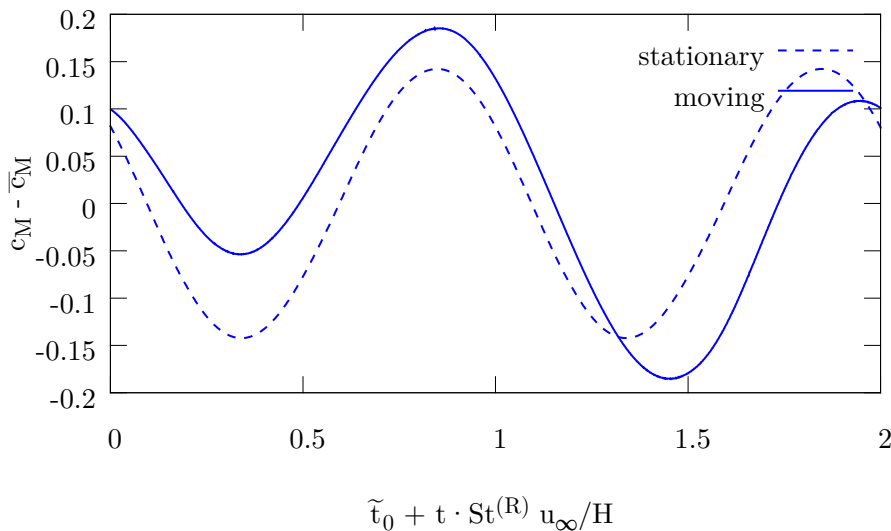


Figure 5.8.: Time-series of the mean-free moment coefficient $c_M - \bar{c}_M$ under the R-flow pattern, compared for the stationary case and $U^* = 14$ (R-flow pattern, SDoF pitch).

For $U^* > 14$ the moment fluctuations and vibration amplitudes due to the motion induced vortex increase. The upswing behaviour is also different to the upswing under VIV: Figure A.7 shows that the pitch amplitudes are initially influenced by the vortex shedding. Then, the amplitudes increase exponentially, but with a smaller time constant. The upswing is much slower than under U-flow VIV. The vibration amplitudes

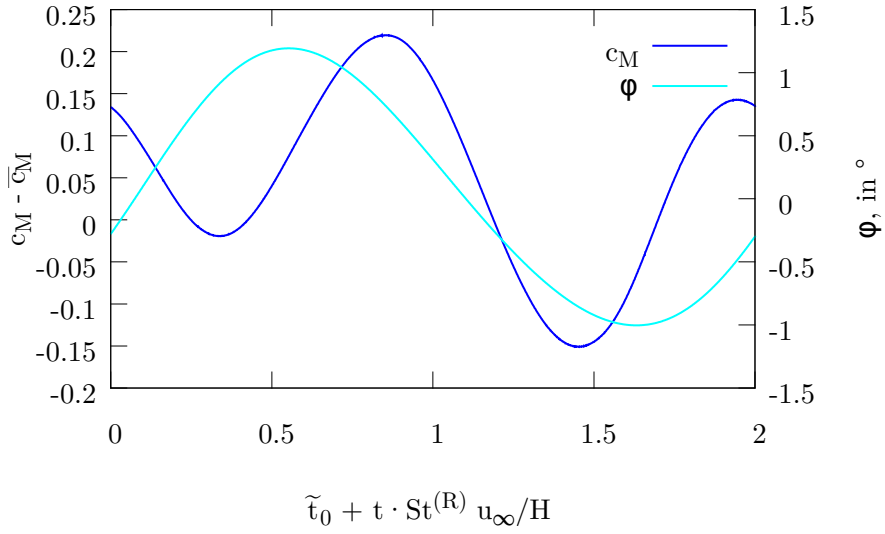


Figure 5.9.: Time-series of the mean-free moment coefficient $c_M - \bar{c}_M$ and pitch angle φ at $U^* = 14$ (R-flow pattern, [SDoF](#) pitch).

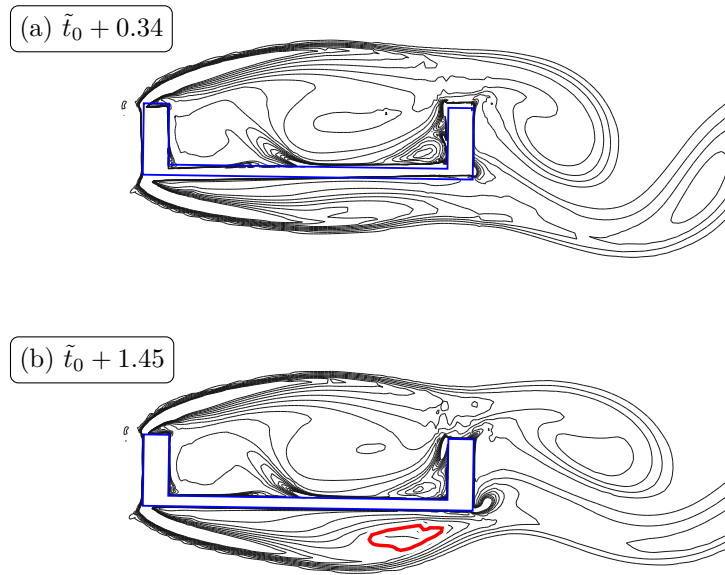


Figure 5.10.: Snapshots of the vorticity contour at $U^* = 14$ (R-flow pattern, [SDoF](#) pitch)

saturate at $\hat{\varphi} \approx 5^\circ$. At large reduced velocities $U^* \geq 28$ the yet unknown saturation mechanism is no longer at work and vibration amplitudes increase to such values that the simulation fails ($\hat{\varphi} > 60^\circ$). This is reflected to some extent in by the aerodynamic derivatives. The direct aerodynamic derivative A_2 is positive and increases in magni-

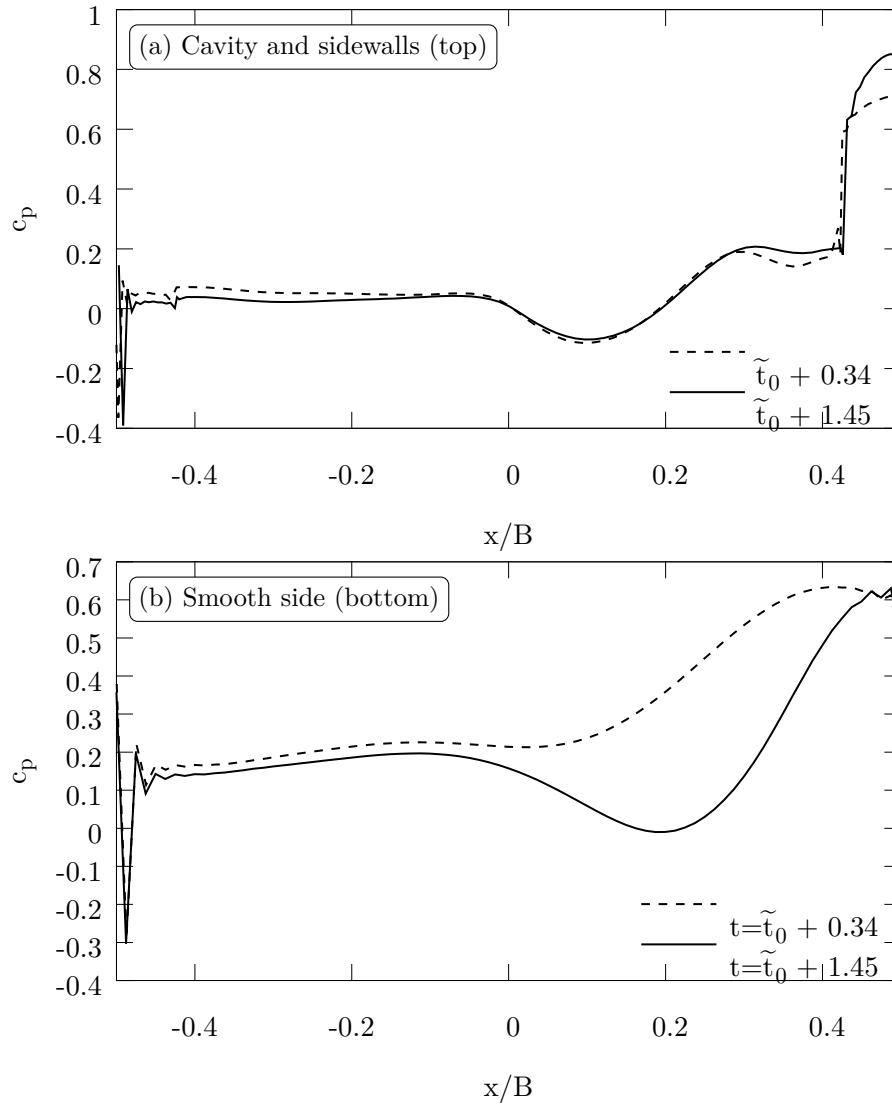


Figure 5.11.: Snapshots of the surface pressures acting on the horizontal sides of the U-beam.

tude with the reduced velocity. Additionally it can be observed that the magnitude of A_2 decreases when the amplitude of the forcing by which the aerodynamic derivatives were determined is increased. Although this could be interpreted as the action of some saturation mechanism, this thought should not be pursued because of the linear nature of the method of aerodynamic derivatives.

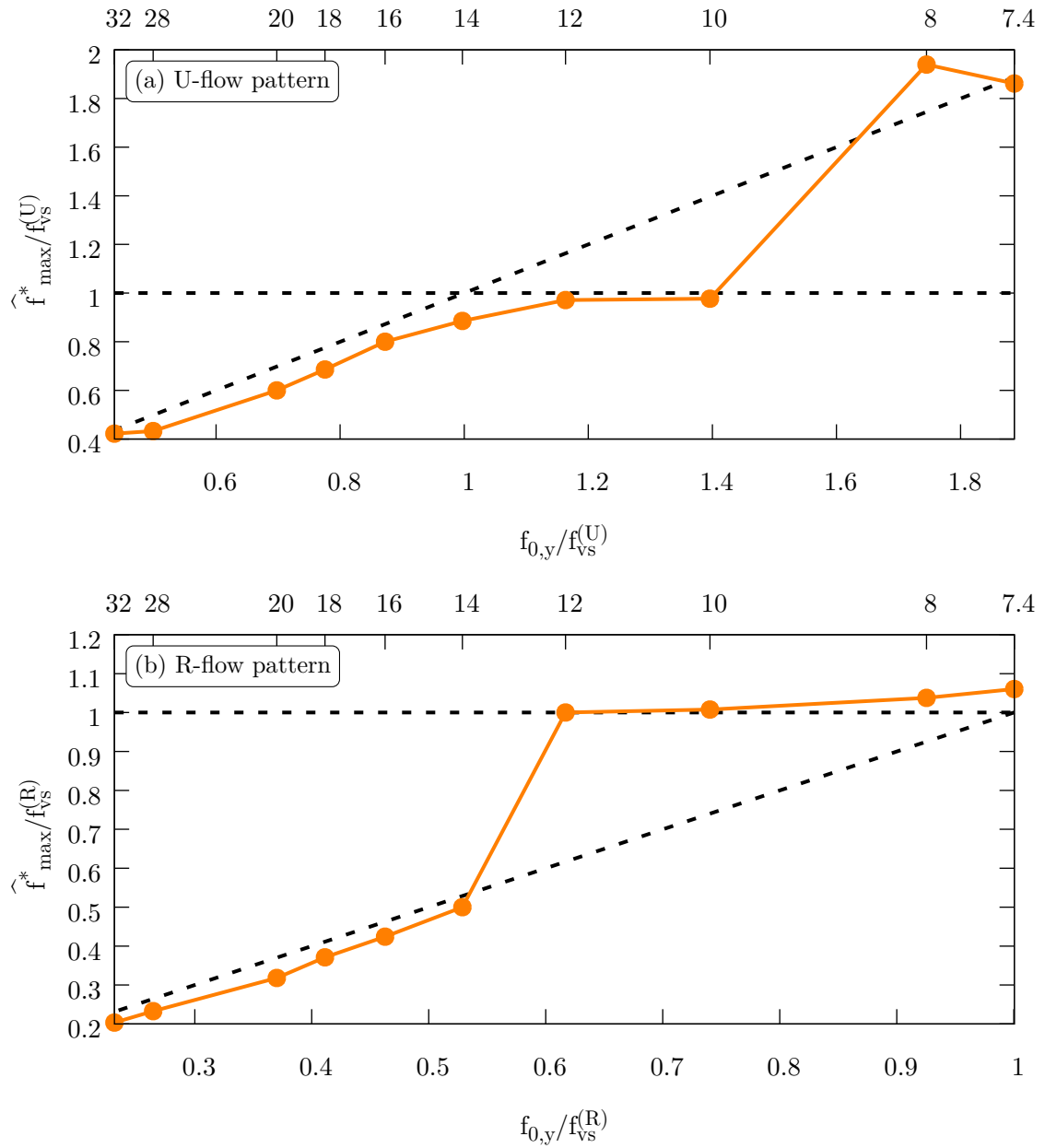


Figure 5.12.: Frequency corresponding to the maximal pitch Fourier coefficient under **SDoF** pitch vibrations.

5.1.3. 2DoF flutter vibrations

We now consider 2DoF flutter vibrations and will discuss whether 2DoF flutter vibrations appear as mere superposition of the SDoF cases or whether new behaviour arises. We begin with the observations under the U-flow pattern at low reduced velocities. At $U^* = 7.4$ and $U^* = 8.0$ excitation by secondary vortices (figure 3.12a) occurs as observed in the SDoF pitch case (figure A.18). A different behaviour can be seen at $10 < U^* = 14$: pitch-dominated vibrations due to the cavity vortices set in. The heave motion does not contribute much to the vibration (figure A.8). At $U^* = 14$, after the upswing phase, vibrations with an almost constant amplitude of $\hat{\varphi} = 10.7^\circ$ and $\hat{y}/H = 0.06$ are reached. Note, that a rotation of $\hat{\varphi} = 10.7^\circ$ displaces the windward corners of the profile by the distance $B/2 \cdot \sin \hat{\varphi} = 0.43H$ in the vertical direction.

Thus, the contribution of the heave motion is not essential. As in the SDoF pitch case, the profile does not respond at eigenfrequency, but at the cavity vortex formation frequency (figure 5.14a). Again, the motion of the profile causes a decrease of this frequency. At the reduced velocity $U^* = 16.0$ transition to the R-flow pattern occurs, at a lower reduced velocity than under SDoF pitch conditions. Flow pattern transition was observed for all reduced velocities $U^* \geq 16$ and the results are equivalent to the corresponding R-flow cases described below.

Under the R-flow pattern a different mode of vibration occurs. Starting from $U^* = 7.4$ vibrations set in at moderate amplitudes $\hat{y}/H = 0.07$ and $\hat{\varphi} = 2.5^\circ$ (see figure 5.13b). The amplitudes increase until $U^* = 14$ where $\hat{y}/H = 0.22$ and $\hat{\varphi} = 5.2^\circ$. In this regime ($7.4 < U^* < 16$) the profile vibrates at eigenfrequency (figure 5.14b). In contrast to the 2DoF U-flow case heave and pitch motion are of equal magnitude (figure A.9). Pitch vibrations with $\hat{\varphi} = 5.2^\circ$ displace the windward edge vertically by the distance $B/2 \cdot \sin \hat{\varphi} = 0.21H$. Recall, that heave and pitch motion decreased and increased the vortex shedding frequency, respectively (figures 5.4b, 5.12). The opposing influences of heave and pitch motion on the vortex shedding frequency combine to enable VIV with larger amplitudes.

The frequency spectra of the aerodynamic forces and the displacements at $U^* = 10$ (figure A.24) show that despite some “noise” in the lift spectrum the vortex shedding occurs at its eigenfrequency f_0 . At $U^* = 14$ (figure A.25) vortex shedding occurs at the original vortex shedding frequency again. The combined heave and lift motion extended the reduced velocity range where vortex induced vibrations occurred. Note that these vibrations are not due to the motion induced vortex observed in the SDoF pitch case. At the time-instance of minimal torsional moment no such vortex can be seen in the flow-field (figure 5.15). The combined heaving and pitching motion also diminishes the influence of the motion induced vortex at reduced velocities $14 \leq U^* \leq 28$. Only minimal vibration amplitudes can be observed in this reduced velocity interval (figure 5.13b). While pitch vibration amplitudes at $U^* = 28$ in the SDoF pitch case were already extremely large, they remain very small in the 2DoF case at the same reduced velocity.

Vibrations with very large amplitudes set in at $U^* = 32$ (figure A.10). Again the simulation run ended prematurely due to the extremely large grid displacement. Note, that after an initial transient phase almost exponential amplitude growth can be observed.

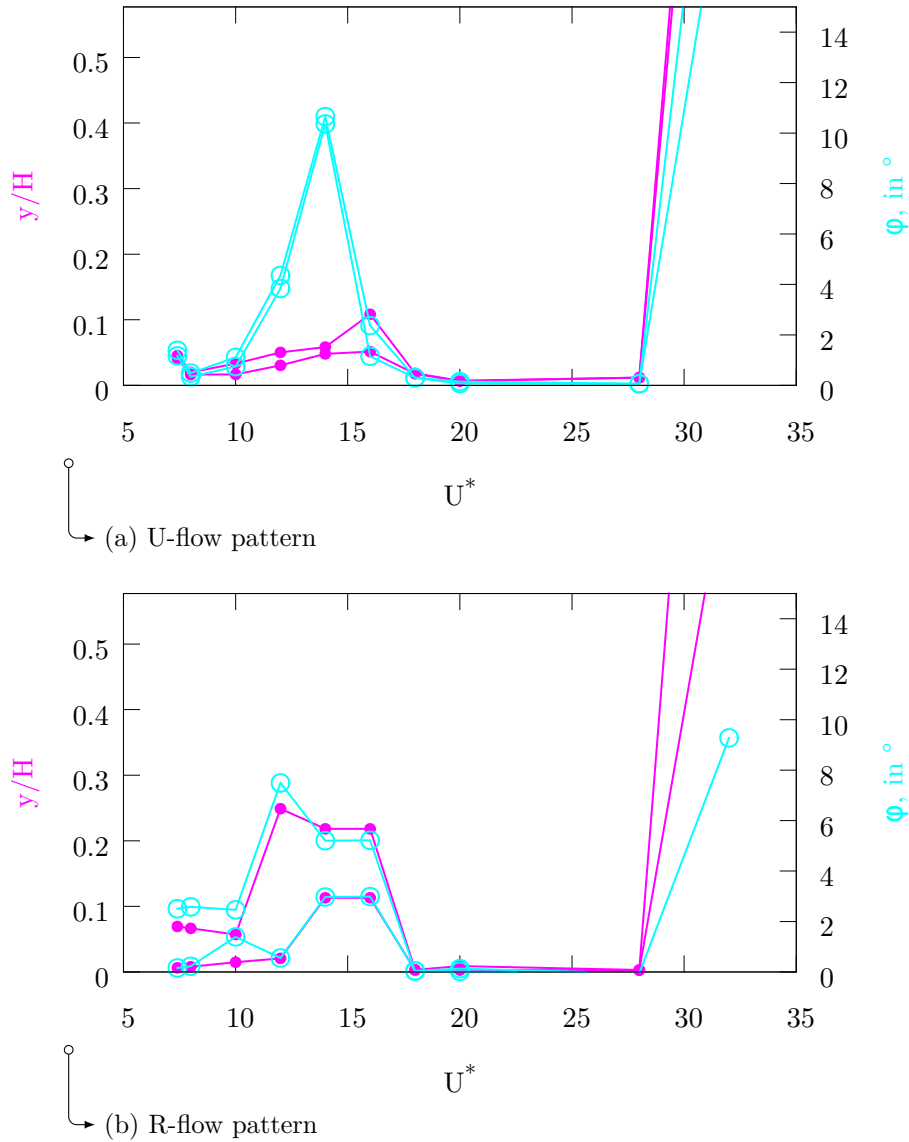


Figure 5.13.: 2DoF simulation ($\text{Re} = 2.45 \cdot 10^5$): Maximal and minimal average peak amplitudes for several reduced velocities.

The aerodynamic derivatives, obtained with forced vibration amplitudes of $\hat{y}/H = 0.03$, $\hat{\varphi} = 3^\circ$ predict an unstable mode at $U^* = 32$ (figure 4.4). This mode has the dimensionless frequency $K = \omega B/u_\infty = 0.61$, while the dimensionless frequency observed in the simulation is $K = 0.77$. Note that both values are not equal to the dimensionless eigenfrequency $K_0 = \frac{2\pi B}{HU^*} = 0.91$, but smaller. The phase $\psi/2\pi$ between heave and pitch is 0.69 in the simulations and 0.64 in the prediction by the aerodynamic derivatives. The growth rates of heave and pitch motion are not equal in the simulations. Neither growth rate coincides with the predicted value. The aerodynamic derivatives offer no easily un-

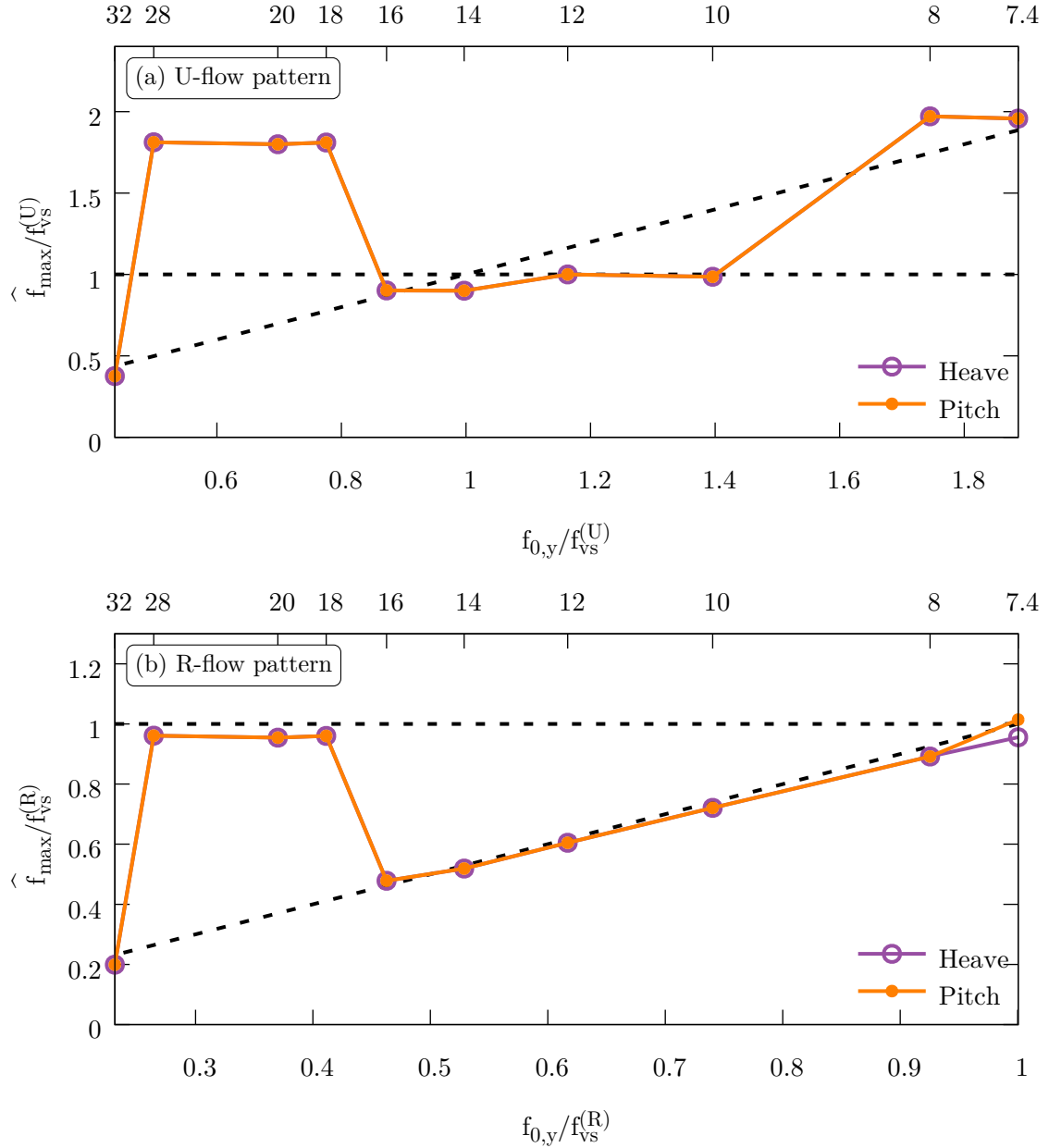


Figure 5.14.: Frequency corresponding to the maximal heave or pitch Fourier coefficient in case of 2DoF vibrations.

derstandable explanation for the small amplitudes for reduced velocities $U^* \lesssim 28$, and why extreme amplitudes already occur at $U^* = 28$ without a heave degree of freedom (i.e. in the SDoF pitch case). Yet the reason for the small observed vibration amplitudes is related to the heave motion that renders the motion induced vortex ineffective.

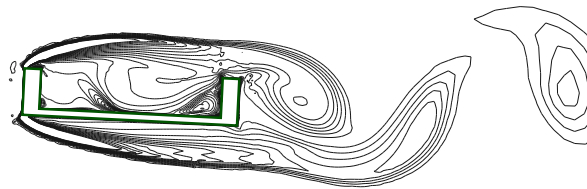


Figure 5.15.: Snapshot of the vorticity magnitude under the R-flow pattern at $U^* = 14$ at the time-instance of minimal torsional moment.

5.2. Rigid section model experiments

Experiments to verify the simulation results were performed following two different approaches. Firstly, a rigid section model with U-shaped cross section was tested with the 2DoF test-stand described in section 2.2.3). The relatively low flow velocities at $U^* = 7.4$ in conjunction with the sometimes large damping of the test stand rendered this approach suitable for large reduced velocities and testing self-excite vibrations. Secondly, a deformable belt was tested as described in section 2.2.4. VIV were studied with this experimental setup.

5.2.1. Verifying the critical velocity for self-excited vibrations

Here, we present the results of tests at three different test-stand eigenfrequencies aimed at verifying the critical velocity for flutter vibrations. Heave and pitch eigenfrequency were tuned to the same value, thus $f_{0,y} = f_{0,\varphi} = f_0$. At lower reduced velocities, $U^* \leq 15$, no vibrations could be observed (figure 5.16). Increasing the flow velocity did not lead to large vibrations until $U^* > 28$. Here, pronounced vibrations were observed at eigenfrequencies $f_0 = 2.0$ Hz and $f_0 = 4.5$ Hz. A large-amplitude limit cycle was reached. At the eigenfrequency $f_0 = 4.5$ Hz small vibrations were already recorded for $U^* \lesssim 28$. These vibrations were intermittent in character. It is not entirely clear whether they were the result of an interaction between model deformation (at approximately 20 Hz) and the approach to the critical velocity or a response to the turbulence in the flow. At the test-stand eigenfrequency $f_0 = 9.5$ Hz the reduced velocity $U^* = 28$ was not reached, but vibrations with small amplitude were also observed at $U^* \approx 25$.

Although the critical reduced velocity coincides with one obtained by simulations, there are some difficulties when comparing with predictions by the aerodynamic derivatives. It is not clear to which extent the mechanical properties of the test-stand should be included in the mass matrix \mathbf{M} in equation (4.16), and how the eigenmodes of the test-stand together with the model really look like. The phase $\psi/2\pi$ between heave and pitch is not equal for the displacements obtained with the test-stand eigenfrequencies $f_0 = 2.0$ Hz and $f_0 = 4.5$ Hz. It is also not equal to the phase predicted by the simulations (see page 92).

5.2.2. Verifying vibrations at low reduced velocities

To achieve reduced velocities $7 < U^* < 14$ at larger flow velocities, the eigenfrequency of the test-stand was increased substantially. Unfortunately, this also increased the damping properties (see table 2.2).

At low reduced velocities $U^* > 7$ heave vibrations could be observed (see figure 5.17). The heave dominated motion indicates VIV observed under the R-flow pattern. Yet vibration amplitudes decreased for $U^* > 7$, as opposed to the 2DoF case, where vibrations continued to $U^* = 10$. Vibrations with small amplitude were recorded for reduced velocities up to $U^* = 16$. At larger reduced velocities intermittent vibrations with increasing amplitude occurred. The data in figure 5.17 was low-pass filtered with a 5th order But-

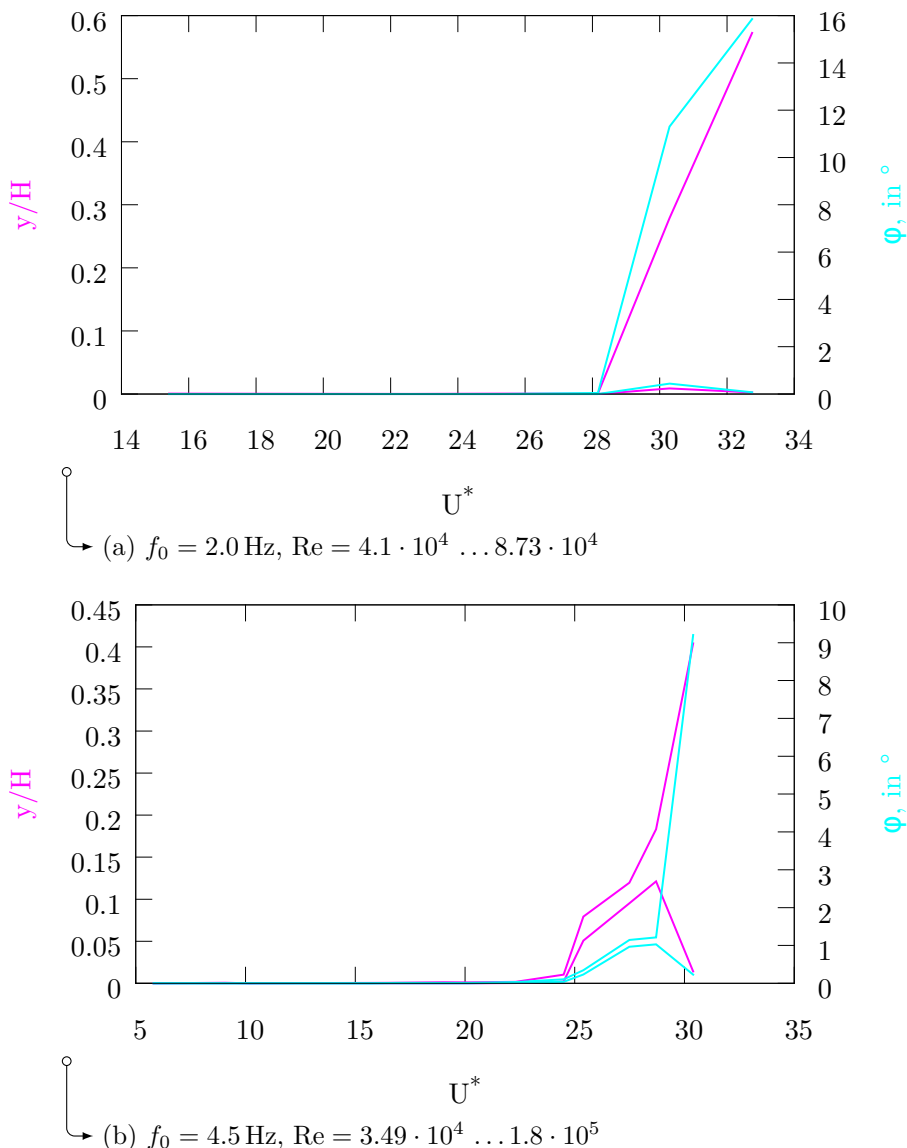


Figure 5.16.: Free vibration tests in the wind tunnel: Dimensionless displacements y/H and angle φ for several reduced velocities. The upper and lower lines correspond to the minimum and maximum average peaks.

terworth filter (cutoff frequency 15 Hz) to discern between model and test-stand motion. Most notably pitch vibrations at $U^* \approx 11$ with $\hat{\varphi} = 0.4^\circ$ at the model eigenfrequency are not displayed.

Several other tests at test-stand eigenfrequency 6.5 Hz with “imperfections” (eigenfrequency ratio not equal to one, initial angle of inclination different from zero) were carried out. The aim was to test whether vibrations at low reduced velocities could be observed under slightly altered conditions. However, this was not the case.

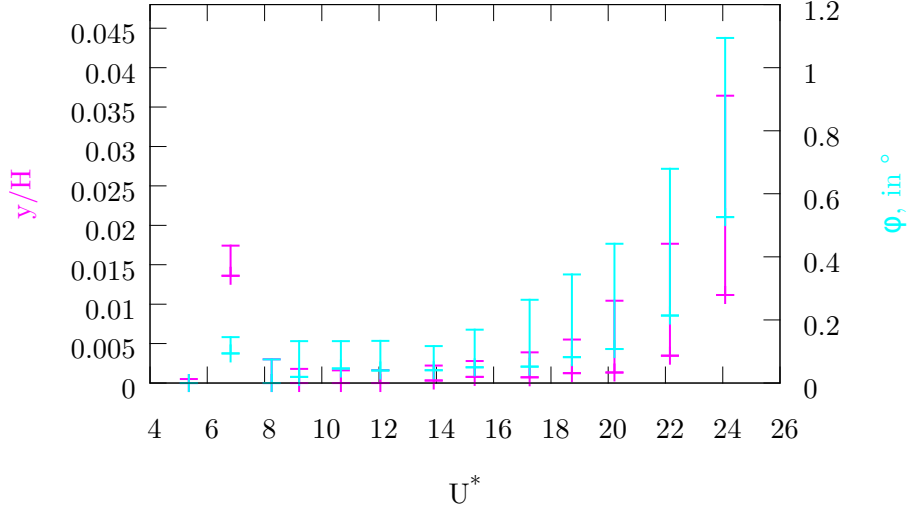


Figure 5.17.: Free vibration tests in the wind tunnel: Dimensionless displacements y/H and angle φ for several reduced velocities at a test-stand eigenfrequency of 9.5 Hz.

5.3. Tensioned belt experiments

The experiments on the tensioned belt were carried out to investigate the behaviour of the U-shaped profile at low reduced velocities under low damping conditions. Due to the limited wind tunnel flow velocity investigations at large reduced velocities (e.g. $U^* > 28$) could not be performed with this model. Tests at two different tunings (eigenfrequencies $f_{0,\varphi} = 13.8$ Hz and $f_{0,\varphi} = 10.8$ Hz) were carried out.

For the eigenfrequency $f_{0,\varphi} = 13.8$ Hz a sharp increase of pitch amplitudes at $U^* = 14$ was observed (see figure 5.18a). This may correspond to vortex induced vibrations under the U-flow pattern, as seen in the the simulations. Since the wind tunnel was operated at almost maximum power at $U^* = 14$, reduced velocities $U^* > 14$ were not investigated at this tuning. Instead, the eigenfrequency was lowered by reducing the tension in the belt ($f_{0,\varphi} = 10.8$ Hz. For reduced velocities up to $U^* = 12$ comparable behaviour was observed (see figure 5.18b). The sharp increase at $U^* = 14$ could not be reproduced. Instead, for $U^* \lesssim 17$ intermittent pitch vibrations occurred. At $U^* \approx 18$, where the wind tunnel was operated at maximum power (97%) the minimum average peaks also increased, indicating perpetual instead of intermittent vibrations. Possible reasons for this discrepancy are the frequency ratio in case of the lower eigenfrequency, which is $f_{0,y}/f_{0,\varphi} = 1.06$ instead of $f_{0,y}/f_{0,\varphi} = 1$ as in the first case. Secondly the damping, represented by the logarithmic decrements in table 2.4, is slightly larger for the lower eigenfrequency. Unfortunately these properties appeared to depend sensitively on the tension of the individual cables in the belt.

Another possibility to influence the flow pattern is the angle of inclination (see section 3.1.4). Vibrations at the lower eigenfrequency and the angles $\varphi_0 = 5^\circ$ and $\varphi_0 = -5^\circ$

were investigated.

At positive inclination it can be reasoned that U-flow vortices play a more important role. Indeed, pitch dominant vibrations set in at $U^* \approx 14$ (see figure 5.19). The heaving amplitudes also increase from this velocity onwards. At negative inclinations vibration amplitudes are much smaller. Only a slight increase for growing reduced velocities can be observed. This behaviour is a direct consequence of the flow pattern: Vortices shed behind the windward flange do not come close enough to the leeward flange to excite vibrations.

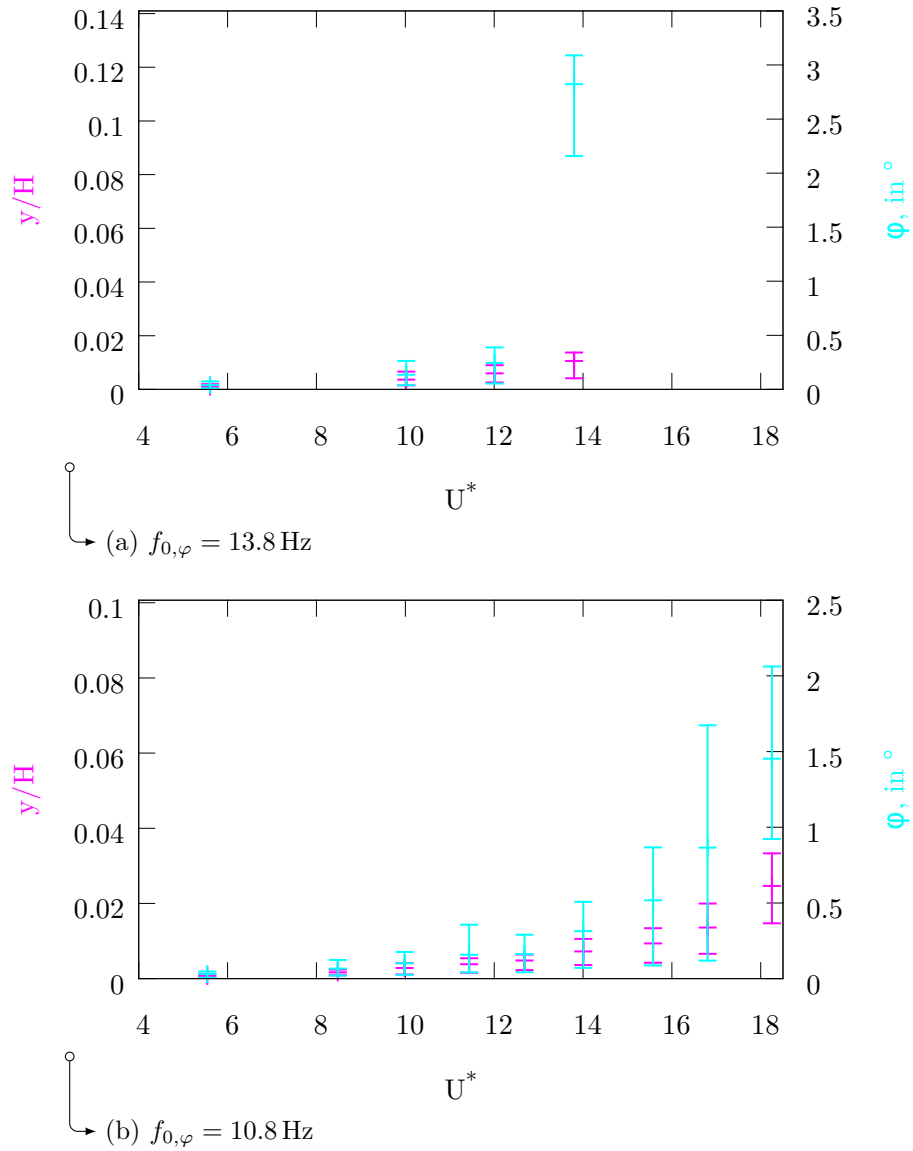


Figure 5.18.: Mode-1 Heave y/H and pitch φ motion of a tensioned belt at zero inclination for several reduced velocities $U^* = u_\infty/Hf_{0,\varphi}$.

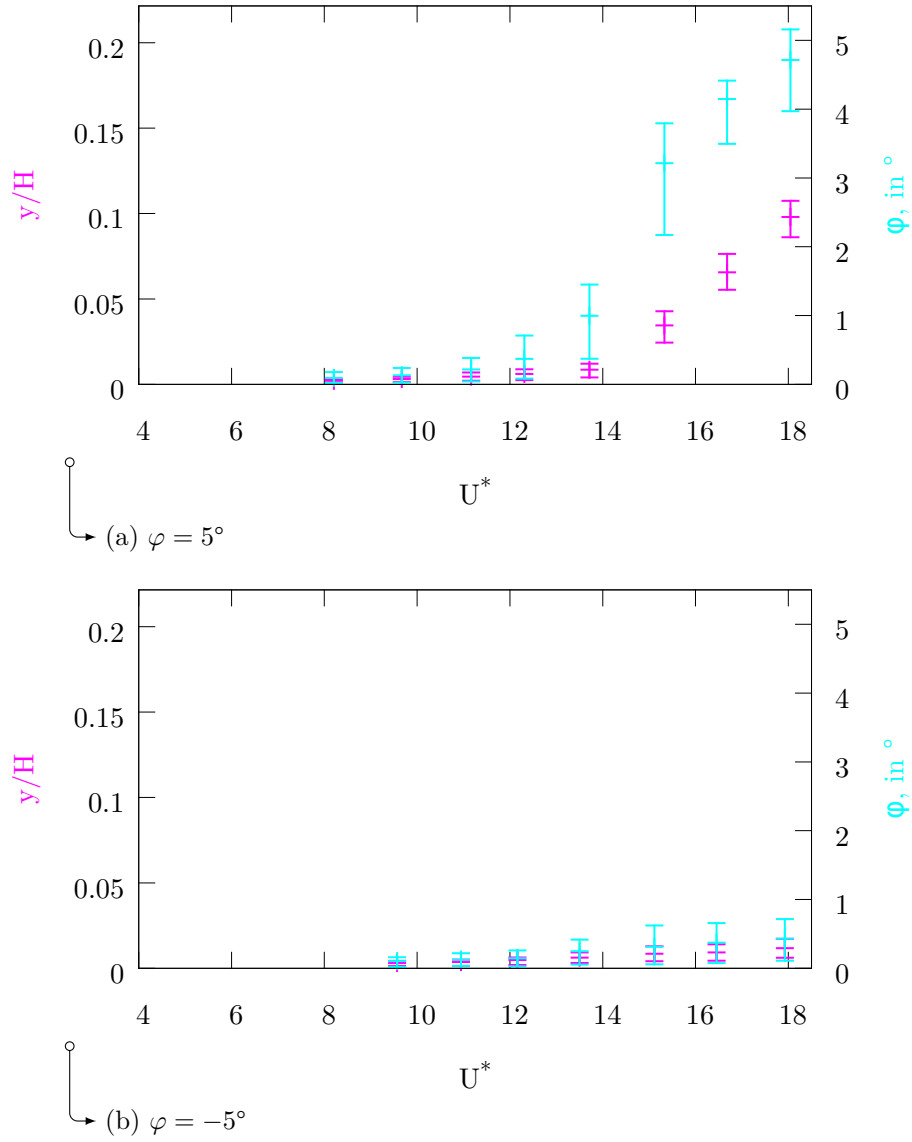


Figure 5.19.: Mode-1 Heave y/H and pitch ϕ motion of a tensioned belt at $f_{0,\phi} = 10.8$ Hz for several reduced velocities $U^* = u_\infty/H f_{0,\phi}$.

6. Conclusions

Flow induced vibrations of a U-shaped belt or prism at Reynolds numbers $Re \sim 10^5$ were studied with the help of 2D-CFD simulations and wind tunnel experiments. After taking the available time and resources into account it was chosen to employ unsteady RANS simulations in a two-dimensional computational domain. This choice made it possible to perform several simulation series with limited computational power. Most computations were performed in parallel and using 4 CPU cores, and finished within a few days wall clock time. Thus, many insights about the flow around this particular profile and the vibration excitation mechanisms could be gained.

6.1. The flow around a stationary profile

The simulations show two different flow patterns, the U-flow and R-flow pattern, which were found to exist under the same boundary conditions.

- Under the U-flow pattern, the shear layer originating from the top windward corner rolls up in the cavity of the U. The cavity vortex forms. It travels to the leeward flange of the U, from where it is swept into the wake of the profile.
- Under the R-flow pattern, the free shear layer is weakly curved and reaches towards the wake of the profile. Large vortices form behind the profile.
- PIV wind tunnel experiments showed that the flow patterns change intermittently. This was not captured by our simulations.

The two flow patterns correspond to similar vortex formation patterns observed in the flow around a rectangular prism or an H-prism. The R-flow pattern is also known as LEVS regime in rectangular-prism flows. The U-flow pattern is similar to the ILEV regime, [25]. The vortices forming at the leading edge of a rectangular prism impinge on its sidewalls. The aspect ratio of the prism influences whether the ILEV or LEVS regime forms [25]. A rectangular prism with an aspect ratio of $B/H = 4.65$ (as the U-profile under consideration) is in the ILEV regime, but close to the LEVS-regime.

The flow around an H-prism admits several flow patterns. Kubo and Hirata, [46], reported several possible ILEV regimes with different numbers of vortices travelling along the sides of an H-prism (aspect ratio $B/H = 10$). The number of travelling vortices could be influenced by forced motion of the prism. Here, no more than one vortex travelling through the cavity could be observed.

Two intermittently changing flow patterns can also be observed in the flow around a short rectangular prism ($B/H=1/5$). Again, the flow patterns are related to a weak

or strong shear layer roll-up. This was reported by Tamura and Itoh [100] by simulations, explaining wind tunnel tests by Nakamura and Matsukawa [70]. Promising, modern methods for simulating turbulent flows exist. Published results indicate that 3D URANS simulations of the flow around bluff bodies tend to yield solutions that are two-dimensional in character [32]. It is stated that the implicit assumption of time-scales required for the success of URANS simulations does not hold when simulating bluff body flows. The largest vortices in the wake evolve on time-scales that are much larger than the time scales of the turbulent fluctuations. But the development of the important free shear layers, and therefore ultimately also the largest vortices, depends on much smaller time-scales which cannot be resolved by URANS simulations. Thus, it can be easily understood how the assumptions implied by the URANS model lead to the notions of the U-flow and R-flow pattern, as they can be discerned by the behaviour of the free shear layer above the cavity.

There are many recent studies reporting simulation of bluff body flows using LES-like techniques [5, 58] or blending RANS and LES approaches [104]. However, successful these simulations were, there is no established scale resolving turbulence model available at present. A recent review of the simulation effort in the BARC benchmark (flow around a rectangular prism with an aspect ratio of $B/H = 5$) [13] highlighted this by finding that four research groups reported a total of sixteen different different time and spanwise averaged flow fields in the year 2011. All but two of these were 3D LES simulations.

6.2. Aeroelastic stability by forced motion simulations

The critical reduced velocity for flutter vibrations of the U-profile was estimated by the method of aerodynamic derivatives. A critical velocity close to $U^* = 32$, where 2D-CFD simulations predicted flutter vibrations, was obtained. However, the exact value is sensitive to changes of the aerodynamic derivatives. At low reduced velocities influences of the flow-pattern were deemed too important. Due to the inherent nonlinearities, these could not be captured reliably with such methods. To sum up:

- Plausible results were obtained by employing the method of aerodynamic derivatives in conjunction with 2D URANS simulations.

6.3. 2D Simulation of flow induced vibrations

The vibration simulations share the same limitations as the simulations of the flow around the stationary profile. Each SDoF or 2DoF configuration had to be simulated twice to account for each flow pattern. Bearing in mind, that the flow pattern change is also influenced by the motion of the profile it is an open question which flow pattern is relevant at which reduced velocity. The observed flow induced vibration phenomena can be roughly split into the following two regimes:

- At reduced velocities smaller than 16 ($U^* < 16$) the excitation is due to vortices forming in the wake or the cavity vortices.

- At larger reduced velocities, $U^* > 16$ excitation due to the motion induced vortex is relevant.

The vibrations due to the motion induced vortex could be reproduced by wind tunnel experiments (section 5.2). An indication that vibrations due to cavity vortices exist could be achieved by the tensioned belt experiments (section 5.3).

An experimental study of flow induced **SDoF** vibrations of a $B/H = 4$ rectangular prism is [64]. Therein, our **SDoF** heave and pitch results are confirmed qualitatively. **SDoF** heave vibrations are confined to one reduced velocity interval. Two unstable regimes for **SDoF** pitch vibrations were observed. Furthermore, Matsumoto et al. [64] reason that the vortices travelling along the side of the profile (“surface vortices”) are the cause for the observed vibrations at low reduced velocities, $U^* < 10$. The main difference to the present results is that the cavity vortices (the analogue to the surface vortices) lead to larger vibration amplitudes and can excite vibrations in a broader range of reduced velocities. In another publication, Matsumoto et al. [63] describe two different excitation mechanisms for vibrations of a Tacoma narrows bridge scale model. These two excitation mechanisms correspond to vibration excitation due to the cavity vortex and the motion induced vortex.

6.3.1. Unique aspects of this thesis

The investigation of excitation mechanisms of a tensioned belt with U-shaped cross-section at low reduced velocities by coupled **CFD** simulations is unique to this thesis. Despite remarkable progress in the development of turbulence models and a vast increase in the available computer power in the last years, this investigation could not have been carried out with scale resolving turbulence models. The demand of computational power of such simulations and the required time to fine-tune these turbulence models render this endeavour impossible today. Surely, future research will lead to better turbulence models and more efficient numeric schemes to revisit the findings presented herein. The headstone for further investigations is laid.

A. Simulation data

Displacements: SDoF heave, $U^* = 7.4$, U-flow pattern

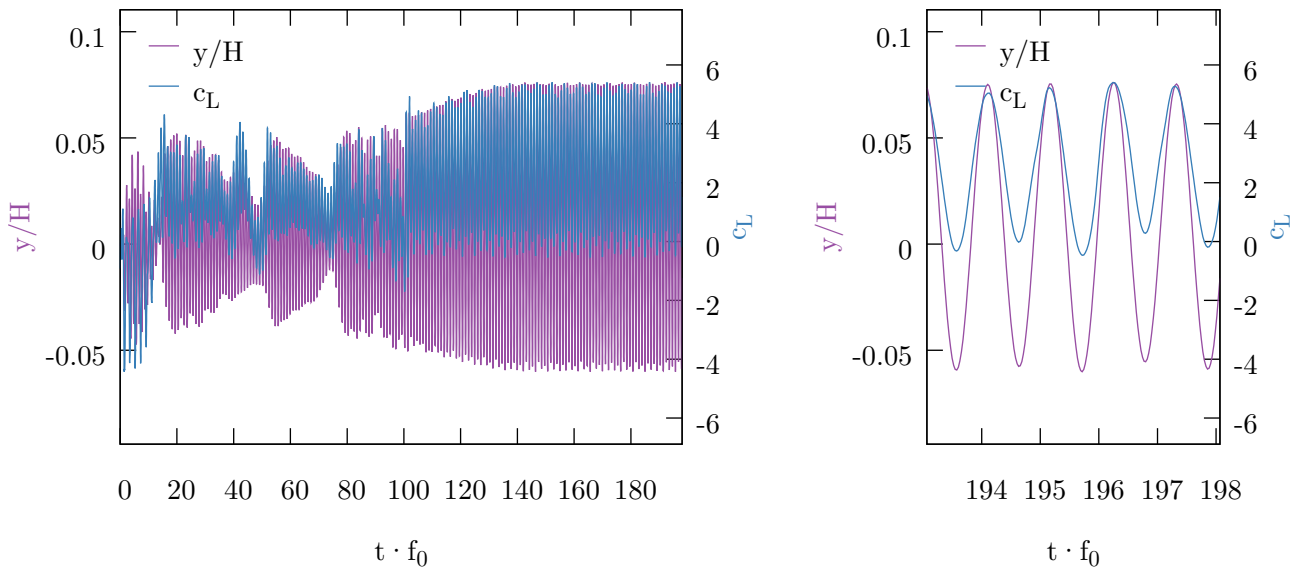


Figure A.1.: Time-series of the dimensionless heave y/H and the lift coefficient c_L at $U^* = 7.4$; Simulation at $Re = 2.45 \cdot 10^5$ under the U-flow pattern.

Displacements: SDoF heave, $U^* = 10.0$, U-flow pattern

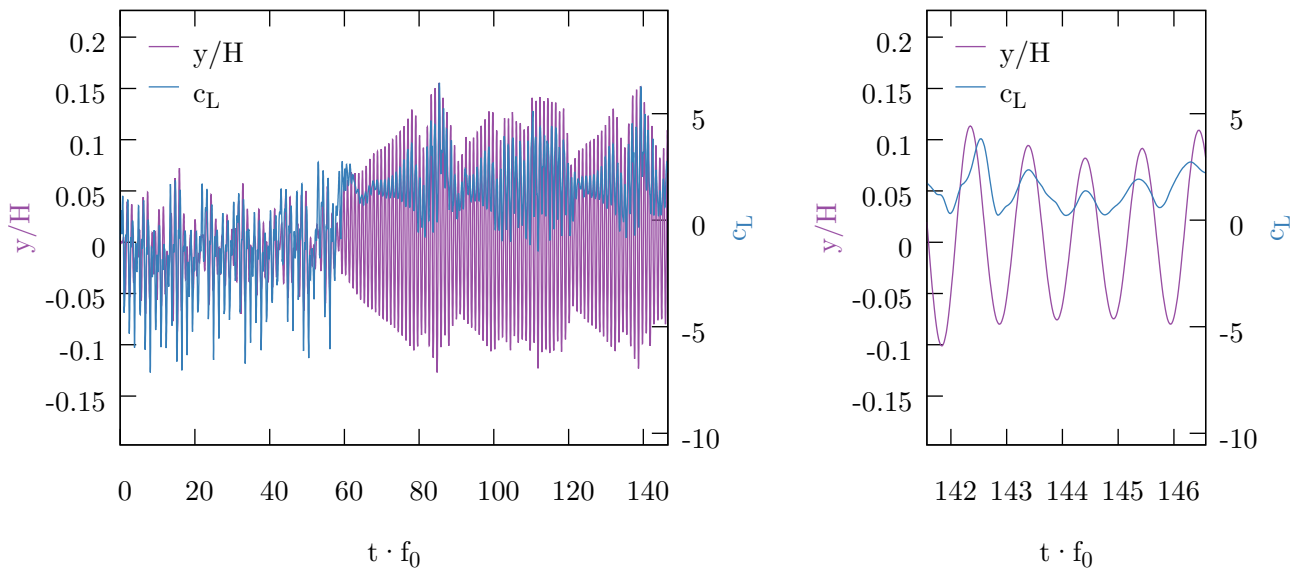


Figure A.2.: Time-series of the dimensionless heave y/H and the lift coefficient c_L at $U^* = 10.0$; Simulation at $Re = 2.45 \cdot 10^5$ under the U-flow pattern.

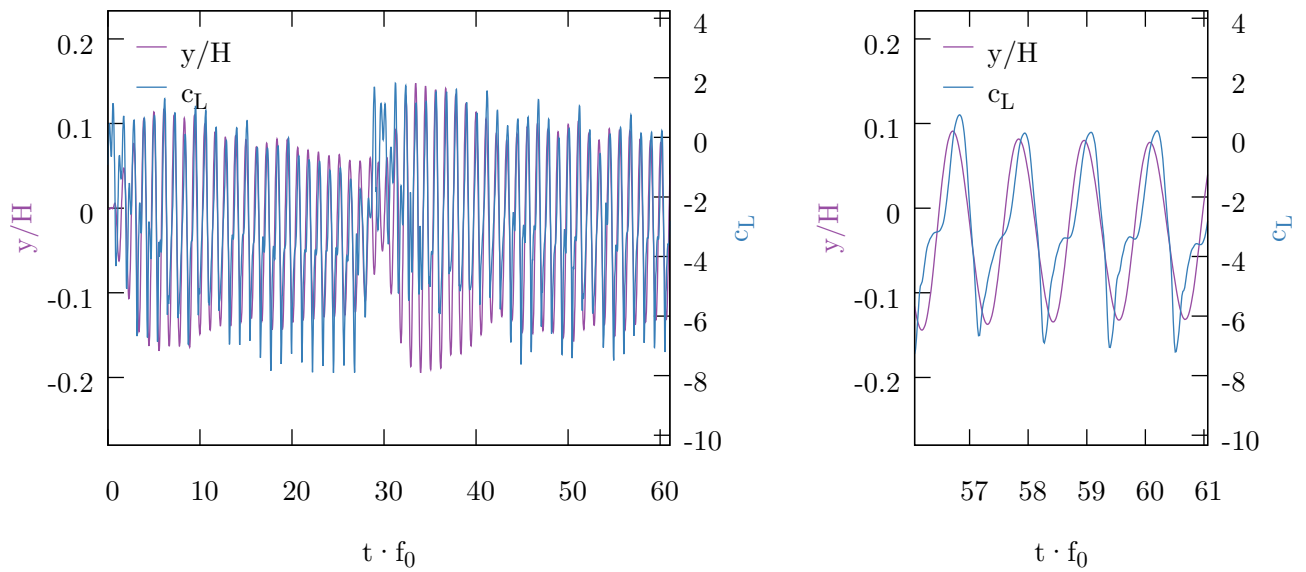
Displacements: SDoF heave, $U^* = 12.0$, U-flow pattern

Figure A.3.: Time-series of the dimensionless heave y/H and the lift coefficient c_L at $U^* = 12.0$; Simulation at $\text{Re} = 2.45 \cdot 10^5$ under the U-flow pattern.

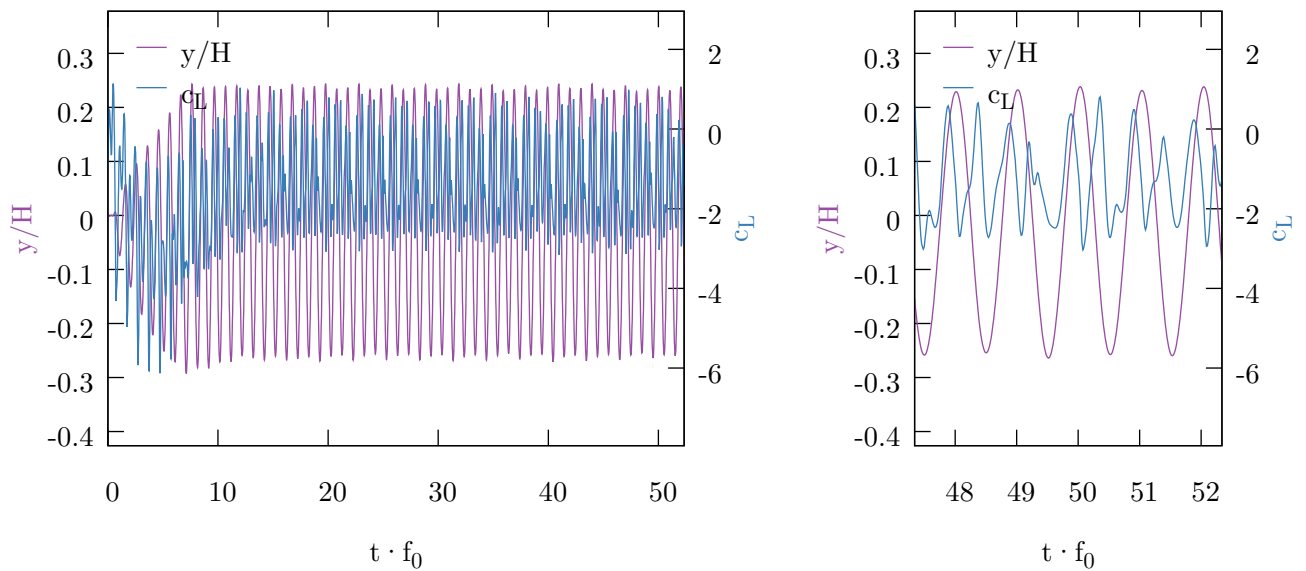
Displacements: SDoF heave, $U^* = 14.0$, U-flow pattern

Figure A.4.: Time-series of the dimensionless heave y/H and the lift coefficient c_L at $U^* = 14.0$; Simulation at $\text{Re} = 2.45 \cdot 10^5$ under the U-flow pattern.

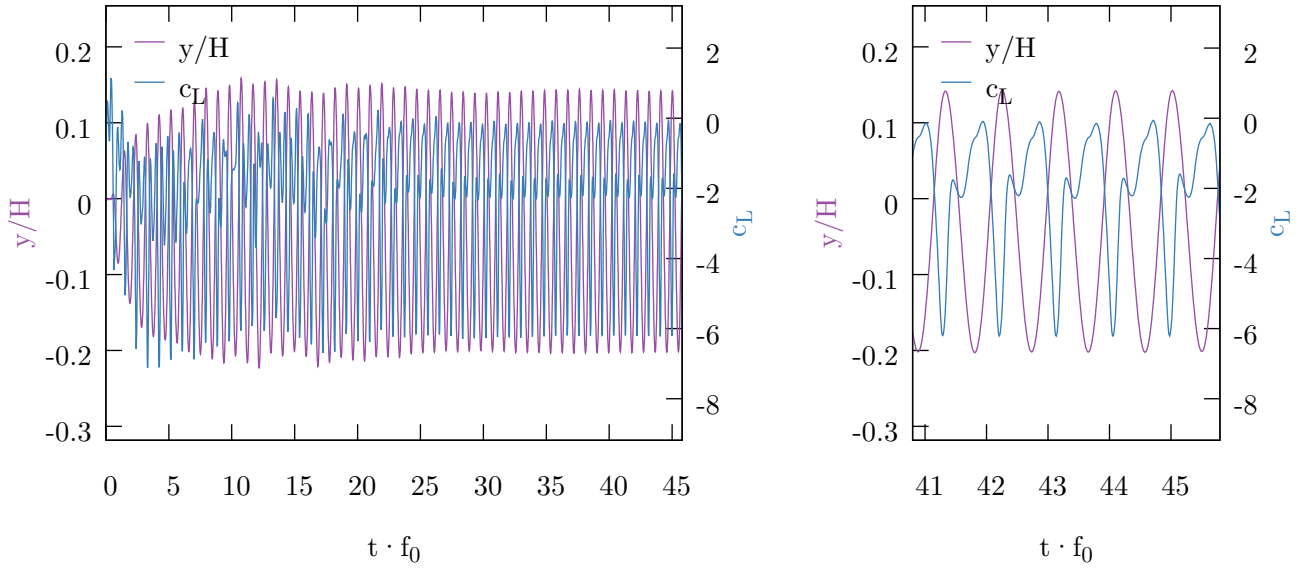
Displacements: SDoF heave, $U^* = 16.0$, U-flow pattern

Figure A.5.: Time-series of the dimensionless heave y/H and the lift coefficient c_L at $U^* = 16.0$; Simulation at $\text{Re} = 2.45 \cdot 10^5$ under the U-flow pattern.

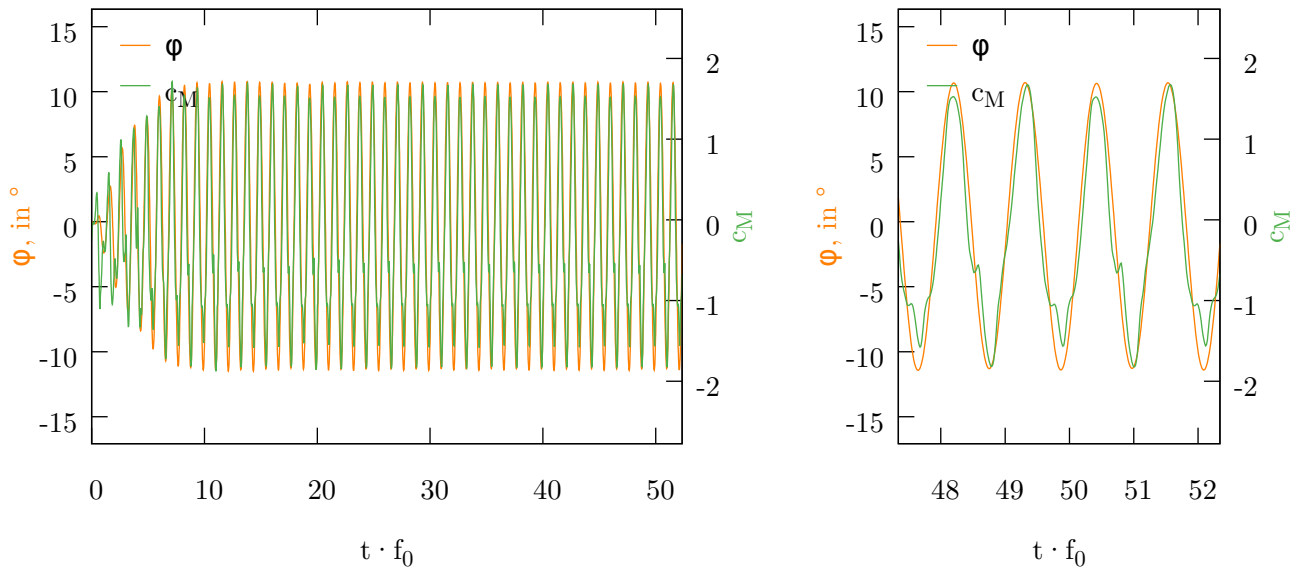
Displacements: SDoF pitch, $U^* = 14.0$, U-flow pattern

Figure A.6.: Time-series of the pitch angle φ and the moment coefficient c_M at $U^* = 14.0$; Simulation at $\text{Re} = 2.45 \cdot 10^5$ under the U-flow pattern.

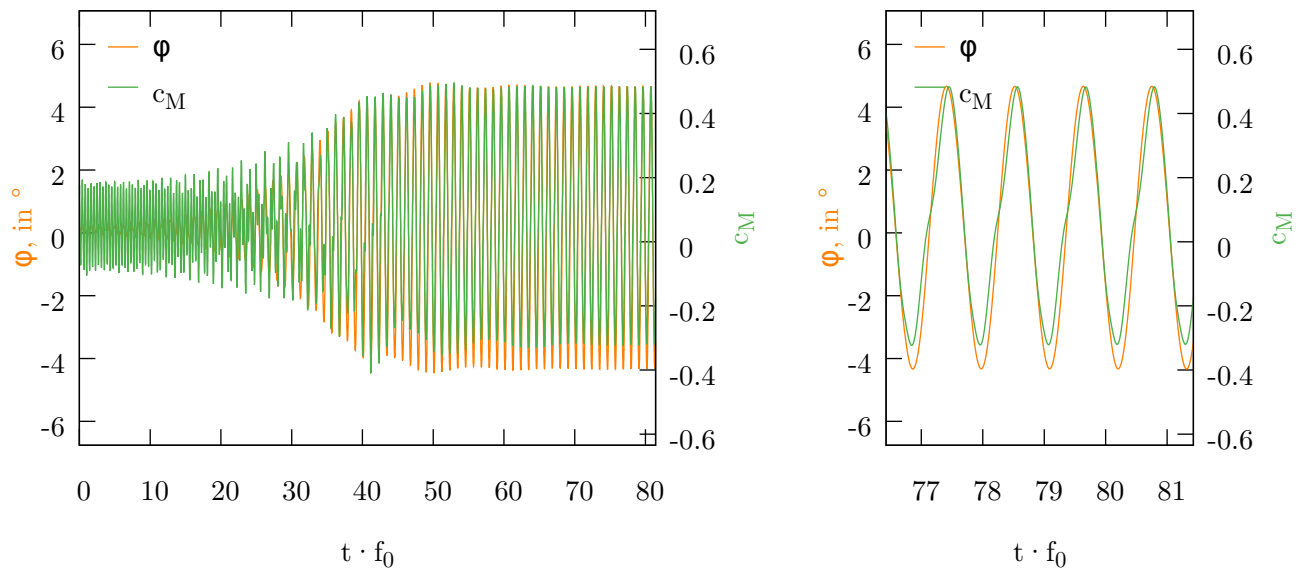
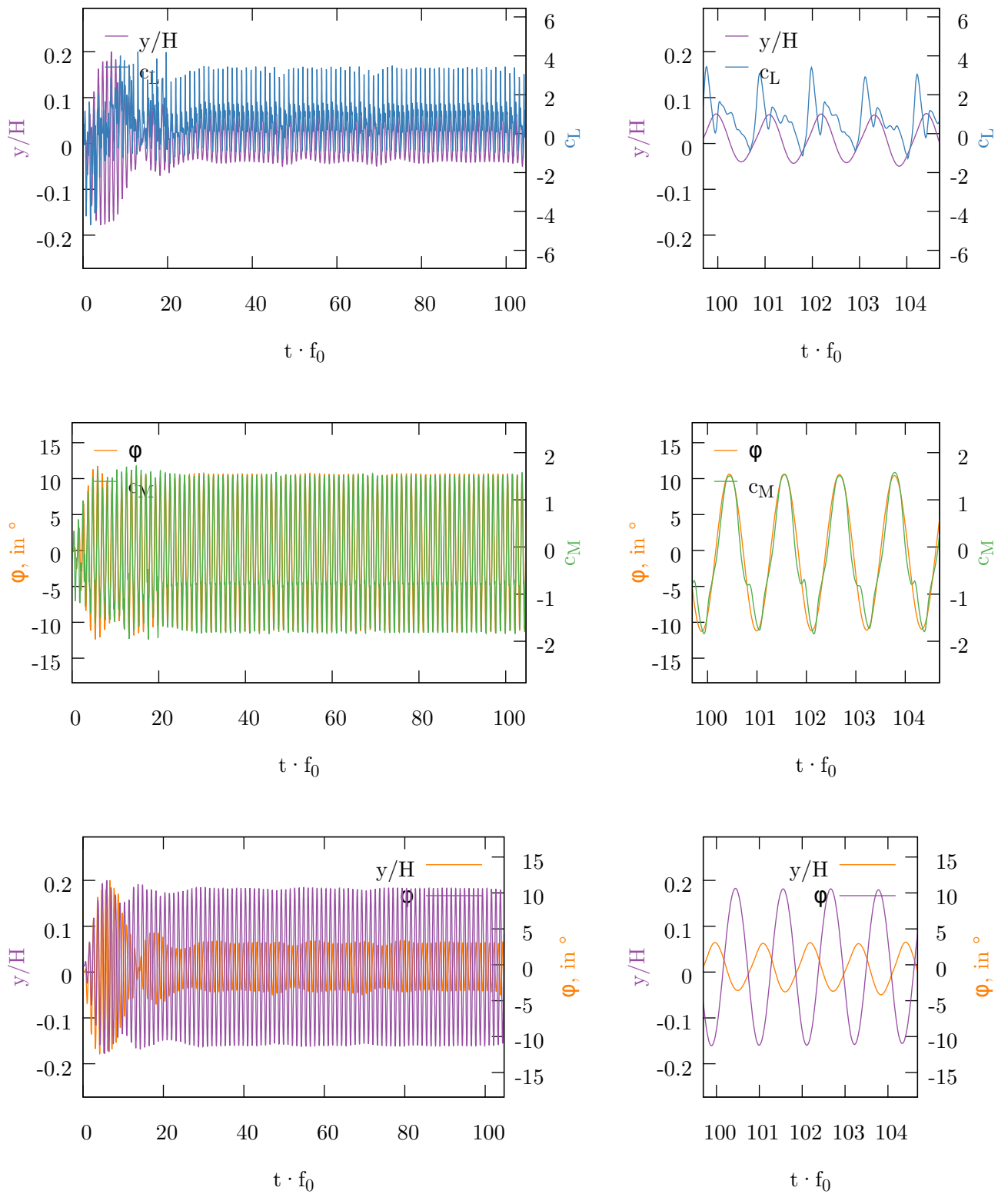
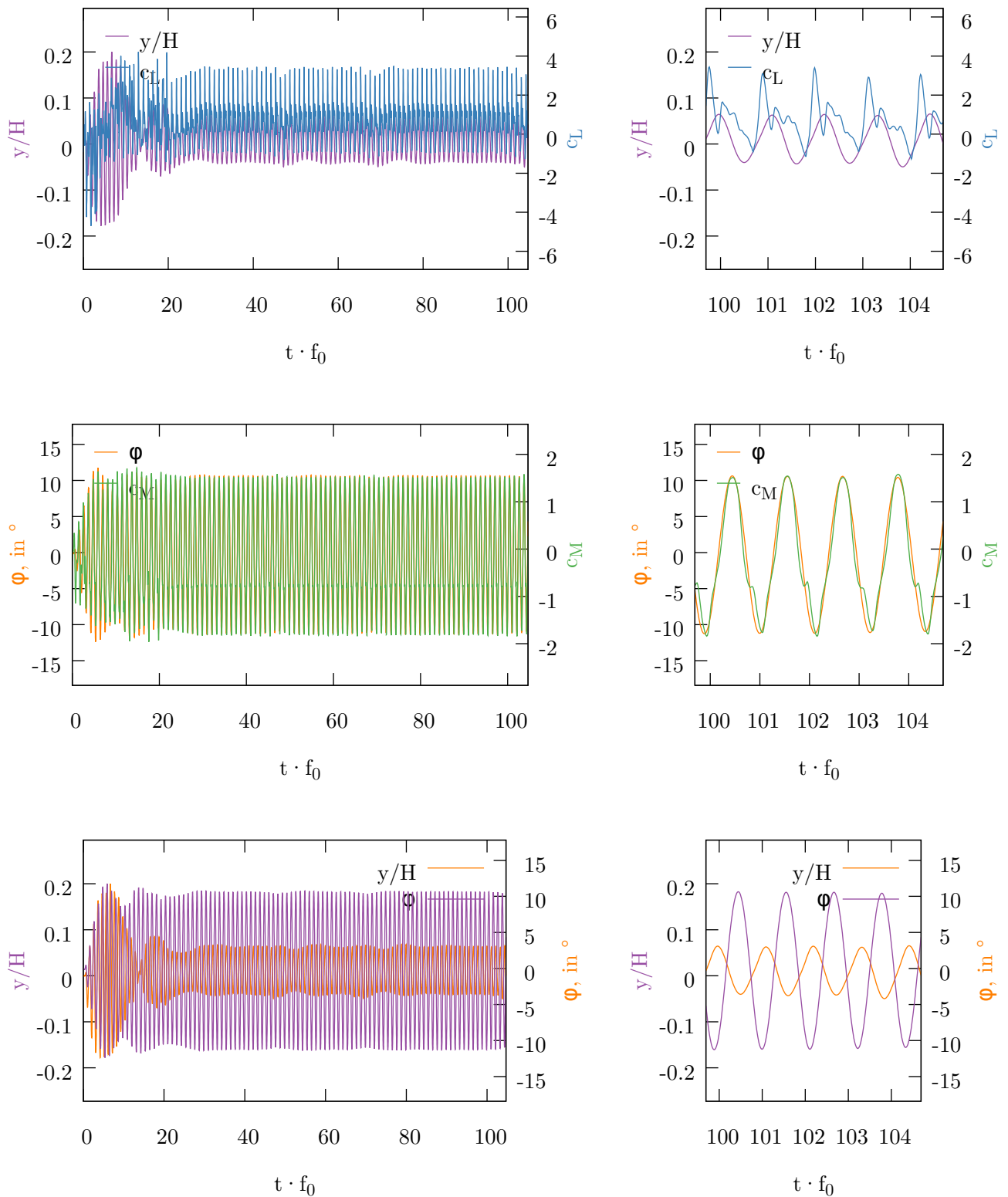
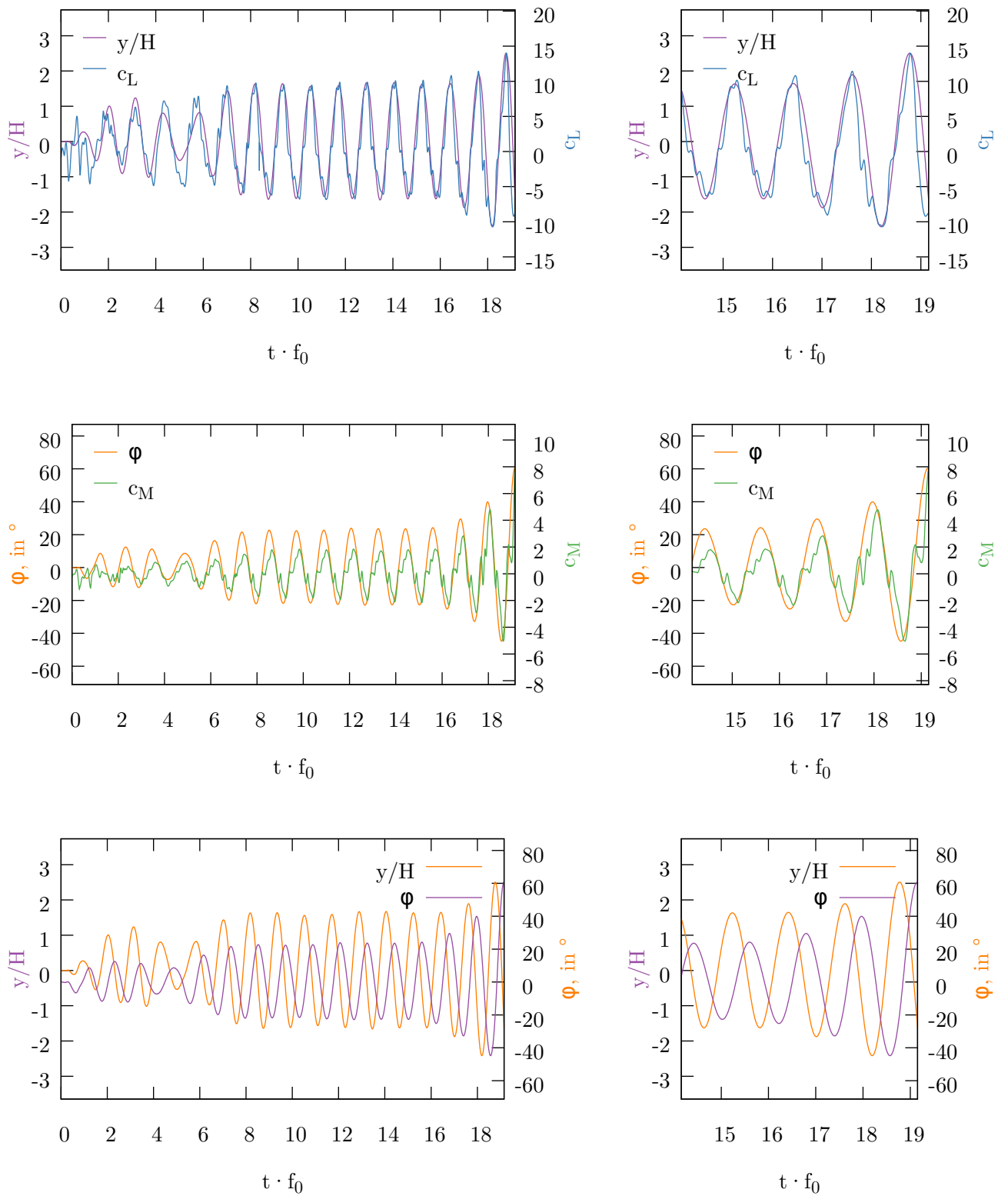
Displacements: SDoF pitch, $U^* = 18.0$, R-flow pattern

Figure A.7.: Time-series of the pitch angle φ and the moment coefficient c_M at $U^* = 18.0$; Simulation at $\text{Re} = 2.45 \cdot 10^5$ under the R-flow pattern.

Displacements: 2DoF, $U^* = 14.0$, U-flow patternFigure A.8.: Simulation at $Re = 2.45 \cdot 10^5$ under the U-flow pattern, $U^* = 14.0$.

Displacements: 2DoF, $U^* = 14.0$, R-flow patternFigure A.9.: Simulation at $Re = 2.45 \cdot 10^5$ under the R-flow pattern, $U^* = 14.0$.

Displacements: 2DoF, $U^* = 32.0$, R-flow patternFigure A.10.: Simulation at $Re = 2.45 \cdot 10^5$ under the R-flow pattern, $U^* = 32.0$.

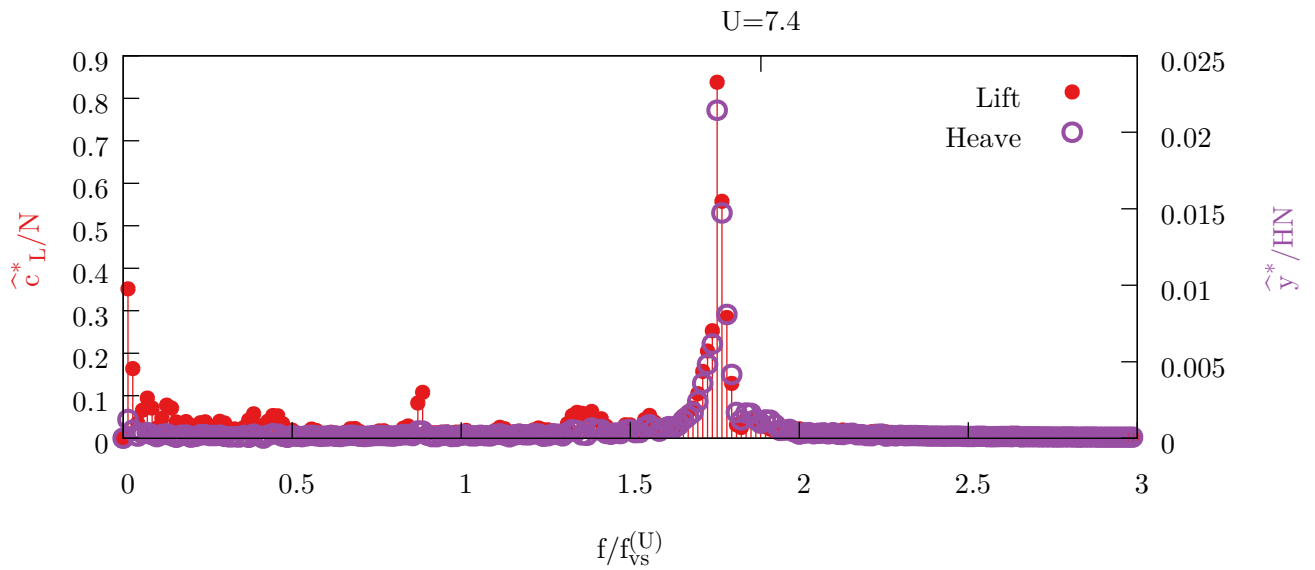
Spectra: SDoF heave, $U^* = 7.4$, U-flow pattern

Figure A.11.: Frequency spectra of the dimensionless heave y/H and the lift coefficient c_L at $U^* = 7.4$; Simulation at $\text{Re} = 2.45 \cdot 10^5$ under the U-flow pattern.

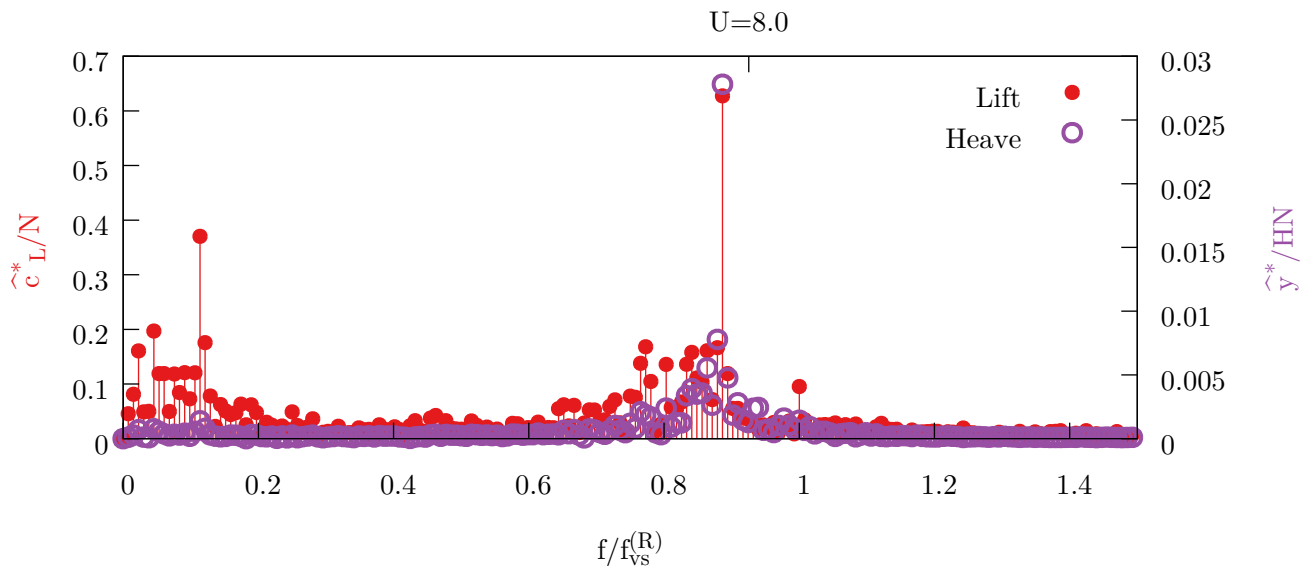
Spectra: SDoF heave, $U^* = 8.0$, R-flow pattern

Figure A.12.: Frequency spectra of the dimensionless heave y/H and the lift coefficient c_L at $U^* = 8.0$; Simulation at $\text{Re} = 2.45 \cdot 10^5$ under the R-flow pattern.

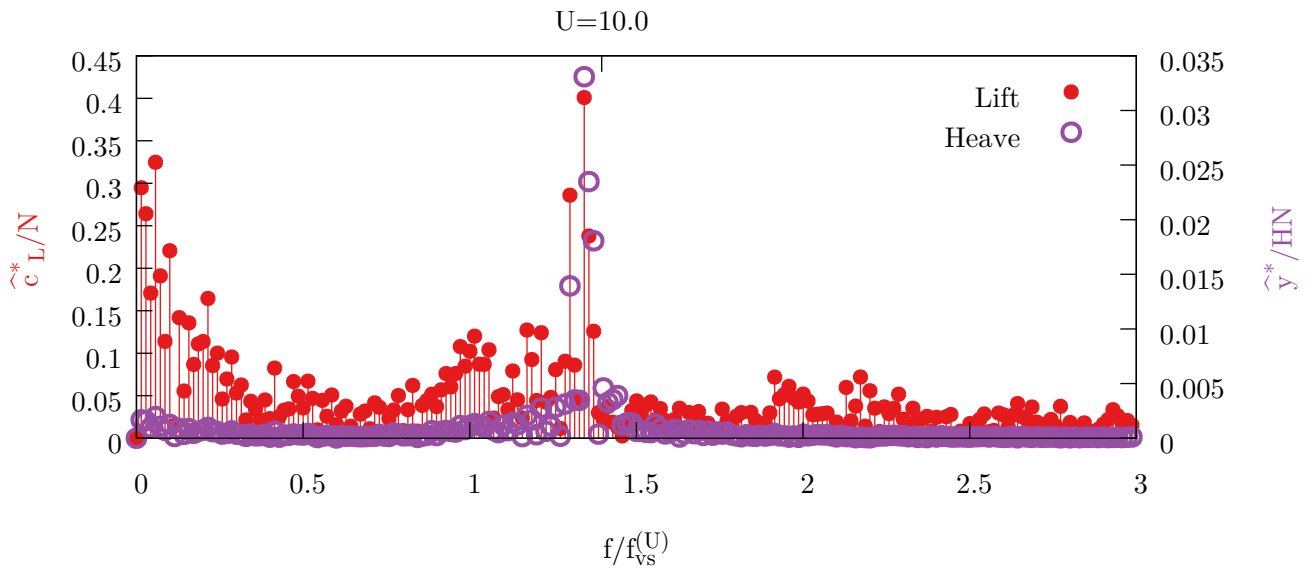
Spectra: SDoF heave, $U^* = 10.0$, U-flow pattern

Figure A.13.: Frequency spectra of the dimensionless heave y/H and the lift coefficient c_L at $U^* = 10.0$; Simulation at $Re = 2.45 \cdot 10^5$ under the U-flow pattern.

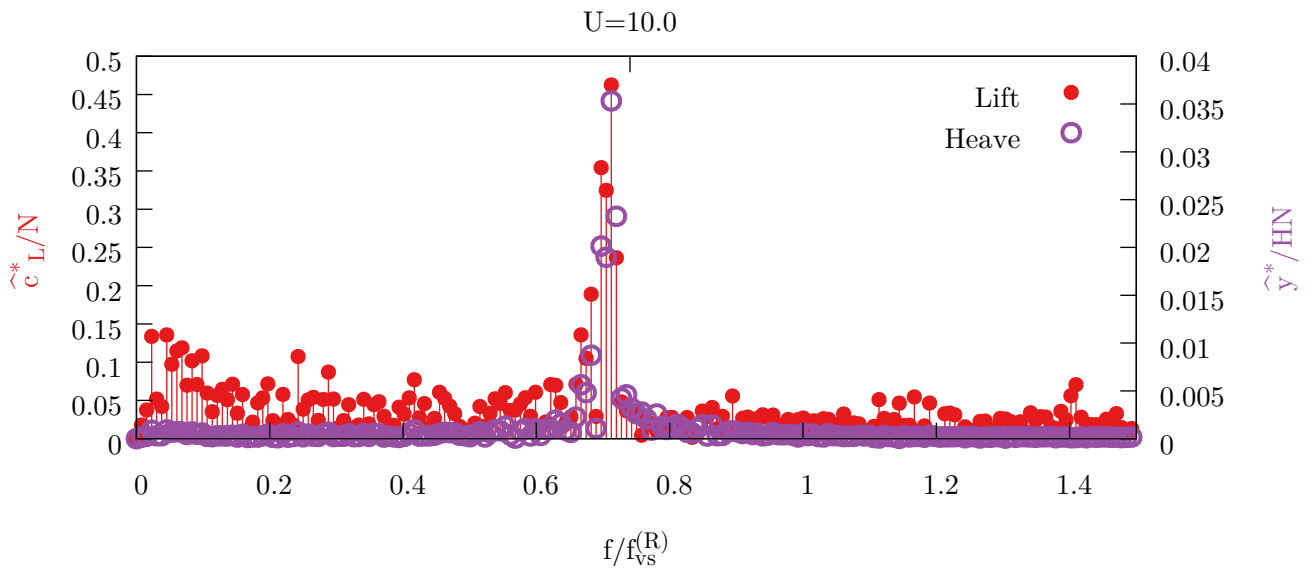
Spectra: SDoF heave, $U^* = 10.0$, R-flow pattern

Figure A.14.: Frequency spectra of the dimensionless heave y/H and the lift coefficient c_L at $U^* = 10.0$; Simulation at $Re = 2.45 \cdot 10^5$ under the R-flow pattern.

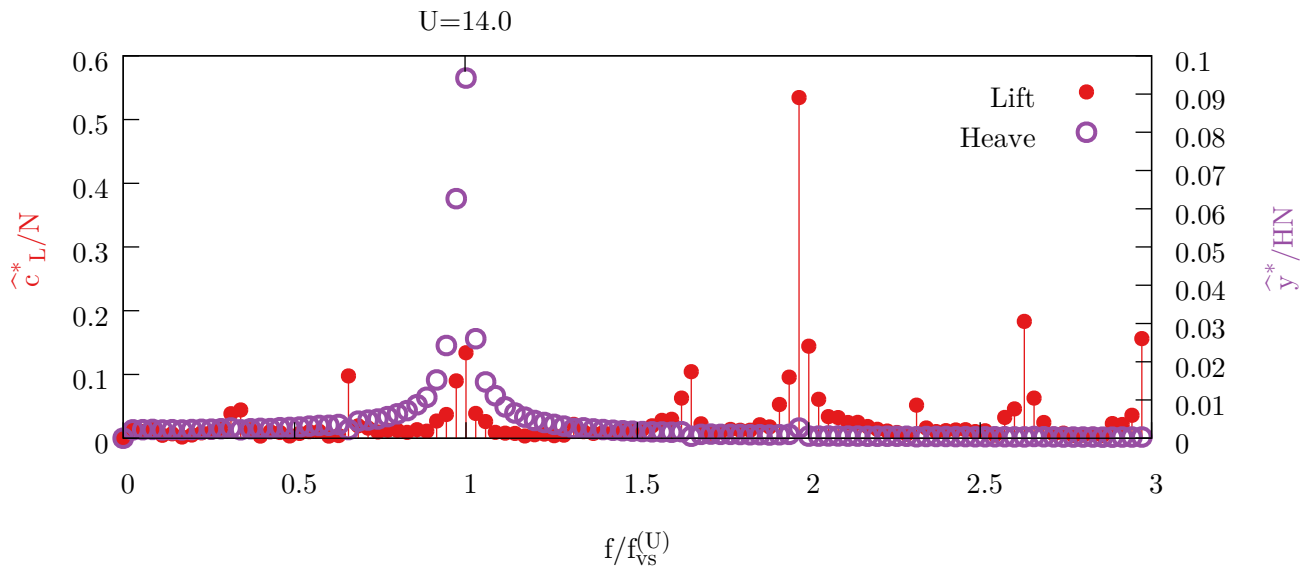
Spectra: SDoF heave, $U^* = 14.0$, U-flow pattern

Figure A.15.: Frequency spectra of the dimensionless heave y/H and the lift coefficient c_L at $U^* = 14.0$; Simulation at $\text{Re} = 2.45 \cdot 10^5$ under the U-flow pattern.

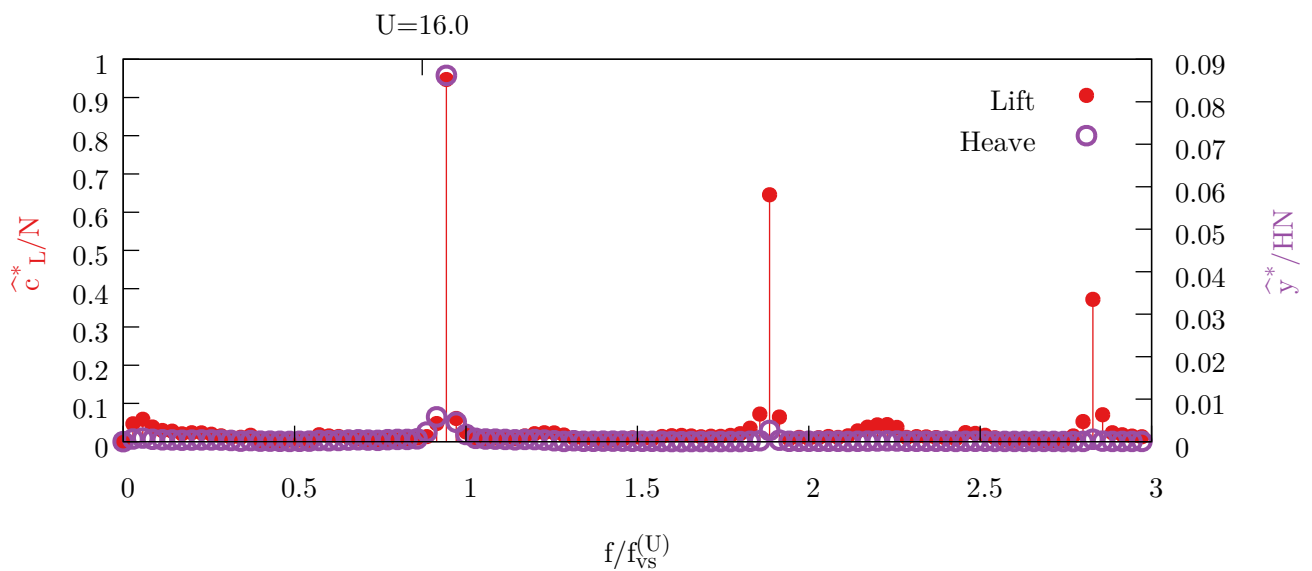
Spectra: SDoF heave, $U^* = 16.0$, U-flow pattern

Figure A.16.: Frequency spectra of the dimensionless heave y/H and the lift coefficient c_L at $U^* = 16.0$; Simulation at $\text{Re} = 2.45 \cdot 10^5$ under the U-flow pattern.

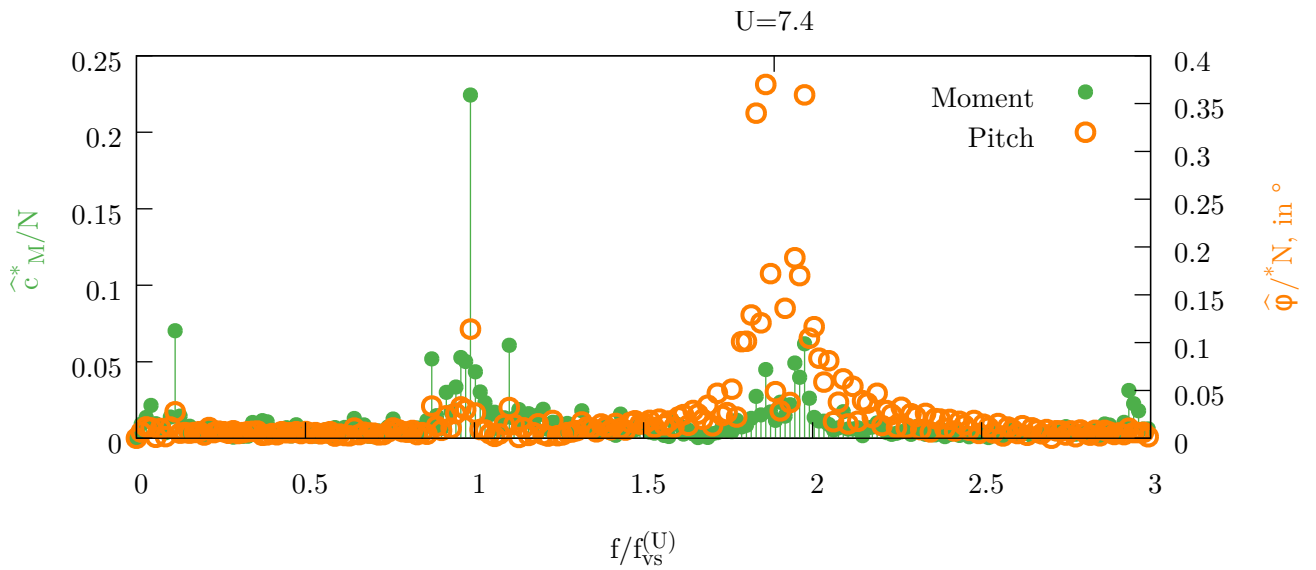
Spectra: SDoF pitch, $U^* = 7.4$, U-flow pattern

Figure A.17.: Frequency spectra of the pitch φ and the moment coefficient c_M at $U^* = 7.4$; Simulation at $\text{Re} = 2.45 \cdot 10^5$ under the U-flow pattern.

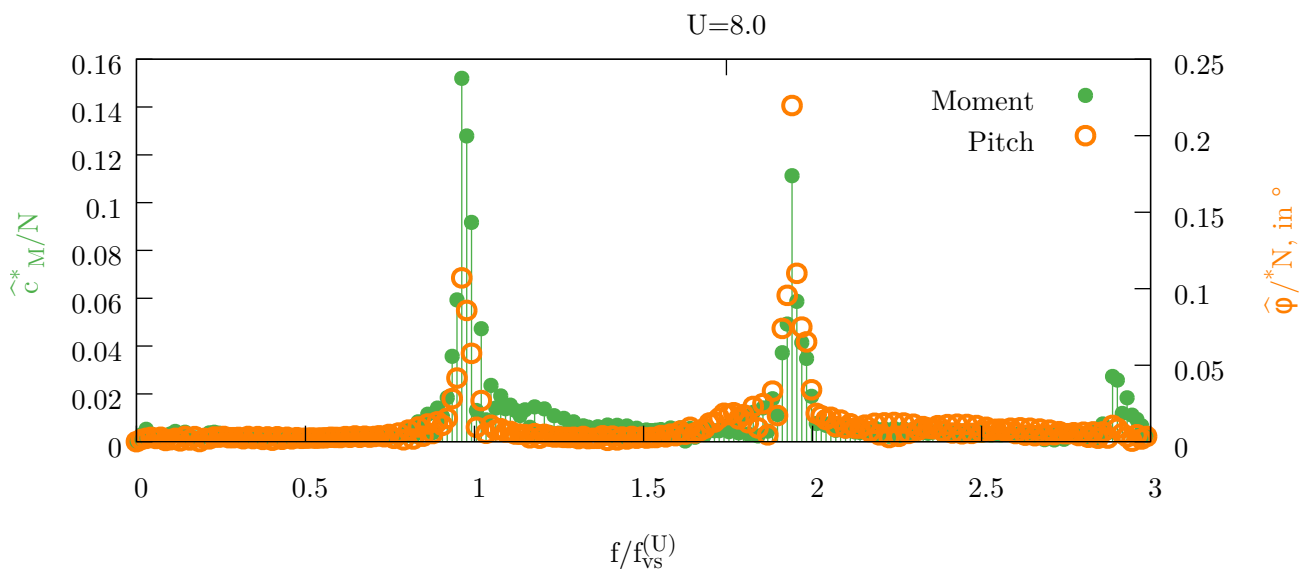
Spectra: SDoF pitch, $U^* = 8.0$, U-flow pattern

Figure A.18.: Frequency spectra of the pitch φ and the moment coefficient c_M at $U^* = 8.0$; Simulation at $\text{Re} = 2.45 \cdot 10^5$ under the U-flow pattern.

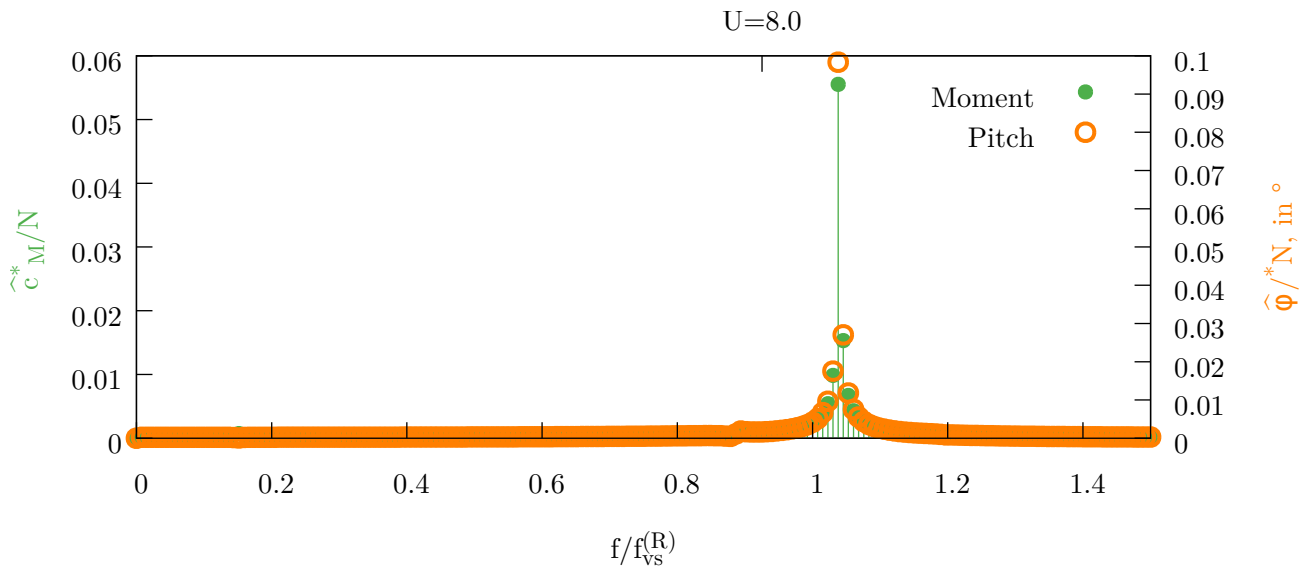
Spectra: SDoF pitch, $U^* = 8.0$, R-flow pattern

Figure A.19.: Frequency spectra of the pitch φ and the moment coefficient c_M at $U^* = 8.0$; Simulation at $\text{Re} = 2.45 \cdot 10^5$ under the R-flow pattern.

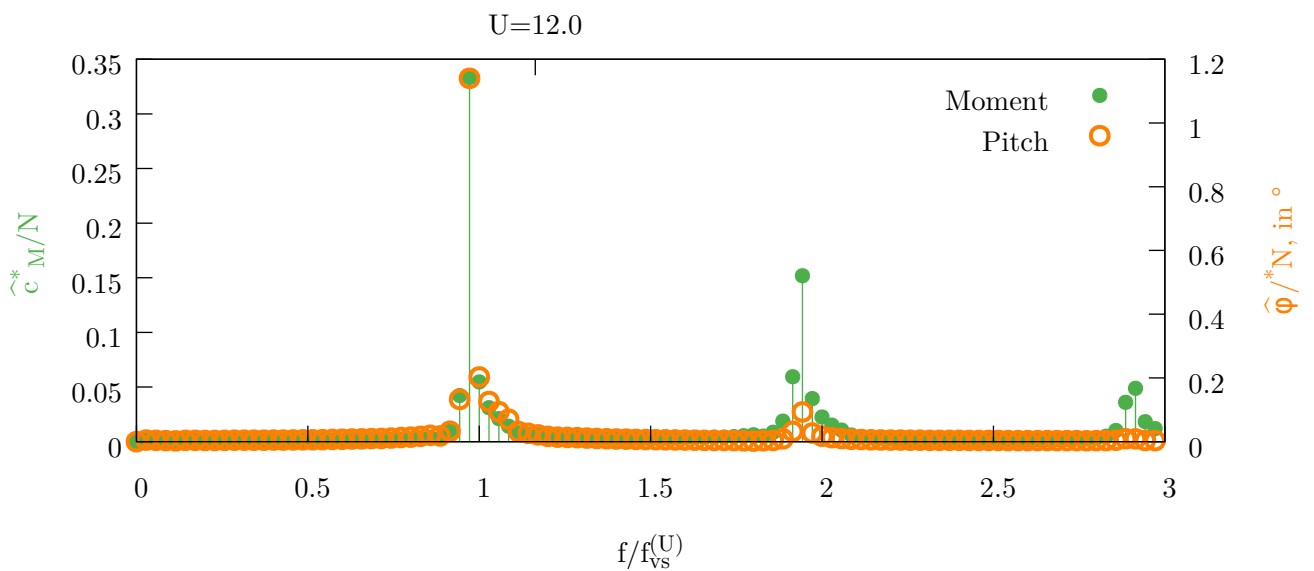
Spectra: SDoF pitch, $U^* = 12.0$, U-flow pattern

Figure A.20.: Frequency spectra of the pitch φ and the moment coefficient c_M at $U^* = 12.0$; Simulation at $\text{Re} = 2.45 \cdot 10^5$ under the U-flow pattern.

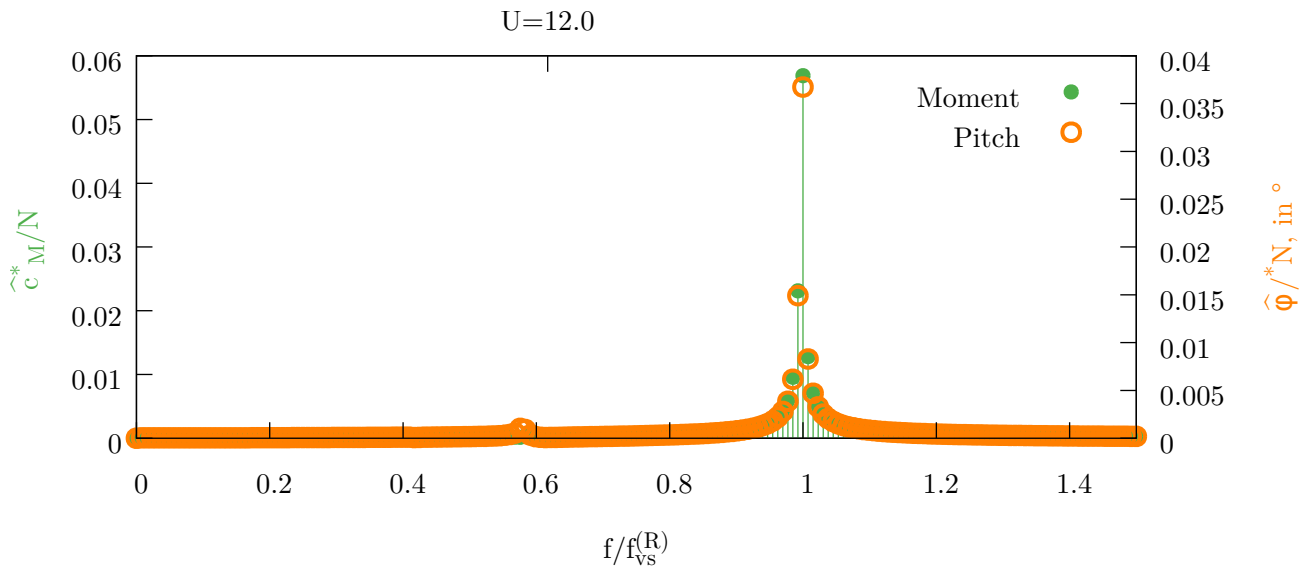
Spectra: SDoF pitch, $U^* = 12.0$, R-flow pattern

Figure A.21.: Frequency spectra of the pitch φ and the moment coefficient c_M at $U^* = 12.0$; Simulation at $\text{Re} = 2.45 \cdot 10^5$ under the R-flow pattern.

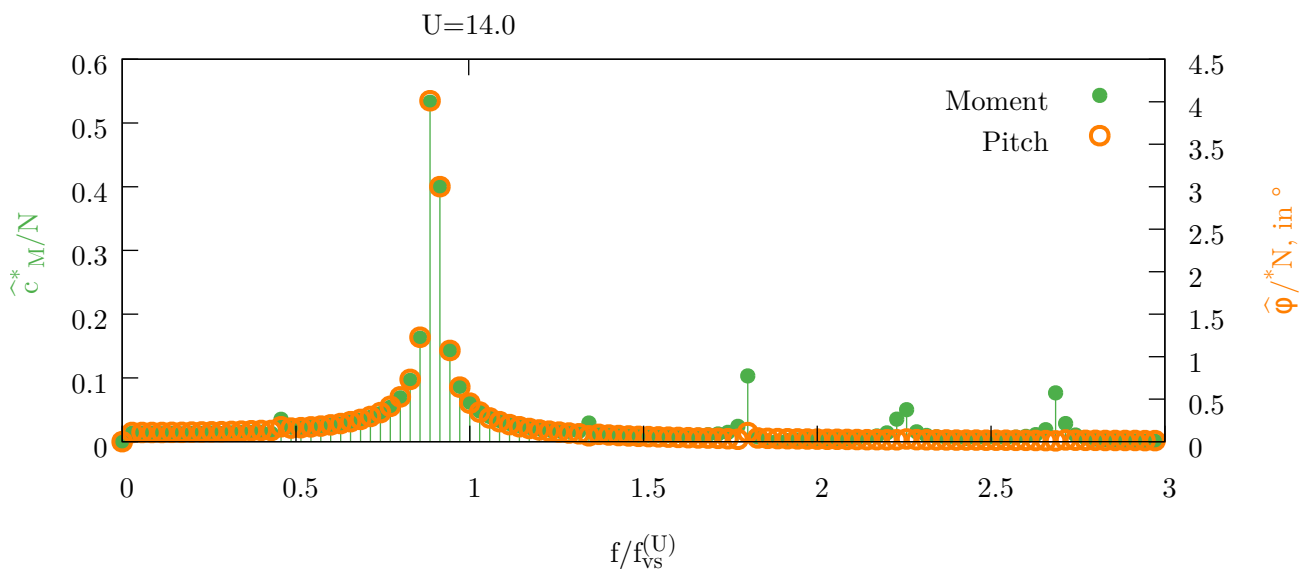
Spectra: SDoF pitch, $U^* = 14.0$, U-flow pattern

Figure A.22.: Frequency spectra of the pitch φ and the moment coefficient c_M at $U^* = 14.0$; Simulation at $\text{Re} = 2.45 \cdot 10^5$ under the U-flow pattern.

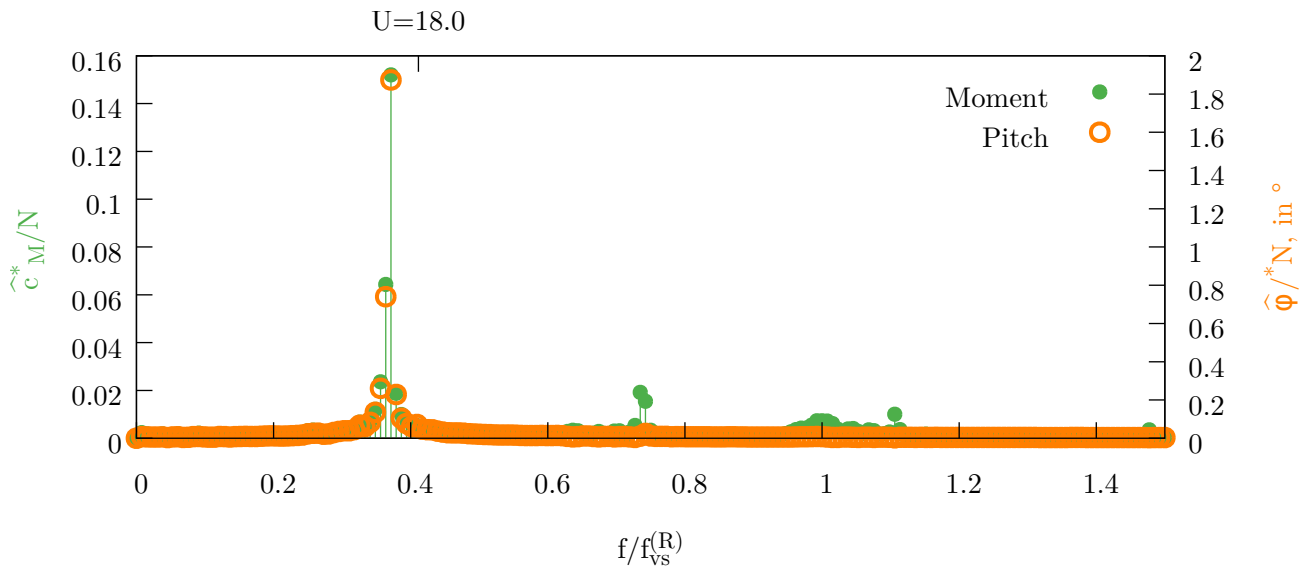
Spectra: SDoF pitch, $U^* = 18.0$, R-flow pattern

Figure A.23.: Frequency spectra of the pitch φ and the moment coefficient c_M at $U^* = 18.0$; Simulation at $\text{Re} = 2.45 \cdot 10^5$ under the R-flow pattern.

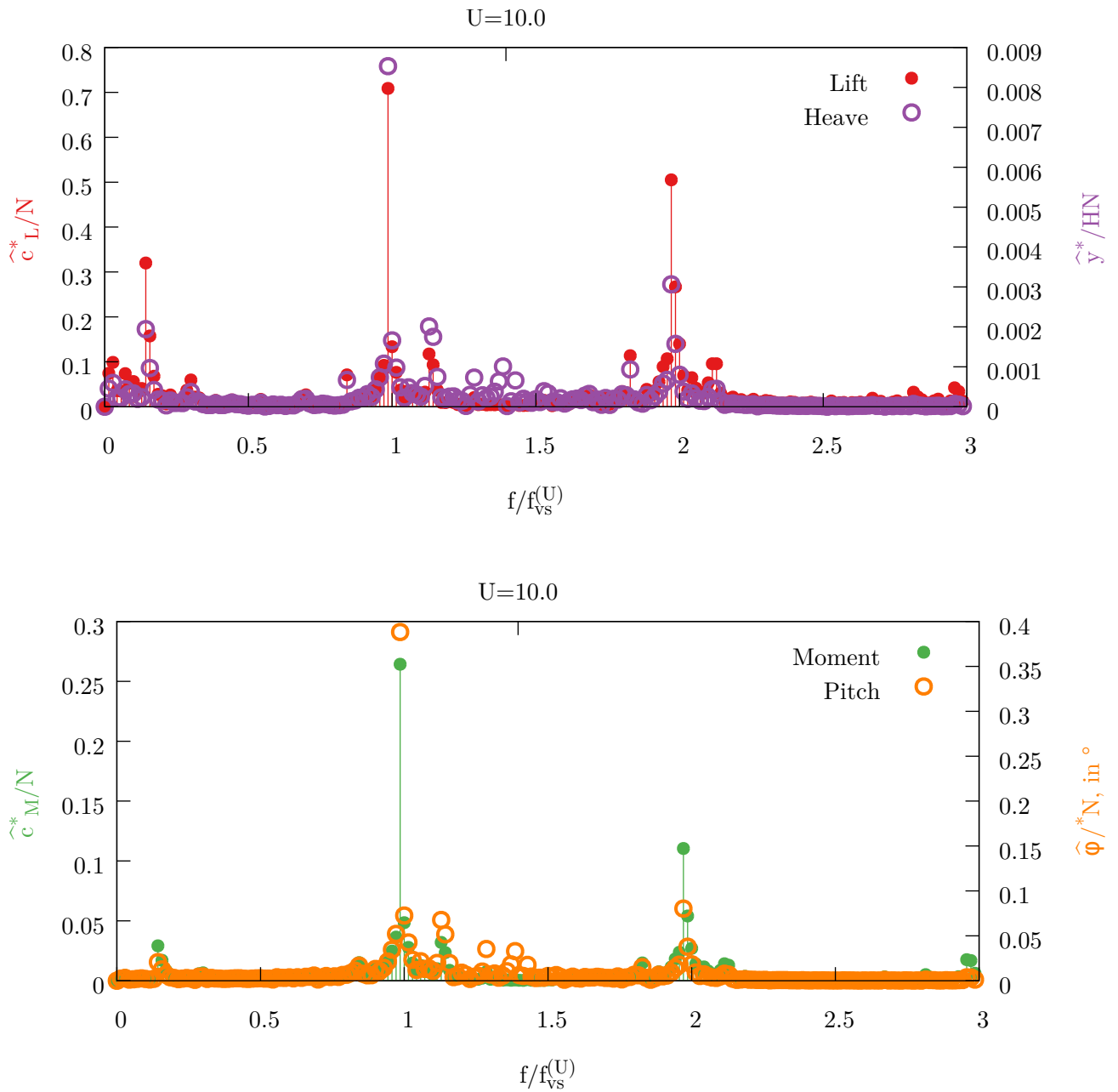
Spectra: 2DoF, $U^* = 10.0$, R-flow pattern

Figure A.24.: Frequency spectra of the heave y , the lift coefficient c_L , the pitch φ and the moment coefficient c_M at $U^* = 10.0$. Simulation at $\text{Re} = 2.45 \cdot 10^5$ under the R-flow pattern.

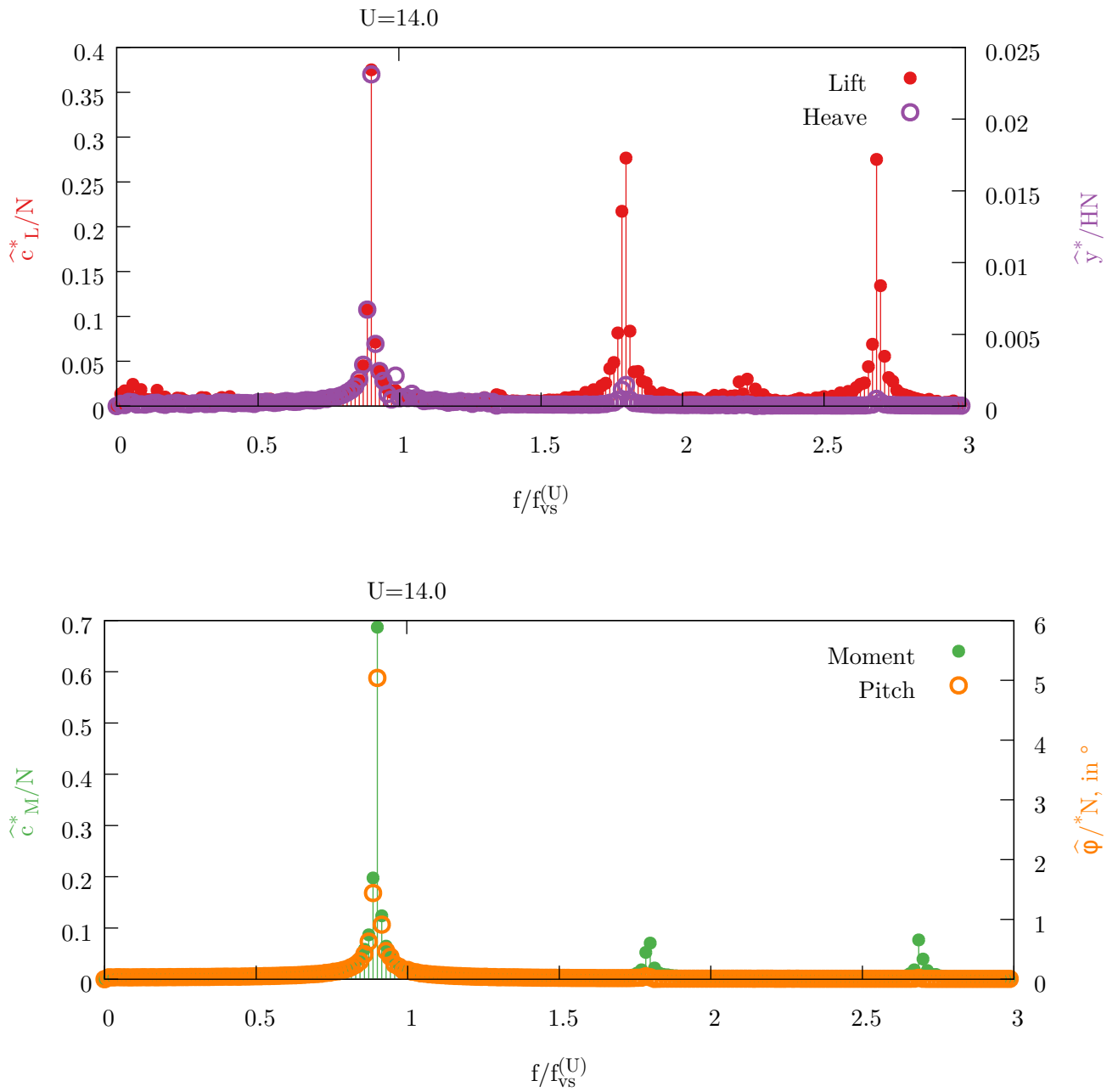
Spectra: 2DoF, $U^* = 14.0$, R-flow pattern

Figure A.25.: Frequency spectra of the heave y , the lift coefficient c_L , the pitch φ and the moment coefficient c_M at $U^* = 14.0$. Simulation at $\text{Re} = 2.45 \cdot 10^5$ under the R-flow pattern.

B. Rigid body solver

```
#define VERSION "0.2.0-15.0"

#include "udf.h"
/* #include "ui-helper-functions.h" */

#include "stdbool.h"
#include "stdio.h"
#include "stdlib.h"
#include "dlfcn.h"
#include "string.h"
#include "unistd.h"
#include "pthread.h"
#include "math.h"

/* Debug */
#include "sys/types.h"

/* -----
   -- Function Prototypes
   ----- */
void *solve_motion( void *arg );
void _global_init();
#if RP_HOST
void rk4part( double*, double*, double, double, double );
#endif
#if RP_NODE
void calc_forces();
#endif

void read_rp_real( double*, char* );
void read_rp_int( int*, char* );

/* -----
   -- Global variable declarations
   ----- */
/* grid constants */
double r1, r2;

/* mode selection */
int mode[] = {1, 1, 1, 1};
```



```

/* host and node global variable declarations */
bool state, mutex_initialized = false;
int rk4done, nZones=2;
int zone_id=0;
double z_0[4], z_1[4];
pthread_mutex_t mutex;
/* Debug */
/* pid_t pid; */

/* aerodynamic forces */
double l1, d1, m1;

/* node global variable declarations */
#if RP_NODE
#endif

/* host global variable declarations */
#if RP_HOST

double delta_t;
double lm1, dm1, mm1, l0, d0, m0;

/* Parameters, set by initializer */
double k, c, m, kT, cT, IT;

int extrap_order;
int do_rblog=0;
FILE *rblog;

char *rp_mode, *logfile_name, rp_buffer[16];

double y_accel=0, phi_accel=0;

/* external library (forced motion) vars */
void *fmotion_handle;
void (*fmotion_function)(double, int, double*, double*)=NULL;
void (*fmotion_default_rotation)(double, double, int, double, int, →
    --> double*, double*)=NULL;

/* external library (forced motion) parameters */
double fmotion_default_rotation_phi1=0.0, →
    --> fmotion_default_rotation_phi2=0.0;
int fmotion_default_rotation_tsteps=1;

#endif

/* -----

```

```

    -- Global initialization
    _____ */
DEFINE_EXECUTE_AFTER_DATA(global_init , libname) {
    _global_init();
}

void _global_init() {

#ifdef RP_HOST
    int librb_initstate=0;

    char *fmotion_error=NULL, fmotion_libname[256], fmotion_funcname[256],
        *fname_sep, fmotion_libpath[256];
#endif

#ifdef RP_HOST
    Message("----_librigidbody:_This_is_is_librigidbody_version_%s\n", →
        --> VERSION);
#endif

    if (!mutex_initialized) {
        pthread_mutex_init(&mutex, NULL);
        mutex_initialized =true;
    }

    rk4done = 0;
    state = false;

#ifdef RP_HOST
    /* set safe default values */
    lm1 = 0; dm1 = 0; mml = 0;
    l0 = 0; d0 = 0; m0 = 0;
    l1 = 0; d1 = 0; m1 = 0;
    z_0[0] = 0; z_0[1] = 0; z_0[2] = 0; z_0[3] = 0;
    z_1[0] = 0; z_1[1] = 0; z_1[2] = 0; z_1[3] = 0;

    /* load parameters */
    read_rp_real(&k, "rigidbody/k");
    read_rp_real(&c, "rigidbody/c");
    read_rp_real(&m, "rigidbody/m");
    read_rp_real(&kT, "rigidbody/kt");
    read_rp_real(&cT, "rigidbody/ct");
    read_rp_real(&IT, "rigidbody/it");

    read_rp_real(&lm1, "rigidbody/lm1");
    read_rp_real(&dm1, "rigidbody/dm1");
    read_rp_real(&mml, "rigidbody/mml");
    read_rp_int(&zone_id, "rigidbody/zone_id");

    /* recover rigid body state */
    read_rp_real(&z_0[0], "rigidbody/z0_0");

```

```

read_rp_real(&z_0[1], "rigidbody/z0_1");
read_rp_real(&z_0[2], "rigidbody/z0_2");
read_rp_real(&z_0[3], "rigidbody/z0_3");

/* read grid constants */
read_rp_real(&r1, "rigidbody/grid/r1");
read_rp_real(&r2, "rigidbody/grid/r2");

memcpy(z_1, z_0, 4*sizeof(double));

read_rp_int(&do_rblog, "rigidbody/log");
logfilename = RP_Get_String("rigidbody/logfilename");

read_rp_int(&extrap_order, "rigidbody/extrap_order");

rp_mode = RP_Get_String("rigidbody/mode");
sprintf(rp_buffer, "%.7s", rp_mode);
if (strcmp("heave", rp_mode)==0) {
    Message("——_librigidbody:_Mode_"heave_"_selected\n");
    mode[2] = 0; mode[3] = 0;
}
else if (strcmp("pitch", rp_mode)==0) {
    mode[0] = 0; mode[1] = 0;
    Message("——_librigidbody:_Mode_"pitch_"_selected\n");
}
else if (strcmp("forced-", rp_buffer)==0) {
    mode[1]=0; mode[3]=0;
    Message("——_librigidbody:_Mode_"forced_"_selected\n");

    fname_sep = strchr(rp_mode, (int) '-');
    *fname_sep='\0'; /* <Pfusich> */

    strcpy(fmotion_libname, &rp_mode[7]);
    fmotion_libpath[0]='\0';
    strcat(fmotion_libpath, "./librigidbody/forced-motion/");
    strcat(fmotion_libpath, fmotion_libname);
    strcat(fmotion_libpath, ".so");
    strcpy(fmotion_funcname, fname_sep+sizeof(char));

    *fname_sep='-'; /* </Pfusich> */
    Message("——_librigidbody:_Using_function_"%s_"_in_library_→
        --> "%s\".\n", fmotion_funcname, fmotion_libpath);

/* open external library */
fmotion_handle = dlopen(fmotion_libpath, RTLD_NOW);

if (!fmotion_handle){
    Message("——_librigidbody:_Could_not_open_forced-motion_→
        --> library\n");
    librb_initstate++;
}

```

```

dlerror();

/* set forced-motion function pointer */
/* Initialize default forced-motion functions*/
if (strcmp(fmotion_libname, "default")==0) {

    if (strcmp(fmotion_funcname, "rotation")==0) {
        fmotion_default_rotation=dlsym(fmotion_handle, fmotion_funcname);
        if (RP_Variable_Exists_P("rigidbody/forced-motion/tsteps"))
            fmotion_default_rotation_tsteps = →
                --> RP_Get_Integer("rigidbody/forced-motion/tsteps");
        else {
            Message("——librigidbody: The forced motion parameter →
                --> 'tsteps' for the function 'rotation' is missing\n");
            librb_initstate++;
        }

        if (RP_Variable_Exists_P("rigidbody/forced-motion/phi1"))
            fmotion_default_rotation_phi1 = →
                --> RP_Get_Real("rigidbody/forced-motion/phi1");
        else {
            Message("——librigidbody: The forced motion parameter →
                --> 'phi1' for the function 'rotation' is missing\n");
            librb_initstate++;
        }

        if (RP_Variable_Exists_P("rigidbody/forced-motion/phi2"))
            fmotion_default_rotation_phi2 = →
                --> RP_Get_Real("rigidbody/forced-motion/phi2");
        else {
            Message("——librigidbody: The forced motion parameter →
                --> 'phi2' for the function 'rotation' is missing\n");
            librb_initstate++;
        }

        Message("——librigidbody: Forced rotation from →
            --> %.3fdeg during the first %i steps will be carried out.\n",
                fmotion_default_rotation_phi1,
                fmotion_default_rotation_phi2,
                fmotion_default_rotation_tsteps);

    }
    else
        Message("——librigidbody: The forced motion function →
            --> %s is not part of the 'default' library\n", fmotion_funcname);
}
else
    fmotion_function = dlsym(fmotion_handle, fmotion_funcname);

```

```

    if ((fmotion_error=dllerror()) != NULL) {
        Message("----librigidbody: Could not open forced-motion->
            --> function\n");
        librb_initstate++;
    }
}
else {
    Message("----librigidbody: Fallback mode \"2 dof/flutter\"->
        --> selected\n");
}

#endif

host_to_node_int_1(zone_id);
host_to_node_real(z_0, 4);
host_to_node_real(z_1, 4);
host_to_node_real_2(r1, r2);

/* compute current forces */
#if RP_NODE
    calc_forces();
#endif
node_to_host_real_3(l1, d1, m1);

#if RP_HOST
    l0 = l1; d0 = d1; m0 = m1;
#endif

#if RP_HOST
    Message("----librigidbody: Global init complete\n");

    if (librb_initstate) {
        Message("----librigidbody: There were errors.\n");
    }
#endif

}

/* -----
   -- Grid motion udf with rk4 solver
   ----- */
DEFINE_GRID_MOTION(rigid_inner, domain, dt, time, dtime)
{
    /* node local variables */
    #if RP_NODE
        Thread *tf = DT_THREAD(dt);
    #endif

```

```

double NV_VEC(dx) , NV_VEC(x) , NV_VEC(x_o) ;
double phi , y ;
face_t f ;
Node *v ;
int n ;
#endif

/* node and host local variables */
pthread_t pt ;

/* host local variables */

#if RP_NODE
SET_DEFORMING_THREAD_FLAG(THREAD_T0(tf)) ;
#endif

pthread_create( &pt , NULL , solve_motion , NULL) ;
pthread_join(pt , NULL) ;

/* set new phi */
#if RP_NODE
y = z_1[0] ;
phi = z_1[2] ;

begin_f_loop(f , tf)
{
    f_node_loop(f , tf , n)
    {
        v = F_NODE(f , tf , n) ;
        NV_V(x , = , NODE_COORD(v)) ;

        if (NODE_POS_NEED_UPDATE (v))
        {
            /* recover original node positions */
            x_o[0] = N_UDMI(v,0) ;
            x_o[1] = N_UDMI(v,1) ;

            /* new coord deltas */
            dx[0] = cos(phi)*x_o[0] - sin(phi)*x_o[1] ;
            dx[1] = sin(phi)*x_o[0] + cos(phi)*x_o[1] + y ;

            /* update node coords */
            NV_V(NODE_COORD(v) , = , dx) ;
            NODE_POS_UPDATED(v) ;
        }
    }
}
end_f_loop(f , tf) ;

#endif

```

```

}

DEFINE_GRID_MOTION(deforming , domain , dt , time , dtime)
{
  /* node and host local variables */
  pthread_t pt;

  /* node local variables */
#ifdef RP_NODE
  Thread *tf = DT_THREAD(dt);
  double NV_VEC(dx) , NV_VEC(x) , NV_VEC(x_o);
  double phi , y;
  double R , s;
  face_t f;
  Node *v;
  int n;
#endif

  /* solve equations of motion */
  pthread_create(&pt, NULL, solve_motion , NULL);
  pthread_join(pt, NULL);

#ifdef RP_NODE
  /* set new phi */
  y = z_1[0];
  phi = z_1[2];

  SET_DEFORMING_THREAD_FLAG(THREAD_T0(tf));

  begin_f_loop(f, tf)
  {
    f_node_loop(f, tf, n)
    {
      v = F_NODE(f, tf, n);
      NV_V(x, =, NODE_COORD(v));

      if (NODE_POS_NEED_UPDATE (v))
      {
        /* recover original node positions */
        x_o[0] = N_UDMI(v,0);
        x_o[1] = N_UDMI(v,1);

        /* calculate radius of cell and weighting factor */
        R = NV_MAG(x_o);
        if (R < (r1+1.0e-5))
          s = 1.0;
        else if (R > (r2-1.0e-5))
          s = 0.0;
        else
          s = (r2-R)/(r2-r1);
      }
    }
  }
#endif
}

```

```

        /* new coord deltas */
        dx[0] = cos(phi)*x_o[0] - sin(phi)*x_o[1];
        dx[1] = sin(phi)*x_o[0] + cos(phi)*x_o[1] + y;

        dx[0] = s*dx[0] + (1-s)*x_o[0];
        dx[1] = s*dx[1] + (1-s)*x_o[1];

        /* update node coords */
        NV_V(NODE_COORD(v), =, dx);
        NODE_POS_UPDATED(v);
    }
}

end_f_loop(f, tf);

#endif
}

/*-----
   -- End of timestep actions
   -----*/
DEFINE_EXECUTE_AT_END(end_of_timestep) {
    state = false;
    rk4done = 0;
    /* recompute and shift aerodynamic forces */
#ifdef RP_NODE
    calc_forces();
#endif
    node_to_host_real_3(l1, d1, m1);

#ifdef RP_HOST
    lm1 = l0; dm1 = d0; mml = m0;
    l0 = l1; d0 = d1; m0 = m1;
#endif

    /* shift rigid body state */
    memcpy(z_0, z_1, 4*sizeof(double));

    /* log state */
#ifdef RP_HOST
    if (do_rblog==1) {
        rblog = fopen(logfilename, "a");
        fprintf(rblog, "%.8g_%.8g_%.8g_%.8g_%.8g_%.8g_%.8g\n", CURRENT_TIME, →
            --> l0, d0, m0, z_0[0], z_0[1], y_accel, z_0[2], z_0[3], →
            --> phi_accel);
    }
#endif
}

```



```

    fclose(rblog);
}
#endif

}

/* -----
   -- Solve the equations of motion (helper function)
   ----- */
void *solve_motion( void *arg ) {

    pthread_mutex_lock(&mutex);

    if (rk4done>0) {
        /* Debug */
        /* #if RP_HOST */
        /*     pid = getpid(); */
        /*     Message("pid: %d, FAST exit\n", pid); */
        /* #endif */
        ++rk4done;
        if (rk4done==nZones)
            rk4done=0;

        pthread_mutex_unlock(&mutex);
        return NULL;
    }

    /* Host local variables */
#ifdef RP_HOST
    /* Runge kutta helper variables */
    double l_05, m_05, d_05;
    double zdot_h[4], z_h[4];
    int i;
#endif

    /* Node local variables */
#ifdef RP_NODE
#endif

    /* update values for aerodynamic forces if we need to */
    /* change this until xxx when calc_forces is reimplemented*/
#ifdef RP_NODE
    if (state) {
        calc_forces(); /* sets m1, l1, d1 ONLY on the compute nodes! */
    }
    else
        state = true;
#endif
}

```

```

/* make m1, l1, d1 available on the host */
node_to_host_real_3(m1, l1, d1);

#if RP_HOST

/* track 1: solve motion (RK4) */

if ( !(fmotion_function || fmotion_default_rotation) ) {
  /* get aerodynamic forces for the end of the current timestep
     (estimation, only necessary for the first execution in a →
     → timestep) */
  if (!state) {
    delta_t = CURRENT_TIMESTEP;
    /*FIXME: When the simulation is restarted with a different →
     → time-step the extrapolation is carried out wrongly. Only →
     → relevant without implicit update, though.*/
    l1 = l0 + ((double) extrap_order)*(l0-lm1); /* cast necessary? */
    d1 = d0 + ((double) extrap_order)*(d0-dm1);
    m1 = m0 + ((double) extrap_order)*(m0-mm1);
    state = true;
  }
  /* else { */
  /*   double interr_y = m*y_accel + k*z_1[0] - l1; */
  /*   double interr_phi = IT*phi_accel + kT*z_1[2] - m1 - d1*z_1[0]; →
     → */

  /*   Message("\nPrevious integration error, y: %g, phi: →
     → %g\n", interr_y, interr_phi); */
  /* } */
  /* xxx */

  /* prepare runge kutta helper variables */
  l_05 = 0.5*(l0+l1);
  d_05 = 0.5*(d0+d1);
  m_05 = 0.5*(m0+m1);

  /* runge kutta 4 solution */
  /* stage 1 */
  rk4part(zdot_h, z_0, l0, d0, m0);
  for(i=0; i<4; ++i) {
    z_h[i] = z_0[i]+delta_t/2*zdot_h[i];
    z_1[i] = zdot_h[i];
  }

  /*stage 2 */
  rk4part(zdot_h, z_h, l_05, d_05, m_05);
  for(i=0; i<4; ++i) {
    z_h[i] = z_0[i]+delta_t/2*zdot_h[i];
    z_1[i] += 2*zdot_h[i];
  }
}

```

```

}

/* stage 3 */
rk4part(zdot_h, z_h, l_05, d_05, m_05);
for(i=0; i<4; ++i) {
    z_h[i] = z_0[i]+delta_t*zdot_h[i];
    z_1[i] += 2*zdot_h[i];
}

/*stage 4 */
rk4part(zdot_h, z_h, l1, d1, m1);
for(i=0; i<4; ++i) {
    z_1[i] += zdot_h[i];
    z_1[i] /= 6;
}

y_accel=mode[0]*z_1[1];
phi_accel=mode[2]*z_1[3];

for(i=0; i<4; ++i) {
    z_1[i] *= delta_t;
    z_1[i] += z_0[i];
    z_1[i] *= mode[i];
}
}
/* track 2: motion prescribed by external library */
else {
    if (fmotion_function)
        (*fmotion_function)(CURRENT_TIME, N_TIME, &z_1[0], &z_1[2]);
    else if (fmotion_default_rotation)
        (*fmotion_default_rotation)(fmotion_default_rotation_phi1,
                                     fmotion_default_rotation_phi2,
                                     fmotion_default_rotation_tsteps,
                                     CURRENT_TIME, N_TIME, &z_1[0], →
                                     →→ &z_1[2]);
}

#endif

/* unlock mutex before synchronization */
++rk4done;
pthread_mutex_unlock(&mutex);

host_to_node_real(z_1, 4);

#if RP_HOST
Message(" lift:␣%.16g,␣drag:␣%.16g,␣moment:␣%.16g\ndisp:␣%.16g,␣→
→→ lin_vel:␣%.16g\nangle:␣%.16g,␣ang_vel:␣%.16g\n", l1, d1, m1, →
→→ z_1[0], z_1[1], z_1[2]*180/3.141, z_1[3]*180/3.141);

/* Debug */

```

```

    /* Message ("Timestep: %d, Iteration: %d", N_TIME, N_ITER); */
#endif

    /* Debug */
    /* pid = getpid(); */
    /* Message("pid: %d, NORMAL exit\n", pid); */

    return NULL;
}

/* -----
   -- Runge Kutta 4 helper function
   ----- */
#if RP_HOST
void rk4part(double* zdot_h, double* z_0, double l, double d, double →
    --> mt) {
    zdot_h[0] = z_0[1];
    zdot_h[1] = -k/m*z_0[0] - c/m*z_0[1] + l/m;
    zdot_h[2] = z_0[3];
    zdot_h[3] = d*z_0[0]/IT - kT/IT*z_0[2] - cT/IT*z_0[3] + mt/IT;
}
#endif

#if RP_NODE
/* This could be substituted with a function that updates the global →
   --> forces for all processes if necessary */
void calc_forces() {
    Domain *dom;
    Thread* tf;
    int domain_id=1;
    face_t f;
    double NV_VEC(fArea), NV_VEC(fNormal), NV_VEC(fCentroid), →
        --> NV_VEC(fTangential);
    double f_p, tau[2];

    l1 = 0;
    d1 = 0;
    m1 = 0;

    dom = Get_Domain(domain_id);
    tf = Lookup_Thread(dom, zone_id);

    begin_f_loop(f, tf) {
        if (PRINCIPAL_FACE_P(f, tf)) {
            f_p = F_P(f, tf);
            tau[0] = F_STORAGE_R_N3V(f, tf, SV_WALL_SHEAR)[0]; /* _N3V is →
                --> necessary here, NV_V & _NV didn't work */

```

```

tau [1] = F_STORAGE_R_N3V(f, tf, SV_WALL_SHEAR) [1];

F_AREA(fArea, f, tf);
NV_V(fNormal, =, fArea);
NV_S(fNormal, /=, NV_MAG(fArea));
fTangential[0] = -fNormal [1];
fTangential[1] = fNormal [0];

F_CENTROID(fCentroid, f, tf);

/* Careful, sign conventions from Fluent apply */
/* Output checked against force reports */
/* Moment about the point (0,0) */
m1 -= (NV_DOT(fTangential, fCentroid)) * (NV_MAG(fArea)) * f_p + →
      --> (NV_DOT(fNormal, fCentroid)) * (NV_DOT(fTangential, tau));
l1 += NV_MAG(fArea) * f_p * fNormal [1] - tau [1];
d1 += NV_MAG(fArea) * f_p * fNormal [0] - tau [0];
}
} end_f_loop(f, tf);

m1 = PRF_GRSUM1(m1);
l1 = PRF_GRSUM1(l1);
d1 = PRF_GRSUM1(d1);
}
#endif

/* -----
   — Auxiliary and Debug functions
   ----- */
DEFINE_ON_DEMAND(displayparams) {
    pid_t pid = getpid();

    Message("pid: %d, zone_id: %d\n", pid, zone_id);
    Message("pid: %d, r1: %g\n", pid, r1);
    Message("pid: %d, r2: %g\n", pid, r2);
    Message("pid: %d, z0_0: %g\n", pid, z_0[0]);
    Message("pid: %d, z0_1: %g\n", pid, z_0[1]);
    Message("pid: %d, z0_2: %g\n", pid, z_0[2]);
    Message("pid: %d, z0_3: %g\n", pid, z_0[3]);

#ifdef RP_HOST
    Message("Host: pid: %d, lm1: %g\n", pid, lm1);
    Message("Host: pid: %d, dm1: %g\n", pid, dm1);
    Message("Host: pid: %d, mml: %g\n", pid, mml);
    Message("Host: pid: %d, l0: %g\n", pid, l0);
    Message("Host: pid: %d, d0: %g\n", pid, d0);
    Message("Host: pid: %d, m0: %g\n", pid, m0);
    Message("Host: pid: %d, k: %g\n", pid, k);
#endif
}

```

```

Message( " Host: pid: %d, c: %g\n", pid, c);
Message( " Host: pid: %d, m: %g\n", pid, m);
Message( " Host: pid: %d, kT: %g\n", pid, kT);
Message( " Host: pid: %d, cT: %g\n", pid, cT);
Message( " Host: pid: %d, IT: %g\n", pid, IT);
Message( " Host: pid: %d, log: %d\n", pid, do_rblog);
Message( " Host: pid: %d, extrap_order: %d\n", pid, extrap_order);
Message( " Host: pid: %d, zone_id: %d\n", pid, zone_id);
Message( " Host: pid: %d, logfilename: %s\n", pid, logfilename);
Message( " Host: pid: %d, rp_mode: %s\n", pid, rp_mode);
Message( " Host: pid: %d, mode: [%d,%d,%d,%d]\n", pid, mode[0], →
    --> mode[1], mode[2], mode[3]);
#endif
}

DEFINE_ON_DEMAND(save_prev_forces) {

#ifdef RP_NODE
    calc_forces();
#endif
    node_to_host_real_3(l1, d1, m1);

#ifdef RP_HOST
    RP_Set_Real( " rigidbody/lm1", l1);
    RP_Set_Real( " rigidbody/dm1", d1);
    RP_Set_Real( " rigidbody/mml", m1);

    Message( " Previous timestep forces set\n");
    Message( " Run one more timestep and save data to create proper →
        --> initialized case\n");
#endif

}

DEFINE_ON_DEMAND(save_rbstate) {
#ifdef RP_HOST
    RP_Set_Real( " rigidbody/lm1", lm1);
    RP_Set_Real( " rigidbody/dm1", dm1);
    RP_Set_Real( " rigidbody/mml", mml);

    RP_Set_Real( " rigidbody/z0_0", z_0[0]);
    RP_Set_Real( " rigidbody/z0_1", z_0[1]);
    RP_Set_Real( " rigidbody/z0_2", z_0[2]);
    RP_Set_Real( " rigidbody/z0_3", z_0[3]);

    Message( " Rigid body state saved, save case and data now.\n");
#endif
}

DEFINE_ON_DEMAND(manual_global_init) {
    _global_init();
}

```

```

}

DEFINE_ON_DEMAND(show_forces) {
#ifdef RP_NODE
    calc_forces();
#endif

    node_to_host_real_3(l1, d1, m1);

#ifdef RP_HOST
    Message("Lift: %g, Drag: %g, Moment: %g\n", l1, d1, m1);
#endif
}

DEFINE_ON_DEMAND(initialize_grid) {
#ifdef RP_NODE

    Domain *dom = Get_Domain(1);
    Thread *t;
    cell_t c;
    int n;
    Node *v;

    thread_loop_c(t, dom) {
        begin_c_loop(c, t) {
            c_node_loop(c, t, n) {
                v = C_NODE(c, t, n);
                N_UDMI(v, 0) = NODE_X(v);
                N_UDMI(v, 1) = NODE_Y(v);
            }
        } end_c_loop(c, t);
    }
#endif

#ifdef RP_HOST
    Message("User-defined memory locations 0 and 1 initialized with →
        → original x and y values.\n");
#endif
}

/* -----
   -- Helper functions
   ----- */
void read_rp_real(double *res, char *name) {
    /* variable_exists doesn't know my defined variables */
    /* if (RP_Variable_Exists_P(name)) */
#ifdef RP_HOST
    *res = RP_Get_Real(name);
#endif
    /* #if RP_NODE */
    /* else */

```

```

/*      Message("Node: Warning, variable %s undefined\n", name); */
/* #endif */
/* #if RP_HOST */
/*     else */
/*      Message("Host: Warning, variable %s undefined\n", name); */
/* #endif */
}

void read_rp_int(int *res, char *name) {
    /* if (RP_Variable_Exists_P(name)) */
    #if RP_HOST
        *res = RP_Get_Integer(name);
    #endif
    /* #if RP_NODE */
    /*     else */
    /*      Message("Node: Warning, variable %s undefined\n", name); */
    /* #endif */
    /* #if RP_HOST */
    /*     else */
    /*      Message("Host: Warning, variable %s undefined\n", name); */
    /* #endif */
}

/*-----
   -- Exit actions
   -----*/

DEFINE_EXECUTE_AT_EXIT(cleanup) {
    #if RP_HOST
        if (fmotion_handle)
            dlclose(fmotion_handle);

        Message("librigidbody: Cleanup complete, exiting.\n");
    #endif
}

```


Bibliography

- [1] *ANSYS Fluent Theory Guide, version 14.5*. 2012.
- [2] *ANSYS Fluent User's Guide, version 14.5*. 2012.
- [3] G. Ashcroft and X. Zhang. "Vortical structures over rectangular cavities at low speed." In: *Physics of Fluids (1994-present)* 17.1 (2005), p. 015104. (Visited on 05/29/2015).
- [4] X. Bai and W. Qin. "Using vortex strength wake oscillator in modelling of vortex induced vibrations in two degrees of freedom." In: *European Journal of Mechanics - B/Fluids* 48 (2014), pp. 165–173.
- [5] Y. Bai, D. Sun, and J. Lin. "Three dimensional numerical simulations of long-span bridge aerodynamics, using block-iterative coupling and DES." In: *Computers & Fluids* 39.9 (2010), pp. 1549–1561.
- [6] BARC. URL: <http://www.aniv-iawe.org/barc/> (visited on 02/03/2015).
- [7] G. Bartoli and M. Righi. "Flutter mechanism for rectangular prisms in smooth and turbulent flow." In: *Journal of Wind Engineering and Industrial Aerodynamics* 94.5 (2006), pp. 275–291.
- [8] K. Y. Billah and R. H. Scanlan. "Resonance, Tacoma Narrows bridge failure, and undergraduate physics textbooks." In: *American Journal of Physics* 59.2 (1991), pp. 118–124. (Visited on 05/21/2015).
- [9] R. E. D. Bishop and A. Y. Hassan. "The Lift and Drag Forces on a Circular Cylinder Oscillating in a Flowing Fluid." In: *Proceedings of the Royal Society of London A: Mathematical, Physical and Engineering Sciences* 277.1368 (1964), pp. 51–75.
- [10] R. L. Bisplinghoff. *Aeroelasticity*. Courier Corporation, 1996. 886 pp.
- [11] R. D. Blevins. *Flow-induced vibration*. Van Nostrand Reinhold, 1990. 474 pp.
- [12] L. Bruno, N. Coste, and D. Fransos. "Simulated flow around a rectangular 5:1 cylinder: Spanwise discretisation effects and emerging flow features." In: *Journal of Wind Engineering and Industrial Aerodynamics* 104–106 (2012), pp. 203–215.
- [13] L. Bruno, M. V. Salvetti, and F. Ricciardelli. "Benchmark on the Aerodynamics of a Rectangular 5:1 Cylinder: An overview after the first four years of activity." In: *Journal of Wind Engineering and Industrial Aerodynamics* 126 (2014), pp. 87–106.
- [14] L. Bruno et al. "3D flow around a rectangular cylinder: A computational study." In: *Journal of Wind Engineering and Industrial Aerodynamics* 98.6 (2010), pp. 263–276.
- [15] F. Brusiani et al. "On the evaluation of bridge deck flutter derivatives using RANS turbulence models." In: *Journal of Wind Engineering and Industrial Aerodynamics* 119 (2013), pp. 39–47. (Visited on 02/02/2015).
- [16] L. Caracoglia and N. P. Jones. "Time domain vs. frequency domain characterization of aeroelastic forces for bridge deck sections." In: *Journal of Wind Engineering and Industrial Aerodynamics* 91.3 (2003), pp. 371–402.
- [17] L. Caracoglia et al. "Comparative and sensitivity study of flutter derivatives of selected bridge deck sections, Part 2: Implications on the aerodynamic stability of long-span bridges." In: *Engineering Structures* 31.9 (2009), pp. 2194–2202.
- [18] P. Causin, J. F. Gerbeau, and F. Nobile. "Added-mass effect in the design of partitioned algorithms for fluid–structure problems." In: *Computer Methods in Applied Mechanics and Engineering* 194.42 (2005), pp. 4506–4527.
- [19] J. E. Cermak. "Aerodynamics of Buildings." In: *Annual Review of Fluid Mechanics* 8.1 (1976), pp. 75–106.

- [20] X. Chen. “Improved Understanding of Bimodal Coupled Bridge Flutter Based on Closed-Form Solutions.” In: *Journal of Structural Engineering* 133.1 (2007), pp. 22–31.
- [21] X. Chen and A. Kareem. “Revisiting Multimode Coupled Bridge Flutter: Some New Insights.” In: *Journal of Engineering Mechanics* 132.10 (2006), pp. 1115–1123.
- [22] X. Chen, A. Kareem, and M. Matsumoto. “Multimode coupled flutter and buffeting analysis of long span bridges.” In: *Journal of Wind Engineering and Industrial Aerodynamics* 89.7 (2001), pp. 649–664.
- [23] Z. Chen et al. “Wind-Induced Self-Excited Loads on Bridges.” In: *Journal of Structural Engineering* 131.12 (2005), pp. 1783–1793.
- [24] *Climatic Wind Engineering Laboratory / Centre of Excellence Telč*. URL: <http://cet.arcchip.cz/wind-laboratory-en> (visited on 02/18/2015).
- [25] S. Deniz and T. Staubli. “Oscillating rectangular and octagonal profiles: interaction of leading- and trailing-edge vortex formation.” In: *Journal of Fluids and Structures* 11.1 (1997), pp. 3–31.
- [26] G. Diana et al. “Aerodynamic instability of a bridge deck section model: Linear and nonlinear approach to force modeling.” In: *Journal of Wind Engineering and Industrial Aerodynamics* 98.6 (2010), pp. 363–374.
- [27] P. G. Drazin. *Introduction to Hydrodynamic Stability*. Cambridge University Press, 2002. 284 pp.
- [28] Y. Egorov et al. “The Scale-Adaptive Simulation Method for Unsteady Turbulent Flow Predictions. Part 2: Application to Complex Flows.” In: *Flow, Turbulence and Combustion* 85.1 (2010), pp. 139–165.
- [29] M. L. Facchinetti, E. de Langre, and F. Biolley. “Coupling of structure and wake oscillators in vortex-induced vibrations.” In: *Journal of Fluids and Structures* 19.2 (2004), pp. 123–140.
- [30] M. L. Facchinetti, E. de Langre, and F. Biolley. “Vortex-induced travelling waves along a cable.” In: *European Journal of Mechanics - B/Fluids* 23.1 (2004), pp. 199–208.
- [31] M. Falco, A. Curami, and A. Zasso. “Nonlinear effects in sectional model aeroelastic parameters identification.” In: *Journal of Wind Engineering and Industrial Aerodynamics* 42.1 (1992), pp. 1321–1332.
- [32] J. Fröhlich and D. von Terzi. “Hybrid LES/RANS methods for the simulation of turbulent flows.” In: *Progress in Aerospace Sciences* 44.5 (2008), pp. 349–377.
- [33] Y. J. Ge and H. F. Xiang. “Computational models and methods for aerodynamic flutter of long-span bridges.” In: *Journal of Wind Engineering and Industrial Aerodynamics* 96.10 (2008), pp. 1912–1924.
- [34] I. Goswami, R. Scanlan, and N. Jones. “Vortex-Induced Vibration of Circular Cylinders. I: Experimental Data.” In: *Journal of Engineering Mechanics* 119.11 (1993), pp. 2270–2287.
- [35] D. Green and W. G. Unruh. “The failure of the Tacoma Bridge: A physical model.” In: *American Journal of Physics* 74.8 (2006), pp. 706–716. (Visited on 06/05/2015).
- [36] M. S. Gritskevich et al. “Development of DDES and IDDES Formulations for the $k - \omega$ Shear Stress Transport Model.” In: *Flow, Turbulence and Combustion* 88.3 (2012), pp. 431–449.
- [37] R. T. Hartlen and I. G. Currie. “Lift-Oscillator Model of Vortex-Induced Vibration.” In: *Journal of the Engineering Mechanics Division* 96.5 (1970), pp. 577–591.
- [38] J. P. D. Hartog. “Transmission Line Vibration Due to Sleet.” In: *American Institute of Electrical Engineers, Transactions of the* 51.4 (1932), pp. 1074–1076.
- [39] *History of the Tacoma Narrows bridge*. URL: <http://www.lib.washington.edu/specialcollections/collections/exhibits/tnb> (visited on 05/20/2015).

- [40] D. H. Hodges and G. A. Pierce. *Introduction to Structural Dynamics and Aeroelasticity*. Cambridge: Cambridge University Press, 2011.
- [41] L. Huang et al. “Numerical simulation for aerodynamic derivatives of bridge deck.” In: *Simulation Modelling Practice and Theory* 17.4 (2009), pp. 719–729.
- [42] W. Kang and H. J. Sung. “Large-scale structures of turbulent flows over an open cavity.” In: *Journal of Fluids and Structures* 25.8 (2009), pp. 1318–1333. (Visited on 05/29/2015).
- [43] J. .-Y. Kim et al. “Comparison of near-wall treatment methods for high Reynolds number backward-facing step flow.” In: *International Journal of Computational Fluid Dynamics* 19.7 (2005), pp. 493–500.
- [44] M. Kiya and K. Sasaki. “Free-stream turbulence effects on a separation bubble.” In: *Journal of Wind Engineering and Industrial Aerodynamics* 14.1 (1983), pp. 375–386.
- [45] R. Král, S. Pospíšil, and J. Náprstek. “Experimental Set-Up for Advanced Aeroelastic Tests on Sectional Models.” In: *Experimental Techniques* (2013), n/a–n/a.
- [46] Y. Kubo and K. Hirata. “Aerodynamic responses and pressure function of shallow H-section cylinder.” In: *Journal of Wind Engineering and Industrial Aerodynamics* 33.1 (1990), pp. 123–130.
- [47] Y. Kubo, K. Hirata, and K. Mikawa. “Mechanism of aerodynamic vibrations of shallow bridge girder sections.” In: *Journal of Wind Engineering and Industrial Aerodynamics* 42.1 (1992), pp. 1297–1308.
- [48] T. Kumarasena, R. H. Scanlan, and F. Ehsan. “Recent observations in bridge deck aeroelasticity.” In: *Journal of Wind Engineering and Industrial Aerodynamics* 40.3 (1992), pp. 225–247.
- [49] S. Kuznetsov. (Head of the climatic wind tunnel at the CET). personal communication. 2015.
- [50] K. C. Kwok and W. H. Melbourne. “Freestream turbulence effects on galloping.” In: *ASCE J Eng Mech Div* 106.2 (1980), pp. 273–288.
- [51] E. de Langre. “Frequency lock-in is caused by coupled-mode flutter.” In: *Journal of Fluids and Structures* 22.6 (2006), pp. 783–791.
- [52] A. Larsen. “Aerodynamics of the Tacoma Narrows Bridge - 60 Years Later.” In: *Structural Engineering International* 10.4 (2000), pp. 243–248.
- [53] A. H. Lee, R. L. Campbell, and S. A. Hambric. “Coupled delayed-detached-eddy simulation and structural vibration of a self-oscillating cylinder due to vortex-shedding.” In: *Journal of Fluids and Structures* 48 (2014), pp. 216–234. (Visited on 02/03/2015).
- [54] B. E. Lee. “The effect of turbulence on the surface pressure field of a square prism.” In: *Journal of Fluid Mechanics* 69.2 (1975), pp. 263–282.
- [55] O. Lehmkuhl et al. “Unsteady forces on a circular cylinder at critical Reynolds numbers.” In: *Physics of Fluids* 26.12 (2014), pp. 125110.1–125110.22. (Visited on 02/06/2015).
- [56] S. C. Luo, Y. T. Chew, and Y. T. Ng. “Hysteresis phenomenon in the galloping oscillation of a square cylinder.” In: *Journal of Fluids and Structures* 18.1 (2003), pp. 103–118.
- [57] C. Mannini, A. M. Marra, and G. Bartoli. “VIV–galloping instability of rectangular cylinders: Review and new experiments.” In: *Journal of Wind Engineering and Industrial Aerodynamics* 132 (2014), pp. 109–124.
- [58] C. Mannini, A. Šoda, and G. Schewe. “Numerical investigation on the three-dimensional unsteady flow past a 5:1 rectangular cylinder.” In: *Journal of Wind Engineering and Industrial Aerodynamics* 99.4 (2011), pp. 469–482.

- [59] C. Mannini, A. Šoda, and G. Schewe. “Unsteady RANS modelling of flow past a rectangular cylinder: Investigation of Reynolds number effects.” In: *Computers & Fluids* 39.9 (2010), pp. 1609–1624.
- [60] C. Mannini et al. “Unsteady RANS simulations of flow around a bridge section.” In: *Journal of Wind Engineering and Industrial Aerodynamics* 98.12 (2010), pp. 742–753.
- [61] S. Manzoor, J. Khawar, and N. A. Sheikh. “Vortex-Induced Vibrations of a Square Cylinder with Damped Free-End Conditions.” In: *Advances in Mechanical Engineering* 2013 (2013), e204974.
- [62] A. M. Marra, C. Mannini, and G. Bartoli. “Van der Pol-type equation for modeling vortex-induced oscillations of bridge decks.” In: *Journal of Wind Engineering and Industrial Aerodynamics* 99.6 (2011), pp. 776–785.
- [63] M. Matsumoto et al. “Effects of aerodynamic interferences between heaving and torsional vibration of bridge decks: the case of Tacoma Narrows Bridge.” In: *Journal of Wind Engineering and Industrial Aerodynamics* 91.12 (2003), pp. 1547–1557.
- [64] M. Matsumoto et al. “Vortex-induced vibration and its effect on torsional flutter instability in the case of B/D=4 rectangular cylinder.” In: *Journal of Wind Engineering and Industrial Aerodynamics* 96.6 (2008), pp. 971–983.
- [65] W. H. Melbourne. “Turbulence and the leading edge phenomenon.” In: *Journal of Wind Engineering and Industrial Aerodynamics* 49.1 (1993), pp. 45–63.
- [66] F. R. Menter and Y. Egorov. “The Scale-Adaptive Simulation Method for Unsteady Turbulent Flow Predictions. Part 1: Theory and Model Description.” In: *Flow, Turbulence and Combustion* 85.1 (2010), pp. 113–138.
- [67] F. R. Menter, M. Kuntz, and R. Langtry. “Ten Years of Industrial Experience with the SST Turbulence Model.” In: *Proceedings of the Fourth International Symposium on Turbulence, Heat and Mass Transfer*. Antalya: Begell House Inc., 2003.
- [68] S. de Miranda et al. “Indicial functions and flutter derivatives: A generalized approach to the motion-related wind loads.” In: *Journal of Fluids and Structures* 42 (2013), pp. 466–487. (Visited on 02/02/2015).
- [69] S. de Miranda et al. “On the identification of flutter derivatives of bridge decks via RANS turbulence models: Benchmarking on rectangular prisms.” In: *Engineering Structures* 76 (2014), pp. 359–370. (Visited on 02/02/2015).
- [70] Y. Nakamura and T. Matsukawa. “Vortex excitation of rectangular cylinders with a long side normal to the flow.” In: *Journal of Fluid Mechanics* 180 (1987), pp. 171–191.
- [71] Y. Nakamura and T. Mizota. “Torsional flutter of rectangular prisms.” In: *ASCE J Eng Mech Div* 101.2 (1975), pp. 125–142.
- [72] Y. Nakamura and M. Nakashima. “Vortex excitation of prisms with elongated rectangular, H and [vertical, dash] cross-sections.” In: *Journal of Fluid Mechanics* 163 (1986), pp. 149–169.
- [73] E. Naudascher and Y. Wang. “Flow-Induced Vibrations of Prismatic Bodies and Grids of Prisms.” In: *Journal of Fluids and Structures* 7.4 (1993), pp. 341–373.
- [74] E. Naudascher and D. Rockwell. *Flow-Induced Vibrations: An Engineering Guide*. Courier Corporation, 2012. 434 pp.
- [75] F. Nieto et al. “Bridge deck flutter derivatives: Efficient numerical evaluation exploiting their interdependence.” In: *Journal of Wind Engineering and Industrial Aerodynamics* 136 (2015), pp. 138–150.
- [76] N. V. Nikitin et al. “An approach to wall modeling in large-eddy simulations.” In: *Physics of Fluids (1994-present)* 12.7 (2000), pp. 1629–1632.

- [77] C. Norberg. “Fluctuating lift on a circular cylinder: review and new measurements.” In: *Journal of Fluids and Structures* 17.1 (2003), pp. 57–96. (Visited on 02/03/2015).
- [78] R. H. M. Ogink and A. V. Metrikine. “A wake oscillator with frequency dependent coupling for the modeling of vortex-induced vibration.” In: *Journal of Sound and Vibration* 329.26 (2010), pp. 5452–5473.
- [79] M. P. Paidoussis. *Fluid-structure Interactions: Slender Structures and Axial Flow*. Academic Press, Incorporated, 1998. 590 pp.
- [80] M. P. Paidoussis. *Fluid-Structure Interactions*. Academic Press, 2003. 1034 pp.
- [81] M. P. Paidoussis. *Fluid-Structure Interactions: Cross-Flow-Induced Instabilities*. New York: Cambridge University Press, 2011. 414 pp.
- [82] G. V. Parkinson and J. D. Smith. “The Square Prism as an Aeroelastic Non-Linear Oscillator.” In: *The Quarterly Journal of Mechanics and Applied Mathematics* 17.2 (1964), pp. 225–239.
- [83] B. Pier and P. Huerre. “Nonlinear self-sustained structures and fronts in spatially developing wake flows.” In: *Journal of Fluid Mechanics* 435 (2001), pp. 145–174.
- [84] A. Roshko. “On the Wake and Drag of Bluff Bodies.” In: *Journal of the Aeronautical Sciences (Institute of the Aeronautical Sciences)* 22.2 (1955), pp. 124–132.
- [85] M. Saghafian et al. “Simulation of turbulent flows around a circular cylinder using nonlinear eddy-viscosity modelling: steady and oscillatory ambient flows.” In: *Journal of Fluids and Structures* 17.8 (2003), pp. 1213–1236. (Visited on 02/11/2015).
- [86] P. P. Sankar, N. P. Jones, and R. H. Scanlan. “System identification for estimation of flutter derivatives.” In: *Journal of Wind Engineering and Industrial Aerodynamics* 42.1 (1992), pp. 1243–1254.
- [87] P. P. Sankar et al. “Comparative and sensitivity study of flutter derivatives of selected bridge deck sections, Part 1: Analysis of inter-laboratory experimental data.” In: *Engineering Structures* 31.1 (2009), pp. 158–169.
- [88] A. Šarkić et al. “Bridge flutter derivatives based on computed, validated pressure fields.” In: *Journal of Wind Engineering and Industrial Aerodynamics* 104–106 (2012), pp. 141–151.
- [89] T. Sarpkaya. “A critical review of the intrinsic nature of vortex-induced vibrations.” In: *Journal of Fluids and Structures* 19.4 (2004), pp. 389–447.
- [90] R. H. Scanlan and J. J. Tomko. “Airfoil and bridge deck flutter derivatives.” In: *ASCE J Eng Mech Div* 97 (EM6 1971), pp. 1717–1737.
- [91] R. H. Scanlan. “Bridge aeroelasticity: Present state and future challenges.” In: *Journal of Wind Engineering and Industrial Aerodynamics* 36, Part 1 (1990), pp. 63–74.
- [92] H. C. Shellard. “Collapse of Cooling Towers in a Gale, Ferrybridge, 1 November 1965.” In: *Weather* 22.6 (1967), pp. 232–240. (Visited on 05/20/2015).
- [93] K. Shimada and T. Ishihara. “Predictability of unsteady two-dimensional $k - \varepsilon$ model on the aerodynamic instabilities of some rectangular prisms.” In: *Journal of Fluids and Structures* 28 (2012), pp. 20–39. (Visited on 06/05/2015).
- [94] M. L. Shur et al. “A hybrid RANS-LES approach with delayed-DES and wall-modelled LES capabilities.” In: *International Journal of Heat and Fluid Flow* 29.6 (2008), pp. 1638–1649.
- [95] P. E. Smirnov and F. R. Menter. “Sensitization of the SST Turbulence Model to Rotation and Curvature by Applying the Spalart–Shur Correction Term.” In: *Journal of Turbomachinery* 131.4 (2009), pp. 041010–041010.

- [96] P. R. Spalart et al. “Comments of the Feasibility of LES for Wings, and on a Hybrid RANS/LES Approach.” In: *Proceedings of the First AFOSR Conference on DNS/LES*. Ed. by C. Liu and Z. Liu. Ruston, LA: Greyden Press Columbus, 1997, pp. 137–147.
- [97] J. Spurk and N. Aksel. *Strömungslehre*. Springer London, Limited, 2006. 577 pp.
- [98] A. Steindl. *Torsionsschwingungen eines Gurtes unter Berücksichtigung der Längsspannung*. Tech. rep. Vienna University of Technology, 2012.
- [99] D. Sun et al. “Fluid–structure interaction of prismatic line-like structures, using LES and block-iterative coupling.” In: *Journal of Wind Engineering and Industrial Aerodynamics* 96.6 (2008), pp. 840–858. (Visited on 02/02/2015).
- [100] T. Tamura and Y. Itoh. “Unstable aerodynamic phenomena of a rectangular cylinder with critical section.” In: *Journal of Wind Engineering and Industrial Aerodynamics* 83.1 (1999), pp. 121–133.
- [101] T. Tamura and T. Miyagi. “The effect of turbulence on aerodynamic forces on a square cylinder with various corner shapes.” In: *Journal of Wind Engineering and Industrial Aerodynamics* 83.1 (1999), pp. 135–145.
- [102] T. Theodorsen. *General theory of aerodynamic instability and the mechanism of flutter*. 496. NACA, 1935, pp. 413–433.
- [103] F. Tubino. “Relationships among aerodynamic admittance functions, flutter derivatives and static coefficients for long-span bridges.” In: *Journal of Wind Engineering and Industrial Aerodynamics* 93.12 (2005), pp. 929–950.
- [104] M. Weinmann, R. D. Sandberg, and C. Doolan. “Tandem cylinder flow and noise predictions using a hybrid RANS/LES approach.” In: *International Journal of Heat and Fluid Flow* 50 (2014), pp. 263–278.
- [105] *Wilcox k-omega Model*. URL: <http://turbmodels.larc.nasa.gov/wilcox.html> (visited on 02/05/2015).
- [106] D. C. Wilcox. *Turbulence Modeling for CFD*. DCW Industries, 2006. 522 pp.
- [107] H. Zhou et al. “GPU implementation of lattice Boltzmann method for flows with curved boundaries.” In: *Computer Methods in Applied Mechanics and Engineering* 225–228 (2012), pp. 65–73. (Visited on 05/20/2015).

Lebenslauf

Name Johannes Strecha
Geburtsdatum, Geburtsort 21. Jänner 1986 in Wien, Österreich
Adresse Heinrich-Waßmuth Straße 4/1/11
2380 Perchtoldsdorf
Österreich

Schule

1992 – 1996 Volksschule, Perchtoldsdorf, Österreich
1996 – 2000 Bundesrealgymnasium, Perchtoldsdorf, Österreich
2000 – 2005 Höhere Technische Bundes-lehr und -versuchsanstalt (HTBLuVA)
Mödling, Österreich
Abschluss der Reife- und Diplomprüfung
Abschlussarbeit: *Ein Prüfstand für Dentalturbinen auf Flüssigkeits-
bremsbasis*

Studien

2006 – 2010 Bachelorstudium *Maschinenbau* an der TU Wien
Bachelorarbeit: *Ein Prüfplan für Sandungssysteme* (betreut durch Jo-
hann Wassermann, TU Wien)
2010 – 2012 Masterstudium *Maschinenbau* an der TU Wien
Masterarbeit: *Leak Testing of Display Cases Using Tracer-Gas Methods*
(betreut durch Herbert Steinrück, TU Wien)
2012 – 2015 Doktoratsstudium der Technischen Wissenschaften *Maschinenbau* an
der TU Wien
Dissertation: *Flow induced vibrations of a U-shaped belt* (betreut durch
Herbert Steinrück, TU Wien)

Berufstätigkeit

2011 – Projektassistent am Institut für Strömungsmechanik und Wärmeüber-
tragung der TU Wien

Johannes Strecha